Applications of Kinetic Inductance Detectors to Astronomy and Particle Physics

Antonio d'Addabbo

SAPIENZA
UNIVERSITÀ DI ROMA

UNIVERSITÉ GRENOBLE ALPES

THÈSE

Pour obtenir le grade de

DOCTEUR DE L'UNIVERSITÉ GRENOBLE ALPES

préparée dans le cadre d'une cotutelle entre l'*Université Grenoble Alpes* et Università degli studi La Sapienza (Rome)

Spécialité : **Astrophysique et milieux dilués**

Arrêté ministériel : le 6 janvier 2005 - 7 août 2006

Présentée par

Antonio D'addabbo

Thèse dirigée par **Alessandro Monfardini** et codirigée par **Paolo de Bernardis et Martino Calvo**

préparée au sein de l'Institut Néel (Grenoble)

dans **l'École doctorale Physique (Grenoble)**

Applications of Kinetic Inductance Detectors to Astronomy and Particle Physics

Thèse soutenue publiquement le **31 octobre 2014**,
devant le jury composé de :

M. Massimo Gervasi
Rapporteur du jury, Professeur, Université de Milan-Bicocca - Italie

M. Stefanos Marnieros
Rapporteur du jury, Charge de Recherche, CNRS Délégation Ile-de-France Sud

M. Flavio Gatti
Membre de jury, Professeur, Université de Gênes - Italie

M. Johann Collot
Président, Professeur, Université Grenoble 1

M. Alessandro Monfardini
Directeur de thèse, Chargé de Recherche, CNRS Délégation Alpes

M. Paolo de Bernardis
co-directeur de thèse, Professeur, Université de Rome "La Sapienza" - Italie

M. Alain BENOIT et M. Martino CALVO
Co-encadrant(s)

Applications of Kinetic Inductance Detectors to Astronomy and Particle Physics

by Antonio D'Addabbo

a joint PhD thesis between

Universitè Joseph Fourier (Grenoble, France)
and
"Sapienza Università" (Rome, Italy)

in agreement with

Institut Nèel, Centre National de la Recherche Scientifique (CNRS, France)

supported by

"Universitè Franco Italienne"

with the participation of

Institut de Radioastronomie Millimétrique (IRAM, France, Spain, Germany)
and Istituto Nazionale di Fisica Nucleare (INFN, Italy)

Principal Advisor: dr. Alessandro Monfardini
French co-Advisor: dr. Martino Calvo
Italian co-Advisor: prof. Paolo de Bernardis

October 2011 – September 2014

Contents

Abstract

Kinetic Inductance Detectors (KID) have recently drawn the attention of the low-temperature detectors community. High sensitivity, low fabrication complexity, small time constant and most notably the intrinsic capability of frequency multiplexed readout open new possibilities for experiments which need large format arrays of ultra sensitive detectors.

In *millimeter Astronomy*, the New IRAM KID Array (*NIKA*) instrument is today the most striking demonstration of this. It is a dual band hundreds-pixels KID based camera permanently installed at the focal plane of the IRAM 30-m telescope of Pico Veleta (Granada, Spain). Thanks to the NIKA observational campaigns, we could demonstrate performances comparable to the state-of-art of bolometers operating at the same wavelengths. The instrument is today open to the astronomers community. This encourages further array scaling and opens the path to next generation kilo-pixels ground-based cameras, like NIKA-2.

Building on the NIKA experience, we designed a cryogenic KID-camera demonstrator devoted to terrestrial millimeter astronomy in the framework of the *AstroKIDs* project (Rome, Italy). This activity concerned in particular the realization of a new optical system custom designed for an existing cryostat, as well as the set-up of the cryogenic and the electronic instrumentation needed for the KID operation. The first results showed encouraging performances.

The will to extend KID technology to space mission demands a careful investigation of their interaction with the Cosmic Rays (CR). The understanding of the physics of high-energy interactions in the substrate of our arrays is crucial in order to optimize the KID performances in the space environment. In the framework of the european *SPACEKIDS* project, this led us to implement a fully independent multiplexed readout system for the phonon-mediated particle detection with KID arrays (Grenoble, France). Using radioactive sources to simulate the primary CR hits, we studied the energy propagation induced by such interactions using different substrate solutions and array geometries. The first tests show promising results in damping the phonon propagation over distance and encourage deeper studies. We also made preliminary measurements of the detector performances in terms of time and energy resolution.

In *Particle Physics*, the rejection of the radioactive background is essential for several

bolometric experiments, especially for those searching for rare interactions, as neutrinoless double-beta decay (CUORE, LUCIFER, etc.). The development of more sensitive light detectors with a strong multiplexing factor is crucial to achieve the ultra-low background levels required, while ensuring a low impact on existing experiments. The *CALDER* project (Rome and LNGS, Italy) is a recent R&D in the framework of the CUORE experiment that aims at achieving this goal using the KID technology. Besides providing an alpha background rejection tool for CUORE, high-sensitivity KID-based light detectors could enable the dark matter search with the LUCIFER technique.

The work reported through this PhD thesis concerns the development of optimized Lumped Element Kinetic Inductance Detectors (LEKID) and the implementation of dedicated readout techniques for the aforementioned activities.

Part I

Introduction to Kinetic Inductance Detectors

Chapter 1

Scientific motivation

1.1 Low temperature detectors and multiplexing

Throughout the last decades, low temperature (sub-Kelvin) detectors have benefited from intense research activity enjoying years of technical improvements. Once intrinsic statistical photon count limits are achieved, better sensitivity can only be realized with longer integration times or by increasing the focal plane area and pixel count. Instruments equipped with hundreds of pixels in focal plane arrays have dominated continuum sub-millimeter and millimeter astronomy in the last years.

This array scaling has resulted in increasingly complex readout electronics that must implement ad-hoc techniques to reduce cryogenic wire-counts. This can be achieved by reading-out several detectors, with a single electrical circuit. These techniques are known as *multiplexing*. For example, in *time-domain multiplexing* (TDM) data coming from different detectors are separated with certain delays, rapidly switching power supply (voltages) between their bias circuits. In *frequency-domain multiplexing* (FDM), the bandwidth ΔF of each wire is shared between multiple pixels. If ΔF is larger then the bandwidth of the expected signal Δf, it is possible to read a number $N \leq \Delta F/\Delta f$ of detectors at once. In order to do this, each of the N signals is suitably modulated, so that the signal transmitted by a single wire is made up by the superposition of N sinusoidal contributes. Demodulating opportunely it is then possible to recover the information relative to a single detector. One of the most adopted method consists in connecting each detector bias system to a resonant RLC circuit, so that it can be fed only at its own resonance frequency $f = \frac{1}{2\pi\sqrt{LC}}$. The multiplexing is then easily achieved by driving the system with an alternate current consisting in a comb of tones, each one corresponding to the specific frequency associated to a single detector.

The FDM technique has been previously demonstrated by integrating *Superconducting QUantum Interference Devices* (SQUIDs) with a type of bolometer known as the *Transition Edge Sensor* (TES) [1]. Full-sampling arrays from hundreds to thousands of pixels in a

single array are reaching maturity, offering increased mapping speed and decreased per-pixel manufacturing costs (e.g., SPT [2], APEX-SZ [3], LABOCA [4], SCUBA-2 [5], BICEPS-2 [6]). Despite these considerable advances, further array scaling is strongly limited by the multiplexing factor of the readout electronics. In order to provide the very large multiplexing ratios required for many-kilopixel arrays, it is advisable to develop detectors intrinsically adapted to strong frequency-domain multiplexing.

1.2 Kinetic Inductance Detectors

First proposed about ten years ago [7], *Kinetic Inductance Detectors* (KID) represent an alternative detector technology to traditional bolometers for future large format array instruments. Based on low-volume superconducting circuits, KID are high-quality microwave resonators that change their electromagnetic properties in response to incoming radiation. Unlike bolometers, where incident optical power is first converted into thermal phonons and then transduced by a suitable thermistor into a measurable electrical signal [8], in a superconductor absorbed photons exceeding the gap energy result in *Cooper Pairs* breaking and change the ratio of paired to unpaired (*quasi-particles*) charge carriers. For specific geometries, the concurrent rise in quasi-particle density results in a change in the surface reactance of the material, which is expressed by the so-called *Kinetic Inductance* [9]. KID harness this changing reactance of the superconductor by embedding it in an high quality resonant circuit. Each detector is electromagnetically coupled to a common readout line (*feedline*), which is driven by a continuous comb of tones at the resonance frequencies. The transmitted phases and amplitudes of these tones are monitored continuously. An optical power load induces deviations in the kinetic inductance, resulting in a shift of the resonant frequencies of the KID and then in a measurable signal (fig. 1.1). Residual resistivity losses are strongly suppressed in a superconductor so that very high quality factors can be achieved. This ensures high sensitivities and strong multiplexing factor [7], making KID the suitable technology for next generation thousand-pixels cameras.

Another remarkable property of KID is the easiness of fabrication. Building standard bolometers requires a complex process with many different lithography steps, while the basic version of a KID is obtained with a single deposition. The typical devices used in this thesis are fabricated with a thin (tens of nanometers) Aluminum (Al) deposition on a standard (hundreds on microns) Silicon (Si) wafer, referred to as *substrate*. These materials and the simple architecture make the KID array very resistant to mechanical shock, thermal cycling and radiation, so they are well suited also for space environments. Several device geometries have been proposed in the last years. The two mostly used KID designs are:

1. *Antenna-coupled KID.* A distributed (quarter-wave) resonator is terminated by an absorber structure (antenna + microlens) (fig. 1.2(a));

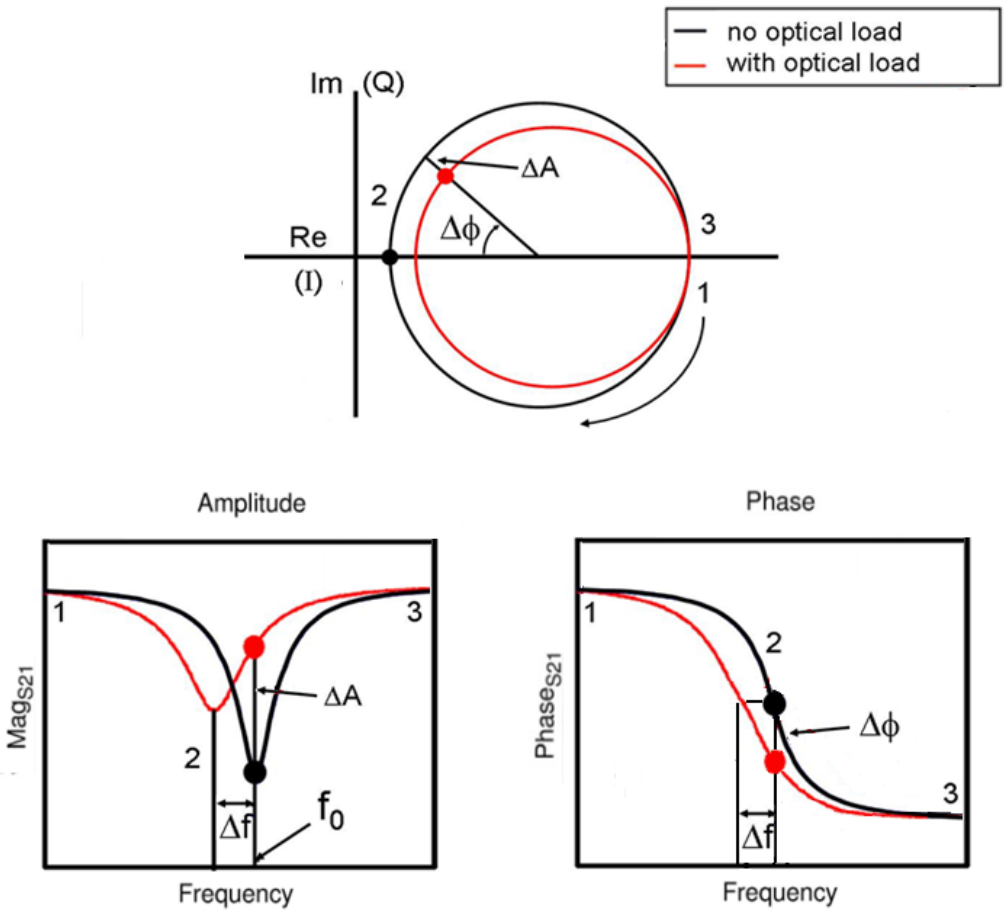

Figure 1.1: *Typical resonance shape of a Kinetic Inductance Detector, obtained performing a frequency sweep towards increasing frequencies* ($1 \rightarrow 3$). *(Top) The resonance circle in the complex plane (*IQ-circle*); (left) the transmitted amplitude and (right) phase of the signal.* f_0 *represents the resonance frequency with no optical load (black lines). Illuminating the detector (red lines) results in a shift of the signal amplitude* (ΔA) *and phase* ($\Delta\phi$).

2. *Lumped Element KID (LEKID).* A fully planar design is properly shaped to enable direct absorption in the resonator itself [10] (fig. 1.2(b)).

This thesis concerns detectors of the latter type. In the former part of this thesis we will deeply describe the LEKID theory and the multiplexed readout techniques involved in this work.

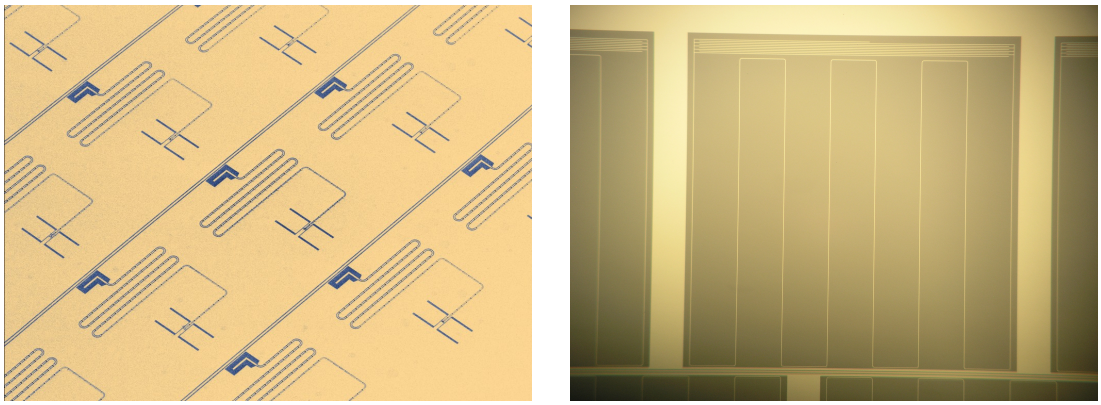

(a) (b)

Figure 1.2: *(a) Antenna-coupled KID and (b) Lumped Element KID typical design.*

1.3 Millimeter Astronomy

The last years saw an increasing importance of millimeter observations for Cosmology and Astrophysics. The advent of kilo-pixel arrays opened up the sub-mm/mm-wave sky and revolutionized the way we understand our Universe. Thanks to their increased sensitivity and mapping speed, such arrays allowed high-precision studies of *Cosmic Microwave Background* (CMB) temperature and polarization anisotropies, providing an unprecedented understanding of the early Universe and of the formation of the first proto-structures [11] [12]. Moreover, such arrays have detected galaxy clusters out to their redshift of formation, resolved a significant portion of the *Cosmic far-Infrared Background* (CIB) into dusty star-forming galaxies, and surveyed for proto-stellar cores and young stellar objects in our own and nearby galaxies [13].

In the following we present a brief overview of current topics in millimeter and sub-millimeter astronomy. We divided this research in three main areas that are motivating the rapid development of new technologies over recent years.

1.3.1 Star-forming regions in the Galaxy

.

The pre-stellar phases in molecular clouds are hidden by cold dust ($\sim 10K$) which can only be observed at sub-millimeter wavelengths [14]. The presence of filamentary structures connecting cores revealed by ground-based (e.g. MAMBO [15]) and satellite-born (e.g. Herschel [16]) telescopes suggest a close connection between the observed filaments and the formation mechanism of prestellar cores and protostars [17]. The linearly-polarized continuum emission from magnetically-aligned dust grains is a powerful tool to measure the morphology and structure of magnetic field lines in star-forming clouds and cores [18]. Polarimetric observations at

sub-millimeter wavelength can thus be precious to understand the role of magnetic fields in shaping these structures. On the other hand, multi-wavelength observations could be used to refine models of the dust grains providing the emission, in order to relate better the observed fluxes to the underlying dust and gas masses. The efficiency of these methods is related to the capability in resolving star-formation region sub-structures. A complete high-resolution census of protostellar cores and young stellar objects in our own galaxy would provide critical input to models of star formation, predicting their mass function and clustering properties.

1.3.2 High-redshift galaxies

.

High-redshift, dusty, star-forming galaxies are a class of objects discovered in the last years of the last century thanks to the first generation of millimeter/submillimeter cameras (e.g. BOLOCAM [19], MAMBO [15], SCUBA [20]). Since the very first surveys, it has looked clear that these objects are the ancestors of present-day elliptical galaxies [21]. Sub-mm galaxies reflect an epoch ($z > 1$) of extremely intense star-formation, hugely larger ($\sim 10^3 \div 10^4$) than in the present-day Universe. As an example,this activity generated roughly half of the energy output of all galaxies in the early Universe, and created a class of very dusty objects whose stellar photon emission was largely reprocessed into the far-infrared and submillimeter bands (*K-correction*) [22]. At wavelengths longer than about $250\mu m$, the flux density from galaxies at $z > 1$ ceases to decline with the inverse square of distance, but instead remains approximately constant with increasing redshift thanks to the K-correction [23]. This provides an essentially redshift-independent measure of the sub-mm galaxies luminosity. The effect is more pronounced at longer wavelengths: in the mm waveband more distant galaxies are expected to produce greater flux densities than their more proximate counterparts.

Realizing complete surveys of high-redshift sub-mm galaxies is therefore essential to our understanding of galaxy formation. The strong K-correction at sub-millimeter wavelengths counteracts the distance dimming, enabling in principle dusty star-forming galaxies detection at redshifts up to $z \sim 10 \div 20$. Discovering these objects requires a millimeter-wavelength camera with fast mapping speed. Multiple wavelengths are however required in order to measure the redshift and to study the role of dark matter halos in the galaxy clustering. It has been proven that a low frequency instrument with sufficiently high sensitivity would also enable the optical counterpart detection (e.g., from Herschel, SPIRE) [24].

1.3.3 Cosmic Microwave Background (CMB)

At a temperature of 2.725 K, the CMB spectrum peaks at millimeter wavelengths. CMB measurements have proven to be an exceptional tool for studying the early Universe [25] and current ground-based and satellite experiments are contributing with new precision data (fig.

1.3). The recent data release of the ESA satellite Planck showed an impressive completeness on the study of CMB science (fig. 1.4), leading to *Lambda Cold Dark Matter* (ΛCDM) model parameters significantly different from those previously estimated, with weaker cosmological constant (by $\sim 2\%$), more baryons (by $\sim 3\%$), and more cold dark matter (by $\sim 5\%$) [26]. At

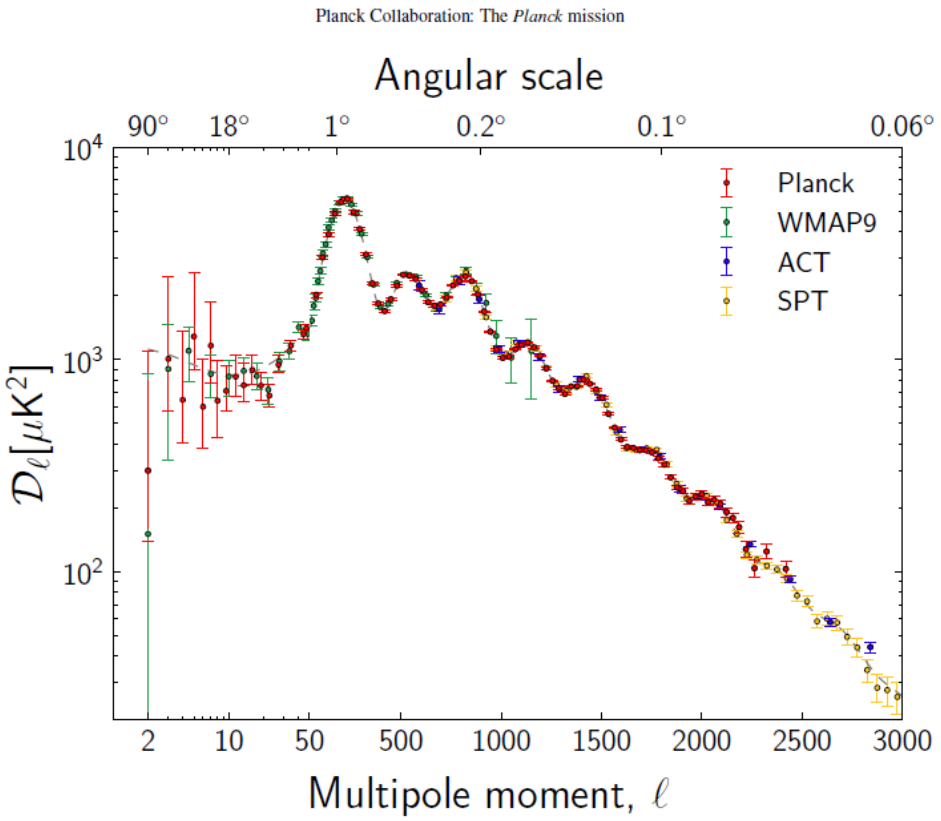

Figure 1.3: *Measured angular power spectra of Planck, WMAP9, ACT, and SPT. The model plotted is Planck's best-fit model (labelled [Planck+WP+HighL] in [26]) including Planck temperature, WMAP polarization, ACT, and SPT. The horizontal axis is logarithmic up to $\ell = 50$, and linear beyond.*

the largest angular scales, CMB surveys are naturally suited for satellite-borne experiment able to avoid the overwhelming contamination due to atmospheric gradients and to cover a wide frequency range. At smallest scales ground-based experiments are very efficient, because they use very large telescopes and shielding systems, difficult to accommodate on a space mission. The atmospheric windows at 140, 220 and 345 GHz include very interesting frequencies for the study of the CMB with ground-based telescopes. Especially the first two bands are widely used for ground-based surveys of CMB temperature and polarization anisotropies. Two ground experiments, South Pole Telescope (SPT) and Atacama Cosmology Telescope (ACT), have already produced important results in the measurement of anisotropies at small scales [27]

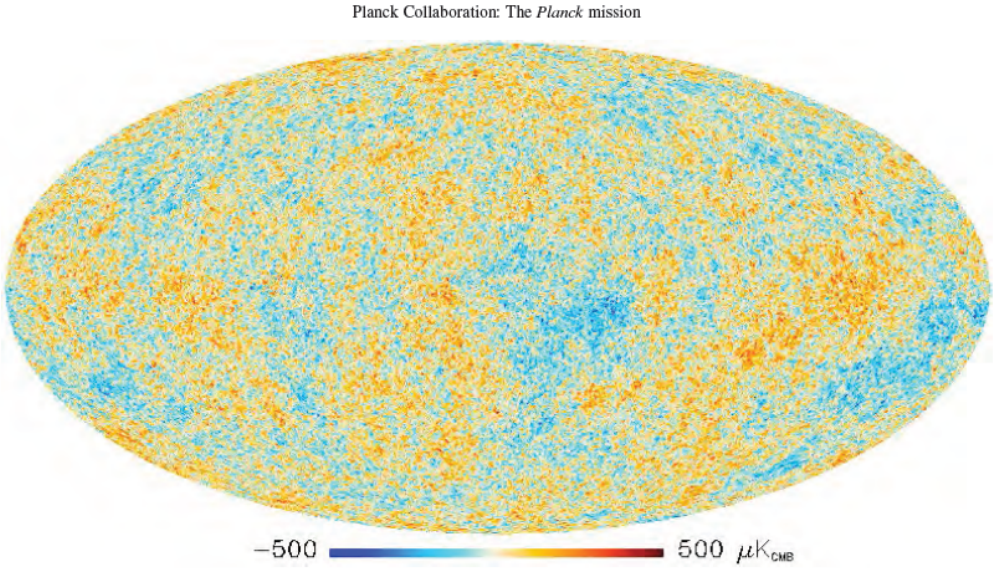

Figure 1.4: *The Planck satellite CMB map. [26]*

[28] (fig. 1.3). Small scale anisotropies data is of extreme importance to test the ΛCDM model. In order to carry out even more precise measurements, the next generation of ground based experiments will require extremely large-format array coupled to very large aperture telescopes.

Of particular interest is the *Sunyaev-Zel'dovich effect* (SZE) [29] in the clusters of galaxies, which distorts the CMB spectrum at millimeter and radio wavelengths. The SZE is induced via inverse-Compton scattering on the CMB photons by the hot electrons of the Intra-Cluster Medium (ICM). The SZE imprints a typical spectral signature in the CMB, which spectral brightness decreases at frequency lower than 220 GHz, while it increases at higher energies. This can be used to map the pressure and thermal energy distribution of the ICM, improving our knowledge about the dynamics and the kinematics of formation and evolution of galaxy clusters. Furthermore, the SZE allows the 'blind' detection of cluster of galaxies, i.e. without a counterpart emission at higher frequencies. This can be used to realize clusters surveys and carry out cosmological studies. The Planck [30], SPT [31] and ACT [32] experiments have published the first catalogs including hundreds of new SZ clusters, enabling their use to probe cosmological models and the properties of diffuse ICM.

However, the three surveys suffer from their relatively poor angular resolutions (from 5' for Planck to 1' for SPT or ACT) and are thus not able to resolve cluster sub-structures. Furthermore, to enable the separation of cluster SZ effects from primordial CMB anisotropy, sub-millimeter galaxies, and radio point sources, an instrument capable of mapping massive galaxy clusters out to the virial radius and in multiple spectral bands is required. A large field

of view ($\sim 10' \div 20'$) with high mapping speed and sub-arcminute angular resolution would be ideal.

The recent detection of the B-modes in the polarization of the CMB by BICEP-2 [33] opens the possibility to access the very first split second after the Big Bang. A stochastic background of tensor fluctuations of the metric (gravitational waves) generated at this moment as consequence of the exponential expansion of the Universe is a general prediction of all the inflation models. These gravitational waves would have imprinted a unique signature upon the CMB, with a sub-dominant 'curl' or *B-mode* pattern polarization component at degree angular scales that cannot be generated primordially by density perturbations [34]. The amplitude of this signal is expected to be below $0.1\mu K$, and is parametrized by r, the tensor-to-scalar ratio, which specifies the power in gravitational waves (tensor perturbations) as a fraction of the power in density (scalar) perturbations [35]. The parameter r depends on the energy scale of inflation and was expected in the range $0.01 - 0.2$. BICEP-2 have measured $r = 0.2$. The detection is still controversial because this value should has been detectable by the Planck satellite too. Although the scientific community is waiting for the confirmation by the Planck collaboration, the first detection of B-mode polarization of the CMB provide a unique confirmation of inflation and a probe of its energy scale. Many experiments like EBEX [36], ACT-pol [37], SPT-pol [38] and LSPE [39], are planned in the next future to confirm the results found by BICEP-2.

1.3.4 Future prospects for KID cameras

Despite these successes, there are many fundamental questions that still wait for an answer. Among them are the role of gravitational waves in the inflation era, the growth of the cosmic web under the influence of dark matter, the evolution of galaxies and cluster of galaxies throughout the cosmic history, and the star formation from dense molecular clouds while interacting with larger structures at the galactic scale. In order to provide these answers, the next generation of high-precision millimeter and sub-millimeter wave experiments will not disregard two key features:

- Increased angular resolution. The size of the telescope is essential in order to provide high-resolution maps of astrophysical objects at high-redshift, which have proven to be an indispensable tool for understanding the early stages of star and galaxy formation. Moreover, the study of cluster of galaxies via SZE can provide deep probes of Cosmology, of the proprieties of the hot intra-cluster gases, and of the evolution of large-scale structures.

- Increased mapping speed. The size of the Field-Of-View (FOV) is crucial in order to map large areas of the sky. The possibility to realize high-sensitivity surveys is related to the

capability to operate large arrays of detectors, obtaining longer integration time-frames on the sky and fully exploiting the telescope FOV.

The development of instruments designed for large telescopes with correspondingly high angular resolution and large FOV will be decisive future cosmological studies. The scientific community is spending remarkable efforts in order to provide multi-colors instruments with square degree FOV combined with few-arcseconds resolution. To meet these requirements, kilo-pixels cameras with multiple band focal planes are mandatory. The high multiplex density of KID arrays relative to bolometer architectures will be decisive in reaching these enormous pixel counts. In this scenario, KID-based instruments can play a major role in the discovery of the new physics inside and beyond the ΛCDM model. The first most striking demonstration is represented by the NIKA project, which is discussed in the middle part of this thesis. We present the results from the last observational campaigns of the New IRAM KID Array (NIKA), a dual-band kinetic inductance camera custom designed and realized for the IRAM (Institut de Radioastronomie Millimétrique) 30-m telescope at Pico Veleta observatory (Granada, Spain) [40]. In its last configuration, the focal plane is equipped with 356 pixels cooled at 100 mK and based on Al LEKID. The NIKA instrument is conceived to observe the sky at wavelengths of 1.25 and 2.14 mm, with resolutions of 13" and 18", and sensitivities of 40 and 14 $mJy \cdot \sqrt{s}$, respectively. These recently demonstrated performances [41] make the NIKA camera a competitive astrophysical instrument, opened to the scientific community as an IRAM common user facility in February 2014. The NIKA camera is a pathfinder instrument devoted to the next generation kilo-pixels kinetic inductance camera, NIKA-2 [42], to be commissioned in 2015. NIKA-2 will mount $\sim$ 5000 LEKID distributed among 140 and 220 GHz focal planes, with the possibility of linear polarization measurements in the latter band.

Other KID-based instruments are in development for mm and sub-mm astronomy. Among these we cite the MUltiwavelength Sub/millimeter Inductance Camera (MUSIC) and the A-MKID instrument. MUSIC is a multi-color instrument for the Caltech Submillimeter Observatory in Hawaii [43]. It is designed to have a 14' field-of-view sampled in four spectral bands at 0.87, 1.04, 1.33, and 1.98 mm. The focal plane is instrumented with 2304 detectors (576 pixels per band), and is based on antenna coupled MKID. A further scaling in the pixel count is represented by the A-MKID instrument, a very large-format, antenna coupled MKID array conceived for the APEX (Atacama Pathfinder EXperiment) 12-m telescope in the northern Chili. The A-MKID is a dual band camera, with bands centered at 350 GHz and 850 GHz. In its final configuration, the focal plane will be equipped with $\sim$ 500 and $\sim$ 16000 pixels respectively, providing a field of view of 15×15 deg^2.

1.4 Application to Particle Physics

The development of KID for Astronomy applications is relatively mature, but this in not the only field of research where their remarkable proprieties turned out to be useful. Thanks to their strong multiplexing factor, KID are well suited for any experiment requiring a very-large number of ultra-sensitive detectors cooled at very low temperatures. These are often the main requirements of many Particle Physics experiments, especially focusing on rare event search. Besides photons, every particle with energy exceeding the superconducting gap, can break Cooper pairs and induce a variation in the quasi-particle density. However, higher energy particles cannot be directly absorbed in the superconductor due to its extremely small thickness (thin films are required in order to get high responsivities, see chap. 2). Nevertheless, the energy produced by particle interactions in the substrate can propagate mediated by the crystal lattice vibrations, before being absorbed in the detectors. This process is called *phonon-mediated detection* and uses the phonons in the array wafer as pair-breaking mechanism. Deploying this mechanism, phonon-mediated KID have been proposed for several different applications:

- X-rays energy resolved detection [44] [45];
- X-rays and cosmic rays position resolved detectors [46] [47] [45];
- Study of the phonon energy propagation in the substrate using α particles [48];
- Direct Dark Matter and WIMPs (Weakly Interacting Massive Particles) detection [49] [50];
- Direct neutrino mass determination [51]
- Rejection tool for neutrino double-β decay search [52] ;

In the last part of this thesis we will report on topics 2. and 3. In particular, with the *SPAKEKIDS* project, we widely studied high energy interactions in KID array, in order to adapt the KID technology to satellite-borne telescopes. In the end, we will also tackle topic 6., presenting the start-up operations of the *CALDER* project, a recent R&D in the framework of the CUORE experiment [53].

1.5 Rare events and neutrino science

In the last two decades, the search for rare events physics has sharply accelerated. The determination of the neutrino nature and the search for Dark Matter are crucial in understanding both new physics beyond the well established Standard Model of interactions and the ΛCDM-model of universe. Neutrinos are extremely abundant in the Universe ($\approx 336/cm^3$) and have

played an essential role in the formation of the large-scale structure of the Universe, in Big Bang nucleosynthesis, in anisotropies of Cosmic Microwave Background radiation, in arising of matter-antimatter asymmetry [54]. Viceversa, the description of these cosmological phenomena can constrains the neutrino physics. Dark Matter as well has surely been important for the early/cold evolutionary stages of the main astrophysical and cosmological structures, whose comprehension can impose strong limits on the Dark Matter nature. Thanks to these mutual benefits, Astrophysics, Cosmology and Particle Physics are increasingly getting in touch.

Extending the use of typical astrophysical tools to Particle Physics experiments, could be the technological challenge which best embodies the spirit of this synergy. In the following, we give a brief overview on the main topics involved in the new born rare event search physics.

1.5.1 Neutrino mass

A *neutrino* is an electrically neutral, weakly interacting elementary subatomic particle with half-integer spin. Oscillation experiments suggest that neutrinos have non-zero mass [55], but the upper bounds established for their mass are tiny even by the standards of subatomic particles. There are three types, or *flavors*, of neutrinos: electron neutrinos, muon neutrinos and tau neutrinos. Each type is associated with an antiparticle, the *antineutrino*, which also has neutral electric charge and half-integer spin. Whether or not the neutrino and its corresponding antineutrino are identical particles has not yet been resolved. The scientific community is working hard in order to determine the neutrino nature and its absolute mass scale. This research can be described by three classes of experiments:

- **Cosmology** – Studying the anisotropies of CMB and the large scale structures data allows to infer the sum of neutrino flavors masses. The main effect of massive neutrinos is to smear out fluctuations at small scales, deformating the high-ℓ anisotropies power spectrum. This approach is strongly model and analysis dependent. The upper limit found by the Planck satellite is $\sum_i(\nu_i) < 0.66eV/c^2$ [26].

- **Direct Neutrino mass determination** – In this case, neutrino mass determination is based purely on relativistic kinematics measurements without further assumptions. Two approaches are possible:

    1. Time-of-flight measurements – It is linked with very energetic cosmic events, like a core-collapse supernova. The first test in this sense was SN1987a through the non-observation of a dependence on energy of the arrival time of supernova neutrinos, that gave an upper limit for the neutrino mass of $5.7eV/c^2$ [56]. These cosmic events are however too rare to give real chances to this kind of measurements in the near future.

2. Precision investigations of weak decays –Here the target of observation is not the neutrino itself, but the charged particles produced by the decay. In this case, the signature of a non-zero electron neutrino mass m_{ν_e} is a tiny modification of the spectrum of the β-electrons near its endpoint, which has to be measured with very high precision. A few groups have started this research, like the MARE experiment [57], and KID could be proposed as detectors for the next generation experiments [58].

- **Neutrinoless double β decay ($0\nu\beta\beta$)** – Neutrinoless double beta decay is an hypothesized nuclear transition, whose existence is forbidden in the minimal Standard model. Its possible discovery is the only known mean of determining the nature of neutrinos, whether Dirac fermions (neutrino and antineutrino are two different particles) or Majorana fermions (neutrino is its own antiparticle). The $0\nu\beta\beta$ decay predicts the occurrence of two simultaneous β-decays in the same nucleus, with the emission of two β-electrons (positrons) while the (anti-)neutrino emitted at one vertex is absorbed at the other vertex as a neutrino(anti-neutrino). Besides establishing that neutrinos are Majorana particles, the first observation of a $0\nu\beta\beta$ transition will definitively demonstrate that neutrinos are massive. Two experimental methods are possible for the measure of $0\nu\beta\beta$ decay:

  1. the source of the decay coincides with the detector, measuring the sum of the energies of the two electrons;
  2. tracking calorimeters able to observe an external source with the capability to measure separately the two electrons.

  Examples of experiments using radioactive materials as cryo-blometers (method 1.) are LUCIFER [59] and CUORE [53] (with its predecessor CUORICINO [60]) at LNGS (Laboratori Nazionali del Gran Sasso, Italy). The development of light detectors for such experiments will provide a discrimination tool that should increase their sensitivity up to a factor ~ 6 compared to present limits. Since the expected decay rate scales as the root of the radioactive mass, these experiments involve huge quantities ($\sim 1 tons$) of bolometers. 'Upholstering' their surface requires wide area low-temperature high-sensitive detectors, with strong multiplexing factors. The CALDER project (chap. 9) has already taken this path, proposing KID as phonon-mediated light detectors for CUORE [52].

1.5.2 Dark Matter experiments

One of the most remarkable results in astrophysics of the recent years is the proof that about one third of the energy density of the Universe is an unknown form of cold, non-baryonic *Dark*

Matter (DM). This DM is inferred from gravitational effects, but is non-luminous and weakly interacts with normal matter [61]. Looking for DM candidates, the only stable, uncharged, and non-zero mass particle in the Standard Model is the neutrino. However the mass of the neutrino is too small to account for the required total DM in the Universe and its relativistic nature is incompatible with clustering in large-structure formation epoch [62]. One promising candidates which would have the properties of non-baryonic cold DM are known as *Weakly-Interacting Massive Particles* (WIMPs), a class of neutral particles with mass and interactions characteristic of the electroweak scale [63]. It is expected that WIMPs can be directly detected via elastic-scattering interactions with ordinary matter nuclei [64]. The WIMP-nucleon cross section is estimated to be around a few interactions per kg of target mass and per day [65]. The average energy imparted to the recoiling nucleus is a few keV to tens of keV, depending on the WIMP mass and energy. Therefore direct detection experiments typically search for nuclear recoils induced by WIMPs, discriminating the background from β/γ particles ($\sim 100eV$). Several experiments have been setup to look for DM. The Cold Dark Matter Search (CDMS and CDMS II [66]) uses TES sensors to measure the phonons deposited in the target crystal. Phonons created by interactions in the crystal travel to the surface where they are converted to quasi-particles in a thin aluminum film. These quasi-particles then diffuse to one of the TES where they are measured. A second, independent measurement of the ionization signal based on the quenching effect distinguishes between electrons and potential WIMP interactions. The ratio of the two signals gives a very efficient discrimination tool for events occurring in the bulk of the detector. Unfortunately events close to the detector surface suffer from a reduced charge signal, which moves some of the electron recoil background into the signal region. The position sensitivity of the detector helps to identify and remove the background of surface events. A more precise determination of the position of event colud be achieved by instrumenting the whole surface of the crystal.

Other DM search experiment, like EDELWEISS [67], use the same basic idea as CDMS, but a Neutron-Transmutation Doped (NTD) thermistor instead of a TES. This makes detector production much easier.

In this context, one of the future possibilities is to substitute the TES with KID, in order to obtain a higher surface sampling with more detectors. KID have been proposed for future experiments, like Super CDMS [66] and EURECA [68], to detect the a-thermal signal from lattice vibrations (*phonon-mediated detectors*). This should lead to a more precise determination of the interaction position and a better measurement of the deposited energy. Hundreds-KID arrays only need one input and one output line, and the possibility of making large room temperature array readouts allow a more straightforward scale-up in the number of detectors than is currently possible. KID are also much simpler to fabricate then TES. A DM detector using phonon-mediated KID could provide significant improvements in both low energy electron rejection and in scalability, the two main requirements for a next generation

WIMP search experiment.

Chapter 2

Kinetic Inductance Detectors theory

The kinetic inductance is an internal characteristic of each conductor, due to the inertia of its charge carriers. In a normal metal it is not significant, because the very short carrier scattering time results in the dissipation of the inertial energy through Joule heating. In a superconductor below its critical temperature however, an energy gap (Δ) in the carriers density of states appears. The conduction electrons are bound two-by-two into charge-carriers that do not undergo scattering with the ion lattice, the so-called *Cooper pairs*. Unlike unbound electrons, Cooper pairs can store their kinetic energy with no dissipation and hence do not contribute any electrical resistance. Though this has no effect in dc, working at non-zero frequencies permits a continuous exchange of energy between the super-current and the electromagnetic field. The electromagnetic energy is stored into Cooper pairs in the form of their kinetic energy, and then returned to the field when it reverses. Before effectively invert current direction, Cooper pairs have to curb. Their inertia delays this energy restitution and results in an effective reactive impedance known as *kinetic inductance* (L_{kin}). As a consequence, a superconductor shows a complex surface impedance

$$Z_s = R_s + jX_s = R_s + j\omega L_{kin} \tag{2.1}$$

where X_s is the surface reactance due to the energy flow between the Cooper pairs and the electromagnetic field at the angular frequency ω, and R_s is the surface resistance accounting for the losses caused by the small fraction of electrons that are not condensed in Cooper pairs. These electrons, in the lattice, are called *quasi-particles*. In the superconductive state $R_s \ll X_s$ and the surface impedance is dominated by the kinetic inductance.

Kinetic Inductance Detectors (KID) are Cooper pairs breaking detectors based on high-quality resonant circuits. The amount of energy required to break a Cooper pair into two quasi-particles is 2Δ. Incident particles exceeding this energy can break a Cooper pair (fig.

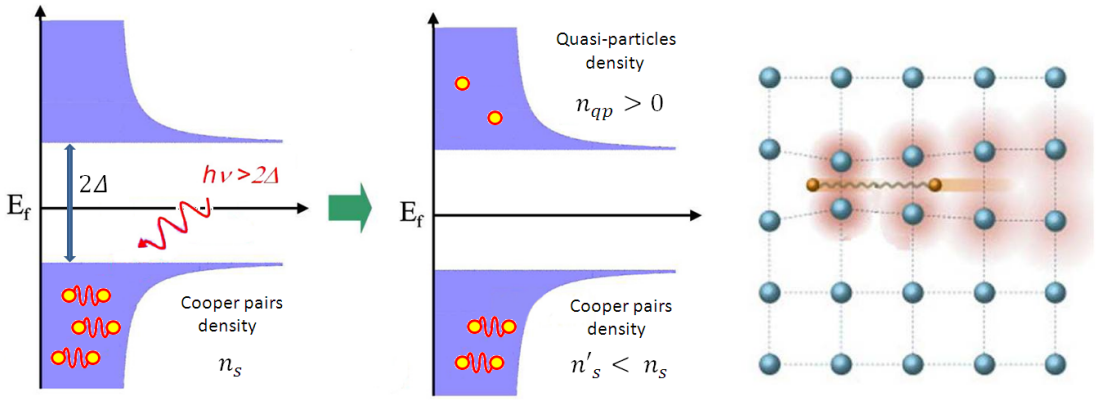

(a) (b)

Figure 2.1: *(a) Schematic of the interaction between radiation and electrons in a superconductor. The incoming energy $E = h\nu > 2\Delta$ can break a Cooper pairs increasing the quasi-particle density. (b) Representation of the interaction between two electrons bound in a Cooper pair.*

2.1(a)), producing a concurrent change in the complex conductivity $\sigma = \sigma_1 - j \cdot \sigma_2$, where σ_2 is directly related to the kinetic inductance. This results in a shift in the KID resonance frequency and a change of the resonator quality factor. Both can be measured by the readout electronics. The non-local Mattis-Bardeen theory can be used to solve for changes in both σ_1 and σ_2 due to incoming energy, allowing a direct calculation of the resonator frequency response to incident power [69].

2.1 Introduction to Superconductivity

We summarize in this paragraph only a few concepts and definitions using in the following chapters. For more details refer to appendix A.

2.1.1 Basic concepts

A superconductor is a material that exhibits zero electrical dc resistance below a given transition temperature T_c, called *critical temperature*. At such temperatures electrons-phonon interactions overcome the electron-electron repulsion at long distances and the electrons condense into Cooper Pairs. The maximum distance over which the binding of the two electrons is effective is called the *coherence length* ξ_0 of a Cooper pair. Typical elemental superconductors exhibit a ξ_0 of about $1\mu m$, such as aluminum with $\xi_0 = 1600nm$ [70]. In a nutshell, this process can be intuitively seen by imaging that each electron was attracted by the positive ions of the lattice just deformed by the passage of another electron (fig. 2.1(b)). In this way

electrons are paired-up two-by-two into the so called *Cooper pairs*, with the binding energy

$$2\Delta \approx 3.52 k_B T_c \tag{2.2}$$

where k_B is the Boltzmann constant and Δ is the *energy gap* of the superconductor, or *superconducting gap* (appendix A.1). Typical value for thin Aluminum film ($\sim 20nm$) are $T_c \sim 1.4K$ and $\Delta \sim 0.2meV$, for $T \ll T_c$ (par. 4.2.2).

The superconductors are not only perfect conductors, but show another remarkable property: perfect diamagnetism. It consists in a complete expulsion of any magnetic field from the bulk of the superconductor itself. The Cooper pairs can indeed generate opposite non-dissipative currents at its surface, that cancel out any magnetic flux trying to penetrate into it. The *London penetration depth* is defined as the distance over which an external field can penetrate into the superconductor, before being damped by a factor e. It is given by

$$\lambda_L = \sqrt{\frac{m}{\mu_0 n_s e^2}} \tag{2.3}$$

where m is the electron mass and and n_s the Cooper pairs density. For bulk aluminum, for example, the theoretic value is $\lambda_L \approx 16nm$ [70].

As previously mentioned, not all the electrons are bound in Cooper pairs. There is still at $T > 0$ a population of unbound charge carriers that we call *quasi-particles*. From T_c down to $0K$ the quasi-particles density n_{qp} decreases from n to 0, namely n the total number of charge carriers for the metal in its normal state. Correspondingly, the Cooper pair density $n_s = n - n_{qp}$ increases. This temperature dependence can be approximated by the empiric formula [71]

$$\frac{n_s}{n} = 1 - \left(\frac{T}{T_c}\right)^4 \tag{2.4}$$

Substituting this equation in 2.3 we can find an empirical approximation of the London penetration depth temperature dependence

$$\lambda_L = \frac{\lambda_{L0}}{\sqrt{1 - \left(\frac{T}{T_c}\right)^4}} \tag{2.5}$$

where $\lambda_{L0} = \sqrt{\frac{m}{\mu_0 n e^2}}$ is the London penetration depth for $T \to 0K$. Here due to the domination of Cooper pairs, $n_s \to n$ and λ_L reaches its minimum value λ_{L0}. If the temperature increases, λ_L increases as well becoming infinite at $T = T_c$, when all Cooper pairs are broken up into quasi particles and there is no supercurrent able to screen the magnetic field. We can

underline this using eq. 2.4, so that

$$\lambda_L = \lambda_{L0}\sqrt{\frac{n}{n_s}} \tag{2.6}$$

2.1.2 Conductivity by Two-fluid model

The total conductivity can be write as the sum of its real and imaginary components

$$\sigma = \sigma_1 - j\sigma_2 \tag{2.7}$$

The phenomenological description of the coexistence of two different populations of charge carriers in a superconductor is provided by the *Two-fluids model* (see A.3). Using this model we can write the conductivity as

$$\sigma = \frac{n_{qp}}{n}\sigma_0 - j\frac{1}{\omega\mu_0\lambda_L^2} \tag{2.8}$$

where σ_0 is the normal conductivity just before crossing the transition T_c (eq. A.13) and

$$\lambda_L = \sqrt{\frac{1}{\omega\mu_0\sigma_2}} \tag{2.9}$$

follows combining eq. 2.3 and A.23. Using 2.4 and 2.5 we can obtain the explicit dependence of the conductivity on temperature of a superconductor described by the two-fluids model

$$\sigma = \left(\frac{T}{T_c}\right)^4\sigma_0 - j\frac{1-\left(\frac{T}{T_c}\right)^4}{\omega\mu_0\lambda_{L0}^2} \tag{2.10}$$

or writing explicitly its real and imaginary components

$$\sigma_1 = \left(\frac{T}{T_c}\right)^4\sigma_0 \tag{2.11}$$

$$\sigma_2 = -\frac{1-\left(\frac{T}{T_c}\right)^4}{\omega\mu_0\lambda_{L0}^2} \tag{2.12}$$

This conductivity depends on the material properties of the superconductor $(T_c, \sigma_0, \lambda_0)$ and on the operating frequency ω and temperature T.

2.1.3 Conductivity by Mattis-Bardeen description

In many superconductors, such as aluminum, the coherence length dominates over the London penetration depth ($\lambda_L << \xi_0$). The large range of the electron-electron interaction somehow

lower their capability to screen an external field, enhancing its penetrating power. This leads to an *effective London penetration depth* λ_{eff}, which values can exceed significantly λ_L (see A.5). For aluminum $\lambda_{eff} \approx 50nm$ with $\lambda_L(0) = 16nm$ and $\xi_0 = 1600nm$ [69]. Due to the dependency of σ_2 from λ_L (eq. 2.12), the increased penetration depth translates into higher surface reactance and so higher kinetic inductance. Usinf the full BCS theory also changes the conductivity equations (2.11, 2.12). Using the so-called *Mattis-Bardeen integrals*, in conditions typical for a KID device ($\hbar\omega, k_BT \ll \Delta$), we obtain the simplified analytic expressions [72]

$$\frac{\sigma_1}{\sigma_n} \approx \frac{2\Delta}{\hbar\omega} e^{-\frac{\Delta_0}{k_BT}} K_0(\frac{\hbar\omega}{2k_BT})[2sinh(\frac{\hbar\omega}{2k_BT})] \tag{2.13}$$

$$\frac{\sigma_2}{\sigma_n} \approx \frac{\pi\Delta}{\hbar\omega}[1 - 2e^{-\frac{\Delta_0}{k_BT}} e^{-\frac{\hbar\omega}{2k_BT}} I_0(\frac{\hbar\omega}{2k_BT})] \tag{2.14}$$

where $I_0(x)$ and $K_0(x)$ are modified Bessel functions of the first and second kind. For $T \ll T_c$ the quasi-particles contribution to conductivity is killed and $\sigma_1 \ll \sigma_2$ (fig. 2.2).

As a consequence of the Mattis-Bardeen relationships we get [73]

$$L_s \approx \hbar R_n / \pi\Delta \tag{2.15}$$

between the normal-state surface resistance R_n and the superconducting surface inductance L_s. This equation can be written in a more operative form (using eq. A.7) as

$$L_s[pH/\square] \approx 1.415 \frac{R_n[\Omega/\square]}{T_c[K]} \tag{2.16}$$

where $/\square$ indicates that we are considering a square metal area of any dimension.

2.1.4 Quasi-particles excitations

In the usual temperature operation of a KID, $T \ll T_C$, it is possible to get a simple expression for the number of thermally excited quasi-particles (appendix A.2)

$$n_{qp} = 2N_0\sqrt{2\pi k_BT\Delta_0} e^{-\frac{\Delta_0}{k_BT}} \tag{2.17}$$

This density results from the thermal equilibrium between the created number of quasi-particles per unit time and the number of electrons recombining into Cooper pairs. A crucial parameter is the characteristic time called the *quasi-particle life time* τ_{qp}. It depends on the film thickness and the purity of the material. A theoretical value is given by [74]

$$\tau_{qp} = \frac{\tau_0}{\sqrt{\pi}} \left(\frac{k_BT_c}{2\Delta}\right)^{\frac{5}{2}} \left(\frac{T_c}{T}\right)^{\frac{1}{2}} e^{\frac{\Delta}{k_BT}} \tag{2.18}$$

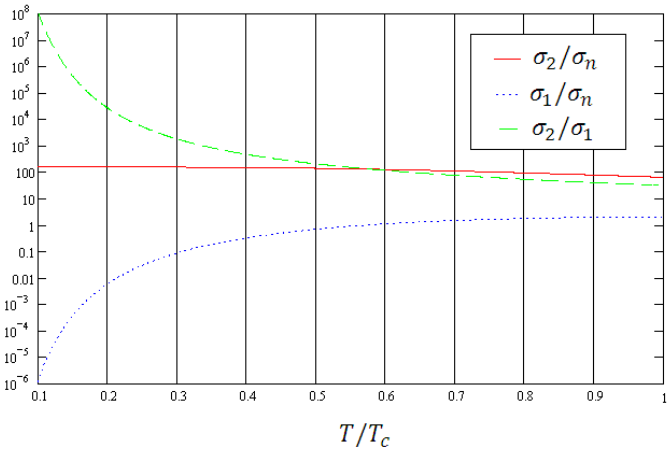

Figure 2.2: *Value of real (σ_1) and imaginary (σ_2) component of conductivity normalized to σ_0, and ratio σ_2/σ_1. The plot are calculated at $f_0 = \omega_0/2\pi \sim 1GHz$ using the full expressions of Mattis-Bardden integrals (eq. A.27 and A.28), for Aluminum thickness of $20nm$ and $T_c \sim 1.35K$. σ_2 dominate the conductivity for $T \ll T_c$*

where τ_0 is a material dependent parameter of the order of $450 \cdot 10^{-9}s$ for bulk aluminum [74]. We can see that the quasi-particle lifetime depends on temperature and diverges, in theory, for $T \to 0K$. Unfortunately, a saturation of the quasi-particle life time is observed at low temperatures [75]. Combining eq.s A.10 and 2.18, we can express τ_{qp} versus the quasi-particle density n_{qp}

$$\tau_{qp} = \frac{\tau_0}{n_{qp}} \frac{N_0 (k_B T_c)^3}{2\Delta^2} \tag{2.19}$$

From the latter equation, we stress that τ_{qp} is inversely proportional to the quasi-particle density. This result is quite intuitive: as the number of quasi-particle density reduces, it is less likely that they meet each other and recombine into Cooper pairs. From eq. 2.18, it is clear that the superconducting film has to be cooled to temperatures well below T_C in order to achieve relatively long lifetimes.

The interest in having long lifetimes is due to the quasi-particles excess δN_{qp} produced by incoming radiation. Imagine a flux of pair-breaking radiation ($E > 2\Delta$) illuminating the superconductor. In this case δN_{qp} will be determined by the equilibrium between the incoming power P_{in} that breaks a given number of quasi-particles per unit of time, and the rate of their recombination $\propto \tau_{qp}^{-1}$. In the approximation of small incident power (i.e. $\delta N_{qp} \ll N_{qp}$), τ_{qp} is constant and the quasi-particle excess can be found by dividing the energy excess $P_{in}\tau_{qp}$ by the amount of energy required to break one Cooper pair, 2Δ. Since each pair is made up of

two electrons, the quasi-particle excess is simply described by

$$\delta N_{qp} = \frac{\eta P_{in} \tau_{qp}}{\Delta} \tag{2.20}$$

where η is the overall efficiency in converting incoming radiation into quasi-particles. This equation shows that the number of excited quasi-particles is proportional to the lifetime τ_{qp}. We will see in the following that this relation indicates the possibility to increase the responsivity (par. 2.6.3) and to reduce the noise (par. 2.6.4) of the KID by lowering its temperature to $T \ll T_c$. The aforementioned quasi-particle life time saturation makes temperatures $T \approx T_c/10$ sufficiently low to reach the best performances.

2.2 Surface impedance and Kinetic Inductance

Let recall the definition of the surface impedance Z_s given in eq. 2.1

$$Z_s = R_s + jX_s = R_s + j\omega L_{kin}$$

where the kinetic inductance is $L_{kin} \equiv \frac{X_s}{\omega}$.

The surface impedance of a superconducting layer with thickness d is directly related to the complex conductivity $\sigma = \sigma_1 - j\sigma_2$, which can be calculated for example using the two fluid approximation (2.11, 2.12) or the Mattis-Bardeen equations (eq.s 2.13, 2.14). We calculate the surface impedance of a superconductor layer in the two following cases: for the most general case of bulk superconductors (thick layers) for which $d \gg \lambda_{eff}$, and for the case of our interest (thin layers) where $d \ll \lambda_{eff}$.

2.2.1 Thick layer

Assuming an harmonic plane wave and normal incidence, the surface impedance of a bulk superconductor is given by [69]

$$Z_s = \frac{\vec{E}}{\vec{H}} = \sqrt{\frac{j\omega\mu_0}{\sigma}} \tag{2.21}$$

Here we can use the two fluid model equation for the conductivity (eq. 2.10), that leads to the approximation [76]

$$Z_s \approx \frac{1}{2}\omega^2\mu_0^2\lambda_L^3\sigma_1 + j\omega\mu_0\lambda_L \tag{2.22}$$

and using eq. 2.9 we can express the surface impedance as a function of the conductivity

$$Z_s \approx \frac{1}{2}\sqrt{\omega\mu_0}\left(\frac{\sigma_1}{\sigma_2^{3/2}}\right) + j\sqrt{\omega\mu_0}\frac{1}{\sqrt{\sigma_2}} \tag{2.23}$$

As a consequence, the kinetic inductance $L_{kin} \equiv \frac{X_s}{\omega}$ is given by

$$L_{kin} = \sqrt{\frac{\mu_0}{\omega}} \frac{1}{\sqrt{\sigma_2}} \tag{2.24}$$

2.2.2 Thin layer

For very thin films, the mean free path l_{mfp} of the electrons is limited by the film thickness d, $l_{mfp} \approx d \ll \xi_0, \lambda_{eff}$. We are in the so called *dirty local limit*. In this case the electrodynamic response of superconductors can be simplified because the field penetrates through the entire film and the current distribution is almost uniform across the thickness. In this particular case Z_s can be expressed by [69]

$$Z_s = \frac{1}{\sigma d} \tag{2.25}$$

The superconducting films used in this work satisfy these approximations. We can therefore use eq. 2.25 to calculate the total surface impedance

$$Z_s = \frac{\sigma_1}{(\sigma_1^2 + \sigma_2^2)d} + j\frac{\sigma_2}{(\sigma_1^2 + \sigma_2^2)d} \tag{2.26}$$

with the kinetic inductance given by

$$L_{kin} = \frac{\sigma_2}{(\sigma_1^2 + \sigma_2^2)\omega d} \approx \frac{1}{\omega \sigma_2 d} \tag{2.27}$$

where the last approximation is valid for $T \ll T_c$, i.e. $\sigma_1 \ll \sigma_2$.

2.3 Inductance contributions in a superconducting strip

Consider now a strip of superconducting material with thickness d, width w and length l. Appliying an alternate electric field at the angular frequency ω, the surface impedance of the strip will depends on the kinetic energy E_k stored in the Cooper pairs and on the magnetic energy E_m stored in the field generated by the current. E_m depends only on the geometry of the superconducting line.

Accordingly to the two fluid model, we can describe the Cooper pairs kinetic energy per unit of volume as:

$$E_{kin} = \frac{1}{2} n_s m_e v^2 = \frac{1}{2} \frac{m_e}{n_s e^2} J_s^2 = \frac{1}{2} \mu_0 \lambda_L^2 J_s^2 \tag{2.28}$$

On the other hand, the magnetic energy is given by

$$E_{mag} = \frac{1}{2} \mu_0 \int_V H dV \equiv \frac{1}{2} L_m I_s^2 \tag{2.29}$$

where the integral is performed over the volume V of the superconductor, and L_m is the

magnetic inductance defined as

$$L_m = L_{m,int} + L_{m,ext} \tag{2.30}$$

$L_{m,int}$ represents the inductance due to the magnetic field that penetrates, depending on λ_L, into the superconductor, while $L_{m,ext}$ is the inductance that arises from the magnetic field around the conductor and is defined by the length, the width and the cross section of the superconductor.

We can collect the different contributions to the total inductance in the following equation:

$$L_{tot} = \underbrace{L_k + L_{m,int}}_{L_{int}} + \underbrace{L_{m,ext}}_{L_{geo}} \tag{2.31}$$

Here we call L_{int} the *total internal inductance*, that includes each contribute from inside the superconductor. On the contrary the part depending on the field outside the superconductor is described by $L_{geo} \equiv L_{m,ext}$ and is called the *geometric inductance*, because it depends on the geometrical design of the superconducting line. For complicated structures it must be calculated by simulation and it contributes to the total impedance with the constant reactance $X_{s,geo} = \omega L_{geo}$.

2.3.1 Internal inductance

To estimate the contribution of the internal inductance, we need to take into account any variations in current density. This can be calculated by performing the integrals for the current over the entire film cross-sectional area. The results is therefore valid in the general working condition $d \leq \lambda_{eff} \ll w$ and is given by [10]

$$L_{kin} = \frac{\mu_0 \lambda_L}{4w} \left[coth\left(\frac{d}{2\lambda_L}\right) + \left(\frac{d}{2\lambda_L}\right) cosec^2\left(\frac{d}{2\lambda_L}\right) \right] \tag{2.32}$$

$$L_{m,int} = \frac{\mu_0 \lambda_L}{4w} \left[coth\left(\frac{d}{2\lambda_L}\right) - \left(\frac{d}{2\lambda_L}\right) cosec^2\left(\frac{d}{2\lambda_L}\right) \right] \tag{2.33}$$

where the inductance values are expressed in henry per units of length $[H/m]$. Adding these two contributions leads to

$$L_{int} = \frac{\mu_0 \lambda_L}{2w} coth\left(\frac{d}{2\lambda_L}\right) \tag{2.34}$$

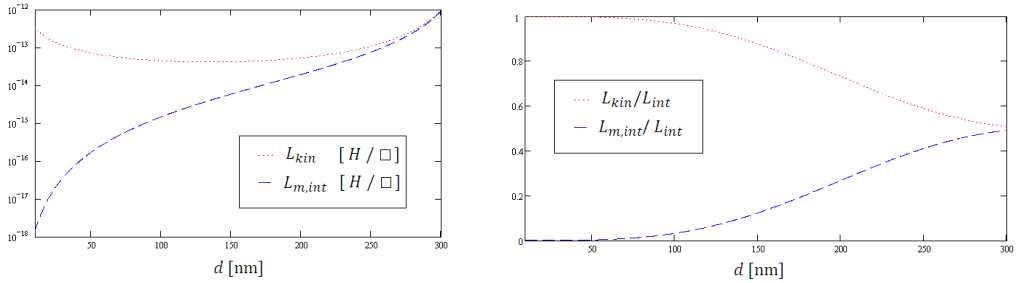

(a) (b)

Figure 2.3: *Comparison of the absolute (a) and relative (b) values between the magnetic internal inductance $L_{m,int}$, and the kinetic inductance L_K, as function of the film thickness. The plot are calculated for an aluminum film 20nm in thickness.*

It is useful to write L_{int} in terms of *square impedance*, i.e. the impedance of a strip where the length l is equal to its width w (a square patch)

$$L\,[H/\square] \equiv \frac{inductance}{number\ of\ squares} = \frac{inductance}{unit\ of\ length} \cdot (length = w) \equiv L[H/m] \cdot (length = w) \tag{2.35}$$

Using this definition we can thus rewrite eq. 2.34 in $[H/\square]$ as

$$L_{int} = \frac{\mu_0 \lambda_L}{2} coth\left(\frac{d}{2\lambda_L}\right) \tag{2.36}$$

or, as function of the conductivity (eq. 2.9)

$$L_{int} = \sqrt{\frac{\mu_0}{4\omega\sigma_2}} coth\left(\frac{d}{2}\sqrt{\mu_0\omega\sigma_2}\right) \tag{2.37}$$

These results depends on the film thickness d, as well as on the temperature, through the conductivity σ_2 (Cooper pairs). As the thickness reduces, the contribution from kinetic inductance become more and more dominant with respect to the magnetic one (fig. 2.3.1).

2.3.2 Thin layers approximation

For a layer with $d \ll \lambda_L$ we can consider an homogeneous current density through the thickness of the superconducting film. In this case, typical for our applications, we can neglect the magnetic contribution $L_{m,int}$ (see fig. 2.3.1) and consider $L_{int} \approx L_k$, so that

$$L_{tot} \approx L_{kin} + L_{geo} \tag{2.38}$$

Let's calculate a more convenient way to express L_k in this approximation. Integrating eq. 2.28 over the volume of the superconductor and equating to the general formula that describes the energy stored by an inductor, we get

$$\frac{1}{2}\mu_0\lambda_L^2\int J_s^2 dV = \frac{1}{2}L_{kin,tot}I_s^2 \tag{2.39}$$

where $L_{kin,tot}$ refers to the total kinetic inductance in the whole strip, and I_s is the supercurrent flowing through the strip. Integrating over the dimension parallel to the current flow does not involve the current density, so that $\int J_s^2 dV = l\int J_s^2 dS$, with dS element of surface perpendicular to $\vec{J_s}$, we obtain

$$\mu_0\lambda_L^2\int J_s^2 dS = \frac{L_{kin,tot}}{l}I_s^2 \tag{2.40}$$

where $\frac{L_{kin,tot}}{l}$ represents the kinetic inductance per unit of length $[H/m]$. Multiplying by a length equal to the width w of the strip leads to

$$w\mu_0\lambda_L^2\int J_s^2 dS = L_{kin}I_s^2 \tag{2.41}$$

where L_{kin} is the *kinetic inductance per square* of superconducting strip $[H/square]$. Considering thin superconducting layers satisfying $d \ll \lambda_{eff} \ll w$, we can assume that the current density in the film is uniform and given by $J_s = I_s/wd$, so that

$$w\mu_0\lambda_L^2\left(\frac{I_s}{wd}\right)^2 wd = L_{kin}I_s^2 \tag{2.42}$$

Finally we get the kinetic inductance per square of a superconducting thin strip

$$L_{kin} = \frac{\mu_0\lambda_L^2}{d} \tag{2.43}$$

The thinner the superconductor film, the higher the kinetic inductance. Notice that substituting eq. 2.9 in eq. 2.43 we get

$$L_{kin} = \frac{1}{\omega\sigma_2 d} \tag{2.44}$$

that is eq. 2.27 in the limit $\sigma_1 \ll \sigma_2$, i.e. at low temperatures $T \ll T_c$.

2.3.3 Kinetic inductance fraction

The kinetic energy depends on the Cooper pairs density, and so on the volume of the superconducting strip and its temperature. On the contrary the magnetic inductance only depends on the geometry of the superconductor. As we discussed before, at $T \ll T_c$ a small variation

in temperature do not influence the magnetic inductance, while it leads to a change in the kinetic inductance and the surface impedance. The fraction of kinetic inductance (variable) with respect to the magnetic inductance (fixed) defines the responsivity of the detector (par. 2.6.3) and is called the *kinetic inductance fraction*

$$\alpha \equiv \frac{L_{kin}}{L_{tot}} \tag{2.45}$$

2.4 Surface impedance in a superconducting strip

The contribution to the surface impedance of a superconducting strip due to the total internal inductance is simply given by

$$X_s = \omega L_{int} = \sqrt{\frac{\mu_0 \omega}{4\sigma_2}} coth\left(\frac{d}{2}\sqrt{\mu_0 \omega \sigma_2}\right) \tag{2.46}$$

where we have used eq. 2.37. The resistive contribution can instead be calculated using the real part of the eq. 2.26, with the usual approximation for low temperatures ($T \ll T_c$)

$$R_s = \frac{\sigma_1}{(\sigma_1^2 + \sigma_2^2)d} \approx \frac{\sigma_1}{\sigma_2^2 d} \tag{2.47}$$

Combining the resistive and reactive parts lead to the final expression for the strip impedance Z_s in terms of conductivities

$$Z_s = R_s + jX_s \approx \frac{\sigma_1}{\sigma_2^2 d} + j\sqrt{\frac{\mu_0 \omega}{4\sigma_2}} coth\left(\frac{d}{2}\sqrt{\mu_0 \omega \sigma_2}\right) \tag{2.48}$$

where conductivities can be evaluated by the Mattis Barden eq.s 2.13 and 2.14. For very thin layers, $d \ll \lambda_L$ implies $L_{int} \approx L_{kin}$ and we can use the thin film approximation (eq. 2.44)

$$Z_s = R_s + jX_s \approx \frac{\sigma_1}{\sigma_2^2 d} + j\frac{1}{\sigma_2 d} \tag{2.49}$$

2.5 Resonators basics concepts

As discussed in the previous sections, particles with energy $E > 2\Delta$ can break Cooper pairs into quasi-particles, leading to a change in the surface impedance of a superconducting film. A Kinetic Inductance Detector (KID) consists of a superconducting resonant circuit where the change in surface impedance due to incident particles affects the properties of the resonator. Since the Lumped Element KID (LEKID), main subject of this thesis, are essentially based on RLC series circuits, it is appropriate to recall their main characteristics.

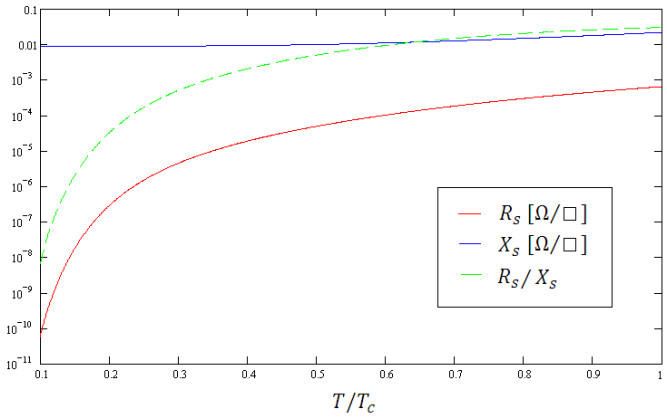

Figure 2.4: *Comparison between the surface resistance R_s and the surface reactance X_s in an aluminum superconducting film 20nm in thickness, as function of the temperature. T_c is the superconducting transition temperature.*

2.5.1 The RLC series circuit

The series circuit resonator is made of a resistor R, a capacitor C and an inductor L in series, as shown in fig. 2.5(a). The *resonance frequency* f_0 is defined as the frequency where the inductive reactance and the capacitive reactance have the same value. In that case the imaginary part of the resonator impedance is zero. We can therefore derive the resonance frequency by setting $Im\{Z_{in}\} = 0$, giving

$$\omega_0 = \frac{1}{\sqrt{LC}} \tag{2.50}$$

where ω_0 is the *angular resonance frequency*, with $\omega_0 = 2\pi f_0$. Another way to see this is to consider that the most favorable energetic configuration for the system occurs when the average electric energy E_e stored in the capacitor C and the average magnetic energy E_m stored in the inductor L are equal. Thi can be easily demonstrated assuming a sinusoidal signal we get

$$E_e = \frac{1}{2}C < V_C^2 >= \frac{1}{2}C \cdot \frac{1}{2}V_C^2 = \frac{1}{4}\frac{I^2}{\omega^2 C} \tag{2.51}$$

$$E_m = \frac{1}{2}L < I^2 >= \frac{1}{2}L \cdot \frac{1}{2}I^2 = \frac{1}{4}LI^2 \tag{2.52}$$

where V_C represents the potential drop across the capacitor and I is the peak current. It is straightforward to see that $\omega = \omega_0 \rightarrow E_e = E_m$

The impedance of an RLC circuit follows from Kirchhoff's law

$$Z_{RLC} = R + j\omega L + \frac{1}{j\omega C} = R + j\omega L\left(\frac{\omega^2 - \omega_0^2}{\omega^2}\right) \tag{2.53}$$

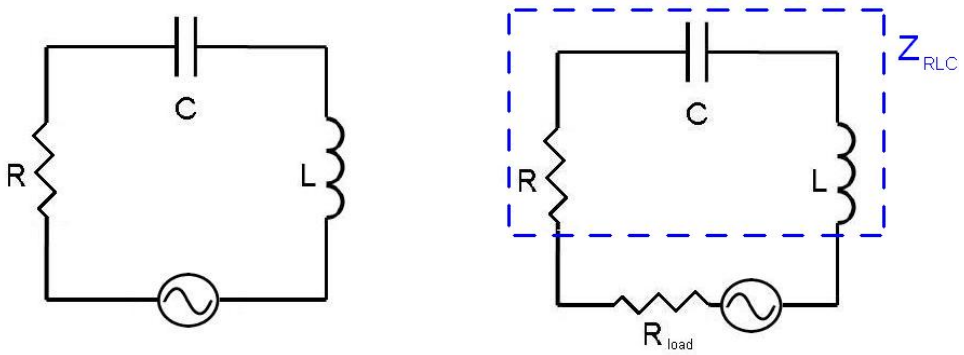

(a) (b)

Figure 2.5: *The series resonator circuit driven by an ideal zero-resistance voltage generator (a) and by a R_{load} resistance one (b).*

where we have used eq. 2.50 for the last equivalence.Defining $\Delta\omega \equiv (\omega - \omega_0)$, we easily derive $\omega^2 - \omega_0^2 \approx 2\omega\Delta\omega$ for $\Delta\omega \ll \omega_0$, and in this case

$$Z_{RLC} \approx R\left(1 + j\frac{2Q_i\Delta\omega}{\omega_0}\right) \tag{2.54}$$

2.5.2 Quality factor

Shutting down the voltage generator, the system continue his oscillation at the resonance frequency f_0. Without dissipation, the system could oscillate forever. This is not the case because we deal with a non-zero resistance R, which in our particular case is provided by quasi-particles. Therefore we define the time constant τ of the circuit as the ratio between the average energy stored in the resonator and the average power lost through Joule dissipation

$$\tau \equiv \frac{E_{stored}}{W_{lost}} \tag{2.55}$$

Assuming to have previously accumulated a certain amount of energy in the circuit, the time constant τ is the time it takes for the circuit to dissipate through the resistance R the electric energy stored in C and the magnetic energy stored in L, until reaching $1/e$ of its initial value. The *quality factor* Q is a dimensionless quantity proportional to the number of periods N necessary before this dissipation happens. It is defined as

$$Q \equiv \omega_0\tau = 2\pi f_0\tau = 2\pi N \tag{2.56}$$

and it actually describes how much a resonator is damped due to its resistive impedance. We describe the *response time* of the detector with

$$\tau_{res} \approx \frac{Q}{\pi f_0} \tag{2.57}$$

where the factor 2 disappears as consequence of reading out voltages instead of energies. For typical resonators, τ_{res} is around $10\mu s$. For millimetric radiation applications this is surely fast enough, whereas it will likely be the dominant limiting factor in determining the rise shape of a higher energy pulse.

Substituting eq. 2.55 in eq. 2.56 we get

$$Q = \omega_0 \frac{E_{stored}}{W_{lost}} \tag{2.58}$$

The total average energy stored in the RLC circuit is the sum of the electric and magnetic contributions $E_{stored} = E_e + E_m = 2E_m = 2E_e$, while the average energy dissipated in the resistance is simple given by $W_{lost} \equiv < I^2 > R = \frac{1}{2} I^2 R$. Substituting in eq. 2.58 gives the intrinsic quality factor of an RLC circuit

$$Q = \omega_0 \frac{\frac{1}{2} L I^2}{\frac{1}{2} I^2 R} = \omega_0 \frac{L}{R} = \frac{1}{\omega_0 RC} \tag{2.59}$$

which underlines that high quality factors corresponds to low ohmic losses.

We have to distinguish between the ohmic losses due to the resonator circuit itself and any other extra dissipation channel that might be present in the system. It is usual to refer to the former as *internal quality factor* Q_i and to the latter as *external quality factor* Q_e. This leads to an effective *total quality factor* Q that derives from eq. 2.58

$$Q = \frac{E_{stored}}{W_{loss,int} + W_{loss,ext}} \rightarrow \frac{1}{Q} = \frac{1}{Q_i} + \frac{1}{Q_e} \tag{2.60}$$

For example, in the case of an RLC series resonator driven by a voltage supply with a non-zero resistance R_{load} (see fig. 2.5(b)), the total quality factor is simply given by $Q = \omega_0 \frac{L}{R+R_{load}}$, with $Q_i = \omega_0 \frac{L}{R}$ and $Q_e = \omega_0 \frac{L}{R_{load}}$

Moreover it is useful to define the *coupling factor* g as

$$g \equiv \frac{Q_i}{Q_e} \tag{2.61}$$

and we refer to under-coupled or over-coupled resonator if $g < 1$, or $g > 1$, respectively. The case $g = 1$ is usually defined as the critical coupling condition.

2.6 Lumped Element KID

2.6.1 Microwaves KID concept and geometries

A Microwave Kinetic Inductance Detector (usually referred to as MKID) is a superconducting resonating RLC circuit electromagnetically coupled to a transmission line. The transmission line plays the role of the supply with its non zero load impedance (fig. 2.5(b)). As previously shown, this introduces an additional channel of dissipation into the system, characterized by an external quality factor Q_e. The transmission line feeds the KID at its proper frequency $\omega_0 = (LC)^{-1/2}$, while the kinetic inductance of the Cooper pairs contributes to L. The non-paired electrons – the quasi-particles – provide a residual resistivity R while the capacitor C can be geometrically designed according to experimental requirements. An incoming particle or photon with an energy exceeding the superconducting gap can break Cooper pairs and change the kinetic inductance, with a consequent shift of the resonance frequency. We can measure this shift by monitoring the signal transmitted past the feedline with dedicated readout electronics.

MKID can therefore be used to detect photons with frequencies $\nu > 2\Delta/h$, corresponding to millimeter wavelengths for superconductors with $T_c \approx 1K$. They were first proposed in 2003 by Day et al. [7] to be used for millimeter Astronomy applications as a valid alternative to traditional bolometers. In this framework, two main MKID architectures have been proposed in the last decade: the $\lambda/4$ resonators and the lumped element resonators. The former geometry consists in a distributed quarter wavelength resonator capacitively coupled to a feedline. This device is not a detector itself; it is instead a sensor since it is not directly coupled to the radiation. The introduction of a separate structure, usually an antenna (or absorber) is needed. For this reason we usually refer to them as *antenna-coupled MKID*. On the other hand, the so-called *Lumped Element Kinetic Inductance Detectors* (LEKID) were first proposed in 2008 by Doyle [10]. This elegant resonator geometry combines a resonator and radiation absorber in a single planar structure inductively and/or capacitively coupled to a feedline. An example of typical design for these two types of KID are sketched in fig. 2.6.1. Due to the increased geometric complexity, it has proven more difficult to achieve satisfactory device performance with antenna structures than with direct absorption LEKIDs [77]. For this reason all detectors which we deal with in this thesis are LEKID. In the following we try to model the electric circuit describing such a resonator and obtain the formulas for LEKID resonators which will be used later in this thesis [10] [78] [76] [47] [79].

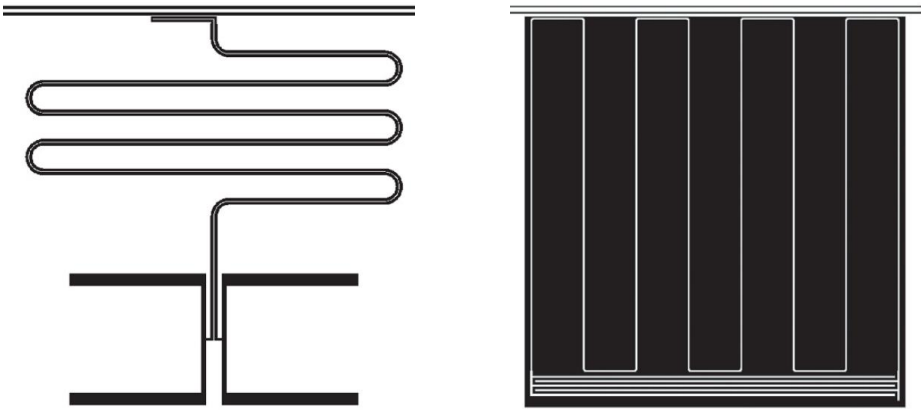

(a) (b)

Figure 2.6: *(a) Single antenna-coupled resonator design and (b) LEKID resonator design.*

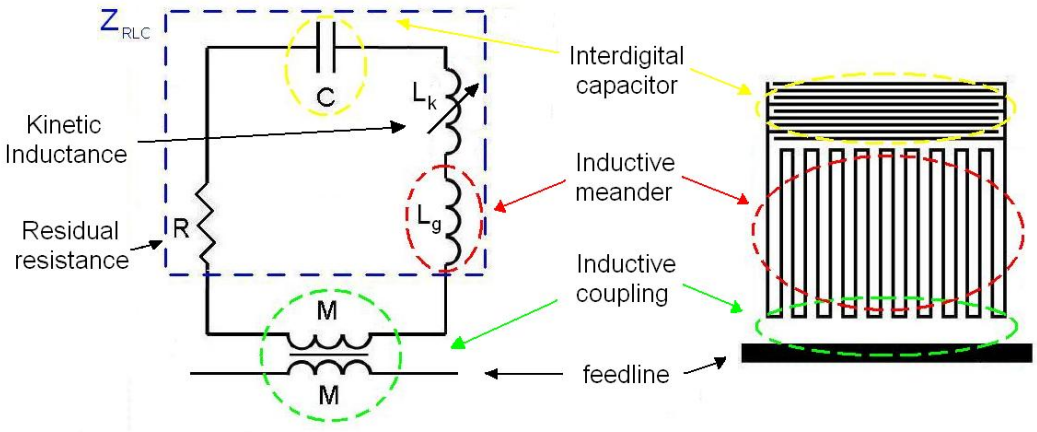

Figure 2.7: *Equivalent circuit for a typical geometry of a LEKID resonator.*

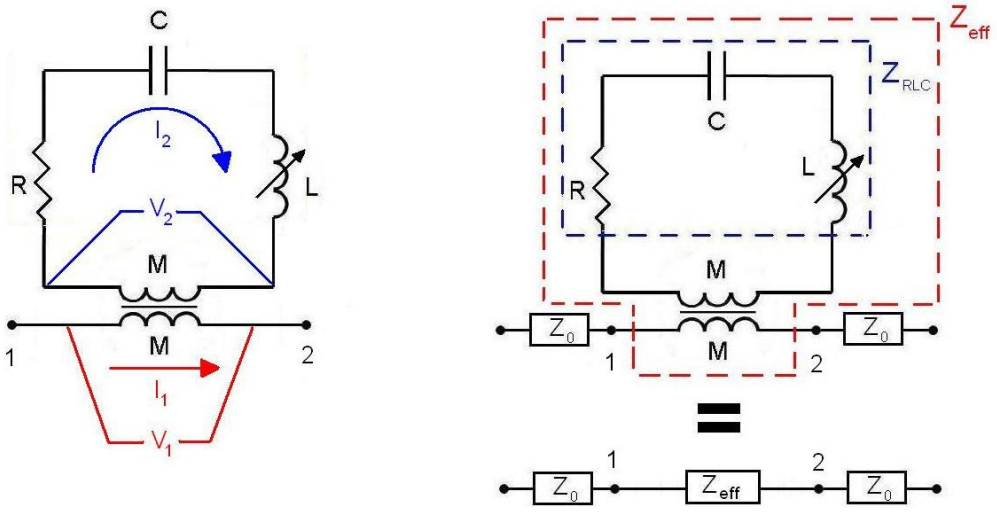

Figure 2.8: *Equivalent circuit describing LEKID resonator coupled to a feedline. All acts like there was a lumped impedance Z_{eff} in series to the characteristic impedance of the feedline Z_0.*

2.6.2 Modeling a LEKID resonator

Equivalent circuit

A circuit is defined as *lumped* if its elements have dimensions much smaller than the excitation wavelength. In that case there are no current gradients along the components themselves. The values of the field, the voltage and the current are univocally defined. The LEKID model work under this assumption.

The typical geometry of a Lumped Element KID consists of an interdigitated capacitor and a meandered inductor coupled to a feedline (fig. 2.7). The geometry of the meander is associated to the fixed geometrical inductance L_g, while the kinetic inductance L_k provides the variable part of the total inductance $L = L_k + L_g$. The resonance frequency is defined by

$$\omega_0 = \frac{1}{\sqrt{LC}} = \frac{1}{\sqrt{(L_k + L_g)C}} \tag{2.62}$$

The inductive meander acts as sensor as well as absorbing element and therefore must have a size comparable to the wavelength of the photons to be detected (see Part II - introduction). The residual resistance R is of course linked to the quasi-particle density.

The coupling between the LEKID and the feedline is described in this model by a *mutual inductance coefficient* M. Referring to fig. 2.8, for a sinusoidal signal of angular frequency ω,

the voltage induced into the resonator by the feedline is

$$V_2 = M\frac{dI_1}{dt} = j\omega M I_1 \tag{2.63}$$

while the voltage induced into the feedline by the resonator is

$$V_1 = M\frac{dI_2}{dt} = j\omega M I_2 \tag{2.64}$$

Due to Kirkoff's rule we can also write

$$I_2 Z_{RLC} + V_2 = 0 \rightarrow I_2 = \frac{-j\omega M I_1}{Z_{RLC}} \tag{2.65}$$

where we have used eq. 2.63. Substituting the latter formula in eq. 2.64, we find that $V_1 = Z_{eff} I_1$ if we define

$$Z_{eff} = \frac{\omega^2 M^2}{Z_{RLC}} \tag{2.66}$$

Z_{eff} is the *effective impedance* of the LEKID resonator, as seen by the feedline (fig. 2.8). Using eq. 2.54, valid for $\Delta\omega = \omega - \omega_0 \sim 0$, we can express the LEKID impedance as function of its characteristics parameters

$$Z_{eff} \approx \frac{\omega_0^2 M^2}{R\left(1 + j2Q_i\frac{\Delta\omega}{\omega_0}\right)} \tag{2.67}$$

Quality factors

The feedline is needed to excite and readout the system. Its presence adds a further dissipation channel for the resonator. The energy stored E_{stored} into the resonator is calculated in par. 2.5.2, while the power loss W_{lost} is expressed by the potential drop over Z_{eff}, dissipated through the feedline. Seen by the resonator, the feedline offers two series dissipation channels, each one with impedance Z_0. Therefore recalling the quality factor definition (eq. 2.58), we can calculate the external quality factor as follows

$$Q_e = \omega_0\frac{E_{stored}}{W_{lost}} = \frac{2\cdot\frac{1}{2}L\left\langle I_2\right\rangle^2}{\frac{\left\langle V_1\right\rangle^2}{2Z_0}} \tag{2.68}$$

and using eq. 2.64, at the resonance frequency we get

$$Q_e = \frac{2LZ_0}{\omega_0 M^2} \tag{2.69}$$

The energy losses due to the resonator itself are, on the other hand, referred to the internal

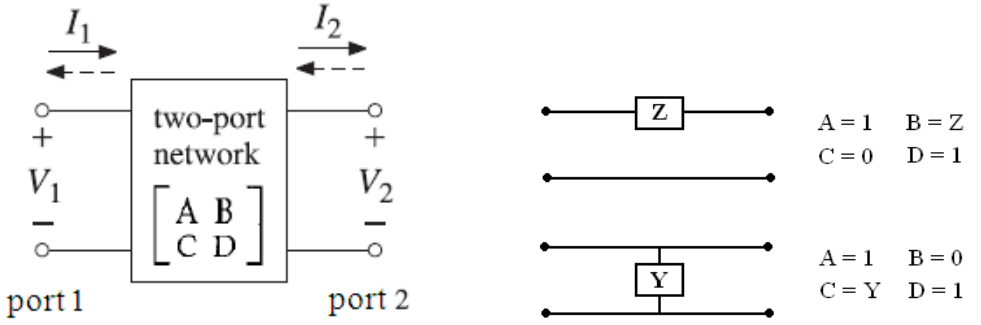

(a) (b)

Figure 2.9: *(a) Representation of a two-port network as an ABCD matrix applied to the in/out voltage/currents. (b) The ABCD matrix in the two most common cases: the series impedance Z and the parallel admittance Y.*

quality factor Q_i (eq. 2.59)

$$Q_i = \omega_0 \frac{L}{R} \tag{2.70}$$

The coupling coefficient for a LEKID is thus calculated (eq. 2.61) as

$$g = \frac{Q_i}{Q_e} = \frac{\omega_0^2 M^2}{Z_0 R} \tag{2.71}$$

Scattering parameters

As illustrated in fig. 2.8, the LEKID can be represented as a 2-ports device. These kind of microwave circuits are usually characterized in term of the ratios between the amplitudes of the transmitted or reflected voltage waves, with respect to the incident one. These complex coefficients are known as the *scattering parameters* (or *S-parameters*). Let us denote with the subscripts 1 or 2 the corresponding port, with the apex "+" the wave coming from the wave generator and entering the network, and "-" the wave that is coming out from the network and going back to the supply power (fig. 2.9(a)). With this notation the scattering parameters for a 2-port device are defined by

$$\begin{pmatrix} V_1^- \\ V_2^- \end{pmatrix} = \begin{pmatrix} S_{11} & S_{12} \\ S_{21} & S_{22} \end{pmatrix} \begin{pmatrix} V_1^+ \\ V_2^+ \end{pmatrix} \tag{2.72}$$

or in a compact notation

$$S_{ij} = \frac{V_i^-}{V_j^+} \tag{2.73}$$

For example $S_{21} = V_2^-/V_1^+$ is the ratio of the voltage wave coming out from port 2 to the voltage wave incident on port 1 and defines the transmission through the system in the direction going from port 1 to port 2.

The S-parameters notation is very convenient to calculate the total effect resulting from the combination of one or more devices. It can be demonstrated that each electrical 2-port device with a given complex impedance $Z = R + jX$ can be described by the so-called ABCD matrix

$$\begin{pmatrix} A & B \\ C & D \end{pmatrix} \tag{2.74}$$

Connecting several 2-port devices in series, the ABCD matrix describing the new overall 2-port network will derive by product of the individual ABCD matrixes. In general, if each of the 2 ports is terminated by an impedance Z_0, the scattering parameters can be calculated as follows [80]:

$$\begin{array}{ll} S_{11} = \frac{A+BZ_0-CZ_0-D}{A+B/Z_0+CZ_0+D} & S_{12} = \frac{2(AD-BC)}{A+B/Z_0+CZ_0+D} \\ S_{21} = \frac{2}{A+B/Z_0+CZ_0+D} & S_{22} = \frac{-A+B/Z_0-CZ_0+D}{A+B/Z_0+CZ_0+D} \end{array} \tag{2.75}$$

For example in the two simplest cases, the series impedance Z and the parallel admittance $Y = 1/Z$ (fig. 2.9(b)), the corresponding ABCD matrixes are respectively

$$\begin{pmatrix} 1 & Z \\ 0 & 1 \end{pmatrix} \tag{2.76}$$

and

$$\begin{pmatrix} 1 & 0 \\ Y & 1 \end{pmatrix} \tag{2.77}$$

To calculate the S-parameters corresponding to one of these devices we then apply eq. 2.75. For example the transmission coefficient from port 1 to port 2 for the series impedance Z whose ports are terminated on the load Z_0, is given by

$$S_{21} = \frac{2}{2 + \frac{Z}{Z_0}} \tag{2.78}$$

S_{21} for a LEKID device

Since our LEKID are excited and readout using a transmitting feedline (2-ports), we want now to calculate the key S_{21} parameter. As described above, the effect of a LEKID coupled to a transmission line is simply an effective impedance Z_{eff} terminated by Z_0. This means that we have just to replace Z by Z_{eff} in eq. 2.78, obtaining

$$S_{21} = \frac{2}{2 + \frac{Z_{eff}}{Z_0}} \tag{2.79}$$

Now recall eq.s 2.66, 2.54 and 2.71. We can write

$$S_{21} = \frac{2}{2 + \frac{\omega_0^2 M^2}{Z_0 Z_{RLC}}} = \frac{2}{2 + \frac{2g}{1+j2Q_i x}} \equiv S_{21}(x) \tag{2.80}$$

where we have defined $x \equiv \frac{\Delta\omega}{\omega_0}$. The minimum value of S_{21} is reached on resonance ($x = 0$) and depends on the coupling coefficient g

$$S_{21,min} \equiv S_{21}(\omega = \omega_0) = S_{21}(x = 0) = \frac{1}{1+g} \tag{2.81}$$

With this definition we can rewrite eq. 2.80 as follows

$$S_{21} = S_{21,min} \frac{1 + j2Q_i x}{1 + jS_{21,min} 2Q_i x} \tag{2.82}$$

If we introduce into the system a mismatch of impedance due to some possible parasitic reactance X_{par}, we can describe the transmitted S-parameters as (appendix B.2)

$$S_{21} = S_{21,min} \frac{1 + j2Q_i x}{1 + jS_{21,min} 2Q_i x + jS_{21,min} P} \tag{2.83}$$

where we have defined $P \equiv X_{par}/Z_0$. The additional term $jS_{21,min}P$ account for the asymmetry of the resonance shape that is sometimes observed in our LEKID devices. From these equations it is easy to calculate the transmitted amplitude and phase of the signal. Following the calculations performed in appendix B.2, we get a simply general formula describing the transmitted amplitude for typical LEKID devices used in this thesis

$$|S_{21}| \approx S_{21,min} \sqrt{\frac{1 + (2Q_i x)^2}{1 + (S_{21,min}(2Q_i x + P))^2}} \tag{2.84}$$

Interpretation of the quality factor with respect to the resonance shape

Using eq. B.7

$$|S_{21}| = S_{21,min} \sqrt{\frac{1 + (2Q_i x)^2}{1 + (S_{21,min} 2Q_i x)^2}}$$

it is possible to relate the quality factors to the shape of the resonance, in particular to its deepness and its width. Simply imposing $x \equiv 1/2Q_i$, we get

$$|S_{21}|_{Q_i} = |S_{21,min}| \sqrt{\frac{2}{1 + |S_{21,min}|^2}} \tag{2.85}$$

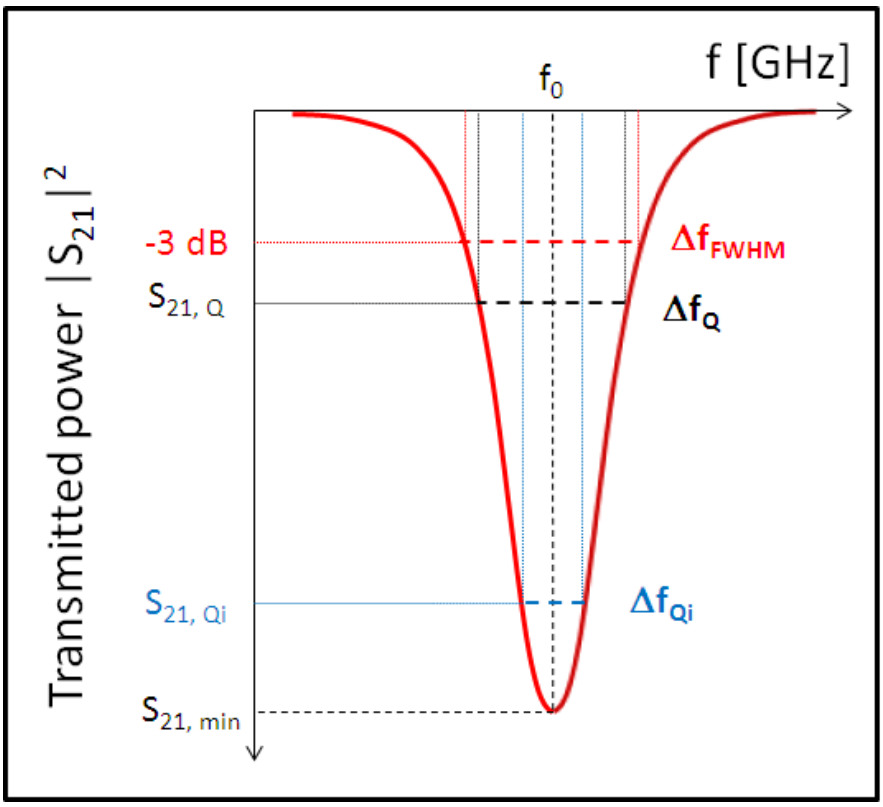

Figure 2.10: *Representation of the typical readout power of the KID resonance. The values* Δ_{fQ_i}, Δ_{fQ} *and* Δ_{FWHM} *measure the width of the resonance (red curve) at the depths* S_{21,Q_i}, $S_{21,Q}$ *and* $-3dB = 1/2S_{21,min}$, *respectively*

From the x definition, this means that

$$Q_i = \frac{f_0}{\Delta f_{Q_i}} \tag{2.86}$$

where Δf_{Q_i} is the full width of the resonance shape calculated at the height given by $|S_{21}|_{Q_i}$.

We can perform the analog calculation for the total quality factor Q. From eqs. 2.60 and 2.61 it follows that

$$Q = \frac{Q_i}{1+g} \tag{2.87}$$

and substituting in eq. B.7 we get

$$|S_{21}| = \sqrt{\frac{|S_{21,min}|^2 + (2Qx)^2}{1+(2Qx)^2}} \tag{2.88}$$

Now imposing $x \equiv 1/2Q$ lead to

$$|S_{21}|_Q = \sqrt{\frac{1 + |S_{21,min}|^2}{2}} \tag{2.89}$$

which means that

$$Q = \frac{f_0}{\Delta f_Q} \tag{2.90}$$

where Δf_Q is the full width of the resonance shape calculated at the height given by $|S_{21}|_Q$.

For typical LEKID devices of this thesis, i.e. over-coupled resonators ($g \gg 1$) with internal quality factors exceeding $\sim 10^5$, $S_{21,min} \to 0$ and

$$Q \approx \frac{f_0}{\Delta f_{FWHM}} \tag{2.91}$$

where Δf_{FWHM} is the *Full Width to Half Maximum* of the resonance. As a consequence, calculating the resonance frequency and its FWHM are direct measurements of total quality factor defined in eq. 2.10.

2.6.3 Responsivity of a LEKID device

Photons or particle with energy exceeding the gap can break Cooper pairs and produce a signal. The typical readout scheme consists on monitoring the transmission through the 2-port system constituted by a LEKID inductively coupled to a feedline. At the resonance frequency the transmission is minimum as a consequence of the maximum impedance mismatch between the feedline and the LEKID. An incoming particle releasing an energy $E > 2\Delta$ in the superconducting material changes the density of Cooper pairs and induces an increase of the inductance, that results in a change of the surface impedance and in a decrease of the resonance frequency. Furthermore, the creation of quasi-particle excitations results in an increment of the residual resistance; the resonance becomes thus shallower, i.e. the internal quality factor Q_i lowers. All that results in a variation δA of the measured transmitted power, monitored at the frequency ω_0 (fig. 2.11). The same things applies to the phase shift $\delta\phi$.

The responsivity of a detector provide us with a proportionality constant between the incident power and the read-out signal choosen. LEKID are usually read-out through the phase ϕ of the transmitted signal. The reason is the steepness of the phase signal variation around the center of the resonance, higher than amplitude case. To estimate the detector responsivity we have thus to calculate the variation of the transmitted phase past the resonator therein induced by an incoming power. Either provided by a quasi-steady flux of photons, or by a single particle hit, this power is proportional to the number of quasi-particles produced,

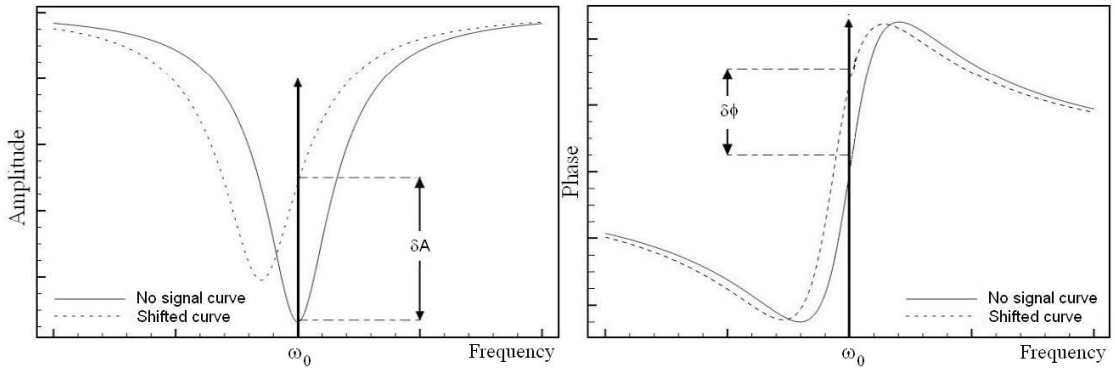

Figure 2.11: *An example of the amplitude δA (left) and phase $\delta\phi$ (right) signals induced in a KID as a consequence of an incoming radiation.*

as stated in eq. 2.19. Therefore we can write the responsivity $\Re$ as follow:

$$\Re \equiv \frac{d\phi}{dN_{qp}} = \frac{d\phi}{d\omega_0}\frac{d\omega_0}{dL}\frac{dL}{dN_{qp}} \tag{2.92}$$

Though the rigorous derivation of this equation should be performed in the framework of the BCS theory (see for example [10]), here we consider a simpler and more instructive derivation using the two fluid model.

Using eq. B.9 we can calculate

$$\begin{aligned}\phi &= arctan\frac{2Q_i\frac{\Delta\omega}{\omega_0}(1-S_{21,min})}{1+S_{21,min}(2Q_i\frac{\Delta\omega}{\omega_0})^2} \\ &\approx 2Q_i\frac{\Delta\omega}{\omega_0}\left(\frac{g}{1+g}\right)\end{aligned} \tag{2.93}$$

where we have neglected the terms of second order in $\Delta\omega/\omega_0$ and approximated $arctan\Delta\omega/\omega_0 \approx \Delta\omega/\omega_0$. Derivating this expression with respect to ω_0 and assuming $\omega/\omega_0^2 \approx 1/\omega_0$, we find

$$\frac{d\phi}{d\omega_0} = -2Q_i\frac{g}{1+g}\frac{\omega}{\omega_0^2} \approx -2Q_i\frac{g}{1+g}\frac{1}{\omega_0} \approx -\frac{2gQ}{\omega_0} \tag{2.94}$$

The second responsivity term can be deduced from eq. 2.62

$$\frac{d\omega_0}{dL} = -\frac{1}{2}L^{-3/2}C^{-1/2} = -\frac{\omega_0}{2L} = -\frac{\omega_0\alpha}{2L_k} \tag{2.95}$$

For very thin layers ($d \ll \lambda_L$) we can use the eq. 2.43 to describe the kinetic inductance. Furthermore from the two fluid model, we use eq. 2.6 linking the penetration depth to the

the quasi-particle density. We get

$$\begin{aligned} L_k &= \frac{\mu_0 \lambda_L^2}{d} \\ &= \frac{\mu_0 \lambda_L(0)^2}{d} \frac{n}{n_s} \\ &= \frac{m}{e^2 d n_s} \end{aligned} \tag{2.96}$$

and therefore

$$\frac{d\omega_0}{dL} = -\frac{e^2 d n_s \omega_0 \alpha}{2m} \tag{2.97}$$

For the third term, the total inductance is $L = L_k + L_g$, where L_g depends only on the geometric properties of the circuit and hence do not vary with the quasi-particles number. Using the eq. 2.96 for a thin layer in the two-fluid framework, we can write

$$\frac{dL}{dN_{qp}} = \frac{dL_k}{dN_{qp}} = \frac{m}{e^2 d(V) n_s^2} \tag{2.98}$$

where we have used $n_{qp} = 1 - n_s = N_{qp}/V$, being V the volume of the superconducting material.

Putting together eq. 2.94, 2.97 and 2.98 and identifying $n_s \sim n$ for $T \ll T_c$, we finally obtain the total responsivity of a LEKID

$$\frac{d\phi}{dN_{qp}} = \frac{\alpha g Q_{tot}}{nV} \tag{2.99}$$

Let's analyze in more detail this equation. First we observe that in order to maximize the response of the detector, we need to maximize the kinetic inductance fraction α with respect to the geometrical inductance. α depends on the intrinsic properties of the superconductor, but also on its thickness (see eq.s 2.45, 2.43). We can thus reach high responsivity by reducing the thickness d of the layer and/or working with intrinsically high kinetic inductance materials. For typical aluminum thin films ($d \sim 20nm, d/\lambda_L < 0.4$) $\alpha \approx 0.2$ [79].

Equation 2.99 confirm that the responsivity is directly proportional to the total quality factor of the resonator, Q_{tot}. In order to make it as large as possible, it is better to fabricate over-coupled resonators ($g > 1$), given the direct proportionality of the responsivity to the coupling coefficient g. This means high internal quality factors Q_i, i.e. high kinetic inductance and low losses, both achievable working at very low temperatures ($T \ll T_c$).

The responsivity is also inversely proportional to the volume of the resonator V. This means, for example, that increasing the area of the resonator will have the payback of a reduction in the detector responsivity. The physical reason is that the surface impedance is directly linked to the quasi-particle density rather than to their absolute number. The

number of quasi-particle produced by a given incoming power, results in a lower density variation because they are diluted over a larger volume. The dependance of the responsivity by the volume emphasizes once more that the thickness of the superconducting layer is crucial to have good performances. Nevertheless, it is worth to stress that we cannot diminish the volume indefinitely, since the increasing quasi-particle density progressively lowers Q_i because of the higher residual resistance R.

The dependence on the Cooper pair density n_s is not very important since we will always work at very low temperatures $T \ll T_c$, where we can assume $n_s \sim n$. It is important to underline that this approximation is valid for incoming energies not strong enough to break a significant fraction of Cooper pair in comparison of the total population n. Under this *small signals* (or *small frequency shift*) assumption, the derivative of the phase with respect to the quasi-particle number N_{qp} do not depends on the quasi-particle number itself. This means that the phase shift is proportional to N_{qp} and hence to the incoming power.

It is worth to stress that the small signals hypothesis is quite limiting particularly for the dynamic range and the calibration of the device. The dependance of the responsivity on the quality factors means that the detector responds differently depending on the shape of the resonance. The non-constant background conditions for on-sky measurements or the huge signals from higher-energy particles in controlled background experiments, affect in a non-negligible way the response of the detector. In the next chapter we will exhaustively study how to characterize a LEKID device in different environment conditions, in order to calibrate the response of the each detector and become able to compare different pixels on the same array.

2.6.4 Fundamental noise limiting a LEKID device

The noise sources in a KID can be either intrinsic, due to the physical processes going on in the resonator itself, or extrinsic, introduced into the system by the readout RF chain. In order to optimize the system performances, we need in general to minimize the intrinsic noise as much as possible, and then to design a readout chain which contribution to the total noise does not exceed the intrinsic one. The two main intrinsic noises limiting a KID are:

- the generation-recombination (GR) noise, arising from the thermal equilibrium between the populations of charge carriers;
- the two-level systems (TLS) noise, due to the presence of dielectric interfaces around the detectors.

On the other hand, extrinsic noise sources are the cold low-noise amplifier (LNA) and the readout electronic chain. When making astronomical observations, all these contributions have to be compared with the fundamental photon noise, the unavoidable contribution coming

from the particle nature of the radiation. A frequently used figure of merit to characterize the sensitivity of a device is the *Noise Equivalent Power* (NEP). It is defined as the input power of a system required to obtain a Signal-to-Noise Ratio (SNR) equal to 1 in a 1Hz bandwidth. The NEP of the resonator signal (x, either amplitude A, or phase θ) can be experimentally determined from a measurement of the *noise power spectrum* (S_x) and the responsivity to radiation (dA/dP_{rad}) and given by

$$NEP(f) = \sqrt{S_x(f)} \left(\frac{dx}{dP_{rad}} \right)^{-1} \sqrt{1 + (2\pi f \tau_{qp})^2} \tag{2.100}$$

with P_{rad} the radiation power and f the modulation frequency. (dx/dP_{rad}) is obtained experimentally by a measurement of x where P_{rad} was slowly varied around the power of interest. The last factor arises because the quasiparticle system cannot respond to fluctuations that are faster than the quasi-particle recombination time τ_{qp}.

Generation-recombination noise

Statistical fluctuations in the quasi-particle population are the main intrinsic source of noise in a KID. Superconductors always operate in thermal equilibrium between quasi-particles and Cooper pairs. As already said, even at very low temperatures there is an average number N_{qp} of thermally excited quasi-particles. This value is maintained by a balance between the continuous random processes of quasi-particles generation and recombination. These processes have the same effect of a background radiation, varying the quasi-particle density and then the kinetic inductance. This noise is called *generation-recombination noise* and is a typical example of shot noise due to a poissonian process, which white spectrum extends in frequency until it is suppressed by the effect of the characteristic times τ_{qp} and τ_{res}. The larger N_{qp}, the larger its fluctuation in absolute terms. Moreover it is quite intuitive that shorter quasi-particle lifetime τ_{qp} leads to lower uncertainty on the N_{qp} value. Given these considerations, the GR noise power spectrum and the corresponding NEP can be expressed by [81]:

$$S_x^{GR} = \frac{4 N_{qp} \tau_{qp}}{1 + (2\pi f \tau_{qp})^2} \left(\frac{dx}{dN_{qp}} \right)^2 \tag{2.101}$$

$$NEP_{GR} = \frac{2\Delta}{\eta_{opt} \eta_{pb}} \sqrt{\frac{\langle N_{qp} \rangle}{\tau_{qp}}} \propto e^{-\Delta_0 / k_B T} \sqrt{vol} \tag{2.102}$$

where η_{opt} is *optical efficiency* with which the incoming power is absorber in the detector, and η_{pb} is the *pair-breaking efficiency* in converting the absorbed energy in quasi-particles. The first factor depends on the optical system and on the absorber design, while the latter depends on the physical process that converts energy into quasi-particles. For aluminum KID absorbing millimeter photons, it is assumed that η_{qp} tends to 0.6 in the limit $h\nu \sim$

2Δ [82]. Using formulas A.10 and 2.18 respectively for quasi-particles density and lifetime, the GR noise is expected to decrease exponentially for temperatures $T < 10T_c$. Values as low as $10^{-20}W/\sqrt{Hz}$ should be attainable at $T \approx 100mK$ with aluminum ($T_c \approx 1.3 \div 1.4K$). The generation-recombination noise can be also reduced by lowering the volume of the superconducting resonator.

Photon noise

Residual quasi-particle density is related to thermal excitations of Cooper pairs due to the non-zero temperature. In the experiments for millimeter Astronomy, especially from ground and from stratospheric balloons, the thermal contribution is usually negligible compared to the excess δN_{qp} due to an incoming radiative background. This non-thermal population of quasi-particles is described by equation 2.20, $\delta N_{qp} = \eta P_{rad}\tau_{qp}/\Delta$, where the overall efficiency is $\eta = \eta_{opt}\eta_{pb}$. The correspondent noise spectrum S_x^R is equivalent to one half of the GR noise spectrum, $S_x^R = 1/2S_x^{GR}$, since now the uncertainty on the quasi-particle number depends only on the recombination process (no generation fluctuations are present since the incident energy breaks always the same amount of Cooper pairs). This results in a factor $1/\sqrt{2}$ in the eq. 2.102 and identifying $\langle N_{qp}\rangle \sim \delta N_{qp}$, we can thus write the *photon recombination noise* as

$$NEP_{ph,R} = \sqrt{\frac{2\Delta P_{rad}}{\eta_{opt}\eta_{pb}}} \tag{2.103}$$

The intrinsic variations in the received optical power due to the bosonic nature of the light is another source of photon-induced quasi-particle fluctuations. If we consider radiation as a flux of randomly incoming particles, they obey to poissonian statistics. Since the power is directly proportional to the number of photons, the so-called *photon shot noise* depends on the square root of the incoming power. The expressions of this noise power spectrum and its contribution to the NEP are given by [82] [81]

$$S_x^{GR} = \frac{2h\nu P_{rad}(1+mB)}{1+(2\pi f\tau_{qp})^2}\left(\frac{dx}{dP_{rad}}\right)^2 \tag{2.104}$$

$$NEP_{ph,S} = \sqrt{\frac{2h\nu P_{rad}(1+mB)}{\eta_{opt}}} \tag{2.105}$$

where ν is the frequency of incoming light and the factor $(1+mB)$ is the correction to Poissonian statistics due to photon bunching [83].

We can therefore calculate the overall *photon noise* as the quadratic sum of these two

contributions, obtaining

$$NEP_{ph} = \sqrt{\frac{2h\nu P_{rad}(1+mB) + 2\Delta P_{rad}/\eta_{pb}}{\eta_{opt}}} \tag{2.106}$$

For example, for ground-based or balloon-borne millimeter Astronomy applications, the optical background due to atmospheric emission leads to a photon noise exceeding $10^{-17}W/\sqrt{Hz}$.

Two-level systems noise

Its has been historically notice that KID devices show a phase noise excess at low frequencies. This component manifests itself with resonator frequency fluctuations and the signal exhibits $1/f^{0.5}$ noise component [84]. In has been recently shown [85] that this noise can be ascribed to random variations of the effective dielectric constant surrounding the KID and give rise to the so-called *Two-Level Systems (TLSs) noise* [86]. The TLSs excitation is favored by high value of the electrical field. As a consequence, for a LEKID device this noise affects in particular the capacitor. It has been shown that a wider spacing of its interdigitated fingers reduce the TLS noise [87]. Finally, the thin oxide layer forming on the substrate and on top of the metallic film itself, create additional interfaces with dielectrics that need to be taken into account. These interfaces introduce more TLSs fluctuators just where the electric field is stronger, degrading the detector performance. One possible solution is to remove, by wet etch (HF) or Ar plasma milling, the native SiO_2 [47].

Non-fundamental noise sources

To achieve the sensitivity limit set by the photon noise, all other potential noise sources have to be minimized. This includes the noise caused by the instrument itself such as the electronics devices in the readout chain. The readout chain is designed to leave the dominant contribution to the front-end cryogenic Low Noise Amplifier (LNA). The effect of the following RF components is reduced by a factor 1/G, being G its gain ($\sim 30dB$ for our LNA). A LNA with noise temperature T_{amp} yields to a NEP contribution of [73]

$$NEP_{LNA} \approx \frac{\Delta N_{qp}}{\eta\tau_{qp}}\sqrt{\frac{k_B T_{amp}}{P_{read}}} \tag{2.107}$$

where P_{read} is the microwave readout power sent into the RF chain. A larger readout power allows a better determination of the output signal, consequently reducing the NEP_{LNA}. The maximum power P_{read} is called the KID *handling power*. The handling power is proportional to $1/Q_i$ [88] so lowering the LNA noise has the tradeoff of reducing the responsivity of the detector.

Chapter 3

Lumped Element KID electronics and techniques for readout

A crucial point in favor of KID is that they are intrinsically suited for Frequency Domain Multiplexing (FDM). Since they are high quality factor resonators ($Q \sim 10^4 \div 10^5$) with central frequencies typically around a few GHz ($f_0 \sim 1 \div 3GHz$), eq. 2.91

$$Q \approx \frac{f_0}{\Delta f_{FWHM}}$$

implies a resonator bandwidth around of $10 \div 100$ kHz. As the KID resonance frequency can be easily controlled during manufacturing, it is possible to couple a large number of detectors to a single transmission line without interference, therefore obtaining high multiplexing ratios (fig.s 3.1–3.2). Currently, hundreds of KID can be coupled to a single transmission line by spacing their resonance peaks by 1 to 2MHz in order to minimize interferences and crosstalk [77] [89]. This is the key advantage of using KID for any experiment requiring a very large format array of high-sensitivity low-temperature detectors. Such arrays are one of the main requirements of next generation millimeter-wave Astronomy cameras and of many Particle Physics experiments searching for rare event, whose sensitivities essentially scale with the on-sky integration time and the mass of the detectors, respectively. In mm-Astronomy, longer integration times are achievable increasing the pixel-count of the focal plane (chap. 4); in rare event Particle Physics, the sensitivity can be enhanced instrumenting the wide surface of the experiment with light detectors able to discriminate between different events, typically in the X-ray domain (chap. 9). In both cases, the increase in the sensitivity of the experiment is related to the capability to operate very large arrays of light detectors. In order to fully exploit the potential of their high Frequency Domain Multiplexing, KID arrays need to be read-out properly. In the following we describe the readout electronics and techniques adopted during this thesis, for instruments dedicated both to mm-Astronomy and to X-ray Particle Physics.

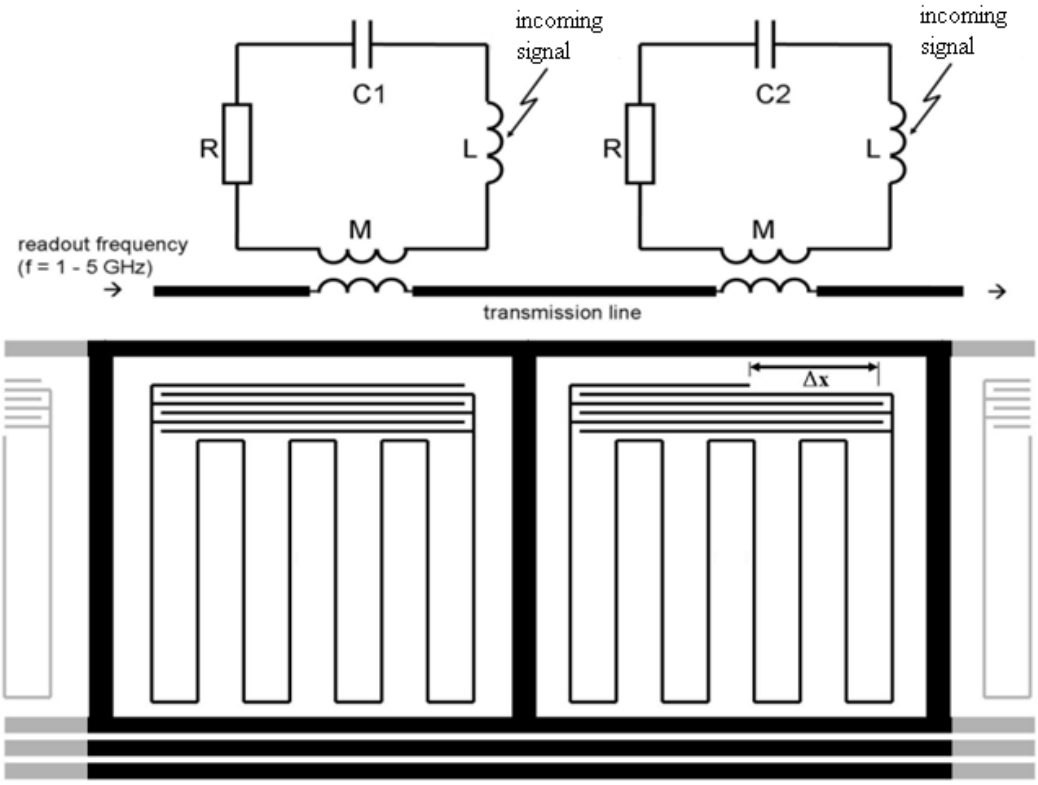

Figure 3.1: *Schematics of a single transmission feedline coupled to several KID. Each detector resonates at a different frequency, thanks to the varying length of the interdigited capacitor.*

3.1 Working principle of the Data AcQuisition

The KID high multiplexing factor results in hundreds of detectors being coupled to a single transmission line. In order to readout the KID array, a frequency comb having all its tones tuned to the different resonators center frequencies must be fed to the detector. Since the energy absorbed by the detectors produces a frequency shift of the resonance, the simultaneous measurement of all the pixels is achieved by monitoring each KID at its own resonant frequency. This is obtained acquiring and analyzing the resultant signal at the output of the transmission line coupled to the KID array, in order to determine the time dependent phase and amplitude variation of each sinusoid.

In order to perform these operations, we build the frequency comb in real time by summing as many tones as necessary. Since the KID resonator frequencies are $> 1GHz$, it is not possible for standard electronics to directly drive the array. Therefore, as shown in fig. 3.3, the frequency comb must be generated at a lower frequency band (baseband) and upconverted to the frequency band of interest. This is obtained by generating the In-phase

(I) and Quadrature-phase (Q) components of the tones and upmixing them with a reference Local Oscillator (LO) carrier using hybrid IQ-mixers. The signal is then passed through the KID array at the appropriate power level using a programmable attenuator. The KID array, typically operated at sub-Kelvin temperatures, is followed by a LNA operated at 4K, and a warm amplifier. The signal is then downconverted and sent to the electronics, where the I and Q components of the tones are obtained using a channelized Direct Down Conversion (DDC) method (fig. 3.4) [90]. With these, the amplitude ($A = \sqrt{I^2 + Q^2}$) and phase ($\phi = arctan(Q/I)$) of each transmitted tones can be continuously monitored using an Analog to Digital Converter (ADC) before the Data AcQuisition (DAQ) readout provided by the DDC.

It is important to note that the use of an IQ mixer is mandatory, because it presents the benefit of strongly attenuating the lower sideband and the carrier in the output up-mixed spectrum. The spectrum resulting from the down-mixing stage still contains residuals of the lower sideband due to the upmixing (fig. 3.5), with a typical rejection of -30 dB.

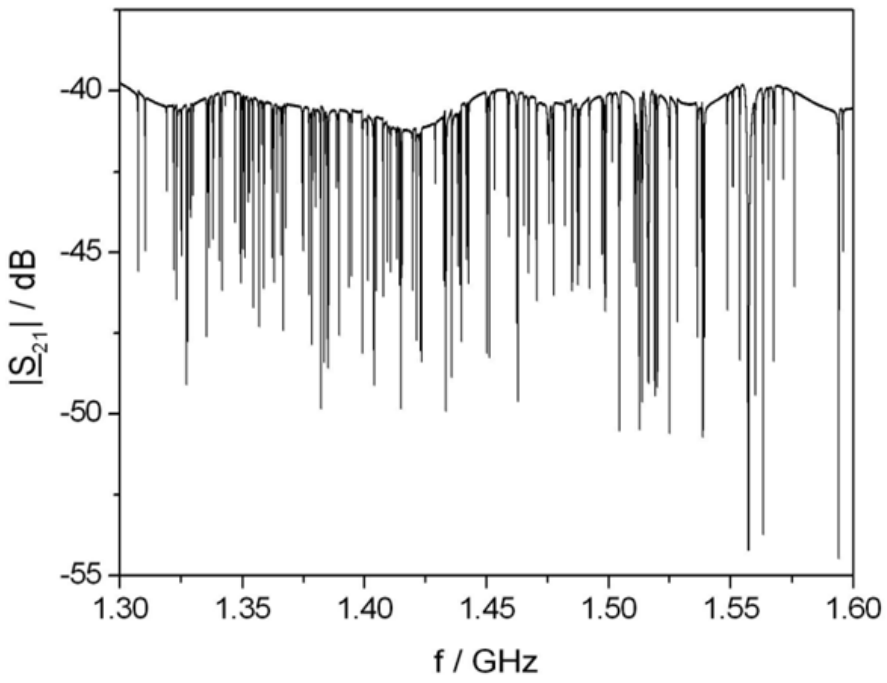

Figure 3.2: *Typical frequency scan of a NIKA hundred-pixels array (chap. 4), showing 128 KID resonances packed in* ~ 300 *MHz total bandwidth.*

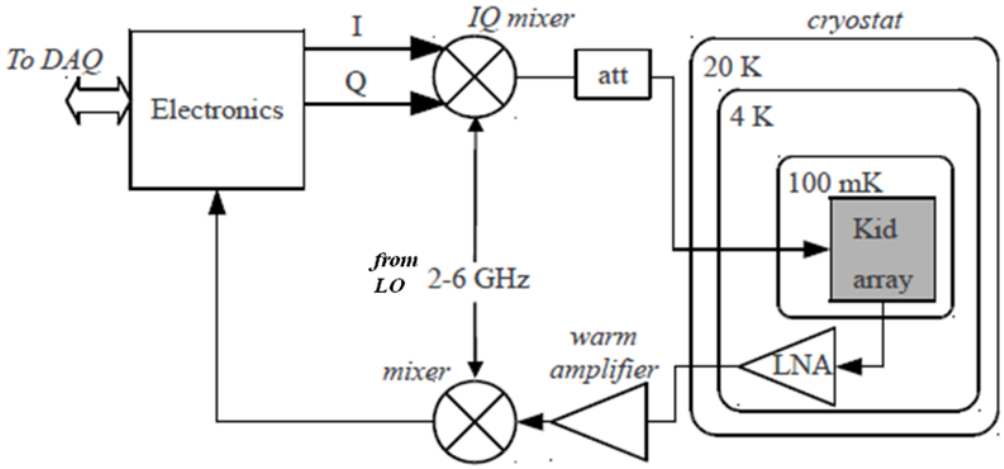

Figure 3.3: *Overview of the setup required to monitor a KID array. The electronics DACs generate the two frequency combs (each tone phase shifted by 90deg between the in-phase I and quadrature-phase Q signals), that are up-converted to GHz frequency with an IQ mixer device before to be sent to the the programmable attenuator for power adjustment and reach the dectors arrays hosted in the cryostat. The signal is finally down-mixed back to the baseband in order to be processed by the electronics. The output signal passes through a Low Noise Amplifier at 4K, eventually further amplified at room temperature before the down-conversion to electronics bandwidth. Finally the signal is red by ADC and send to Data Acquisition (DAQ) system.*

3.2 The NIKEL electronics for mm-Astronomy

The NIKEL electronics is an integrated board developed at LPSC Institut (Grenoble, France) in collaboration with the NIKA team. It requires only two coaxial SMA cables for instrumenting a large KID array. The direct frequency comb synthesis and the data acquisition relies

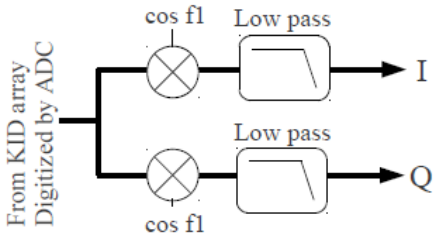

Figure 3.4: *Overview of the Direct Down Conversion (DDC) method. The incoming signal, containing all the frequencies of the comb, is first split in two branches and multiplied by the sine and cosine waves of the tone of interest and finally low pass filtered in order to keep only the lower side band, i.e. the baseband, of the signal.*

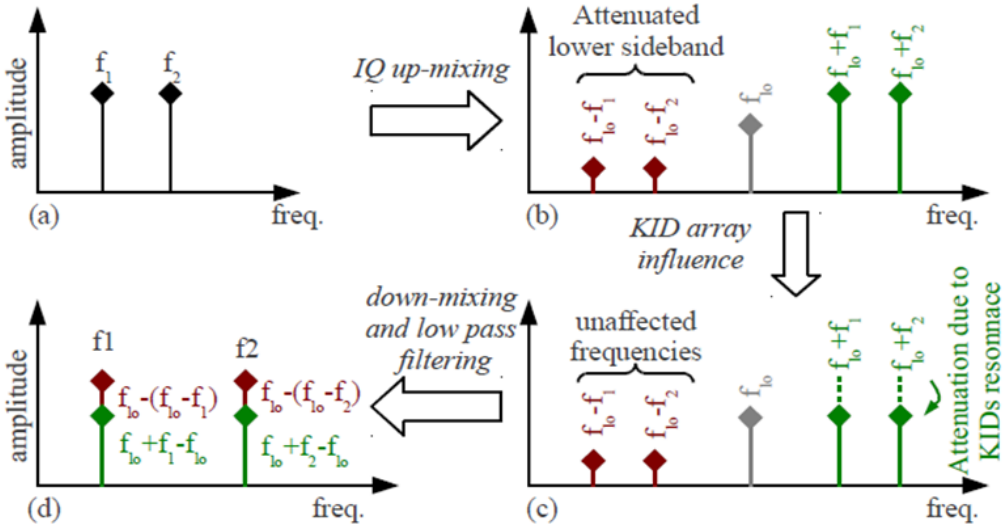

Figure 3.5: *Illustration of the up and down-mixing of two tones f_1 and f_2 by a carrier f_lo with ideal mixers (no harmonics generated). Part (c) depicts the spectrum affected by the KID array, only the green part is attenuated by a maximum of 2 to 10 dB (practical rejection values), i.e it still contains amplitudes 20 to 28 dB larger than the residuals in red. As shown on (d), the tones affected by the KID array and the image frequencies, i.e. the residuals (red), are summed because of the back folding due to the down-mixing.*

heavily on a large Field Programmable Gate Array (FPGA) using parallelized and pipelined processing. The complexity of the design is directly driven by the targeted analog bandwidth and the number of tones to manage. Several versions of the board have been developed with different hardware and firmware architectures.

3.2.1 The NIKEL v0 board

The first prototype of digital frequency multiplexing electronics allowing the real time monitoring of KID arrays, the *NIKEL v0 board* [91], has been developed for mm-Astronomy observations. This first prototype can excite 128 resonators over a bandwidth of 125 MHz and has been successfully tested by the NIKA detectors and instrumentation group, in the Institut NÃ¨el laboratories (Grenoble, France).

The hardware platform is FPGA centered and features a dual DAC for the frequency comb generation, an ADC and a USB2 micro-controller for DAQ and slow control interfacing. A picture of the board can be seen in fig. 3.6. In order to demonstrate the concept feasibility and to keep the design simple, it was chosen to limit the sampling and processing frequency to 250MHz (analog bandwidth of 125 MHz). Therefore a 12 bit ADC (AD9230) having an input dynamic range of $1V_{pp}$ and a SNR of 69 dB, was used, the excitation being performed by a 14

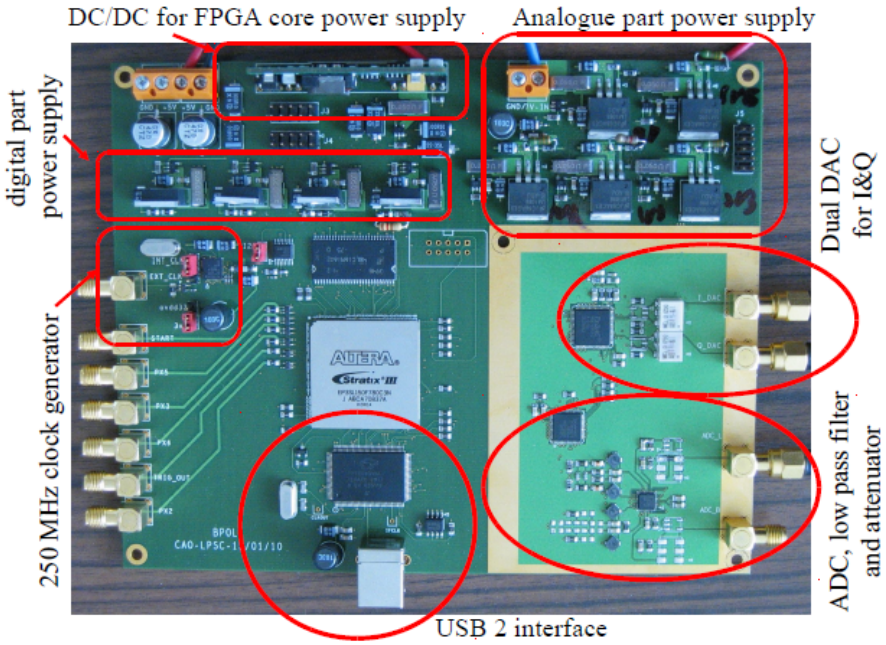

Figure 4. Picture of the prototype board.

Figure 3.6: *Picture of the NIKEL v0 prototype board.*

bit DAC (AD9781). A 17 bit phase accumulator together with a COordinate Rotation DIgital Computer (CORDIC) [92] is used to adjust the frequency with a precision of $f_{step,min} = 250MHz/2^{17} \sim 1.9kHz$.

The selected FPGA was an ALTERA R stratix III (EP3SL150F780) because it provided a large multiplier count coupled to a large amount of user logic. The board can be clocked by its Local Oscillator or by an external reference clock. The latter and the spare trigger inputs are provisions allowing to synchronize several KID arrays.

The NIKEL v1 board

Starting from the previous version, a second prototype, the *NIKEL v1 board*, has been developed [93]. The NIKEL version 1 electronics is an integrated board capable of generating up to 400 tones over a 500 MHz bandwidth. This is achieved by using 6 separate Xilinx Virtex-6 FPGAs (XC6VLX75T-2FFG484C): five of them generate 80 tones each over a 100 MHz band, using five associated DACs. Each of the five FPGAs is equipped with a CORDIC fed by a 18 bit phase accumulator feeds, which allows to adjust the frequency of each tone with a precision of $f_{step,min} = 250MHz/2^{18} \sim 953Hz$. The sixth FPGA acts as a central unit that combines the signals of the other units, appropriately shifting and filtering the different 100 MHz sub-bands to finally cover the whole 500 MHz available for the frequency comb used

to excite the detectors. An analogous, but reversed, process is then applied to the signal acquired by the ADC of the board, which is once again split in 5 different sub-bands treated separately. Each NIKEL v1 board thus allows us to monitor up to 400 tones simultaneously, with a sampling rate of $\sim 24Hz$. Two NIKEL v1 electronics (one per band) were integrated in the NIKA readout chain and successfully operated during the latest observational campaigns [41], whose results are presented in cap. 4.

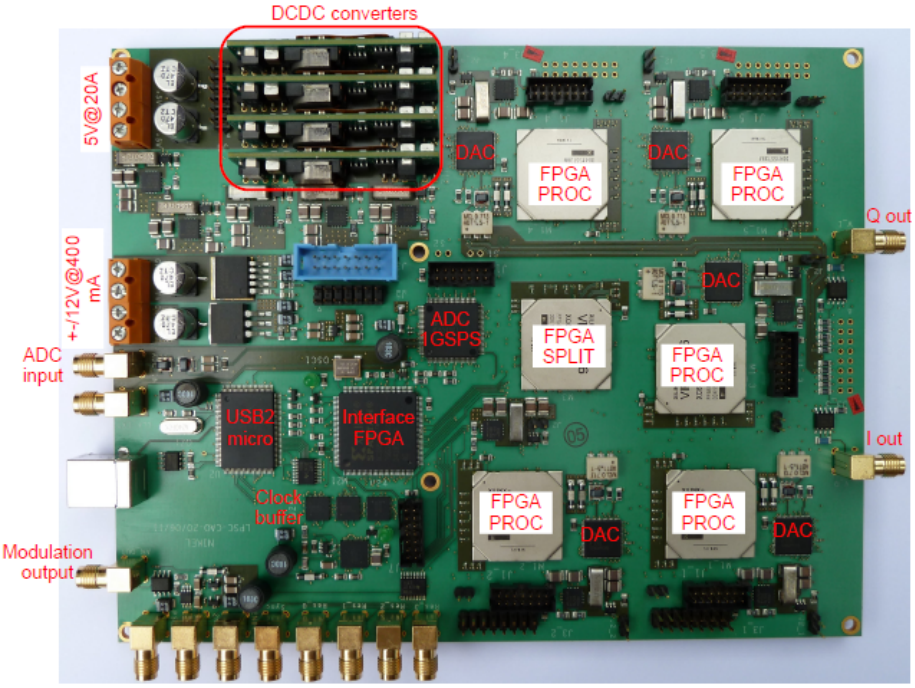

Figure 3.7: *Picture of the NIKEL v1 prototype board.*

3.3 The NIXA high-speed electronics

The high energy ($\sim 10^1 \div 10^3 keV$) particles interacting in the wafer of KID array can be detected through the phonon diffusion in the substrate. The phonon-mediated detection, described in the introduction of the part III of this thesis, can be used for time and energy resolved detection of high-energy interactions, devoted to the optimization of the KID array either for mm-wave space-borne Astronomy or for X-ray Particle Physics.

To this purpose, a dedicated fast readout electronic matching the following requirements has been developed [94]:

- achieve an **acquisition rate up to 2 MSPS** (Mega Sample Per Second) to cope with the phonons propagation speed (typically in the order of few $mm/\mu s$) and with the

typical KID signal rise time τ_{res} (few μs for $f_0 \sim GHz$ with $Q \sim 10^5$, eq. 2.57);

- **read-out an array of at least 3×3 KID** to be able to perform time-resolved two-dimensional detection. Given resonance frequencies separated by a few MHz, this implies that the analog bandwidth must be larger than about 50 MHz;

- have a **triggered acquisition**. Since the array is monitored at high speed, only the useful events must be acquired. This requires an on-line trigger able to select the events of interest by triggering on the amplitude of the transmitted tone. The trigger level must be independently adjustable for each KID, as they have different transfer functions (in terms of transmission gain and dephasing);

- acquire a **data frame of up to 1000 samples**, with the possibility to get up to 500 samples before the trigger (pre-samples), necessary for time-resolved detection. The possibility to record the baseline prior to the event detection also allows for baseline suppression and real time noise studies;

- have a **SNR better than** $\sim 60dB$: the LNA noise is followed by a typical amplifier chain gain of $60 \div 65dB$. Thus the best SNR achievable on this part is already limited to about 60 dB.

The main technological issue in the development of a high-speed multiplexed read-out is the simultaneous generation/acquisition of an high number of tones operating at a $\sim MHz$ sampling rate. The maximum number of tones is actually limited by the amount of computational memory required to strongly filter the different tones in order to avoid crosstalk between them. For this purpose, the DDC is followed by highly selective low pass filters (fig. 3.4) composed by a cascade of sub-filters, allowing a KID sampling rate settable between 1.953 MSPS and 488 KSPS. To allow on-line triggering, the filters outputs are also used to compute the square of the amplitude module ($A = \sqrt{I^2 + Q^2}$) that is constantly compared to the square of the amplitude thresholds (one per KID).

3.3.1 The NIXA board

The electronic board is built around a *main FPGA* (Xilinx Virtex-6) which is in charge of generating the frequency comb and of performing signal processing. The data acquisition and slow control interface to this FPGA is done using a USB2 micro-controller (*mini-pc*) and another FPGA (Xilinx Spartan-3AM) , which we call *interface FPGA*. The combination of the two allows the FPGA reconfiguration from the USB2 interface, providing large flexibility (see next paragraph).

The resources availability in the FPGA constraints the resources available for the filters used to generate the 12 tones. The building block of the firmware features a 14 bit resolution

CORDIC which is used to provide the sine and cosine waves for the DDC and for building the array excitation signal. This CORDIC, driven by a 18 bit phase accumulator, allows a frequency tuning resolution of $250MHz/2^{18} = 953Hz$. The digital version of the frequency comb generated by the main FPGA in its I and Q version is fed to a dual 16 bit DAC operated at 250 MSPS. This DAC is able to provide analog samples at a rate of 1 GSPS over a bandwidth of 100 MHz. A fast ADC , having a resolution of 14 bit and operated at 250 MSPS is used to sample the down-converted KID array signal output and thus to provide the digital samples to the main FPGA for processing.

3.3.2 Dual readout mode of the NIXA board

In order to fulfill other applications, such as for instance mm-wave Astronomy, the high-speed readout board described above was improved adding some of the capabilities of the *NIKEL v0* and *v1* electronics. Thanks to these additional features, it is possible to use the same read-out electronics hardware either for high or for low speed readout. The desired behavior of the board is obtained by loading the corresponding firmware in the main FPGA through the mini-pc. We resume here the principal features of the two different modalities available in the *NIXA board*:

- **NIXA-fast**, high-speed readout for X-ray and Particle Physics applications:

  1. capability of generating up to 12 tones over a 100 MHz band;
  2. on-board digital strong filtering, sampling rate selectable between $\sim 500kHz$, $\sim 1MHz$ and $\sim 2MHz$;
  3. acquisition data frame up to 1000 samples for each tone, or (successive modification) 16000 samples for a single tone (par. 8.7);
  4. threshold on the amplitude of the signal $A = \sqrt{I^2 + Q^2}$ to trigger the acquisition start, customizable for each tone;
  5. buffer memory able to acquire up to 500 pre-samples before the trigger.

  The *NIXA-fast* firmware has been used for the SPACEKIDS (chap. 6-7-8) and the CALDER (chap. 9) projects.

- **NIXA-slow**, low-speed read-out for mm-Astronomy applications:

  1. capability of generating up to 80 tones over a 100 MHz band;
  2. on-board integration, sampling rate up to $\sim 1kHz$;
  3. possibility to achieve multi-board synchronization, thanks to the use of the optional external clock reference and of the start signal input;

4. capability to control a radio-frequency source modulation (up to a few kHz) with a slow DAC.

The *NIXA-slow* firmware has been used for the ASTROKID project (chap. 5)

3.4 The *sNelloX* data acquisition software

In parallel to the realization of the hardware and firmware architectures, it has become increasingly necessary to develop an additional instrument to intuitively operate the electronics. We have thus developed a user-friendly software able to fully manage and control all the steps of the KID multiplexed read-out procedures, called *sNelloX*. This tool has been implemented by using the C-integrated *LabWindows/CVI* development environment, an engineering toolbox by National Instruments with built-in libraries for measurement, analysis, and User Interface (UI) design. The *sNelloX Client* is operated by an external pc, named *Acquisition-PC*, and is connected via ethernet (TCP/IP protocol) to the mini-pc controlling the *interface FPGA*, named *Server*. The *Client* commands, given from a windows UI, are then interpreted and reprocessed before being sent through *Server* to the *main FPGA*. The data flow then follows the opposite path, being registered in dedicated client variables that can be stored for further on-line analysis, or deleted.

The *sNelloX Client* is compatible with both the operating modes of the main FPGA, *NIXA-slow* and *NIXA-fast*. Sample screen-shots of the *Client* UI with its principal functionalities are presented in figs. 3.8–3.12

3.4.1 Detectors characterization

Before reading-out the variation of the phase signal under an optical load or induced by an incoming particle, the optimal working point has to be chosen for each detector. The typical procedure consists the following steps:

1. **Broad scan**. A comb of N equally spaced tones is generated in the Frequency Domain (FD) by the FPGA. The LO frequency is then changed by steps of f_{step} from an initial value f_{start} to a final one f_{end}. Since the tones are continuously up-mixed with the LO carrier, increasing its frequency by f_{step} results in a rigid shift of the comb of the same amount. This allows scanning the frequency domain with a resolution f_{step} over a $\Delta f_{tot} = f_{end} + N \cdot f_{step} - f_{start}$ total bandwidth. During this broad scan, the I and Q components are acquired and the transmitted amplitude A is calculated.

2. **Search**. If Δf_{step} is lower than the bandwidth of the typical single resonance Δf, then each KID resonance will result in a minimum of the amplitude A, detectable with

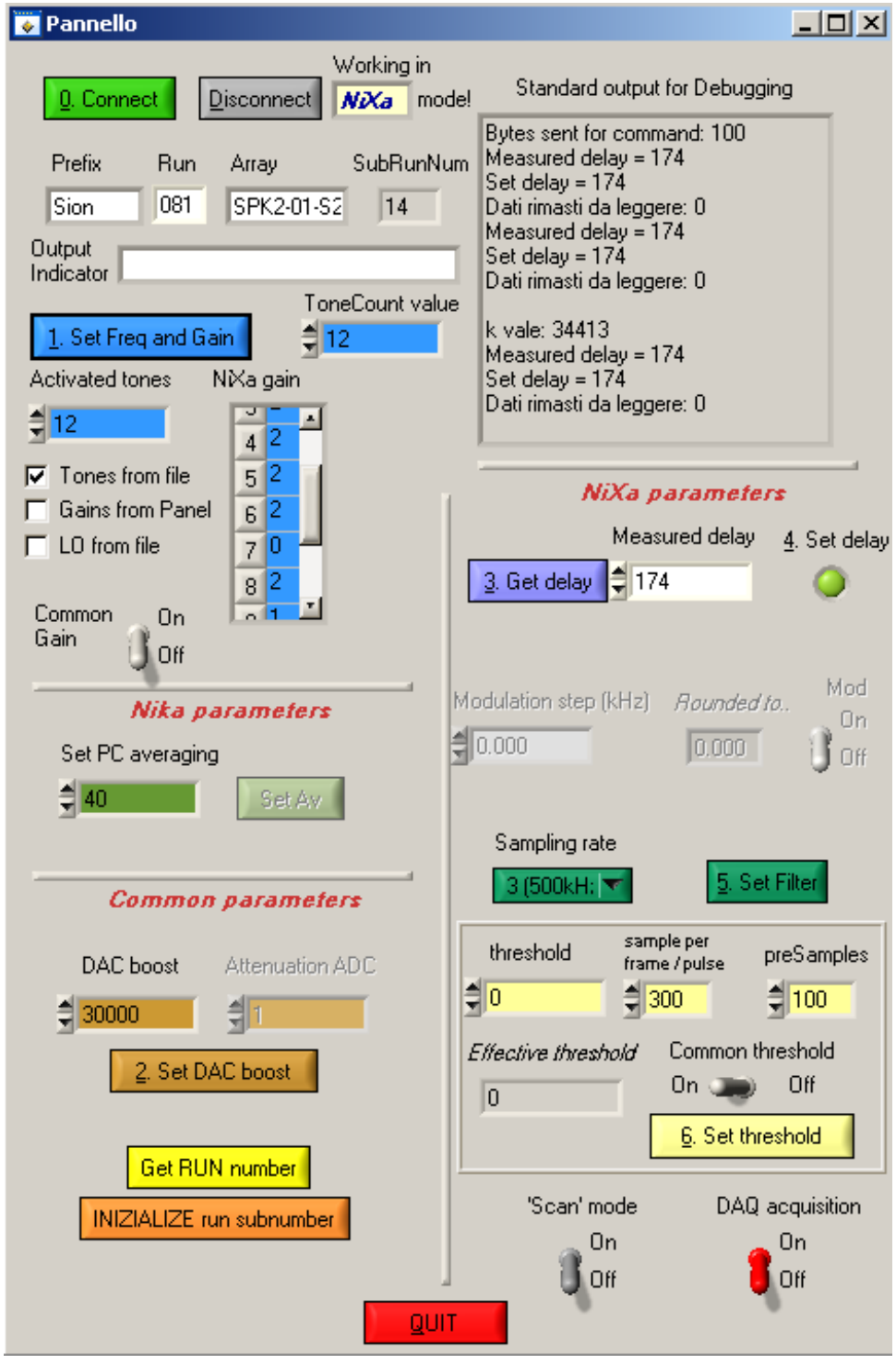

Figure 3.8: *Control User Interface panel to communicate directly with the FPGA.*

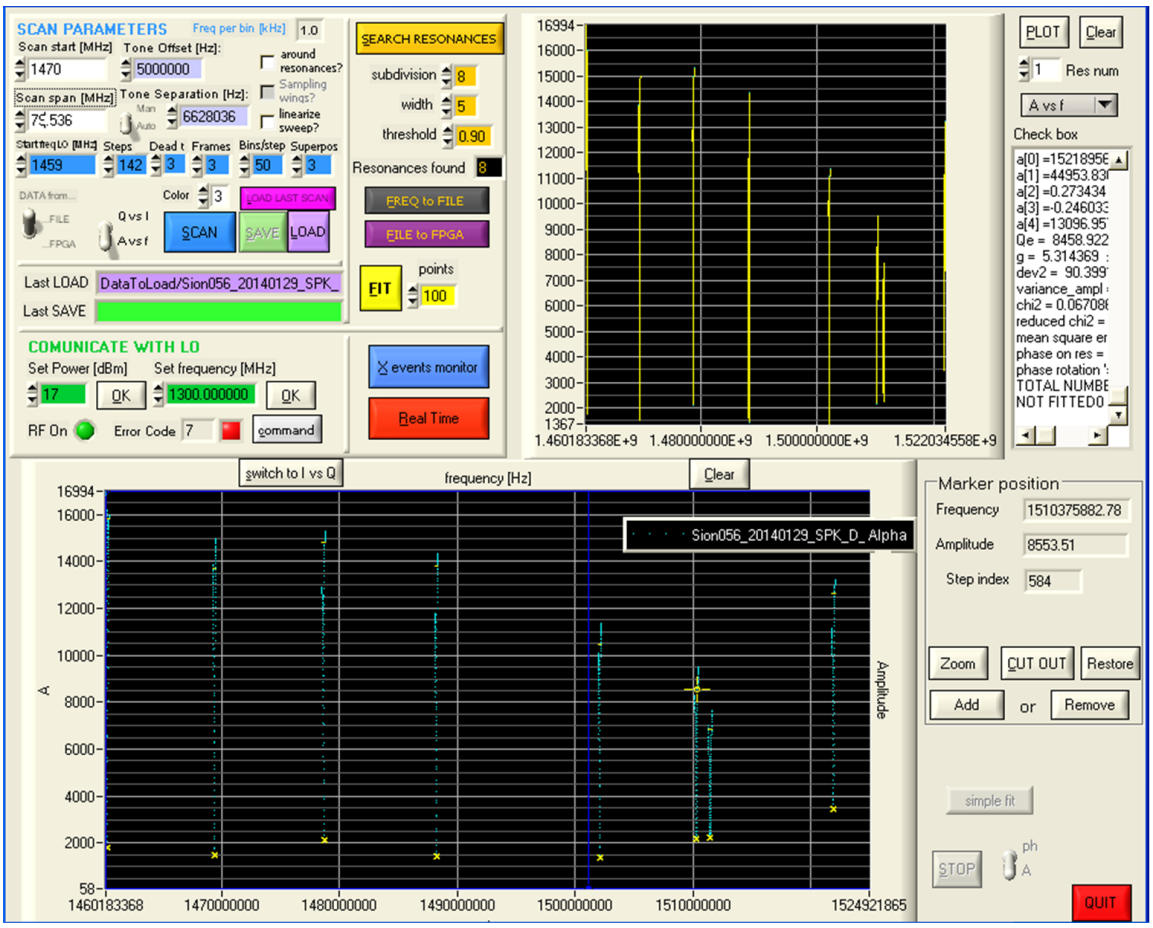

Figure 3.9: *User Interface panel to communicate with the Local Oscillator. This panel allows to perform the Board and Narrow scan in order to find, characterize and calibrate the resonances.*

dedicated algorithms. Once the minima are found, they can be identified with the KID resonance frequencies (within an error $\sim f_{step}/2$).

3. **Narrow scan**. The FPGA generates a new comb with the tones matching the identified frequencies after the up-mixing. A higher resolution scan (*narrow scan*) is then performed around the resonances in order to characterize their response.

4. **Fit**. A fit of the amplitude versus frequency ($Avsf$) response is performed for each resonator using the formula 2.84. The resonator parameters are then calculated: the resonance frequency f_0, the internal and external quality factors Q_i and Q_e, and the parasitic reactance P (see par. B.2).

5. **Calibration**. The phase of the transmitted signal is calibrated in unit of resonance frequency shift, which is independent from the resonator parameters. The approach

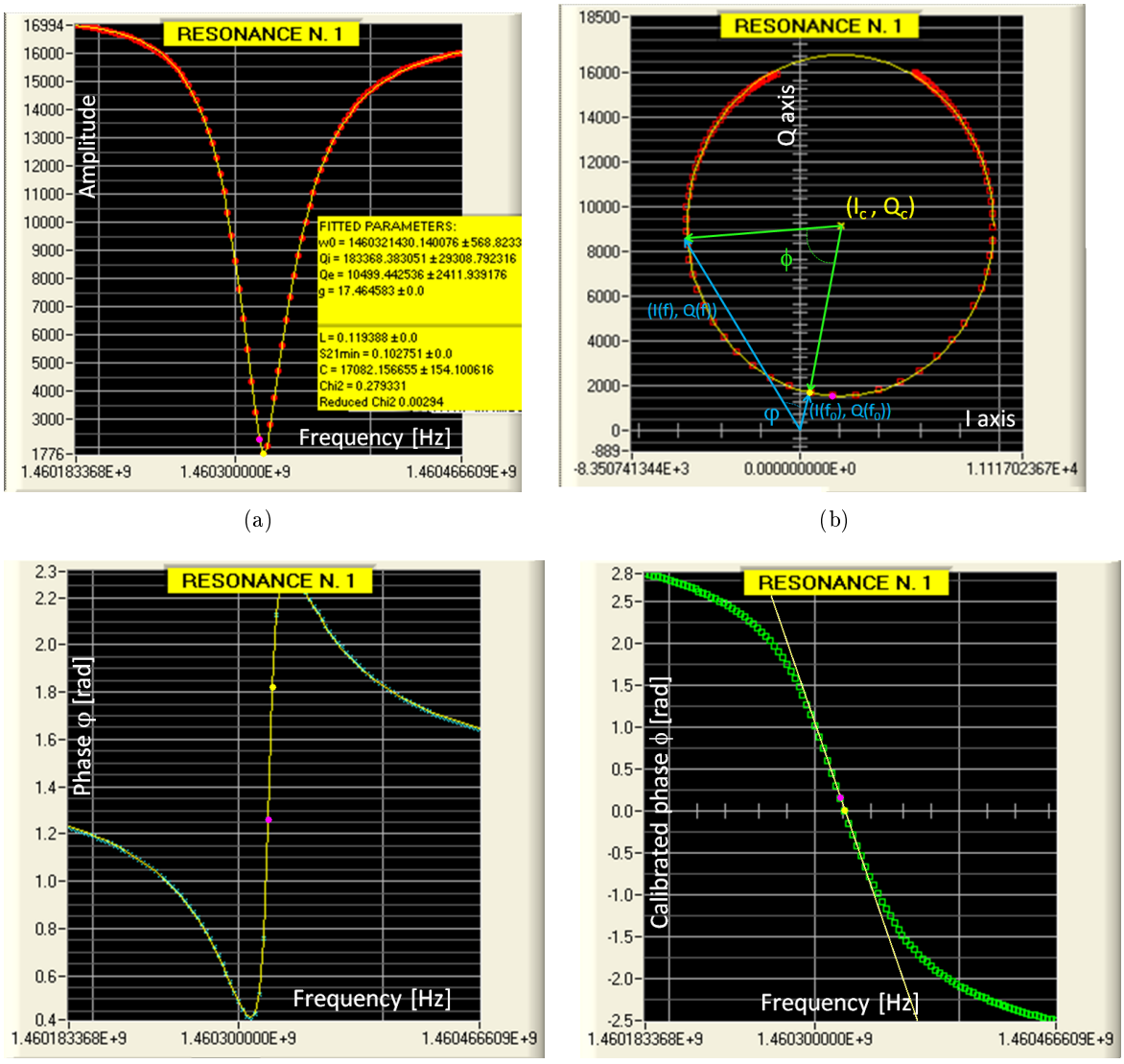

(a) (b)

(c) (d)

Figure 3.10: *sNelloX resonance characterization and calibration. Scattered plots represent data, solid yellow lines represents the fits. (a) The resonance shape(red solid circles) fitted with the eq. 2.84; (b) I-Q frequency sweep across a resonance. The complex phase is calculated by fitting the resonance (red open squares) to a circle equation; the phase angle is then determined with respect to the center of the resonance circle (yellow ×); (c) the phase with respect to IQ-plane center, usually called calibrated phase (cyan ×), fitted with the eq. B.20; (d) calibrated phase shift versus frequency plot (green square). The linear fit in the central region provides the frequency calibration. Alternative calibration can be provided by fitting data to an arctangent (as in chap. 8). The minimum transmission is marked with a bold yellow circle, while the maximum of the calibrated phase variation is highlighted by a bold purple circle.*

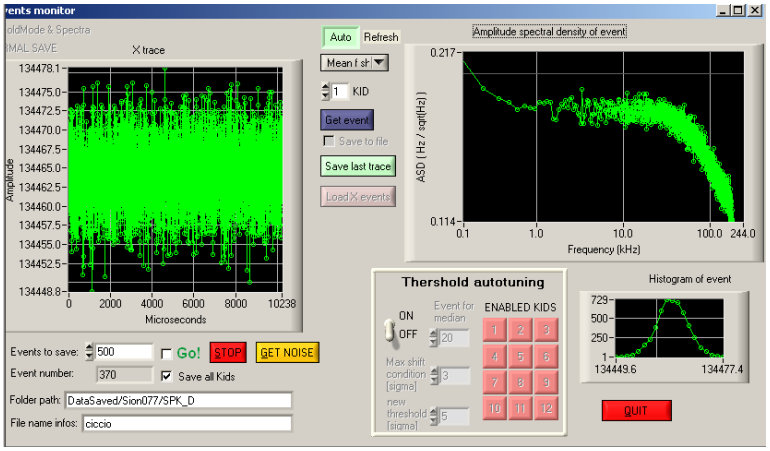

(a)

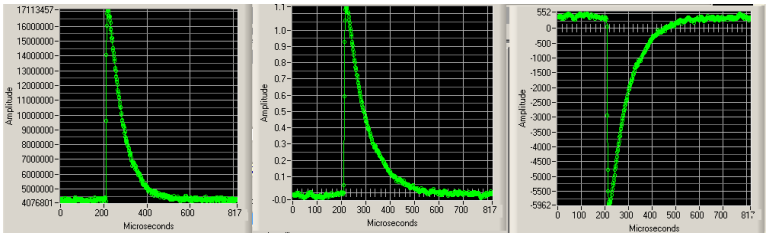

(b)

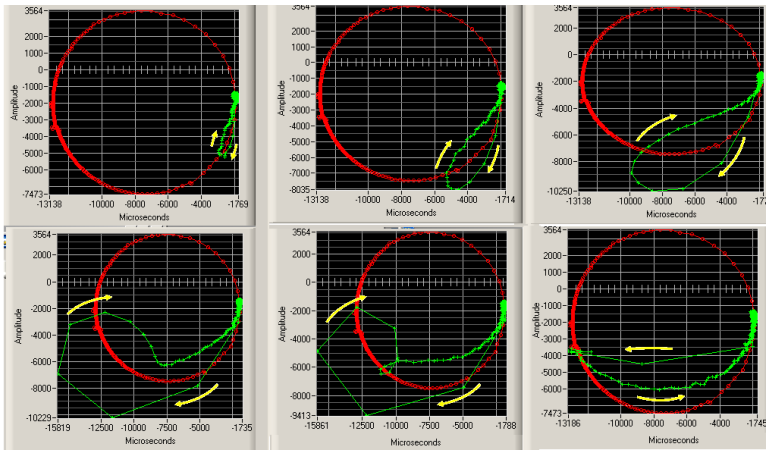

(c)

Figure 3.11: *X and Cosmic Ray event monitor: (a) the panel used to acquired pulses and noise data, with the on-line calibrated noise power spectrum; (b) examples of phonon-mediated detection of an α particle of $\sim 6MeV$, with the plot showing the pulse time trace of the amplitude (left), the calibrated phase (middle), and the frequency shift (right); (c) pulse time evolution (green line) in the complex plane for secondary Cosmic Rays of different energies. The time evolution follows the yellow arrows. The IQ-resonance circle is plotted in red.*

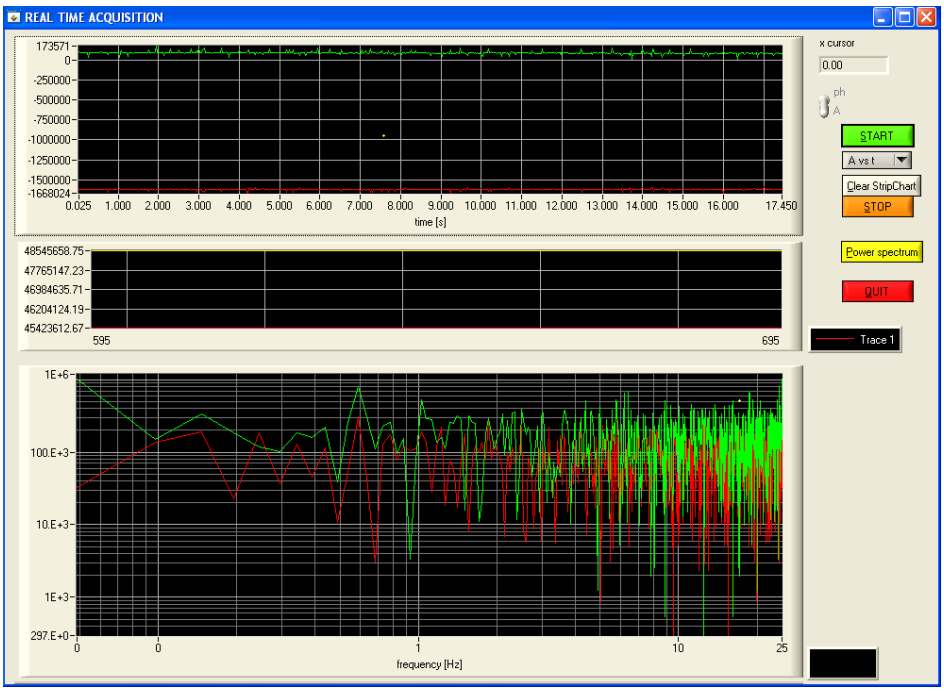

Figure 3.12: *Real time acquisition panel for mm-Astronomy applications. The top monitor shows the signal (amplitude, phase, calibrated phase or frequency shift) acquired in real time, with the corresponding noise power spectrum calculated in the bottom plot.*

used by *sNelloX Client* is described in the next paragraph;

6. **Working point choice**. The optimal working frequency is chosen for each detector and written on the FPGA comb. Two main solutions are possible:

   - the frequency that minimizes the amplitude of the resonance ($Avsf$ response);
   - the frequency that maximize the variation of the calibrated phase (ϕvsf response).

3.4.2 Relative calibration of the detectors

In order to be able to compare the response of different detectors, we need to calibrate them with respect to a variable independent on the specific features of each resonator. The resonance frequency provides such a variable. In fact, combining eqs. 2.99 and 2.94, we obtain

$$\frac{d\omega_0}{dN_{qp}} \approx -\frac{\alpha}{2nV} \tag{3.1}$$

This means that the resonance frequency is proportional to the quasi-particle number and hence to the incoming power (eq. 2.20), through a factor that does not depend on the resonance parameters. Thus, the resonance frequency shift is linear with the incoming power

variation $\delta f_0 \propto \delta P_{in}$ [46] [42], and we can use it as a relative calibration of the responses of different detectors.

This approach consists in characterizing the response of the detectors before the observations. Thanks to a frequency sweep around the resonances, we fit the IQ resonance circle, find its center $I_c + jQ_c$ and evaluate the phase with respect to it (fig. 3.10(b), left). We thus obtain what we generally call the *calibrated phase*

$$\phi(f) = arctan\left(\frac{Q(f) - Q_c}{I(f) - I_c}\right) \tag{3.2}$$

This new variable has the advantage of varying linearly with incident power in a wider interval of frequencies [89]. Then, using the narrow scan characterization, we can associate a frequency f to each value of the measured calibrated phase (fig. 3.10(b), right). A linear or arctangent (see par. 8.2) fit then provides a direct calibration of the signal in unit of frequency shift δf_0, a variable that does not depend on the KID parameters. As this calibration methods has to be applied off-line, it is affected by changes in background conditions: the resonance circles rapidly change with the power load, shifting the optimal working point and lowering photometric accuracy, so that many sweeps are needed to recalibrate the resonances. Yet, it is very well suited for faster impulsive signals in dark environment or under constant optical load.

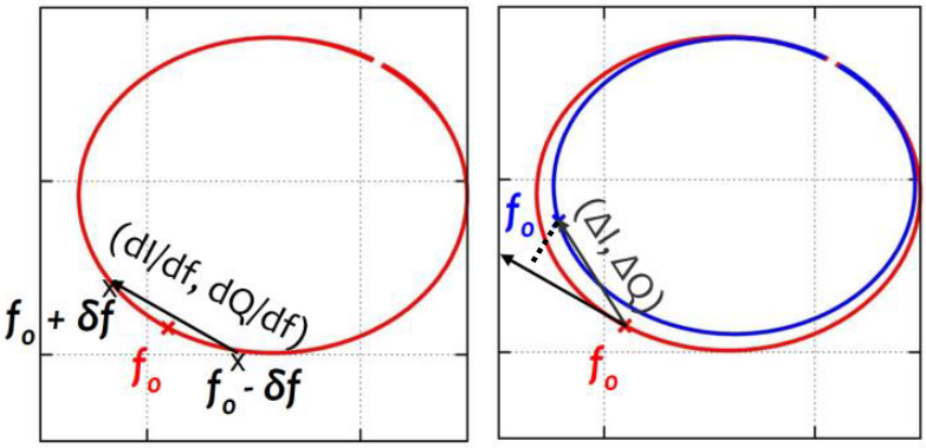

Figure 3.13: *The modulated read-out. On the left, a classical sweep in frequency around a resonance (red circle) in the IQ plane, f_0 (red $\times$) is the resonance frequency. The two points in frequency $f_0 + f$ and $f_0 - f$ are indicated by the black $\times$ on IQ circle. On the right, IQ circle (blue) changed due to an incoming power. The gradient vector (black arrow) is tangent to the resonance circle in the working point. It is used to obtain the shift in frequency simply projecting the vector $(\Delta I, \Delta Q)$ between two successive observations (blue arrow) on this gradient.*

3.5 Readout techniques under variable optical load

3.5.1 Modulated read-out

Finding a reliable way to evaluate $f_0(t)$ starting from $I(t)$ and $Q(t)$ represents a challenge, especially in the case of changing background conditions. This is true for example in ground-based experiments, as these have to cope with the effects induced by the variations in atmospheric opacity. To improve the photometric reproducibility, we have developed a measurement process which we call *modulated read-out*. It consists in modulating the LO carrier frequency, evaluating for each point not only (I,Q), but also (dI/df, dQ/df) (fig. 3.13). This provides us with a *reference gradient* that can be used to calibrate in frequency the shifts of the resonance. This can be done by calculating the vector $(\Delta I, \Delta Q)$ between two successive observations, and projecting it on the reference gradient. The shift in frequency f is given by

$$\Delta f = \frac{(\Delta I, \Delta Q) \cdot (dI/df, dQ/df)}{(dI/df, dQ/df)^2} \cdot \delta f_{LO} \tag{3.3}$$

where δf_{LO} is the amplitude of the LO modulation (fig. 3.13). The main advantage of the modulated read-out is that the reference gradient vector is automatically updated as the observing conditions change, obtaining a sort of real time calibration. This new calibration method was adopted during the NIKA campaigns and led to an improvement by a factor 3 in terms of relative photometric accuracy compared to the previous runs, where the IQ-circle center calibration was used [95].

3.5.2 Automatic tuning procedure

In this paragraph we focus on the strategy to adjust the resonance frequencies during the observations. As already said, the observing conditions often change rapidly. These changes modify the optimal working point, so that a sweep in frequency is required at the end of each observation, to tune again the frequencies. This process consume a lot of time at the expenses of scientific measurements. Our *real-time auto-tuning procedure* is an algorithm that quantifies the shift in frequency due to background fluctuations, without the need for a frequency sweep. The auto-tuning uses the angle θ between the vectors (I, Q) and (dI/df, dQ/df) to characterize the resonance (fig. 3.14). The tuning curve θ vs f is obtained by the initial frequency sweep. First of all, we rescale the θ angle so that $\theta = 0$ on the resonance. Suppose now that after some time we find $\theta \neq 0$. This means that the resonance shape has changed and its optimal frequency has shifted. Starting from the last measured $\theta vs f$ curve, the auto-tuning algorithm evaluates the correction that should re-center the resonance so that $\theta = 0$. Since a change of the resonance implies also a variation of the $\theta vs f$ curve, the correction does not generally leads to $\theta = 0$ after the first step, but it can be easily iterated as many times as needed (fig.

3.15). The whole process requires typically only a few seconds, and lead to an important increase in the observational time.

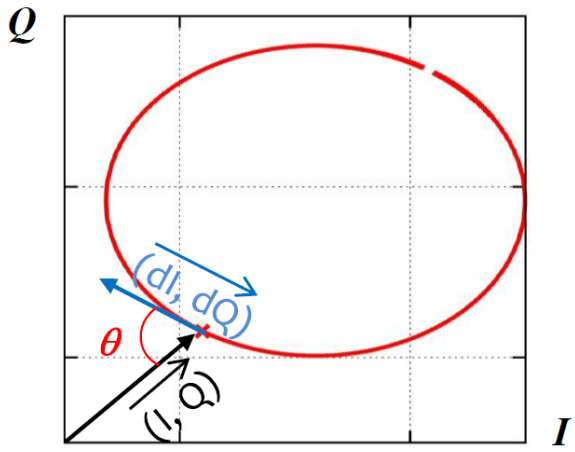

Figure 3.14: *Definition of the angle as the angle the vectors (I, Q) and (dI/df, dQ/df) in the IQ plane.*

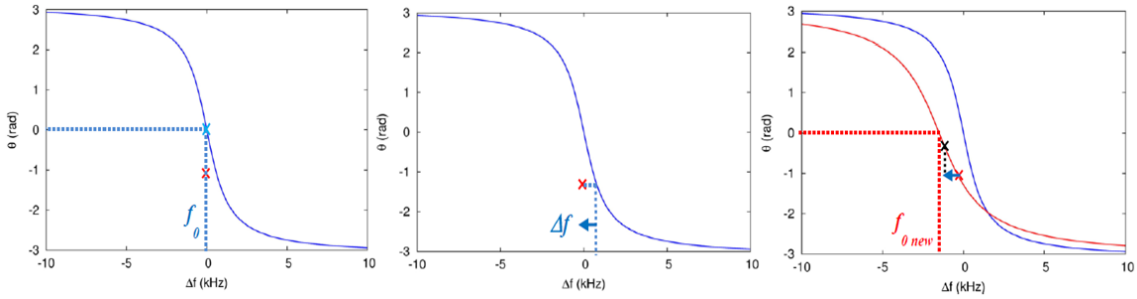

Figure 3.15: *Real time auto-tuning procedure. All the plots show: on the y-axis the angle between the vectors (I, Q) and (dI/df, dQ/df), rescaled to give 0 on the resonance; on the x-axis the shift in frequency f with respect to the initial frequency f_0. (Left) At the end of the initial sweep (blue tuning curve), we are in the working point indicated by a blue ×, that is at f_0. As the observing conditions change (but not the frequency we use to feed the resonance) the working point shifts to the red ×, because the tuning curve has changed to the red one shown on the bottom plot. As the exact form of the red tuning curve is unknown, (Middle) we calculate the shift in frequency that would be needed to get back to $\theta = 0$ if we still were on the blue tuning curve. (Right) Applying this correction to f_0 we are actually moving on the new tuning curve (the red one). At the end we are on the working point indicated by the black × and then we have approached the new resonance frequency f_{0new}. We can finally use these last two points (black and red ×) to evaluate the slope of the new tuning curve and iterate the process.*

Part II

Applications to millimeter Astronomy

Kinetic Inductance Detectors are naturally suited for very-large array applications. The high-sensitivity, the easiness of realization, and most notably the strong multiplexing factor makes KID technology a viable solution for next future cameras of millimeter Astronomy. In order to absorb incident radiation, it is necessary to match the KID impedance to free space at the target wavelength. In chap. 1, we have mentioned the current mostly used methods for meeting this criterion. The first is the use of coupling structure – usually a lens with an antenna – to adapt the resonator to free space (antenna coupled KID). Alternatively, the Lumped Element KID (LEKID) design provide both the absorber and the sensor in an single, planar geometry. We have chosen the latter solution and widely described its sensor architecture in chap. 2. The absorber is provided by the inductive meander of the resonance circuit, which acts as a solid absorber at the target wavelength. In fact, if the pitch of the meander arms (s) is much smaller than the wavelength of incoming radiation (λ), the effective optical impedance Z_{opt} that the wave sees is given by the averaged effect of the conducting arms and the empty spaces between them (fig. 3.16). The ratio of metallized surface is called the *filling factor* $f \approx w/(s+w)$, where w is the meander width. Therefore, the effective optical impedance of the resonator is given by $Z_{opt} = Z_{\square}/f$, where $Z_{\square}$ – called *normal sheet impedance* – is the impedance per square of metal film, as measured just above the superconducting transition. This corresponds to the electric resistance of the normal metal, or *normal sheet resistance*

$$R_{\square} \equiv R_n[\Omega/\square] = 10 \cdot \frac{\rho_n[\Omega \cdot cm]}{d[nm]}$$

where ρ_n is the normal resistivity of the metal film and d its thickness. Tuning s, w and t values it is thus possible to match the free space impedance $Z_0 = 377\Omega$.

Our LEKID arrays are fabricated on a silicon substrate. For our scopes, we always used silicon, with relative permittivity $\epsilon_r \sim 11.7$. Except for pixel's area, the surface of the array is uniformly filled with a conductor, a thin (tens of nm) aluminum film in most of this thesis. The usual strategy is to back-illuminate the array, using the cavity formed with the sample holder as a proper backshort. Tuning its distance from the array surface, it is possible to reflect back in the detectors the wave that they did not absorb in the 'first pass'. If the meander impedance is purely resistive, the reflected back wave is maximized on the detectors when this distance is equal to $\lambda_{eff}/4$ or $\lambda_{eff}3/4$, where $\lambda_{eff} = \lambda\sqrt{\epsilon_r}$ is the wavelength in the substrate. Tuning the resonator parameters and accounting for the substrate impedance $Z_r = Z_0/\sqrt{\epsilon_r}$, it is possible to directly match the LEKID impedance to free space [96].

One of the best advantages in using LEKID is the absence of additional focusing/macthing 3-D structures on the array, like lenses and/or feed-horns. Considering this, LEKID arrays are ideally suited for full-filled focal planes with respect to feed-horn coupled focal-plane architectures [97]. This allows to collect basically all the incoming energy and to increase the

mapping speed. The payback is a reduction in the intrinsic directionality of the focal plane, requiring a more efficient stray-light rejection strategy (e.g. cold stop).

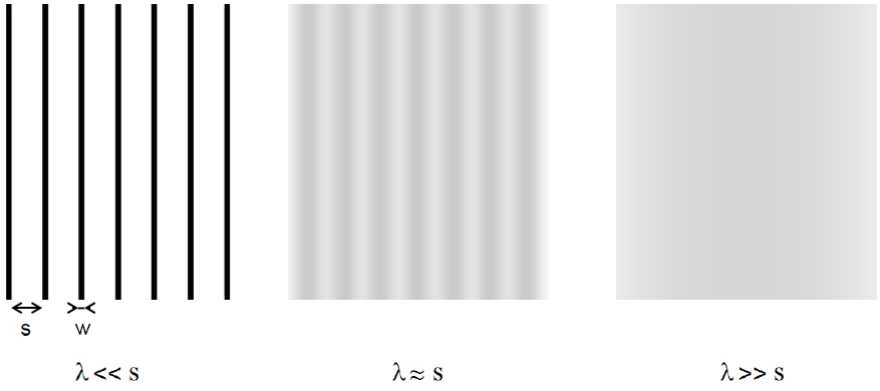

Figure 3.16: *Different effect of a wiregrid on the incoming radiation λ. From left to right the ratio λ/s increases. For short wavelengths, the radiation can resolve the different grids and spaces between them. On the contrary, when $\lambda \gg s$ the structure is no longer resolved. In this case the radiation feels only the effect of an averaged effective impedance, Z_{opt} , that can thus be tuned by varying w, s and d [78].*

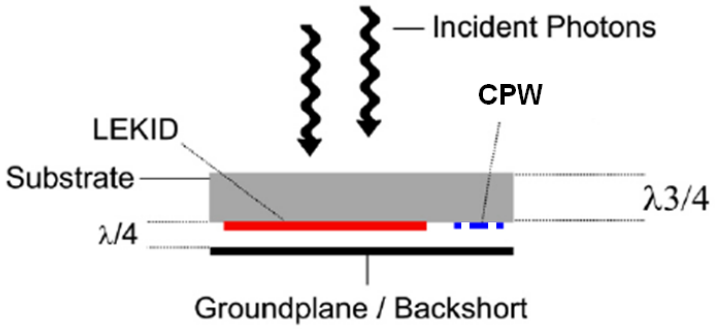

Figure 3.17: *Schematic of the back-illumination setup of a KID array.*

A LEKID acts as absorber and sensor at the same time. The characteristics of the materials used for the resonator determine both its electrical and optical proprieties. The photon frequency detection threshold is governed by the superconducting gap $\nu_{gap} = 2\Delta/h = 3.53 k_B T_c/h$, which depends on the critical temperature T_c. Two useful formulas that link these quantities are

$$T_c[K] \approx 1.363 \cdot 10^{-2} \cdot \nu[GHz]$$

$$\Delta[\mu eV] \approx 2.068 \cdot \nu[GHz]$$

So far, KID for millimeter-wave applications mostly use Al ($\nu_{gap} \sim 100GHz$ for thin films) and TiN films ($\nu_{gap} = 80 \div 400GHz$). Aluminum - our the standard choice - has a low normal sheet resistance ($\sim 1\Omega/\square$). This complexify the optical efficiency optimization and is associated with a limited kinetic inductance fraction compared to TiN (eq. 2.16). Nevertheless, aluminum low temperature properties are less dependent by the deposition process rather than a metal alloy, resulting in more reproducible characteristics and a more predictable superconducting behavior.

Chapter 4

The NIKA project

The New IRAM KIDs Array (NIKA) is a pathfinder instrument devoted to millimetrer Astronomy. In 2009 it has been the first multiplexed KID camera on the sky; nowadays it is permanently installed at the focal plane of the IRAM 30-meters telescope at Pico Veleta observatory (Spain). The LEKID arrays designed and fabricated among our collaboration have shown good on sky performances, with sensitivities getting better and better all along the NIKA campaigns. The latest observational runs definitively demonstrated sensitivities comparable to the state-of-art bolometer cameras operating at the same wavelength, and culminated in February 2014 with the opening of the NIKA instrument to the astronomers community. We report here on the work done to reach this result, with particular attention to the optimization of the detectors performances and read-out techniques. We conclude presenting a few sample images of sources detected by NIKA and the ongoing developments devoted to the next NIKA-2 kilo-pixels camera, to be commissioned in 2015. We also present a study on new superconducting materials as possible candidates for future space-borne telescopes.

The NIKA project is an international collaboration involving many European institutions. The core of the collaboration is based in Grenoble (France) and is formed by the Institut Néel (IN), the Laboratoire de Physique Subatomique et de Cosmologie (LPSC), the Institut de Planétologie et d'Astrophysique (IPAG), and the Istutut de RadioAstronomie Millimétrique (IRAM). One of the goals of the NIKA collaboration is to assess the viability of KID for terrestrial millimeter astronomy, developing a fully integrated measurement system devoted to the investigation of high redshift objects, an intense study of galaxies and the CMB, in particular the Sunyaev-Zel'dovich effect. In order to hit this target, the NIKA team aims to provide an effective ground-based millimeter-waves facility with two fundamental characteristics: a large aperture telescope to increase the angular resolution and a large and oversampled field of view to increase the mapping speed. For this reason, the NIKA camera has been conceived to work at the focal plane of the IRAM (Institut de Radioastronomie Millimétrique) 30 meters telescope at Pico Veleta, Spain (fig. 4.1).

Figure 4.1: *Photograph of the 30 meter telescope site at Pico Veleta*

4.1 The IRAM Pico Veleta Telescope

The IRAM 30-m telescope was built in 1984 in the spanish Sierra Nevada. Located in a dry area, at about 2850 a.s.l, it is one of today's most powerful telescopes in the millimeter band. It consists in a 30-meter diameter single dish parabolic antenna, whose surface is adjusted to a precision of 55 micrometers. The large and smooth surface of the primary mirror is integrated in an optic system providing a Nasmyth (Nasmyth-focus) field of view of 6.5 arcmin and angular resolution down to few arcseconds at higher frequencies ($\sim 350GHz$). Thanks to these features, the IRAM Pico Veleta telescope is unrivaled in its sensitivity and is well adapted to detect weak sources.

The main limitations for ground based observations are due to atmospheric opacity and instability. Nevertheless, radio observations are possible exploiting the atmospheric windows present in the millimeter band. The transmissivity in these windows typically decreases at high altitude, depending mainly on the precipitable water vapor content and on the temperature of the atmosphere. Figure 4.2 shows the four available millimeter frequency bands at Pico Veleta, which central wavelengths at 3.2, 2.05, 1.25 and 0.87 mm. The 30-meter telescope is already equipped with a series of single pixel receivers operating in all these four bands, and with two spectroscopic instrument: 1) EMIR [98] with 1 pixel, working in all the four mentioned atmospheric windows, and 2) HERA, with a 3×3 pixels array, working in the

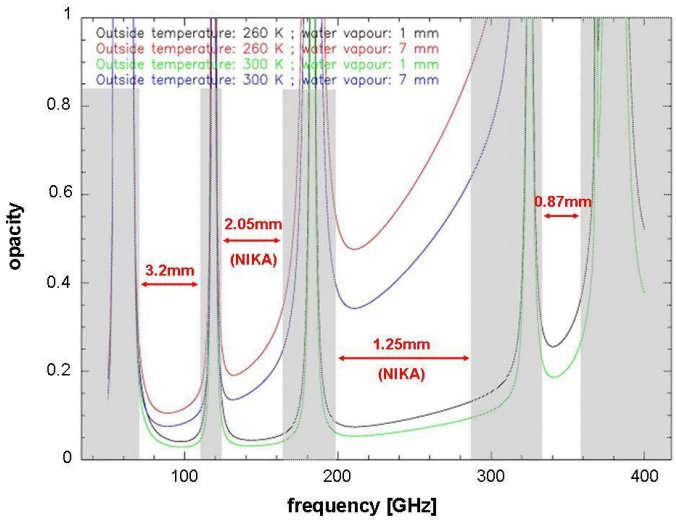

Figure 4.2: *Available frequency bands at the IRAM 30m telescope for observations at radio frequencies up to 400 GHz (for higher frequencies the surface precision of the primary mirror is not sufficient). Outside conditions are slightly different in summer and winter, so that opacity of the atmosphere is shown for a water vapor of 1 and 7 mm and temperatures of 260 and 300 Kelvin.*

1.25 mm band. Though offering good resolutions, these cameras are not sufficient to fill the focal plane of the telescope and a multiband large-format array instrument fully exploiting the huge potential of the telescope is required. In order to accomplish this need, two cameras are currently installed at the focal plane of the IRAM telescope: GISMO [99], a 128 bolometers array at $2mm$, and NIKA, which we are going to describe.

4.2 The NIKA instrument

In agreement with the principal interests of the IRAM, our collaboration developed a dual-band resident instrument custom designed for the 30-m Pico Veleta telescope. In its latest configuration, the NIKA camera consists in two filled arrays optimized to operate in the atmospheric windows at 2 mm (155 GHz) and 1.2 mm (245 GHz). The focal plane is equipped with a total of 356 pixels and cooled down to about 150 mK by a $^4He-^3He$ dilution cryostat. The control of the instrument is done via automatic tuning sequences between each scan (par. 3.5.2). The data are on-line processed in order to obtain rapid feedback on pointing, focus, phase calibration (par. 3.5.1), photometric calibration (par. 4.3), atmospheric correction (par. 4.3.1), and on-sky observations.

4.2.1 The dual-band optics

The dual-band NIKA optics is designed to fit the receiver cabin of the IRAM telescope in Pico Veleta. The 30-m primary mirror (M1) and the hyperbolic secondary (M2, D = 2 m) are installed directly on a large alt-azimuth mounting. The incident beam is directed into the receiver cabin through a hole in M1 using a standard Cassegrain configuration. A rotating tertiary (M3) provides a fixed focal plane (Nasmyth focus). The optical axis, in order to conform to the dimensions of the cabin, is deviated by a flat mirror (M4). M4 can rotate between two fixed positions, selecting either spectroscopic (EMIR, HERA) or continuum (GISMO, NIKA) instruments.

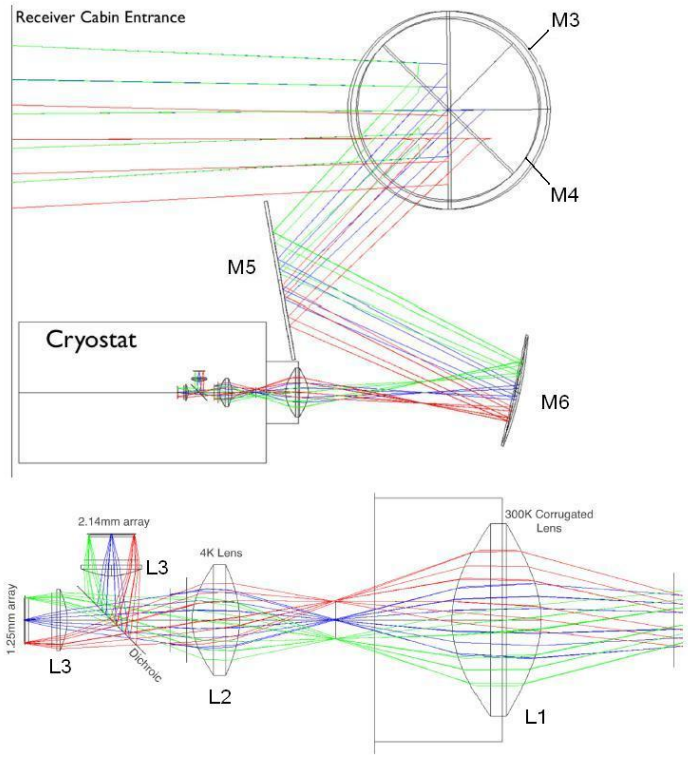

Figure 4.3: *Snapshot from the Zemax simulation used to optimize the optical system of NIKA. Top panel: ray tracing from the entrance of the receiver cabin of the 30-m telescope (which is simulated but not shown on the image), viewed from the elevation axis (which is symbolized by the big circles and contain the 2 mirrors of the Nasmyth system, M3 and M4). The NIKA cryostat and entrance nose are symbolised by the rectangles. Bottom panel: zoomed plot of the optical system inside the NIKA cryostat. All the elements presented on this figure are real optical elements except for the vertical segment showing the entrance of the receiver cabin and the vertical segments inside the cryostat (field and pupil diaphragms, filters, dichroic and detectors arrays).*

The optical coupling between the telescope and the detectors is made by warm aluminum mirrors and cold refractive optics. It consists of a flat mirror at the top of the cryostat (M5) and an off-axis biconic-polynomial curved mirror (M6) mounted in front of it. Then a 300 K window lens (L1) let the beam enter the cryostat, where a field stop, a 4 K lens (L2) and an aperture stop allow the radiation to the lower temperature stage. Here a dichroic is used to split the long/short wavelengths such that both channels can observe the same portion of the sky simultaneously. A 150 mK (L3) lens is placed in front of the back-illuminated KID arrays, where a backshort matching the corresponding wavelength maximize the signal on the detectors plane. A schematic view of the optics of the NIKA instrument and the coupling with the 30 m telescope is presented in fig. 4.3.

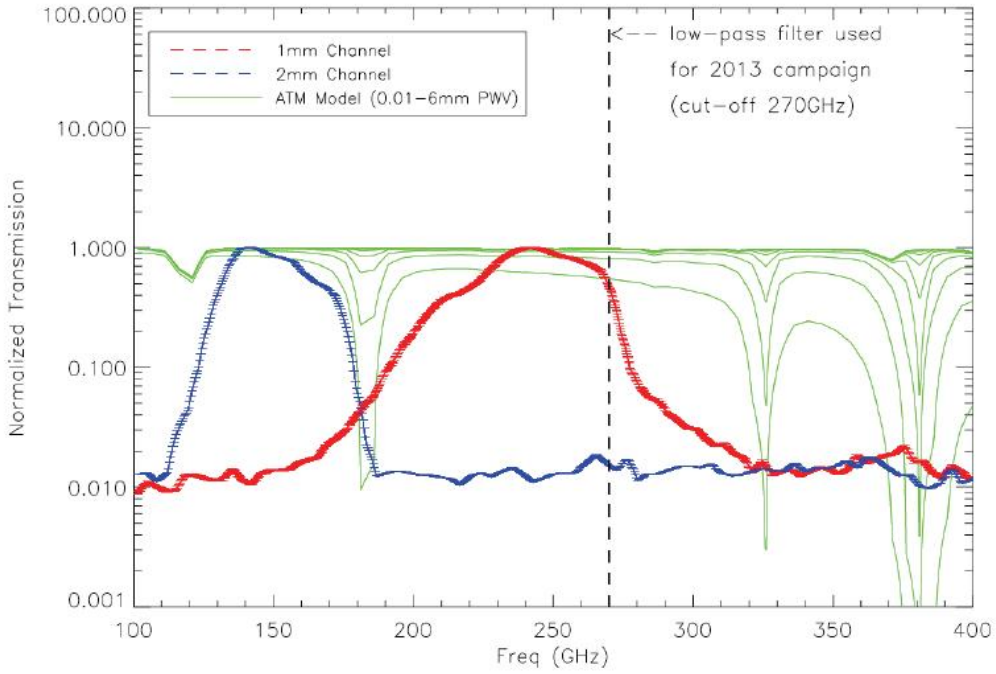

Figure 4.4: *NIKA bands. The 1.25 mm channel (2.14 mm) is shown in red (blue). The bands are averaged over all valid pixels, with dispersion (rms) of 2 % at 1.25 mm and 1 % at 2.14 mm. The atmospheric model is calculated for different water vapor contents and is shown in green. The spectral response of NIKA was characterized using a Martin-Puplett interferometer allowing to recover the spectral performance of each pixel of the two NIKA channels with uncertainties of a few percent. Here are shown the NIKA bands together with the atmospheric model calculated for different water vapor contents [100]. The dotted vertical lines indicates the low pass filter with a cut-off at 270GHz added for the 2012 and 2013 observation campaigns.*

The rejection of off-band radiation is achieved by using a series of filters. To reduce off-axis radiation, a multi-stage, black coated baffle is installed at 4 K between L1 and L2. The

baffling is further improved with a cold pupil at 150 mK. A series of three infrared blocking filters are mounted on the first two radiative screens held at a temperature of $\sim 150K$ and $\sim 70K$. Three additional low-pass metal mesh filters are installed on the 4 K and 1 K screens. The radiation entering the 150 mK stage is thus restricted to frequencies $\nu < 300GHz$. The final band definition is achieved using band-pass filters behind the final lens L3, just in front of the detector array. Spectral characterization of NIKA was performed using a Martin-Puplett interferometer [101] and the results, shown in fig. 4.4, exhibit good agreement with the atmospheric transparency windows and coincide with the expected response based on the individual filter cutoff frequencies. Taking into consideration the tabulated HDPE transmission and the individual filter specifications, we estimate a total optical transmission coefficient of ~ 0.35 for the NIKA optics.

4.2.2 LEKID arrays

In its last configuration, NIKA mounts two arrays with 224 and 132 pixels, with optical transmission peaking at 240 GHz and 155 GHz respectively. Fig. 4.5 shows a summary of their characteristics. The 240 GHz (155 GHz) detector array is made by a 20 nm (18 nm) Aluminum film fabricated on a $180\mu m$ ($300\mu m$) High-Resistivity Silicon substrate ($> 1k\Omega \cdot cm$). The detector design is based on LEKID geometry with a Hilbert pattern inductor [76], sensitive to both the polarization and ensuring a symmetric design with a constant filling factor over the whole direct sensitive area. The inductor line width is $4 \div 6\mu m$, coupled to the feed-line through a spacing of roughly $15\mu m$. The LEKID are $1.6 \times 1.6mm^2$ ($2.3 \times 2.3mm^2$) square pixels, spaced by 6.82" (9.82"), with a focal plane sampling of approximately 0.8 $F\lambda$ (0.7 $F\lambda$) with respect to the nominal telescope resolution. A picture of the $2mm$ array is shown in fig. 4.7.

The superconducting gap of the Al films has been measured thanks to absorption spectra taken in our laboratory. The measurements show that below roughly $\nu_{cut} = 100 \div 105GHz$ no radiation is absorbed (fig. 4.6), meaning that the energy gap in the case of 20nm (18nm) Al films is of approximately $0.21 \div 0.22meV$, and the T_c around $1.4 \div 1.43K$ (see Part II introduction). The expected film impedance for incoming, above-gap radiation, is actually that of the normal film state. This has been measured to be around $1\Omega/\square$ for the 20nm film, while around $2\Omega/\square$ for the 18 nm. These values have been used when designing the detectors in order to match their effective impedance to that of the incoming radiation, in a 'back-illumination' configuration.

4.2.3 Readout electronics

As readout, we used two NIKEL v1 electronics, one per array. The system is described in more detail in chap. 3. Each NIKEL v1 board allows us to monitor up to 400 KID simultaneously.

	Array	1.25 mm	2.14 mm
	Peak of transmission	240 GHz	155 GHz
Detectors	material	20 nm Al	18 nm Al
Detectors	number	244	132
Detectors	geometry	Hilbert LEKID	Hilbert LEKID
Detectors	pitch	1.6×1.6 mm^2	2.3×2.3 mm^2
Array	design label	'NICA8e'	'NICA8f1'
Array	distribution	16 × 16 (-4 per corner)	12 × 12 (-4 per corner)
Array	spacing	6.82″	9.82″
Array	sampling	0.8 $F\lambda$	0.7 $F\lambda$
Substrate	material	HD Si (> 1 $k\Omega \cdot cm$)	HD Si (> 1 $k\Omega \cdot cm$)
Substrate	dimension	36×36 mm^2	36×36 mm^2
Substrate	thickness	180 μm	300 μm

Figure 4.5: *Resume of the properties of the two NIKA detector arrays.*

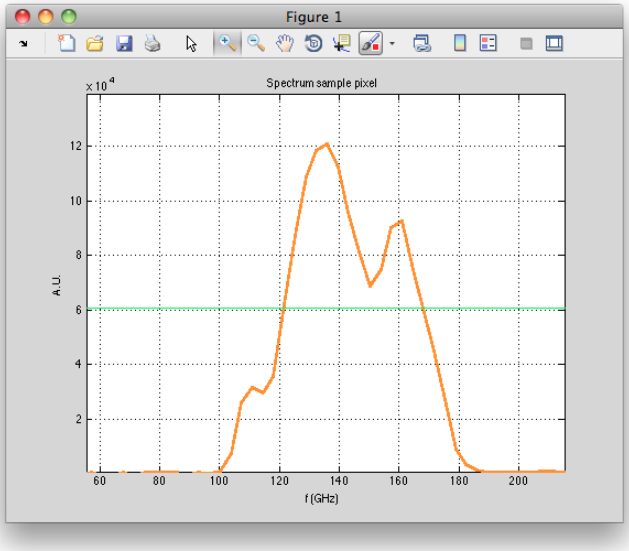

Figure 4.6: *Mean spectrum of the 20nm Al NIKA array, as measured in our laboratory with a Martin-Pupplet interferometer. The spectrum shows a* $\nu_{gap} \approx 100GHz$. *The cut at high frequency is instead provided by a low-pass filter.*

We choose a sampling rate of ~ 24 Hz, synchronously over the two arrays. Binary files are provided as output, containing the raw data as well as the resonant frequency of each KID used to set the corresponding excitation tone.

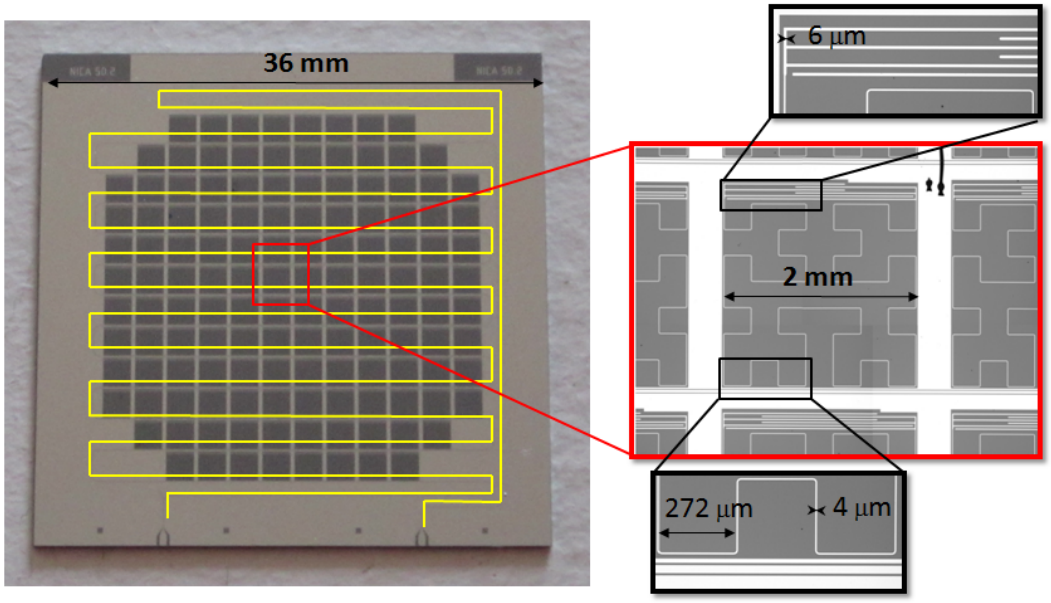

Figure 4.7: *A photograph of the 2mm array. Each pixel correspond to a darker square in the imagae. The feedline has been highlighted in yellow. In inset zooms show of one LEKID (middle), with the interdigitated capacitor (top) and the meandered inductor coupled to the transmission feedline (bottom).*

4.3 Photometric calibration pipeline

The acquired data undergo an accurate calibration process before being reduced into the final sky maps. A detailed description of this pipeline and of the evaluated systematics can be found in [41]. In the following we summarize the main steps:

1. Choice of a primary calibrator (Uranus in our case). Evaluation of the accuracy of the obtained absolute photometric calibration;
2. Evaluation of the elevation dependent gain of the telescope;
3. Correction for the custom spectral response of each pixel;
4. Field-of-view reconstruction in order to recover pointing direction of each pixel;
5. Correction for the atmospheric emission

All these steps are very important in order to get an accurate photometric calibration. We have developed a technique to evaluate in real time the opacity correction (item 5). Each KID is used as a total power detector in parallel to normal astronomical observations. This is achieved via a previous elevation scan technique (*sky dip*) with the telescope itself.

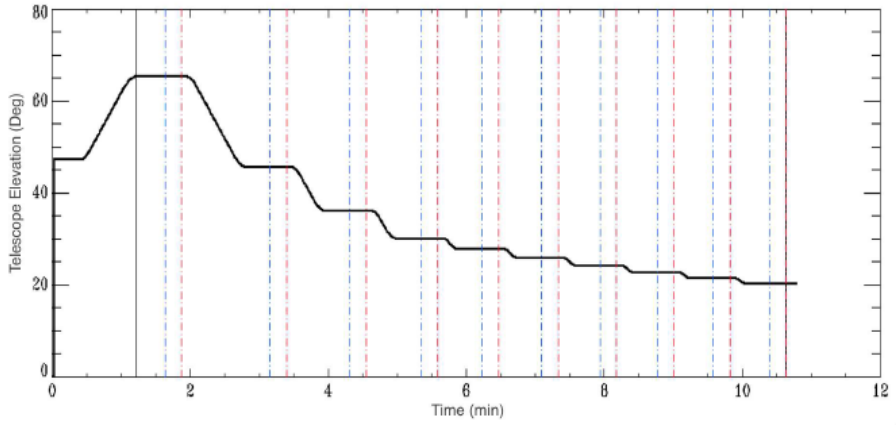

Figure 4.8: *Telescope positions during an elevation scan procedure: 10 steps in elevation have been performed without changing the azimuthal position. Data for absolute calibration are taken in the region between the blue and the red lines.*

4.3.1 Sky Dip

Normally the atmospheric absorption correction was estimated using the IRAM tau-meter. This resident instrument performs elevation scans continuously at a fixed azimuth and at a frequency of 225 GHz. To derive the opacity at the exact position of the scan and at the NIKA frequencies, we implemented a procedure in order to use the NIKA instrument itself as a real-time tau-meter. This procedure consists in measuring the variation of the KID resonance frequencies versus the airmass via elevation scans [102] (fig. 4.8) from 65 to 20 degrees above the horizon. Since the power load on the detectors increases with the air mass value, the resonance frequencies are expected to decrease when lowering the telescope elevation. By performing a fit of this trend, it is possible to characterize the curve for each detector and to estimate a common array sky opacity at zenith. In fig. 4.9(a)–4.9(c) it is shown one of the sky dip performed during the NIKA campaign of June 2013. The procedure is based on the idea that the change in resonant frequency for a given change in absorbed power is a constant property of each detector [42]. This means that the non-linearity of the KID frequency signals is negligible in the considered range of backgrounds, and the coefficients characterizing each detector can be applied to any observing campaign to recover the opacity of the considered observation.

A sky dip thus provide a reference for direct measurement of the atmosphere opacity along the line-of-sight for each scan. This method have several advantages: 1) we do not need to perform the Skydip at the exact time of the source observations to correct properly the atmospheric contribution in the considered scan; 2) we can estimate the atmospheric opacity at the same position (Azimuth- Elevation) of the source, instead of the average sky opacity;

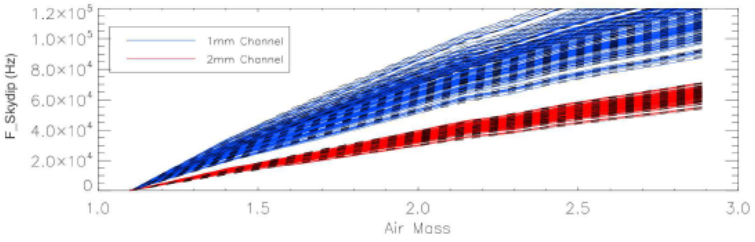

(a)

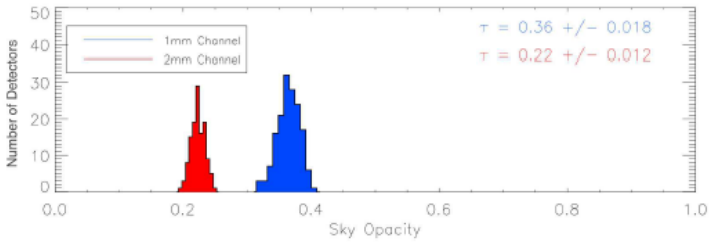

(b)

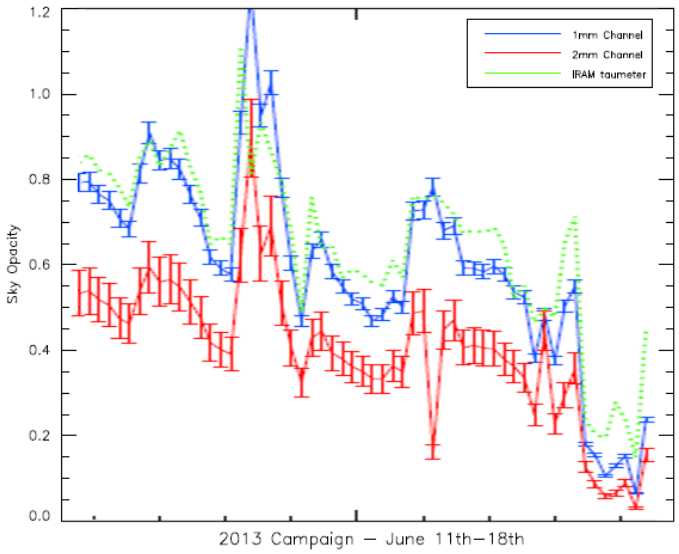

(c)

Figure 4.9: *(a) Signal in Hz of each valid KID (blue for 1.25 mm detectors, red for 2.14 mm) as a function of air mass together with the fitted model (black dotted lines). (b) Histogram of the deduced integrated in-band opacities for 1.25 mm and 2.14 mm channel. (c) Atmospheric opacity evolution for the NIKA 2012 and 2013 observing campaigns calculated from the Skydip analysis. The error bars were estimated by analysing different Skydip observations. During the 2013 observing campaign the agreement with 225 GHz IRAM taumeter is good.*

Array	1.25 mm	2.14 mm
Valid Pixels (all Pixels)	190 (224)	125 (132)
Field Of View (arcmin)	2.2	2.2
Band-Pass (GHz)	125-175	200-270
FWHM (arcsec)	12.3	18.1
Sensitivity (mJy·$s^{\frac{1}{2}}$)	40	14
Mapping Speed (arcmin^2/mJy^2/hour)	8	57

Figure 4.10: *Summary of the NIKA characteristics and performance from the campaign on June 2013.*

3) this method automatically accounts for the NIKA band passes transmission.

Tipically skydips must be performed once per day to adjust the calibration of the total power opacity relationship, accounting for any degeneracy of the atmospheric temperature with the opacity in our model. The sky maps are then corrected for the atmospheric contribution. The NIKA skydip procedure was successfully tested during the last NIKA observational campaigns. The calculated opacity were not only compatible with the resident tau-meter values, but produced a lower dispersion of the opacity correction at different elevation (fig. 4.9(a)).

4.4 Results and performances

The results from the last observational campaigns (January-February 2014) are still not published. We briefly report here on the NIKA camera performances as measured on sky in November 2012 and June 2013 campaigns. More details can be found in [41].

We summarize the main NIKA characteristics in fig. 4.10. We have obtained an array averaged NEFD (Noise Equivalent Flux Density) of 40 and 13 $mJy \cdot \sqrt{s}$ for best weather conditions for the 1.25 mm and 2.14 mm arrays respectively, estimated on point-like sources. Yet, we expect the 1.25 mm channel sensitivity to be improved in the next observation campaigns. The effective fields of view are about 2.2 arcmin in diameter for both the arrays, with angular resolutions (Half Peak Beam Width) of 12.3 and 18 arcsec for the 1.25 and 2.14 mm bands, respectively. The camera performance has been also quantified with the area that can be observed per unit time at a given sensitivity (*mapping speed*). The overall photometric calibration uncertainty for point sources on the final data at the map level is estimated to be 15 % for 1.25 mm channel and 10 % for 2.14 mm channel.

Thermal sensitivity for the two arrays has been measured by lowering the cryostat base temperature to 130mK. The 20mK variation made $\sim 3kHz$ shift on the 1mm and $\sim 0,3kHz$ on the 2mm. The sensitivities to base T are thus 150Hz/mK and 15Hz/mK for the 1mm and 2mm channel, respectively. Considering that the noise in T measured on the thermometer is

of the order of 0.02mK RMS, that gives 3Hz on the 1mm and 0.3Hz on the 2mm.

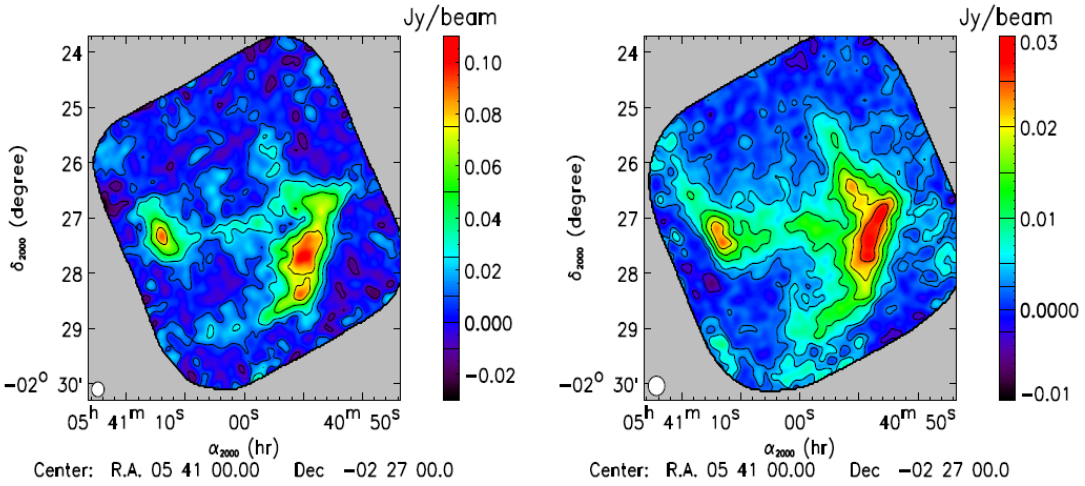

Figure 4.11: *NIKA maps at 1.25 (left) and 2.14 mm (right) of the well-known extended source Horsehead Nebula.*

The NIKA camera has been used to observe faint point-like sources, in order to assess the NIKA photometry with sources having fluxes of the order of few tens of mJy. We have chosen to observe four point-source high redshift sub-millimeter galaxies: MM18423+5938, HLSJ091828.6+514223, SXDF1100.001 and HFLS3. The weakest source detected was the latter, with a flux of $16\pm2mJy$ at 1.25 mm, and $4.0\pm0.6mJy$ at 2.14 mm. The spectral energy distribution (SED) of the selected sources are in agreement with previous measurements found in literature.

We have observed simultaneously at 1 and 2 mm several well-known extended sources to test the capabilities of the NIKA camera to recover large angular scales up to few arcmin. We present an example of extended source, namely the Horsehead Nebula. In fig. 4.11 we show the 1.25 (left) and 2.14 (right) mm NIKA maps. The typical 1-sigma error in the map with the pixel size of 3 arcsec is of 14.5 and 2 mJy/beam at 1.25 and 2.14 mm, respectively. The NIKA 1.25 mm is consistent with the 1.2mm continuum map [103] obtained with MAMBO-2, the MPIfR 117-channel bolometer array from 30 m IRAM telescope [104].

To demonstrate the full potential of the NIKA instrument, we finally present thermal Sunayev Zel'dovich (tSZ) observations of the cluster RX J1347.5-1145 [105]. It was observed simultaneously in the two NIKA bands, using a spectral decorrelation technique to remove the atmospheric noise and obtain a map of the cluster at 2.14 mm (fig. 4.12), which presents a decrement at the cluster position consistent with the tSZ nature of the signal. For the first time, we demonstrate the tSZ capability of KID-based instruments.

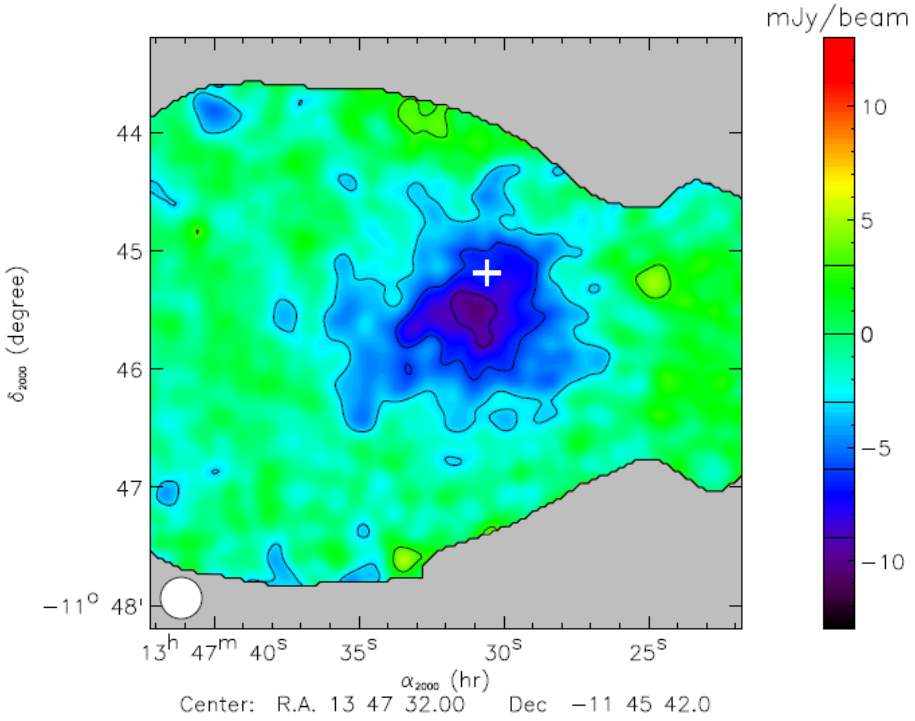

Figure 4.12: *NIKA map of RX J1347.5-1145 at 140 GHz. The map is given in mJy/beam. The X-ray center location is represented by a white cross. The radio source location also corresponds to the white cross within 3 arcsec.*

4.5 Future perspectives

4.5.1 NIKA-2

The NIKA camera has demonstrated the capability of multiplexed LEKID arrays to take significant data from astrophysical sources. The sensitivities achieved by the NIKA camera are comparable to the performances of the state-of-art bolometers arrays (e.g. GISMO). The next generation NIKA-2 kilo-pixels camera (fig. 4.14) will be made of about 1000 detectors at 2 mm and 2×2000 detectors at 1.2 mm, with a circular field of view of ~ 6.5 arcmin diameter (fig. 4.13). The NIKA-2 instrument will have linear polarization capabilities at 1.2 mm.

The NIKA-2 focal planes will be cooled down to $\sim 100mK$ by a one-ton cryogen-free cryostat consisting in the combination of a pulse-tubes system and an ^{3}He/^{4}He dilution refrigerator (fig. 4.14). The NIKA-2 cryostat has been recently tested in our laboratories at Institut Neel in Grenoble, successfully reaching the base temperature of $\sim 100mK$.

The NIKA-2 instrument, to be commissioned in 2015, will provide a next generation mm-wave facility for astronomical and cosmological observations with remarkable sensitivity, mapping speed and angular resolution. The NIKA-2 camera will be a well-suited instrument

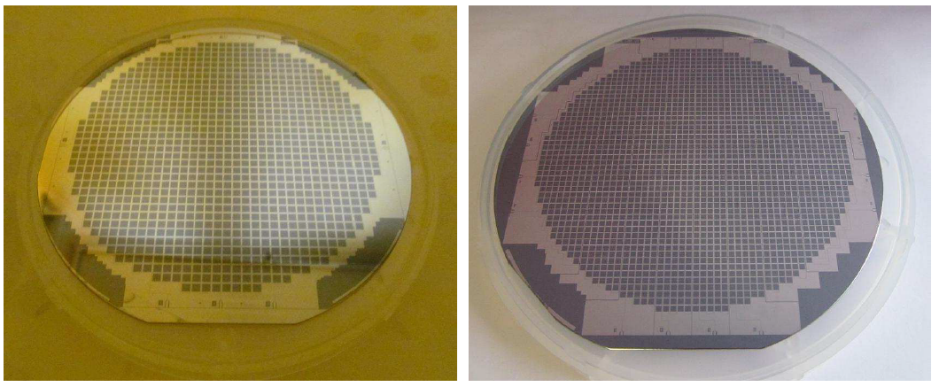

Figure 4.13: *The NIKA-2 arrays recently fabricated at IRAM. On the left, the 1020 KID array for the 2 mm band; on the right, the 1932 KID array for the 1.2 mm band.*

for in-depth studies of the ICM from intermediate to distant clusters, establishing the role of filaments in star-forming region, high-resolution SZ imaging, and so for the follow-up of recently detected clusters by the Planck satellite.

4.5.2 KID for space-borne applications: new superconducting materials

Building on the NIKA experience, we have started considering the possibility of using KID for future space based missions. In space, the background power on the detectors and the signal that we expect to measure are up to two orders of magnitude lower than the ones observed on ground. The pixel design and fabrication therefore need to be thoroughly revised, starting from the choice of the materials used. Titanium Nitride has been first deployed in 2010 to make superconducting resonators [73]. The physical properties of $Ti_{1-x}N_x$, such as its critical temperature T_c, can be changed by appropriately choosing the amount x of nitrogen present. Ti1-xNx has shown a surprisingly high value of kinetic inductance, $L_k \sim 20pH/\square$, and of normal state surface resistivity, $\rho_n \sim 100\mu\Omega \cdot cm$ [73]. The high resistivity (relative to Al) is very convenient for obtaining highly efficient far-infrared photon absorption in lumped-element resonator structures [96]. As a consequence of the Mattis-Bardeen relationship (eq. 2.15) $L_s \approx \hbar R_s/\pi\Delta$ between the normal-state surface resistance R_s and the superconducting surface inductance L_s, the large resistivity also guarantees a large kinetic inductance fraction $\alpha = L_k/L_{tot} \rightarrow 1$. This increases the responsivity of the detectors, making lower values of Noise Equivalent Power (NEP) achievable. In the case of LEKID, the larger resistivity represents a further advantage, as it makes directly coupling to the incoming radiation, in particular at shorter wavelengths, easier to achieve leading to increase optical efficiency. While undoubtedly a promising material, TiN has also some major drawbacks, in particular for what concerns the uniformity of the film composition and of its electromagnetic properties across

wide areas, which are essential to fruitfully deploy the material for the fabrication of large arrays of detectors. Developments are ongoing, mainly in the US, in order to solve these problems.

In the following we describe our first investigations for an alternative solution. In particular, we have investigated the properties of Niobium Silicon ($NbSi$) and Titanium Vanadium (TiV) alloys, two promising candidate materials for the fabrication of highly sensitive Kinetic Inductance Detectors (KID), optimized for very low optical loads.

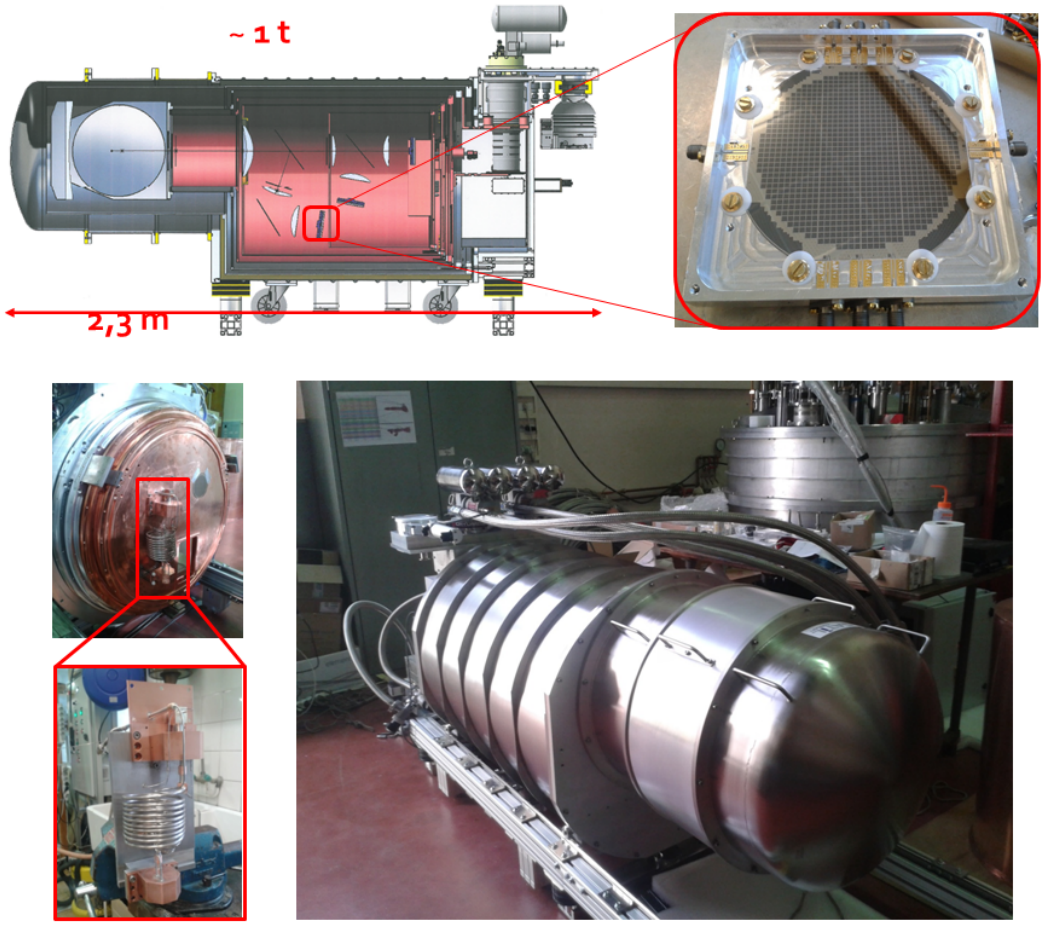

Figure 4.14: *(Top) A schematic of the NIKA-2 cryostat project, with a particular of the 2mm array mounted in its aluminum holder (inset zoom). (Bottom left) The NIKA-2 cryostat opened with its inner plates at about* $50K$*,* $4K$*,* $1K$ *and* $100mK$*, with the dilution system (inset zoom) mounted on the latter. (Bottom right) A photograph of the whole NIKA-2 cryostat during one of the first cooling down tests in the Institut Neel laboratories.*

Niobium Silicon alloy ($NbSi$)

Taking advantage of the long experience accumulated in France on $NbSi$ films [106], we have first studied the properties of Niobium Silicon amorphous alloys. As in the case of other composite materials, the NbSi properties can be changed by varying the relative amounts of its components. Using a NbSi film with $T_c \approx 1K$ we have been able to obtain the first NbSi KID resonators, observing an optical response and acquiring a spectrum in the band 50 to 300 GHz. The data taken show that this material has very high kinetic inductance L_k and normal state surface resistivity ρ_n.

1. **Device fabrication** As in the case of $Ti_{1-x}N_x$, the properties of Niobium Silicon alloys (Nb_xSi_{1-x}) depend on the relative abundance of the components. This alloy exhibit a metal to insulator transition for $x \approx 9\%$. Above this value, the critical temperature grows linearly with x. Thus, Nb_xSi_{1-x} can be used both for the fabrication of high impedance bolometers [107] and of Transition Edge Sensors (TES) [108]. The films are deposited at CSNSM (Centre de Sciences Nucléaires et de Sciences de la Matière, Orsay, France) by co-evaporation of pure Nb and Si under ultra-high vacuum conditions. For our first test we chose a film thickness t = 50nm, and a value of $x \approx 18\%$. This corresponds to an expected T_c of $\sim 1K$, which is ideal for operation up to 3 millimeter wavelength. The design used for the first devices is a classical, single polarization sensitive LEKID geometry. Two masks have been developed:

   - *NICA v.4.7* (fig. 4.16(a)-4.16(b)): This had been actually designed for aluminum detectors. It is a 25 $2 \times 2mm$ pixel design with 5 different interdigited capacitors, containing from 2 up to 6 'fingers' lines. The meander width is $4\mu m$, with a pitch of $272\mu m$ and a filling factor of $\sim 1.5\%$. The coupling to the feedline is $16\mu m - 16\mu m$ (in sequence towards feedline: separation between meander and ground strip - ground strip width). The bandwidth is about 100 MHz per 'finger' ($100\mu m/step$). Since this mask was designed for Al KID, some parameters of our device were not optimized. Examples are the matching to the incoming radiation and the impedance of the feedline. The latter is a $12 - 20 - 12\mu m$ (in sequence towards down: gap-center line width-gap) CoPlanar Waveguide (CPW), which impedance is expected to exceed 100Ω for $NbSi$ film. Even though this leads to reflections on the line and poor optical efficiency, it does not represent any hindrance for establishing the fundamental properties of the compound under test.
   - *NISBA v.1* (fig. 4.16(c)-4.16(d)): This mask has been custom developed for $NbSi$ devices employing a Niobium feedline. The principal characteristics of this mask are resumed in fig. 4.15. Unfortunately, the mask was designed for kinetic inductance of $\sim 25pH/\square$, while we expected values ~ 10 times higher for $x \sim 18\%$. As a

consequence, the calculated values in the last three columns will not agree with observations. The common parameters for all array are: a) the coupling $15\mu m - 10\mu m$, with an expected value of the coupling quality factor $Q_e \sim 5.5 \cdot 10^4$; b) the $5 - 30 - 5\mu m$ CPW. The expected value of the feedline impedance of 78Ω. To match 50Ω a further reduction in the CPW separation would have been required. We preferred however not to lower this value below $5\mu m$, in order to reduce the risk of short on the feedline. Only the arrays NISBA 1.2 and NISBA 1.8 shown resonances. We report here on the measurements performed on the NISBA 1.2 array.

Name	Geometry	Pixel dim (num)	Line width-pitch	Filling factor	left	top	right	C-L [μm]	num (varying)	[μm]	resonances [MHz]	[kHz / μm / finger]	separation[MHz]
NISBA 1.1	Labyrinth	2400 (5x5 = 25)	10-10	0.5	40	45	40	10	39 (39)	320	195.4 - 351	12.5	6.2
NISBA 1.2	Classic meander	2400 (5x5 = 25)	10-100	0.1	40	35	40	35	6 (4)	900	640.8 - 846.7	57.2	8.2
NISBA 1.3	Hilbert	1800 (6x6 = 36)	10-10	0.5	40	40	40	40	6 (4)	600	536 - 682.5	61.0	4.1
NISBA 1.4	Labyrinth	2400 (5x5 = 25)	10-90	0.11	35	35	35	90	26 (26)	190	588 - 990	81.4	16.1
NISBA 1.5	Classic meander	2400 (5x5 = 25)	10-10	0.5	40	35	40	35	6 (4)	900	291 - 375	23.3	3.4
NISBA 1.6	Hilbert	2400 (5x5 = 25)	10-100	0.1	35	35	35	120	6 (4)	680	773.2 - 990.9	80.0	8.7
NISBA 1.7	Classic meander	2400 (5x5 = 25)	5-5	0.5	47.5	35	47.5	43.5	6 (4)	900	153 - 197.9	12.5	1.80
NISBA 1.8	Classic meander	1600 (7x7 = 49)	10-10	0.5	40	40	40	35	6 (4)	600	594.1 - 774.5	75.2	3.7
NISBA 1.9	Classic meander	1600 (7x7 = 49)	5-5	0.5	37.5	46.5	37.5	43.5	6 (4)	600	306.3 - 398.6	38.5	1.9

Figure 4.15: *List of the designed parameters of the* NISBA *mask. The red line highlights the tested array,* NISBA 1.2

2. **Electrical properties** The first measurements have been carried out with NICA 4.7 under dark conditions, with the chip mounted on the cold plate of a dilution refrigerator. The base temperature of this system is around 100mK. The resistance of a RuO_2 thermometer mounted on the cold plate is read using a four wire configuration. At the same time, and using the same configuration, we can monitor the resistivity of the CPW line used to excite the resonators. As shown in fig. 4.17, the transition is observed at $T \approx 1.05K$, in very good agreement with our expectations. The transition is relatively sharp, i.e. less than $10mK$, and we measured a normal resistance just above the transition of $\sim 550 \div 600k\Omega$. The feedline, also fabricated with $NbSi$, has an overall length $l \sim 86mm$ and a width $w = 20\mu m$. Since it the thickness is $t = 50nm$, we estimate the normal state resistivity of $Nb_{.18}Si_{.82}$ to be as high as $\rho_n \approx 640 \div 700\mu\Omega \cdot cm$ (see Part II introduction). The resistance of the sample is thus $\sim 130 \div 140\Omega/\square$, which leads to $L_k/\square \sim 170 \div 190pH/\square$ (eq. 2.16). During a second cooldown, we connected the chip to the RF readout chain to be able to perform frequency sweeps with a Vector Network Analyzer (VNA). We can clearly identify the resonances, in a frequency interval lying between 500 and 900MHz. For comparison, the same resonator design lead to the resonances lying in the $1.5 \div 2GHz$ range for $t = 50nm$ Aluminum films. This immediately indicates a larger value of L_k. To actually estimate the kinetic inductance value we perform a series of simulations using the SONNET software, and vary L_k in order to find the resonant frequencies near to the observed ones. The result indicates $L_k \sim 23pH/\square$,

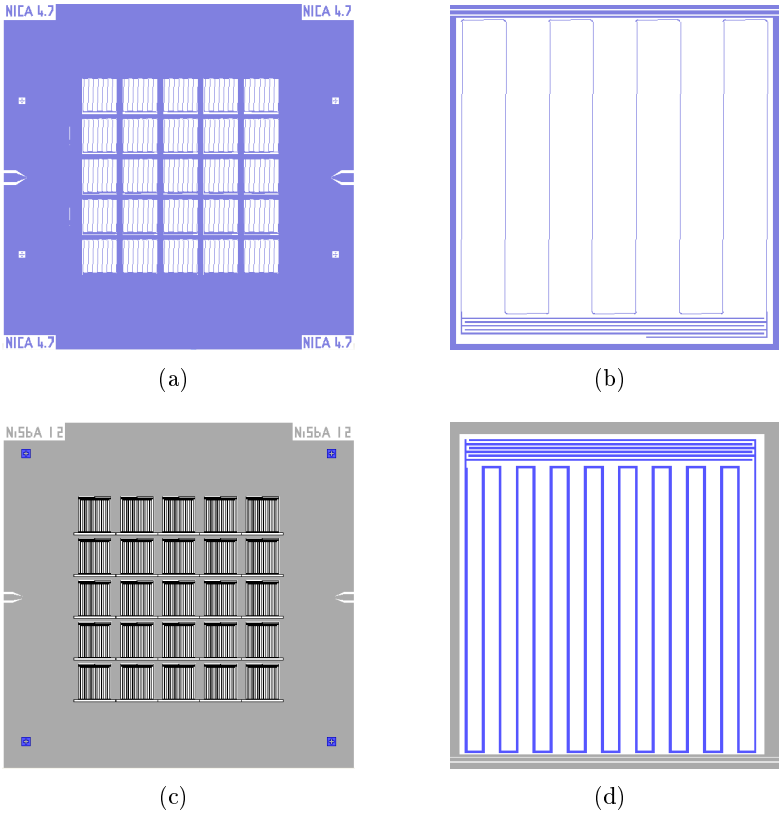

(a) (b)

(c) (d)

Figure 4.16: *Design of the two tested NbSi arrays, with the software* L-edit. *(a) The* NICA 4.7 *array with (b) a zoom of one of its pixels. (c) The* NISBA 1.2 *array with (d) a zoom of one of its pixels. The different metallization are shown in blue (NbSi alloy) and grey (Nb).*

which differs of about a factor 7.5 from the expected value of kinetic inductance. This can be explain if we suppose that we are not observing the lumped resonance, e.g. the ones simulated by the software, but actually the 1st order distributed resonance ($\lambda/2$). This means that the lumped resonances should be found at very low frequencies (below $100MHz$). This does not prevent us to test optical properties on the arrays.

Since also the NISBA mask were designed for such low kinetic inductance values, we expect to found the lumped resonances at frequencies $230 \div 240MHz$, much lower than what estimated by table in fig. 4.15. This is actually what we observe. By accident, the 1st order distributed resonance fell approximately where we expected the lumped one, in the range $750 \div 770MHz$ (fig. 4.18), so that in the beginning we misunderstood their actual nature, underestimating the L_k [109]. The reduced spacing between the resonances and sonnet simulations further endorsed our explanation, definitively confirmed by a successive experiment performed without the LNA (fig. 4.19(a)). In fig. 4.20(a)-4.20(c) we show the VNA scan of the distributed resonances and the resume of

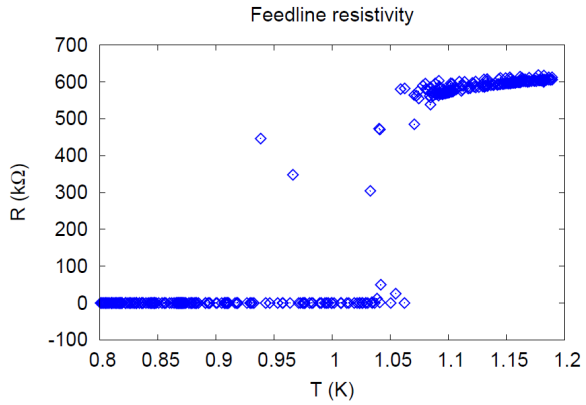

Figure 4.17: *Resistivity of the $Nb_{.18}Si_{.82}$ as a function of temperature. The scatter of the data is due to the measurement system changing the readout current as a consequence of the rapid resistivity variation. The transition is evident at $T_c \sim 1.05K$. The normal resistance of the line just above the transition is $\rho_n \approx 550 \div k\Omega$.*

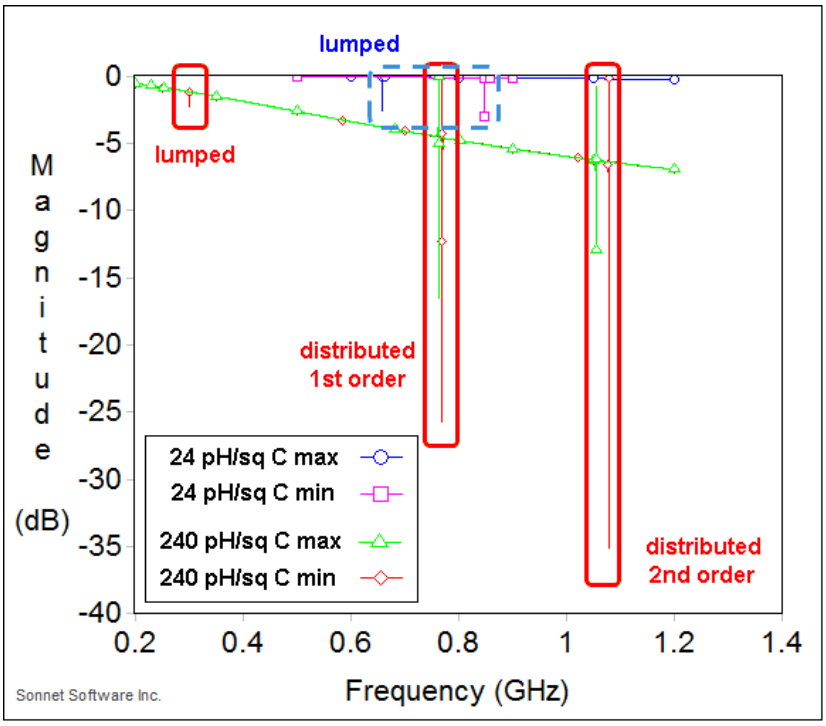

Figure 4.18: *The resonances of the* NISBA 1.2 *NbSi array as simulated by the* SONNET *software assuming different values of the kinetic inductance L_k (in units of $pH/\square$). The plot shows that the 1-st order distributed resonances assuming $L_k = 240pH/\square$ fell within the expected range of the lumped resonance assuming $L_k = 24pH/\square$.*

the resonance parameters of the NISBA 1.2 array that we have tested in 'dark' conditions. From the SONNET simulations we estimate a kinetic inductance for $Nb_{.18}Si_{.82}$ alloys of $L_k \approx 248pH/\square$ (fig. 4.20(d)), which is almost a factor 10 larger then the values obtained using $Ti_{1-x}N_x$.

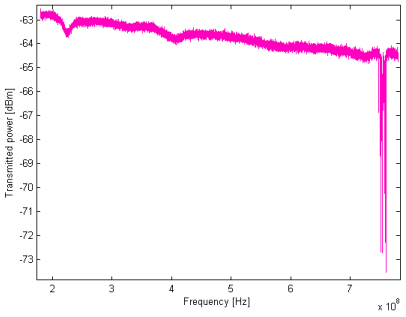

(a)

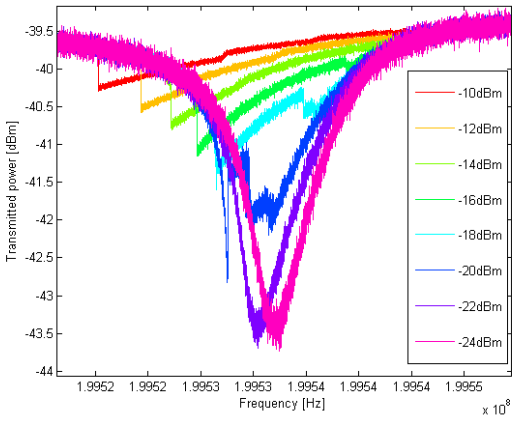

(b)

Figure 4.19: *(a) A VNA scan of the $NISBA$1.2 array without the LNA in the Sionludi cryostat (see par. 6.4.1). As expected (fig. 4.18), two groups of resonances are evident: the lumped resonances on the left packed in a unique , and the 1-st order distributed resonances on the right. (b) A power sweep of the lumped resonances of the* NISBA 1.8 *array obtained with the same experimental setup: the VNA scan at different powers highlights that the resonances overlap.*

3. **Optical properties** We mounted the two $Nb_{.18}Si_{.82}$ chips in the cryostat designed for optical measurements, which is actually a copy of the one used for the NIKA camera at the IRAM 30m telescope. First of all, we observed a drastic change in resonance quality factor when introducing an optical load with respect to the 'dark' conditions (fig. 4.21). This is what we expected, since the optic of the cryostat was designed for

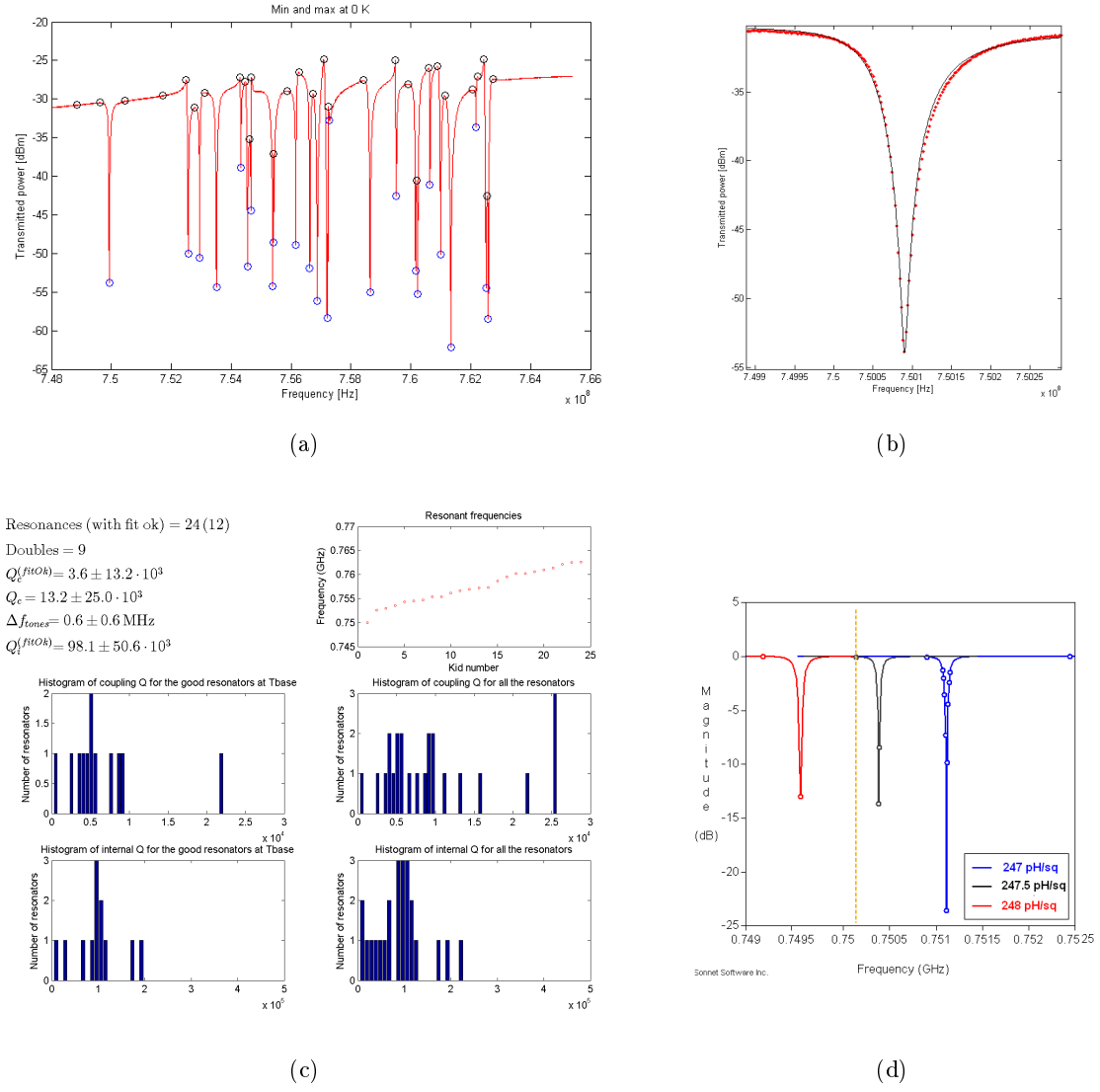

Figure 4.20: *Analysis of the* NISBA 1.2 *array: (a) a VNA scan of the 1-st order resonances; (b) zoom of the first resonance (red points) and fit (black line); (c) a summary of the array properties in term of resonance frequency distribution and quality factors; (d) a SONNET simulation of the first resonance assuming different kinetic inductance values. The orange dotted line indicates the measured position of the resonance, so that we can estimate* $L_k \sim 248 pH/\square$

NIKA detectors, which were optimized for a higher optical load. A possible solution to overcome this problem in the next runs is the use of a narrower band bass filter in the colder stage. We then measured the optical signal on the NICA 4.7 array, observing two different blackbody sources, one at 300K and one at 50K. The latter is obtained by means of a sky simulator [89], based on a dedicated Pulse Tube cooler. As can be seen in

figure 4.22, the frequency shift induced by these different optical loads is $\Delta f = 2.7MHz$, which corresponds to a responsivity of $R \approx 11kHz/K$. For comparison, using pixels of the same size but made of thin Al films ($12 \div 20nm$), and for the same variation of optical load, we obtained $R \sim 1kHz/K$ at most.

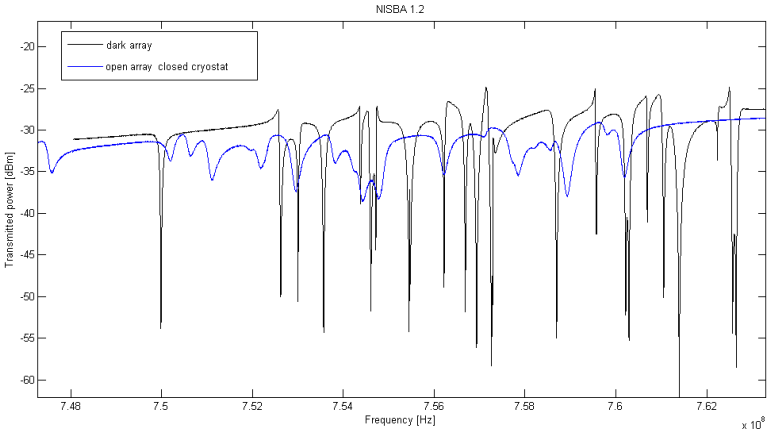

Figure 4.21: *A comparison between the VNA scan detectors in 'dark' conditions (black) and under an optical load (blue).*

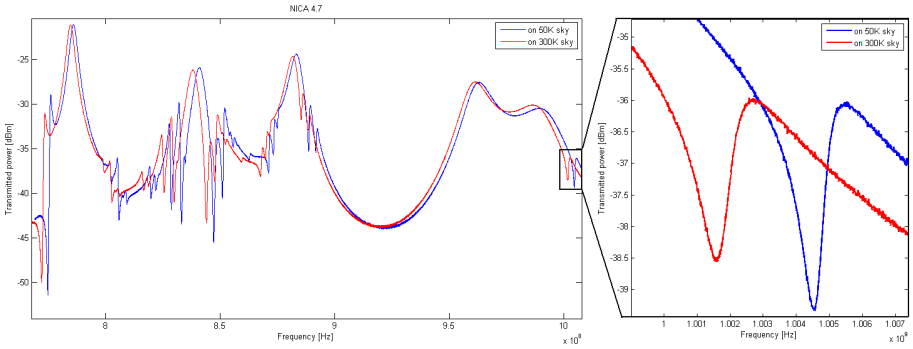

Figure 4.22: *Effect of a change of optical load on the $Nb_{.18}Si_{.82}$ detectors. A frequency shift of $\Delta f = 2.7MHz$ is measured when passing from a 300K to a 50K blackbody. The different values of S_{21} below and above the resonances are a consequence of the off-resonance level not being flat. This is due to the standing waves introduced by the impedance mismatches in the readout line.*

As a final step, we performed an absorption spectra to compare the properties of $Nb_{.18}Si_{.82}$ to those of other materials tested before. In this case a Martin-Pupplett Interferometer (MPI) is placed in front of the entrance lens of the cryostat. The MPI allows us to make spectra up to a few THz with a resolution which is typically set to

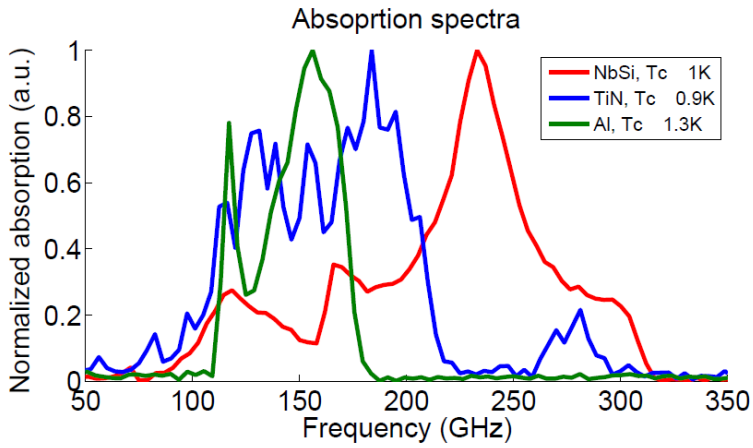

Figure 4.23: *Absorption spectra for different materials [109]. It is evident the different behavior of compounds like TiN and NbSi, whose absorption reduces smoothly below the gap frequency, from that of a pure metal like Al, which on the contrary shows a sharp cutoff at ν_{gap}. The differences at higher frequencies are due to the different low-pass filters mounted in the various cooldowns.*

3GHz. The results show an interesting analogy with an effect that we had previously observed in TiN. As can be seen in figure 4.23, the behavior of composite materials and that of a pure material like Al are remarkably different at frequencies below the cutoff value $\nu_{cut} = 3.5k_bT_c/h$. In the case of Al we observe, as expected, a very sharp cutoff at ν_{cut}, below which the material cannot absorb any incoming radiation as the photons are not energetic enough to break a Cooper Pair. This is in agreement with the classical description of a superconductor as a material with a well-defined energy gap separating the superconducting carriers from the unpaired electrons. On the other hand, for both $Nb_{.18}Si_{.82}$ and for TiN, no clear cutoff is evident, although we still observe a clear suppression of absorption efficiency for frequencies well below ν_{cut}. Possible explanations might be the presence of sub-gap states in compound materials, or inhomogeneities in the deposited films leading to local variations of the gap [110]. This point clearly needs further investigation to understand the underlying physical processes, before adopting such materials as the baseline for satellite missions.

In conclusion, $NbSi$ alloy offers advantages similar to those of $Ti_{1-x}N_x$, in particular the possibility to tune T_c changing x and the very high values of L_k and ρ_n. We made samples starting from a 50nm film of $Nb_{.18}Si_{.82}$, measuring $T_c \approx 1.05K$, $\rho_n \approx 700\mu\Omega \cdot cm$, $L_k = 180pH/\square$ for the NICA4.7 array. The optical responsivity is also particularly high, $R \sim 11kHz/K$, in particular considering that the geometry was not optimized for free space matching. We then performed an analysis of the electrical properties of the NISBA1.2 array

kept in the dark, founding coupling quality factors compatible with simulations, and internal quality factors of the order of 10^5. Comparing with the simulations, the kinetic inductance on this latter array gave $L_k \sim 248pH/\square$.

Nb_xSi_{1-x} has therefore many properties that would make it well suited for Kinetic Inductance Detectors working at very low optical powers. The high film resistivity ($\sim 140\Omega/\square$) is also well suited for UV and optical applications, where the short wavelengths require the single meander line to be directly coupled to incoming radiation. Moreover, the corresponding high value of kinetic inductance will help in reducing the dimension of the pixels, keeping the resonance frequencies in the optimal working range of a typical RF readout chain. Although the first results are very encouraging, more work needs to be carried out to confirm the potential of this alloy. In particular, the mask we used was not optimized for such a highly inductive material. This had two main consequences: 1) the CPW feedline impedance was not 50Ω, so that strong reflections were present along the readout chain, leading to the onset of standing waves in the circuit. 2) the resonances were shifted at frequencies well below 1GHz, out of the optimal operating range of the available RF setup. For this reason in the future it will be necessary to design a new dedicated mask for this material, which can be optimized starting from the measured values of ρ_n and L_k. With these new detectors we will be able to deepen our knowledge of the properties of Nb_xSi_{1-x} alloys, and to obtain noise measurements and information about the quasiparticle lifetime, τ_{qp}. Very preliminarily, we also measured the 50nm $Nb_{.18}Si_{.82}$ LEKID relaxation time in $5 - 10\mu s$ by exposing the detectors to Cosmic Rays radiation.

Titanium Vanadium alloy (TiV)

In the last months of my PhD, we have started to test the Titanium Vanadium (TiV), a new promising alloy for millimeter band observations. As in the $NbSi$ case, the films are deposited at CSNSM by evaporation under ultra-high vacuum conditions. The first sample was fabricated with a 2% Vanadium content, realizing a film thickness of $42nm$ on a $330\mu m$ high-resistivity Silicon wafer. From previous experiences [111], the superconducting transition temperature is expected to be $T_c \approx 740mK$. The array geometry is an old NIKA mask designed to test Al detectors. It provides 25 pixels with a meandered inductor $4\mu m$ wide, grouped 5 by 5 depending on different coupling to the feedline. The resonance are expected to cover a $\sim 150MHz$ bandwidth, in the range $0.83 \div 1GHz$. The optical coupling to incoming radiation was not fully optimized.

The first test was performed in dark condition in the 'Sionludi' cryostat. The observed transition temperature was between $700mk$ and $750mK$, in agreement with expectations. At the base temperature of $\sim 105mK$, the $TiV2\%$ array showed 16 resonances placed in the expected range between 830 and 950MHz. We then performed a temperature sweep and

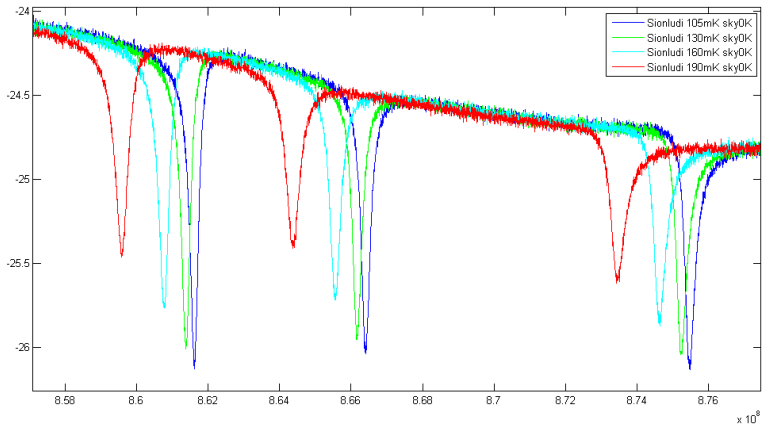

Figure 4.24: *The VNA scan of three resonances of the TiV2% at different temperature: 105mK, 130mK, 160mK, 190mK. Since $T_c \approx 740mK$, the minimum of the resonance is still moving towards higher frequency even at the base temperature.*

acquired VNA scans (fig. 4.24). We then fitted the resonances and calculated the internal quality factors Q_i, of the order of $4 \cdot 10^3$ at 105mK, a very low value compared with typical ones ($\sim 10^5 \div 10^6$).

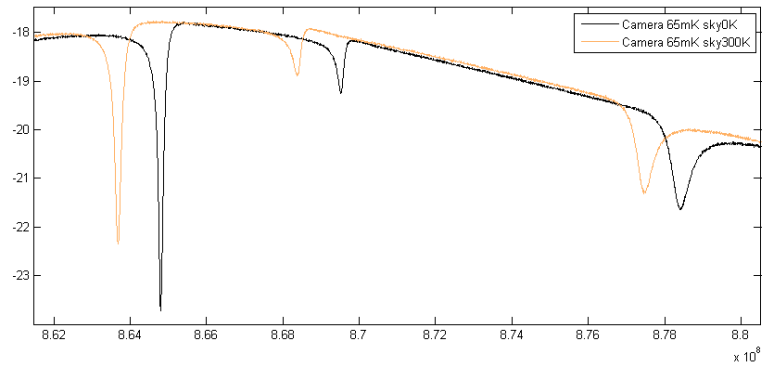

Figure 4.25: *The VNA scan of three resonances of the TiV2% with different illumination conditions: cryostat closed with a mirror ('0K') and cryostat opened on a room temperature eccosorb sheet ('300K'). The measured frequency shifts are $\sim 1.1MHz$.*

The second test was performed inside the 'NIKA' cryostat, with a base temperature of $\sim 70mK$. During this test the array was opened to the incoming radiation, with a face-back illumination and a $700\mu m$ backshort. At the reached base temperature of $65mK$, the array showed 17 resonances. We took VNA scans under two distinct illumination conditions: 1) with a mirror on the cryostat input ('0K') and; 2) a room temperature eccosorb sheet on

the cryostat window ('300K'). The measured frequncy shift between these two illumination was roughly 1.1MHz, similar to TiN and $NbSi$ alloys (fig. 4.25). The array average internal quality factors Q_i were around $8 \cdot 10^3$ at 65mK. These values are better than what found in 'Sionludi', as a consequence of the lower temperature. We finally resume here the array average internal quality factors $\langle Q_i \rangle$ at different temperatures:

$$\begin{aligned}
&(7.5 \pm 2.8) \cdot 10^3 \quad 65mK \\
&(5.6 \pm 1.7) \cdot 10^3 \quad 65mK + background(BB \sim 300K) \\
&(3.7 \pm 0.3) \cdot 10^3 \quad 105mK \\
&(3.5 \pm 0.2) \cdot 10^3 \quad 130mK \\
&(3.2 \pm 0.2) \cdot 10^3 \quad 160mK \\
&(2.7 \pm 0.2) \cdot 10^3 \quad 190mK
\end{aligned}$$

As a final measurement, optical spectra were taken using the MPI. The result (fig. 4.26) showed that the array starts responding from $\sim 55GHz$, corresponding to a critical temperature of about $750mK$, consistent with DC measurements. The spectrum, as in the case of $NbSi$ and TiN, shows no clear cutoff.

A new dedicated mask is currently under study in order to improve the quality factors and the optical coupling. Further measurements are planned in the next future to measure the signal-to-noise and the optical performances varying the pixel geometry, the Vanadium concentration and the thickness of the superconducting film.

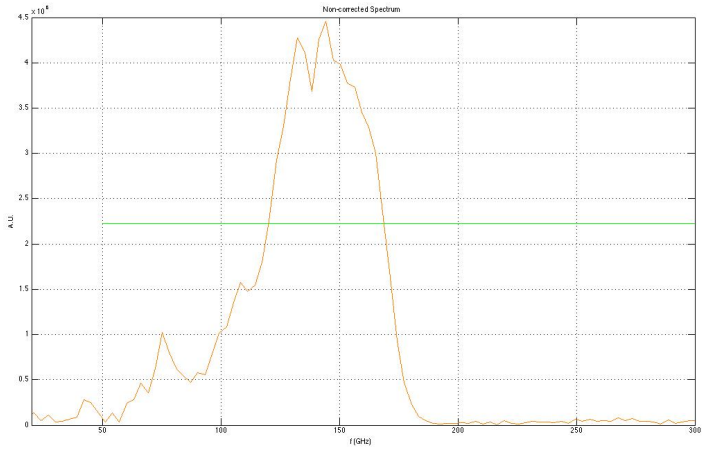

Figure 4.26: *The optical spectrum of the TiV2% array pixel as measured in the 'NIKA' cryostat.*

Chapter 5

Development of a KID camera prototype in Rome

During my PhD, I spent four months for year in *Sapienza* University of Rome. Here I collaborated with the Experimental Cosmology group lead by professor Paolo de Bernardis, working in the framework of the AstroKID project. The main goal of this project is the development of KID arrays for ground-borne experiment dedicated to millimeter Astronomy. In order to assess the performances of a KID-based instrument working in the atmospheric windows at 240 GHz, 140GHz, and 90GHz, we needed to redesign the inner stages of a dilution cryostat already present in the G31 laboratories, non equipped with an optical access. Its mechanical and optical upgrade, custom design on the existent structure, allowed to open the cryostat on the laboratory without spoiling the cryogenic performances. First of all, we tested different silicon substrate solution in dark condition; then we measured the Noise Equivalent Power of the best array under an optical load. Finally, in order to evaluate the 90GHz band measurement capability of our Aluminum, we measured its energy gap deploying the new optical access of the cryostat. It is worthy to stress that all the optical measurements were performed using the same readout electronics and the acquisition software developed in Grenoble, adapted for millimeter wavelength experiments .

5.1 Experimental setup

5.1.1 The detectors

The detectors consist of 40 nm Aluminum LEKID fabricated on a $300\mu m$ thick silicon wafer. The pixel geometry is inspired to the LEKID architecture [10], consisting in a meandered inductor $4 \div 6\mu m$ wide with a $\sim 5\%$ filling factor, and a broader interdigited capacitor coupled to a CPW feedline (fig. 5.1).

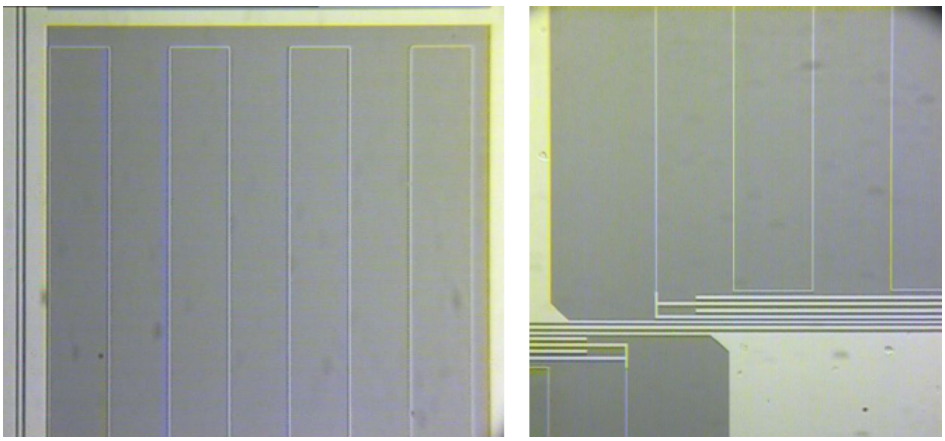

Figure 5.1: *A SEM picture of one of the first designed ASTROKID.*

The substrates change in term of resistivity and manufacturing company. The first array has been fabricated on a $300\mu m$ thick high-resistivity intrinsic silicon (HR-Si, $> 5000\Omega{\cdot}cm$), by the Silicon Radiation Sensor Institut of the Bruno Kessler Foundation (FBK), based in Trento. We will refer to this array as to *FBK*. Driven by the interest in having an on-site supplier, we committed the next array fabrication to the Institut of Photonic and Nanotechnologies (IFN), based in Rome. The array produced by the IFN and tested in this thesis are three:

1. *IFN1*: first committed prototype. Nine 40nm evaporated *Al* pixels, with changing coupling. This array is fabricated on doped non-intrinsic high-resistivity silicon (dopedHR-Si, $> 5000\Omega \cdot cm$), oriented (111);

2. *IFN2*: same pixel geometry (Nine 40nm evaporated *Al* pixels). Fabricated on intrinsic high-resistivity silicon (HR-Si, $> 5000\Omega \cdot cm$), re-crystallized with floating zone method, [112]), oriented (100);

3. *IFN3*: two 40nm evaporated *Al* pixels on same HR-Si wafer.

5.1.2 Control and read-out electronics

The detectors are read-out by the *NIXA* electronics (par. 3.3.2). A Local Oscillator capable to generate a wave carrier in the range $300Hz \div 8GHz$ is connected to the FPGA output, producing the KID feeding comb. The signal is opportunely attenuated and sent to the KID array in the coolest stage of the cryostat. Then it is amplified by the Low Noise Amplifier (Si-Ge citlf4 LNA) and read-out after being opportunely demodulated. The FPGA firmware provides the first mediated raw data, at a sampling rate of $\sim 25Hz$. Finally the *sNelloX* acquisition software is used to further analyze and save the data (par. 3.4). The cryogenic

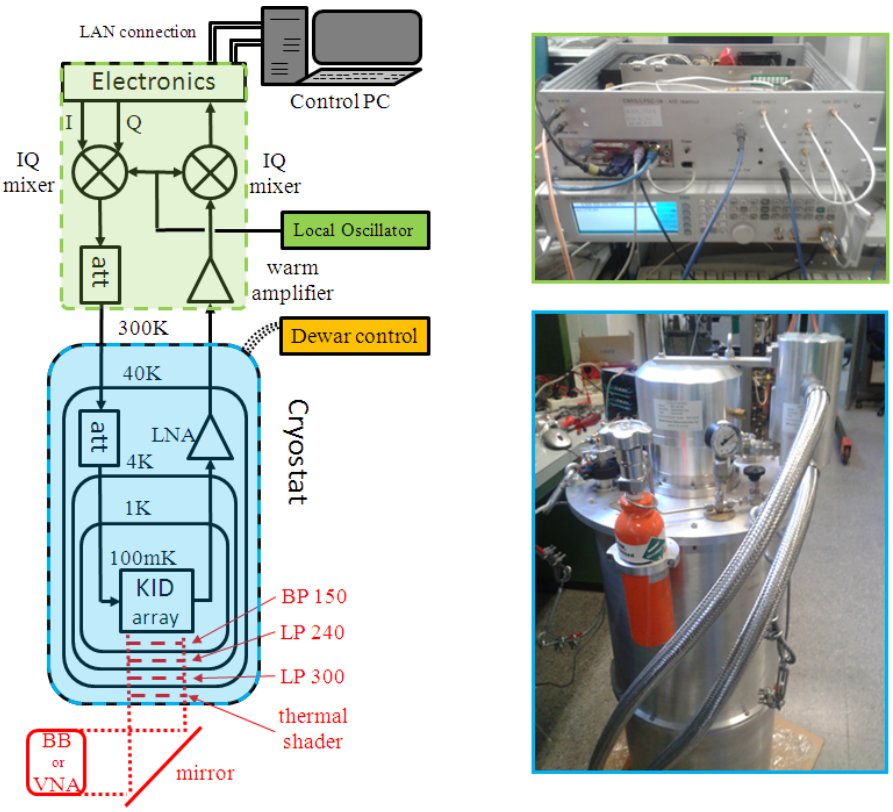

Figure 5.2: *The experimental setup in G31 laboratory. The elements labeled in red have been introduced in the system after the optical upgrade of the cryostat*

operations are performed by the *Dewar control*. It is a multi-channel board able to remote read-out and control up to 4+8 thermometers and 6 heaters. The Dewar control uses a LAN connection with a html graphic interface.

5.1.3 The cryostat

The cryostat is a four-stages cooling system [113], compound by the sum of a pulse-tube cryo-cooler (PTC), two absoption cryo-pumps (^4He and ^3He respectively), and a final $^4He/^3He$ dilution refrigerator. A schematic of the system is presented in fig. 5.3.

The first stage is provided by a Sumitomo062B PTC. Typical running temperatures are $\sim 42K$ and $\sim 4K$ for the first and second PTC plates, respectively. However, these temperatures are elevated by operation of the various cryo-pumps. For example, the second stage temperature may increase to approximately 15 K during operation of the large ^4He cryo pump.

The second and third stages of cooling are respectively provided by a ^4He and a ^3He adsorption cooler. In each case a charcoal loaded cryo pump (shaded grey in fig. 5.3) is

mounted between the first and second PTC stages, and connected by thin-walled stainless-steel tube to an evaporator within the second-stage space. Each cryo-pump is equipped with a ruthenium oxide thermometer and a heater supplied by an external electronics board (*Dewar controller*). Heating the cryo-pump causes ^4He (^3He) to be de-adsorbed; this then condenses in the evaporator. When the heater is switched off and the cryo-pump cooled by means of a heat switch to the PTC second-stage plate, the charcoal starts to re-adsorb helium vapour, thus pumping on, and consequently cooling, the condensed liquid.

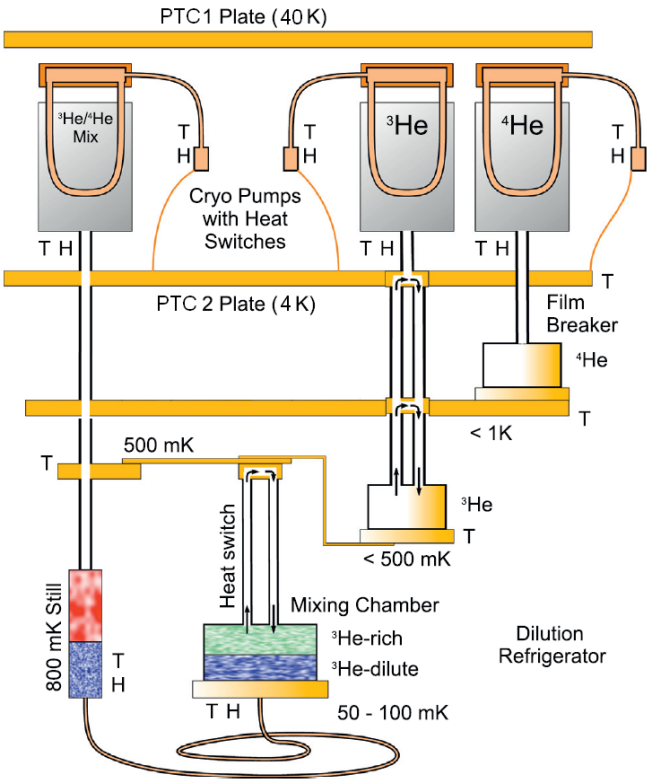

Figure 5.3: *Schematic of the MDR system. Thermometers are indicated by a T and heaters by an H.*

The last cooling stage is provided by a single-shot Miniature Dilution Refrigerator (MDR). The still is constructed from copper, providing thermal connections to a ruthenium oxide thermometer and a heater, supplied from the Dewar controller. Its internal volume is 8 ml. The mixing chamber is constructed from copper, with thermal connections for thermometers (germanium resistance). Its internal volume is 15 ml. The capillary connection is to the bottom of the mixing chamber. The chamber is filled with oxygen-free copper braid to improve the thermal connection from the chamber walls to the mixture. At the top of the mixing chamber two further stainless steel tubes (110-mm length, 3.175-mm outside diameter and

0.1 mm in wall thickness) are connected to a small copper chamber above, in thermal contact with the ^3He link. When the MDR is warm and its cryo pump is heated, the tubes of the MDR circuit contain $^4He/^3He$ gas. Working by convection the twin tubes act as a passive heat switch or thermal diode between the mixing chamber and the ^3He fridge. The mixing chamber otherwise has very good thermal isolation and will not cool without this. Once mixture has been condensed within the mixing chamber, pre-cooled to the ^3He fridge temperature by the action of the passive heat switch, the cryo pump is cooled and the still warmed to start the dilution process. The mixing chamber then cools further. When it is colder than the ^3He fridge, convection through the heat switch tubes stops (the switch opens).

Each of the three cool plates at $1K$, $4K$ and $40K$ is radiatively isolated from the others through three $0.5mm$ thick copper shields mounted on the plate at the corresponding temperature. The MDR is enclosed by the $1K$ shield.

A full cycle of the cryostat lasts $36 \div 48$ hours. During this cycle it is capable to maintain a base temperature of $\sim 100mK$ for about 6 hours, depending on the still heating. The corresponding temperatures reached by the still and the ^3He stage are roughly 800mK and 400mK, respectively.

5.2 Cryostat upgrade for dark and optical test

In order to test the detector performances at low temperature, large part of my thesis work has concerned the almost fully refurbishment of the cryostat to match the requirements of KID. During the first months of my PhD, we have equipped this cryostat with two independent RF channels (1 input, 1 output), using Cu-Ni coaxial SMA cables down to the coolest stage at $\sim 100mK$. The output channel is further equipped with the LNA, mounted on the 4K plate and operating in the frequency range $1 \div 4GHz$.

After these preliminary operations, we studied the problem of adding an optical access to the cryostat. Our final goal was to design an optical system suited for a hundred-pixel array at millimeter wavelength, able to concentrate the most of the optical power onto the surface covered by a single pixel. Once the entrance pupil diameter has been maximize in order to reduce the diffraction limit, this requirement can be achieved minimizing the f-number $f/\#$. First of all, we reproduced the mechanical structure of the cryostat in a digital format, using the software *AUTOCAD* (fig. 5.4). Then we used the software *ZEMAX* to simulate different optical configuration fitting the available spaces between the fixed parts of the cryostat, i.e. the dilution plate at $\sim 100mK$, and the cryostat bottom plate at $300K$. Designing an optical system with an f-number as low as possible means to have an high optical rapidity, or *throughput*. This can be achieved in two ways:

- Make the entrance pupil diameter very large. This is limited by the manufacturing costs of the optical and mechanical elements, in particular of the optical filters necessary to

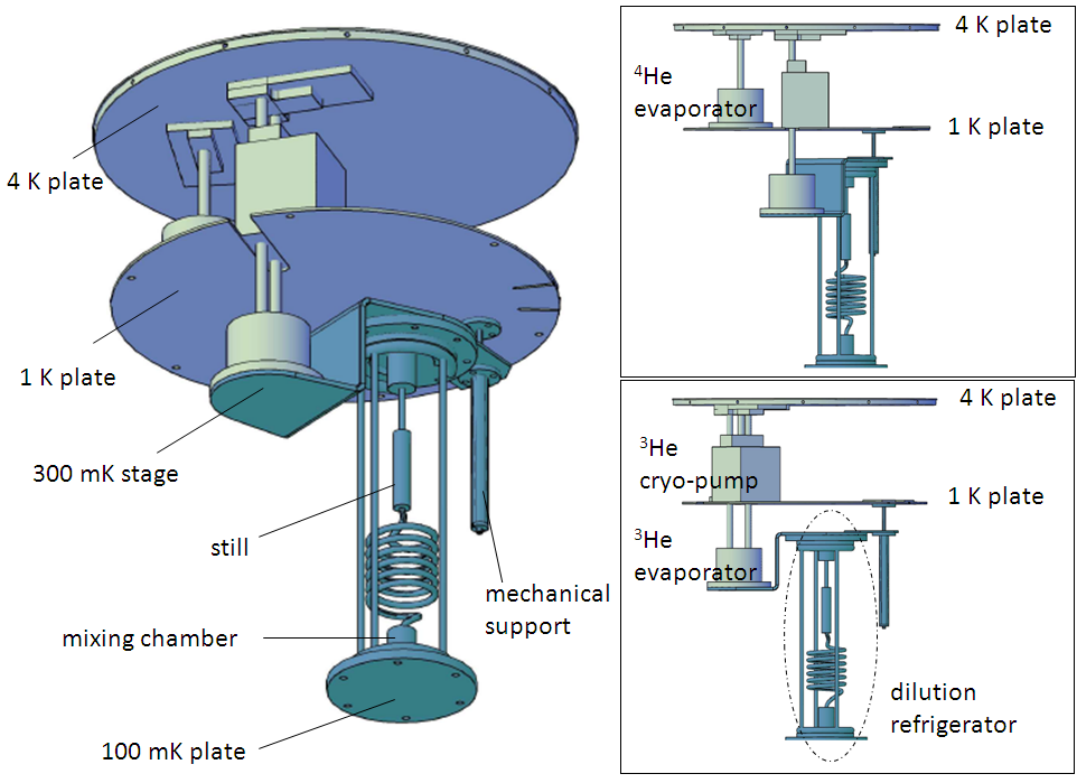

Figure 5.4: *Layout of the 4K, 1K and 100K stages of the cryostat before the optical upgrade. The model has been realized using the* AUTOCAD *solid modeling software.*

cutoff the unwanted radiation at higher frequencies.

- Make the optical system able to focus the ray light on a very short focal distance. This is achievable by putting a very low curvature radius lens in front of the array, which minimum value is limited by the field dimension.

The first condition also determines the Airy Disk size and the resolution of the system, so that this is our main requirement. We then brought the following filters:

1. *Thermal shader.* Mounted in rings with 100 mm inner diameter, 120 mm outer diameter and assembly thickness 6 mm. Operation at 50 K (upstream from item 2.). The thermal shader is the entrance pupil of our system.

2. *300 GHz low-pass blocker* (fig. 5.5(a)). Unmounted, 100 mm diameter. Operation at 50 K.

3. *240 GHz low-pass blocker* (fig. 5.5(b)). Unmounted, 85 mm diameter. Operation at 4K.

4. *210 GHz band-pass.* Unmounted 85 mm diameter. Operation at 1 K.

5. *150 GHz band-pass* (fig. 5.5(c)). Unmounted 85 mm diameter. Operation at 1 K.

6. *wide 90 GHz band-pass*. Unmounted 85 mm diameter. Operation at 1 K.

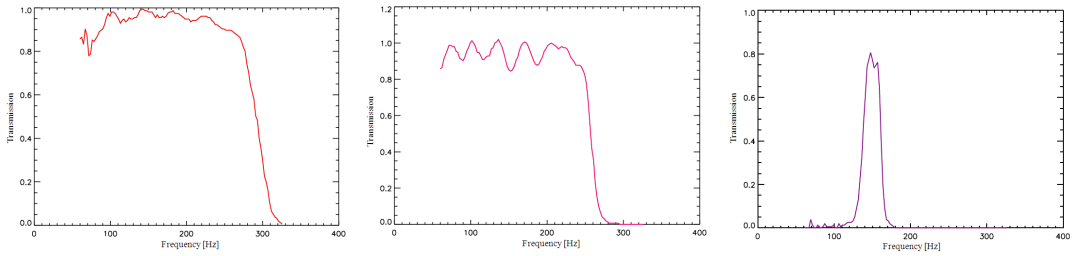

(a) (b) (c)

Figure 5.5: *Spectra of the optical filters: (a) Low-Pass blocker at 300GHz; (b) Low-Pass blocker at 240GHz; (c) Band-Pass filter at 150 GHz.*

The successive sizing of the optical and mechanical elements was subordinated to the dimensions and the positioning of these objects at their specified working temperature. We finally decided to design a two-lenses optical system. The two lenses have a plano-convex geometry, with the curvature facing towards the incoming beam in order to minimize the aberrations. The first one, slightly converges the beam to fit the requirements of the decreasing diameter of the optical filters. Then a second lens place just in front of the array provides the strong focusing of the beam size. The lenses have been fabricated with High-density polyethylene (HDPE), whose refractive index at low temperatures was previously studied in G31 laboratories [114]. Starting from these conditions, we have optimized an optical system fitting our requirements. The ZEMAX optical simulations are shown in fig.s 5.6(a)–5.6(b) and 5.7.

A schematic of the mechanical structure with all the optical elements mounted is shown in fig.s 5.12–5.11. It has been designed following three main directives, in order of priority : 1) minimization of the additional thermal load on coolest stages; 2) correct positioning of all the optical elements (lenses, filters, focal plane array); 3) mechanical stability (deformation, loading capacity, ecc.). The design has been also thought in order to fit an additional thermal shader, whose purchase was strictly recommended by the supplier company. Unfortunately, the purchase of this item did not fall within our budget. We list and comment here the modifications introduced in the existent structure:

- **Shields**: the existent copper screens were replaced with an aluminum ones. For this first demonstrator, we used commercial $1050 - Al$ (purity $> 99.5\%$). The thermal conductivity of aluminum is in general fairly less than that of oxigen-free copper, except for very high purity aluminum (fig. 5.8). Nevertheless, the previous shields were made of low-quality electrolytic Cu, whose thermal conductivity differs from that of $1050 - Al$ of

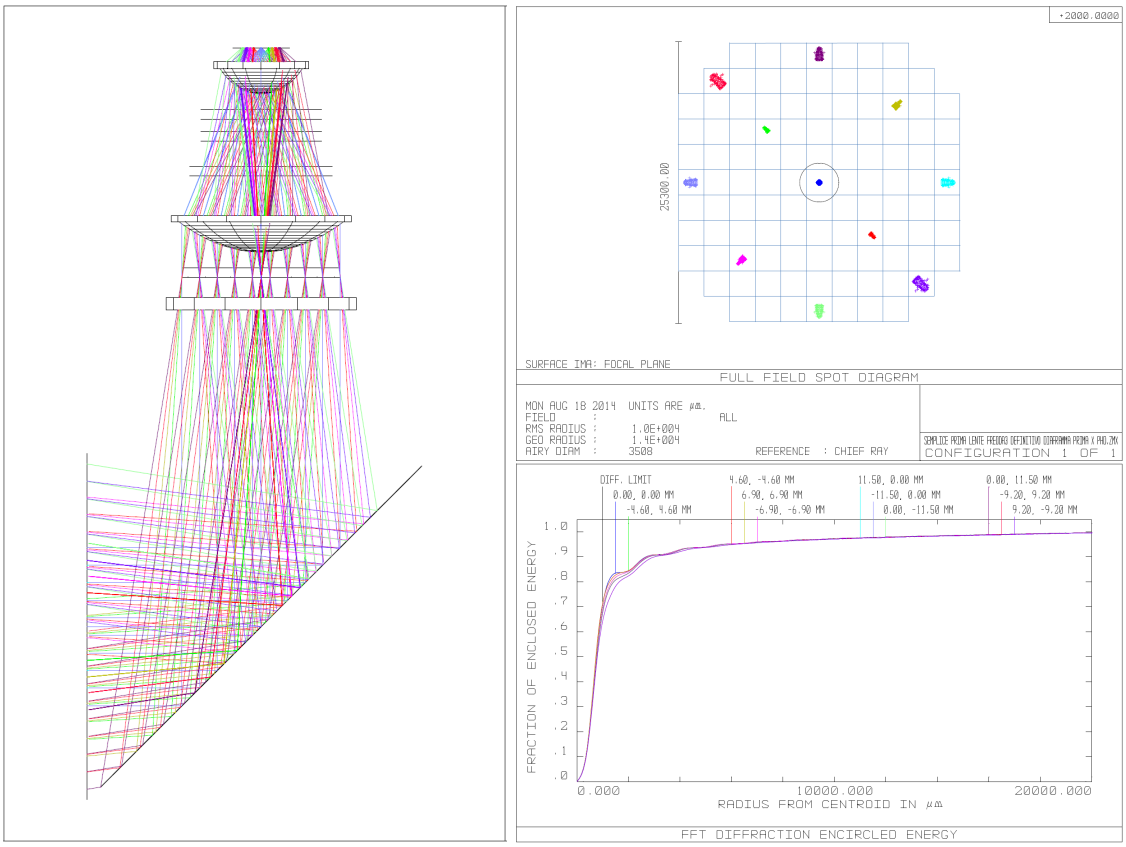

(a) (b)

Figure 5.6: *Optic model simulated with the* ZEMAX *optical and illumination design software. In the figure eleven far fields are shown. (a) Solid model of the optic system; from the bottom left corner, the radiation is reflected by a 45deg mirror towards the 300K HDPE window of the cryostat; then the radiation traverses the thermal shader, the first HDPE lens and the LP300 (at 40K), the LP240 at 4K, the BP150 at 1K, and finally the second HDPE lens at 0.1K before to reach the KID array. (b, top) The full field spot diagram (FFSD) of the focal plane. The Airy Disk (diameter* $\sim 3.5mm$*) is represented by the black circle in the middle of the focal plane. The focal plane has been designed to house a 109 KID array at 2mm wavelength (pixel pitch 2.3 mm). The layout on this array is traced in blue. The model can be easily adapt to 1mm and 3mm bands. (b, bottom) The fraction of encircled energy with respect to the diffraction limit. The plot shows that at the Airy radius (*$\sim 1.75mm$*) it is comprised between 83.8% (diffraction limited, center of the array) and 78% (array edge). The corresponding energy collected by the detectors, supposing circular pixel of 2.3mm diameter, ranges from 75% (diffraction limited, central pixels) to 68% (outer pixels).*

a factor in the range $\sim 3 \div 10$, depending on the operative temperature. To compensate this effect, the shield thickness was increased of the same factor (~ 3), that is from $0.5mm$ to $1.5mm$. The length of the shield was then dimensioned in order to fit the

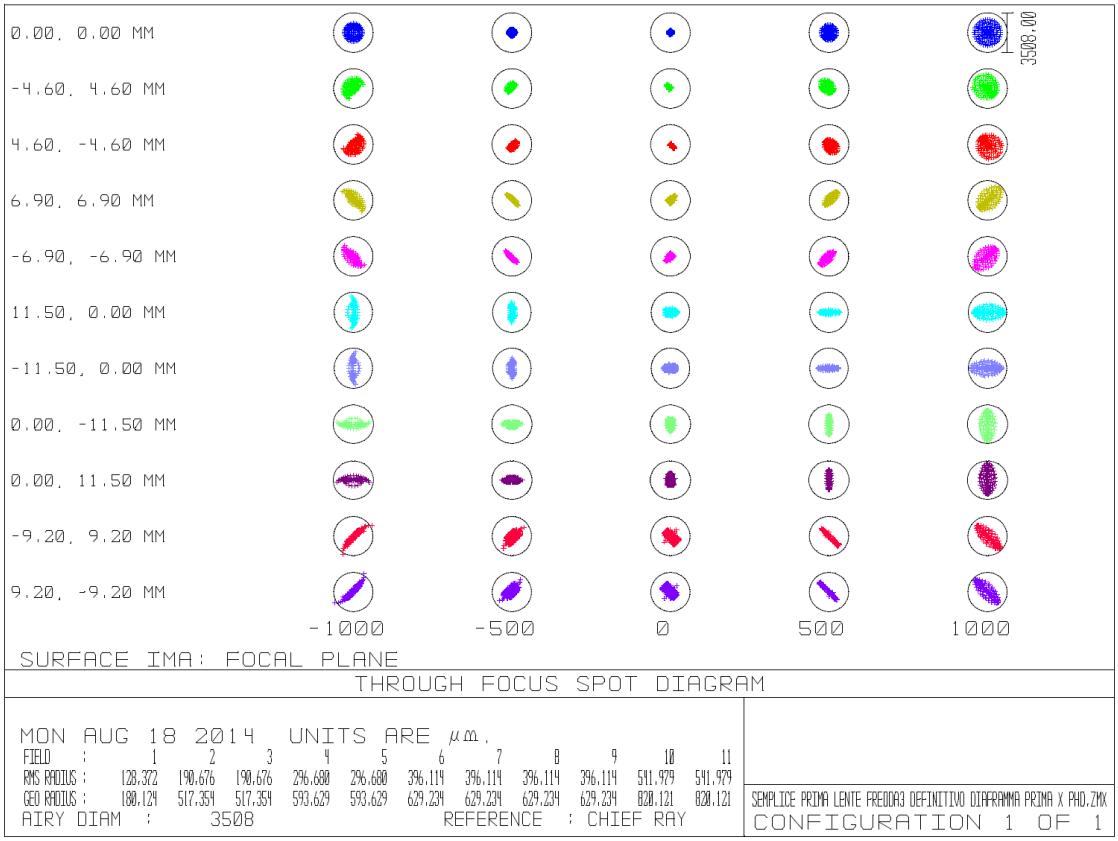

Figure 5.7: *Through Focus Spot Diagram (TFSD) for all the eleven field shown in fig. 5.6(a)–5.6(b). The model shows the defocusing produced by a displacement of the focal plane. The model shows that the focus spot still falls within the Airy Disk (black circles in figure) for displacement between* $1mm$ *and* $-1mm$*, even for outer pixels.*

optic system requirements.

- **Plugs**: Each shield is equipped with a removable plug at the bottom, whose assembly is provided by an *Al* annulus. Each plug houses the optical elements, that are represented by the filters and the brass 'glasses' using as holders, and the HDPE lenses. The deformation of the plug due to this load may cause a bad-positioning of the optical elements, which has been calculated with the solid modeling software *SolidWorks*; it is maximum for the 40K plug (which mounts two glasses and one lens), in which case it does not exceed few tenth of millimeter.

- **Shield + Plugs + Optics**: The set of the shield plus the plug with its optical elements must be sustained by the cryogenic plates. The total weight of these structures must not exceed the maximum loading capacity of the plates. Unfortunately we did not know exactly this value, although it is important especially for the 1K plate, which is

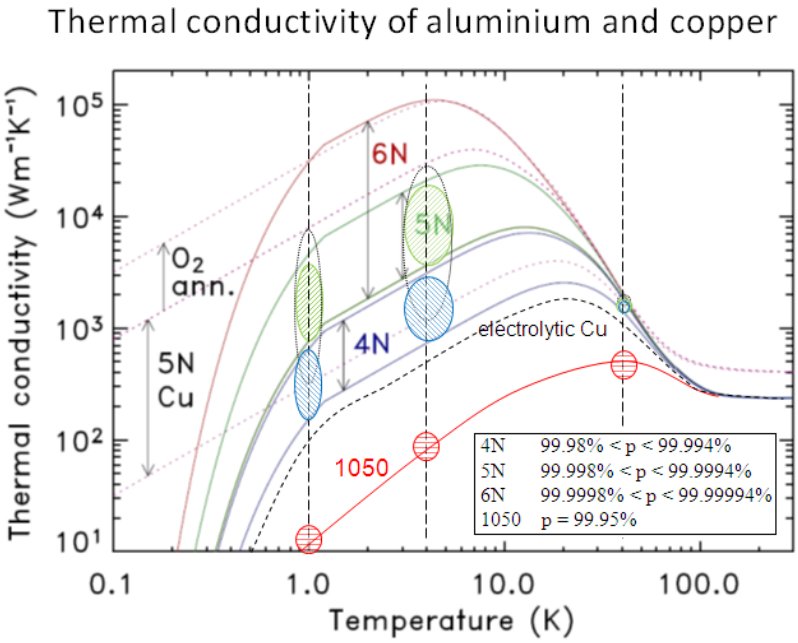

Figure 5.8: *Recommended ranges for the conductivity of annealed Aluminum (solid lines purple, green, and blue) with 4N, 5N, and 6N purity (p in the plot) and for vacuum annealed 5N purity copper at low temperatures, together with the higher conductivity values possible following oxygen annealing (dashed lines) [115]. For comparison, the thermal conductivity of 1050 Aluminum (solid red line) and of the Electrolytic Copper (dotted black line) are also shown. In the former case, the thermal conductivity $k(T)$ is calculated following the formula $k(T) = T/(a + bT^3)$ with $a = 0.0546K^2m/W$, $b = 5.3 \cdot 10^{-7}m/K/W$ [116]. The encircled areas correspond to the thermal conductivities at the shield temperatures, i.e. at 1K, 4K and 40K.*

sustained from the 4K plate just by a few thin steel tubes. We thus simply tried to not exceed the previous load provided by the three 'naked' copper shields. This is another important reason for choosing Aluminum instead of copper: their densities stand in a ratio $1 : 3.3$ (Al density $= 2.70g \cdot cm^{-3}$, Cu density $= 8.96g \cdot cm^{-3}$), so that increasing the Aluminum thickness of a factor 3 compensate the lower thermal conductivity of Al, leaving a margin for an extra load, that in our case is represented by the optical elements.

- **Fiberglass tubes**: It is provided by a $1050 - Al$ annulus ('support') sustained by six fiberglass (G-10) straws, screwed on a top annulus mounted below the 1K plate, which also provide the radial screw pattern to which the 1K shield is fixed. Each one of the six G-10 supports is a fiberglass tube 245mm long, with internal diameter 10mm and external diameter 12mm. The fibreglass tubes can be reduced to three if

necessary, without any substantial drawback for our laboratory purposes. The calculated total thermal power input from the 1K on the 0.1K stage due to the six G-10 tubes is $18.73 \cdot \mu W$, where we have used the functional form $k = \alpha T^{\beta+\gamma T^n}$ for the thermal conductivity, with the coefficients specified in [117]. Referring to the load curve of the cryostat at our adopted $T_{still} = 800mK$ (fig. 5.9), considering that we reached a base temperature of $120mK$ before the cryostat upgrading, we estimate further $\sim 9\mu W$ coming from additional non-optical sources. We thus finally estimate a thermal load on the $100mK$ stage around $\sim 28\mu W$ using six fiberglass tubes, or around $\sim 19\mu W$ using only three tubes.

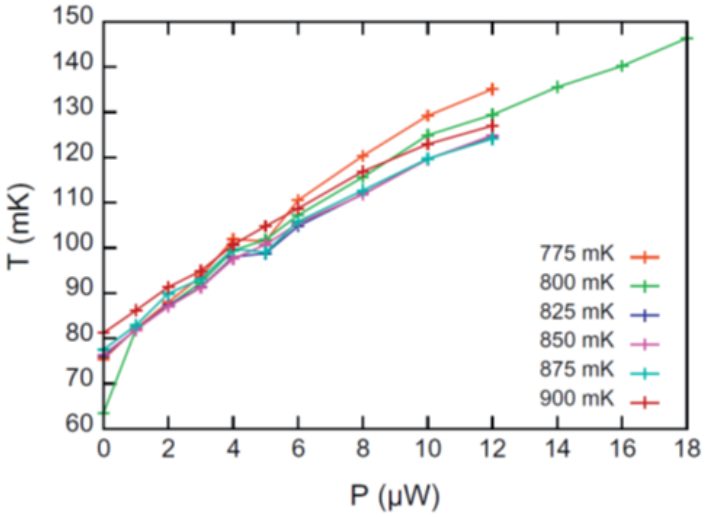

Figure 5.9: *Load curves for values of T_{still} from 775 to 900 mK. The mixing chamber load power P varies up to $P = 12\mu W$, and $18\mu W$ in the case of our adopted $T_{still} = 800mK$.*

- **100 mK structure**: the inner part of the support is designed to hold up the last HDPE lens and the sample holder housing the KID array. By design, the 100mK plate stands just few centimeters above the sample holder, shifted with respect the axis of cylindrical symmetry of the system. The thermal link to the 100mK stage was provided by a single golden copper braid.

The first optical tests on the cryostat revealed deteriorated performances. The coolest stage Ge thermometer was placed on the sample holder instead that on the 100mK plate, measuring a base temperature increasing from $120mK$ to $220mK$. This value actually does not correspond to the base temperature of the system, be due to the bad thermalization of the the array and its holder. Improving this thermalization led to a base temperature of $180mK$ and $145mK$ in the successive second and third runs, carried out adopting six and three fiberglass

tubes respectively. We want to stress that, in this latter case, the predicted temperature from the load curve ($\sim 145mK$ for a thermal load of $\sim 19\mu W$) match the measured value. We can conclude that the main cause of the the cooling power reduction is of course the introduction of the fiberglass supports. Further improvements in the cryogenic performances should surely be achievable by adding/replacing the described mechanical and/or thermal items in the current design (par. 5.5). In particular, the reduction of the thickness of the fiberglass tubes or their substitution them with a lower thermal conductivity materials (Vespel, Graphlite, ecc.) shall results in a remarkable reduction of the thermal load on the 100mK stage. In this context, an easily obtainable improvement would be obtained creating an additional thermal link connecting an intermediate point of the fiberglass tubes to the ^3He $400mK$ stage (fig. 5.10).

5.3 'Dark' tests: study of the quality factors with different substrates

In this section we report on the characterization of the electrical response of different arrays with no optical load ('dark' condition). Our first tests concerned the measurement of the quality factor of the same pixel geometry fabricated of silicon substrate of different resistivities. We present here the results obtained comparing the IFN1 and IFN2 arrays with the FBK one. Since there is a missing KID on each array, the electromagnetic crosstalk modifies the behavior

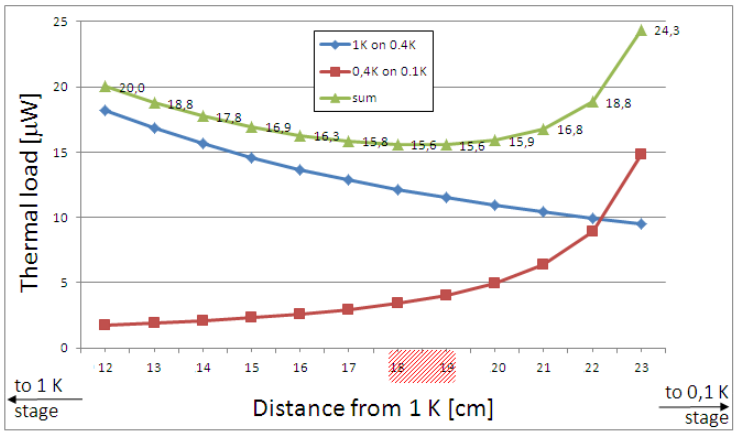

Figure 5.10: *Effect of introduction of a thermal link between the six fiberglass tubes and the 400mK stage. The plot shows the load power on the 400mK (blue) and 100mK (red) stages as function of the distance of the connected point, that is supposed to be the same for all the six tubes. The sum of the two contribution (green) is minimized for the distance* $18 \div 19cm$ *starting from the 400mK stage.*

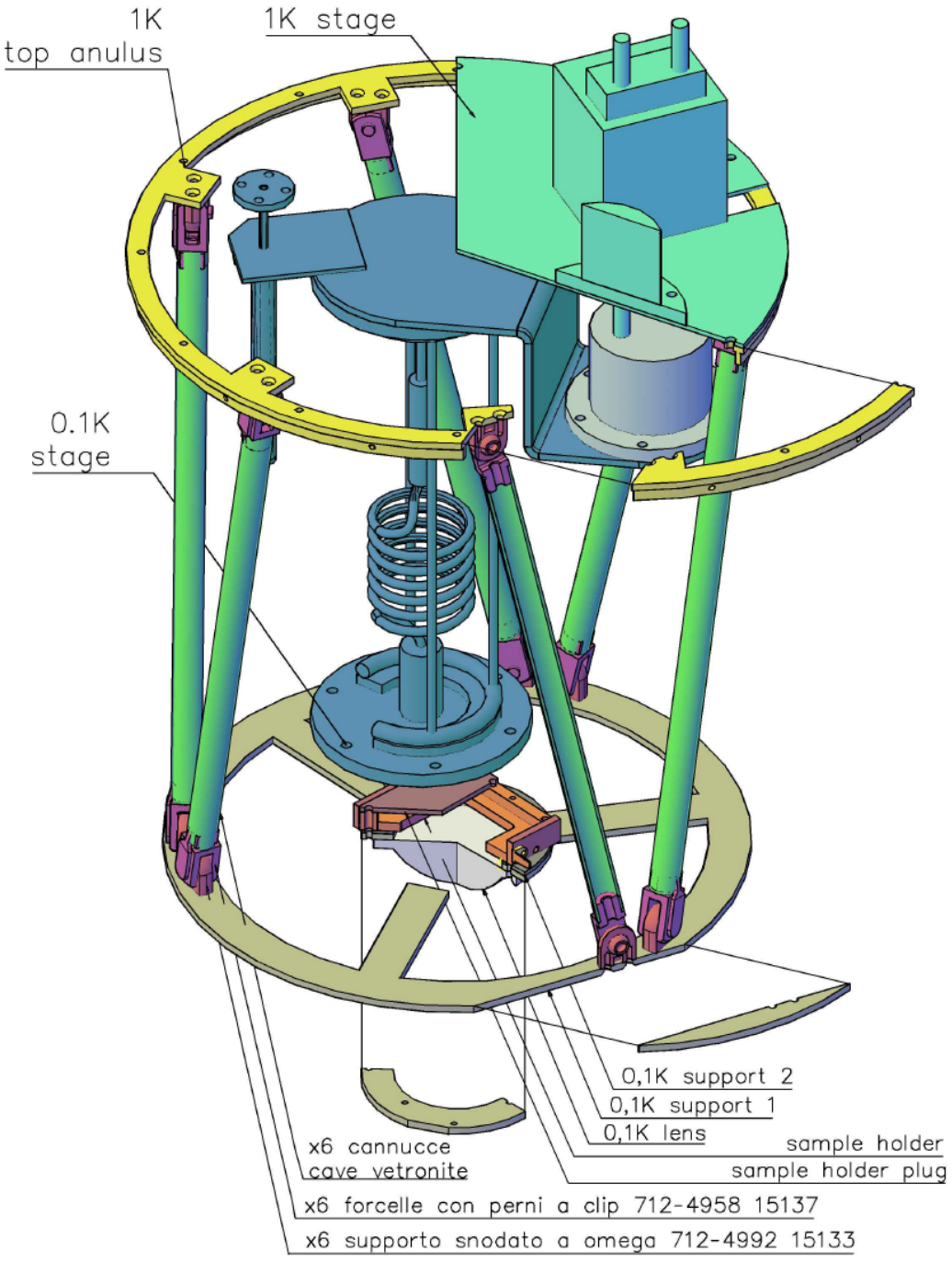

Figure 5.11: *Mounting scheme for the 100mK support sustained by the six fiberglass tubes and the top annulus connected to 1K plate.*

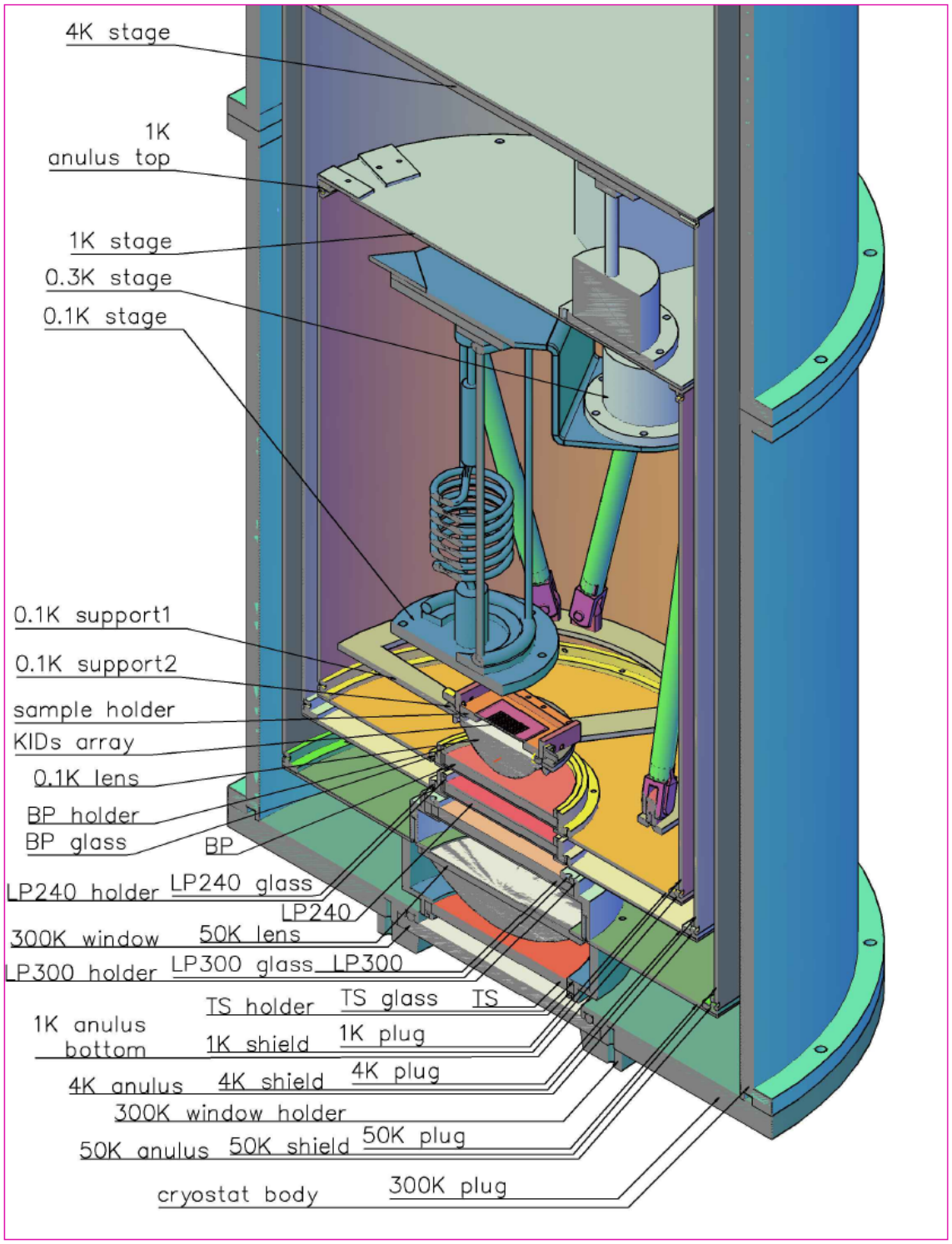

Figure 5.12: *Complete design of the cryostat after the optical upgrade.*

Figure 5.13: *Some photographs of the optical and mechanical element fabricated for the cryostat upgrade. (a) The three thermal shields at 1K, 4K and 40K equipped with the filter holder 'glasses' and the 40K HPDE lens; (b) the six G-10 fiberglass tubes during fixed to the ruler after the glue baking process; (c) the 100mK support with the corresponding HDPE lens; (d) the 1k-0.1K mechanical system mounted throught the top annulus to the 1K plate; (e) the bottom plug of the cryostat external body, with the 300K HDPE window; (f) a from the bottom image of the 1K shield and the 100mK structure mounted on the cryostat; (g) a zoom of the 100mK plate with the first used golden copper thermal link; (h) the inner part of the cryostat, from top to bottom the four plates at 300K, 40K, 4K and 1K, with the 0.1K structure mounted with only three fiberglass tubes; same photograph with the corresponding shields mounted: (i) 1K shield, (j) 4K shield, (k) 40K shield.*

of all the resonator in terms of coupling to the feed-line. It is thus not possible to perform a pixel-to-pixel comparison.

The tests on the IFN1 and FBK arrays were performed at the same temperature, $\sim 100mK$, before the cryostat upgrade. The INF2 and IFN3 arrays were tested after this, so the base temperature was slightly higher, of $\sim 180mK$ and $145mK$ respectively. As an example, fig. 5.14 shows the fitted resonances in the latter case. We thus present the fitted

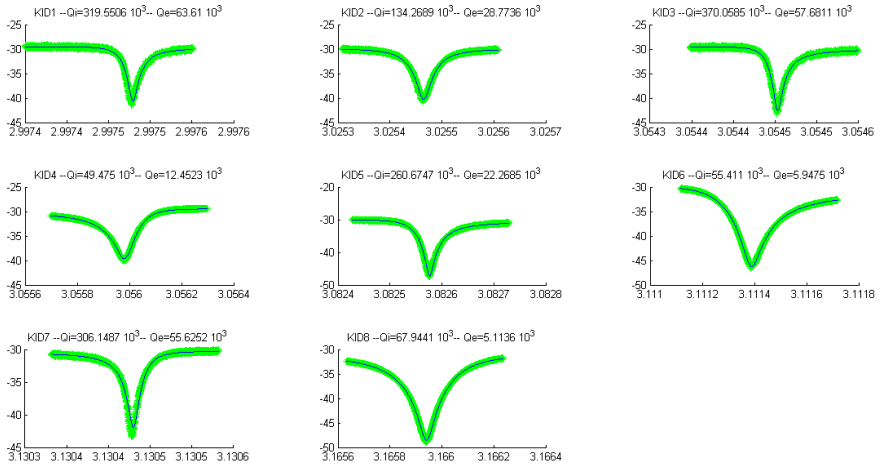

Figure 5.14: *Example of fitting resonances for the IFN2 array tested at 145mK.*

values of the internal (Q_i) and external (Q_e) quality factors in fig. 5.15. Here we resume the results in terms of mean values and standard deviation:

$$\begin{aligned}
\langle Qi_{FBK} \rangle &= (2.05 \pm 1.06) \cdot 10^5 \quad Qi_{FBK,max} = 4.2 \cdot 10^5 \\
\langle Qi_{IFN} \rangle &= (2.9 \pm 2.0) \cdot 10^4 \quad Qi_{IFN,max} = 5.6 \cdot 10^4 \\
\langle Qi_{IFN2,180mK} \rangle &= (1.71 \pm 1.09) \cdot 10^5 \quad Qi_{IFN2,max} = 3.20 \cdot 10^5 \\
\langle Qi_{IFN2,145mK} \rangle &= (1.96 \pm 1.33) \cdot 10^5 \quad Qi_{IFN2,max} = 3.70 \cdot 10^5
\end{aligned}$$

The dispersion of the Q_i values is quite high, and it is linked to the detectors coupling Q_e, which has intentionally fairly scattered values for the chosen geometry. It is worth to stress that our measure of the internal quality factor does not discriminate between losses inside the superconductor or external through the substrate. It is however evident that the internal quality factor (film + substrate) of the IFN chip is significantly lower than that of the others chips. Since we did not register this effect in the IFN2 chip, which differs from IFN only by the intrinsic HR silicon wafer, the Q_i reduction in the IFN array must be explained only by the lower resistivity of the substrate. This result validate the IFN Aluminum quality and its deposition process.

Referring to fig. 5.15, we notice that Q_i and Q_e values are correlated: the most coupled resonator (low Q_e) deposit higher energy in the resonator, deteriorating the Q_i value. It can be notice that four resonator of the IFN chip show a sensibly higher coupling: for exactly the same geometry, this might be due to the different dielectric constant on the non-intrinsic low resistivity substrate. Another important observation is that the IFN curve saturates at a lower value of Q_i with respect to the other chips; this Q_i saturation value has to be interpreted as the effective quality factor of the aluminum, around $5 \cdot 10^4$ for the IFN array, roughly $3 \cdot 10^5$ for the FBK array, may be even higher for the IFN2 array despite being at $145 \div 180mK$. This is a further element that confirm that the quality of the Aluminum film produced by IFN is substantially similar to that of FBK.

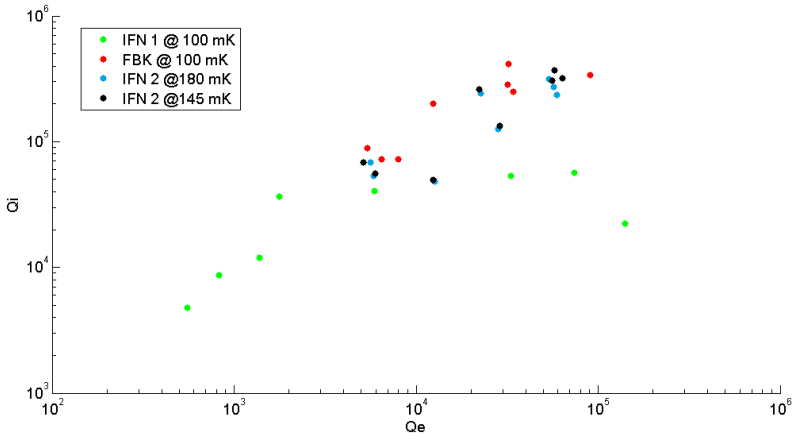

Figure 5.15: *Internal quality factor Q_i versus external quality factor Q_e for the three tested arrays FBK, IFN1 and IFN2 with the same 9-pixel geometry.*

5.4 'Optical' tests

5.4.1 Measurement of the gap of 40nm Aluminum

As first test, we want to measure the energy gap of the superconductor material that we use for our detectors, i.e. an Aluminum film 40nm in thickness. We know that the Aluminum gap decreases with the thickness of the film. We thus want to measure its value for 40nm aluminum in order to evaluate its possible use for $3mm$ band applications ($\sim 90GHz$).

The tests were performed on the IFN3 chip, using the Vector Network Analyzer (VNA) as a millimeter wave radiation source. Besides performing RF measurements, the VNA is able to produce millimeter wavelength radiation through a feedhorn coupled to free space. One of the available ranges falls in the interval $80 \div 120GHz$, well suited for our purpose. The cryostat

have been cooled down with all the optical filter, except for the last BP. After having installed the VNA in the source position, we set the bandwidth and the power on their minimum values, $< 10kHz$ and $\sim 1mW$ respectively. Then we sampled the radiation frequencies performing an acquisition of the KID resonance for each of them. The results (fig. 5.16) clearly show that the cut frequency of the 40nm thick IFN Aluminum is of about $\nu_{gap} = 96GHz$, corresponding to an energy gap of $E_{gap} \sim 198.5\mu eV$ and to a critical transition temperature of roughly $T_c = 1.31K$. The cut-off frequency of $40nm$ aluminum detectors does not allow to observe radiation at $\sim 90GHz$. In terrestrial Astronomy applications for example, the measured ν_{gap} is still to high to entirely cover the bandwidth of the atmospheric window at 3mm wavelength (as an example see fig. 4.2).

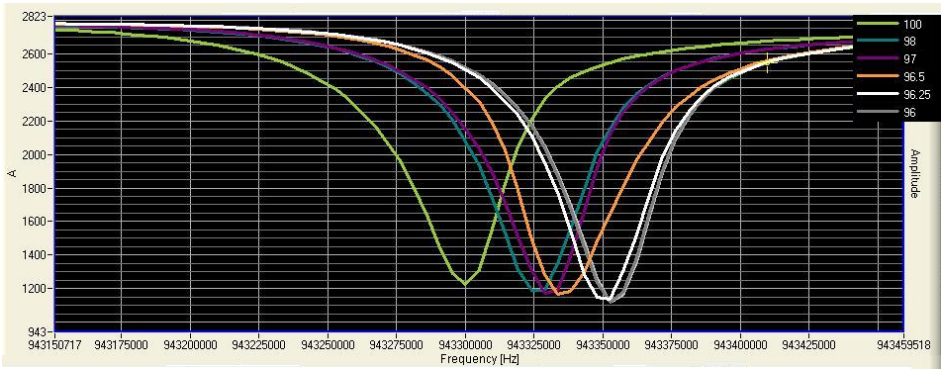

Figure 5.16: *Frequency sweep around the resonance of one of the detectors of the IFN3 array. It is evident that the resonance start to shift for radiation frequencies around* $96GHz$.

5.4.2 Noise Equivalent Power calculation

The Noise Equivalent Power (NEP) of a system is defined as the input power required to obtain a signal to noise ratio equal to 1 in a 1Hz bandwidth. To experimentally determined the NEP of the system, we can use eq. 2.100

$$NEP(f) \approx \sqrt{S_x(f)} \left(\frac{dx}{dP_{rad}} \right)^{-1} \tag{5.1}$$

where we have neglected the last term because we are interested in modulation frequencies of the order of $\sim 1 \div 10Hz$, typical for millimeter Astronomy observations. (dx/dP_{rad}) can be obtained by a direct measurement of the variation of the signal x as a consequence of varying the input power. The detector signal can be either the amplitude A or the phase θ. The ideal calculation would be performed by slightly variations of P_{rad} around the power of interest. For ground based observations, the background on the detectors is given by the atmospheric emission which corresponds to a black body (BB) with an equivalent temperature roughly in

the range $\sim 20 \div 60K$.

The follow NEP measurements have been performed mounting the IFN3 chip in the cryostat after its optical upgrade. The radiation enter the cryostat through the 300K window, then it traverse the thermal shader and the LP-300 filter on 40K stage, the LP-240 on 4K stage, and the BP-150 on 1K stage before reaching the KID array. The readout electronics was controlled using the acquisition software *sNelloX*. The experimental setup is schematized in fig. 5.2. The experimental conditions were not optimized for several reasons:

1. We do not have any available sky simulator in the power range of interest. We thus used as optical power sources two eccosorb sheets, the first at room temperature $\sim 300K$, the second cooled down to $\sim 77K$ by liquid nitrogen. Its emission is not uniform due to the high evaporation rate at room temperature, which results in a noise spectrum significantly higher than 300K eccosorb. This makes the difference in the noise spectra more significant, resulting in an higher NEP.

2. The image on the array is not in focus. This increases the received power from the others fields entering the cryostat, deteriorating the NEP.

3. The cryogenic performances after optical upgrade were still not optimized. The resulting base temperature was fairly 'high', of about $\sim 220mK$. This lowers the detector responsivity, increasing the NEP value.

For these motivations, the NEP calculation represents just an indication of the expected value. By removing these limitations in the next future, this estimation would improve sensibly.

Before measuring the Noise Equivalent Power of the system, we have characterized the electrical response of the two resonances. We thus performed a sweep of the supply power for the two resonators closing the window of the cryostat in order to reproduce low-optical load conditions. The power that maximizes the KID response, i.e. the internal quality factor Q_i, has been found $-18dBm$ and $-20dBm$ for the two resonator, respectively (fig. 5.17). We then set these powers and proceed with the optical characterization (fig. 5.18) in three different background conditions: 300K eccosorb, 77K eccosorb, and closed cryostat. From the resonances analysis it is clear that the lowest background condition corresponds to 77K eccosorb. We therefore used this condition to chose the feeding tones and calibrate the resonator responses, like the calibrated phase θ (transmitted phase with respect to the center of the resonance circle, see par. 3.4.2).

Once have characterized and calibrated the resonances, we proceeded to the NEP calculation. In the following we will refer to the 951 MHz resonance as $KID1$, and to 943 MHz resonance as $KID2$. The NEP is calculated using the formula 5.1, which can be expressed as

$$NEP \approx \frac{\Delta P}{\Delta(S/N)} \tag{5.2}$$

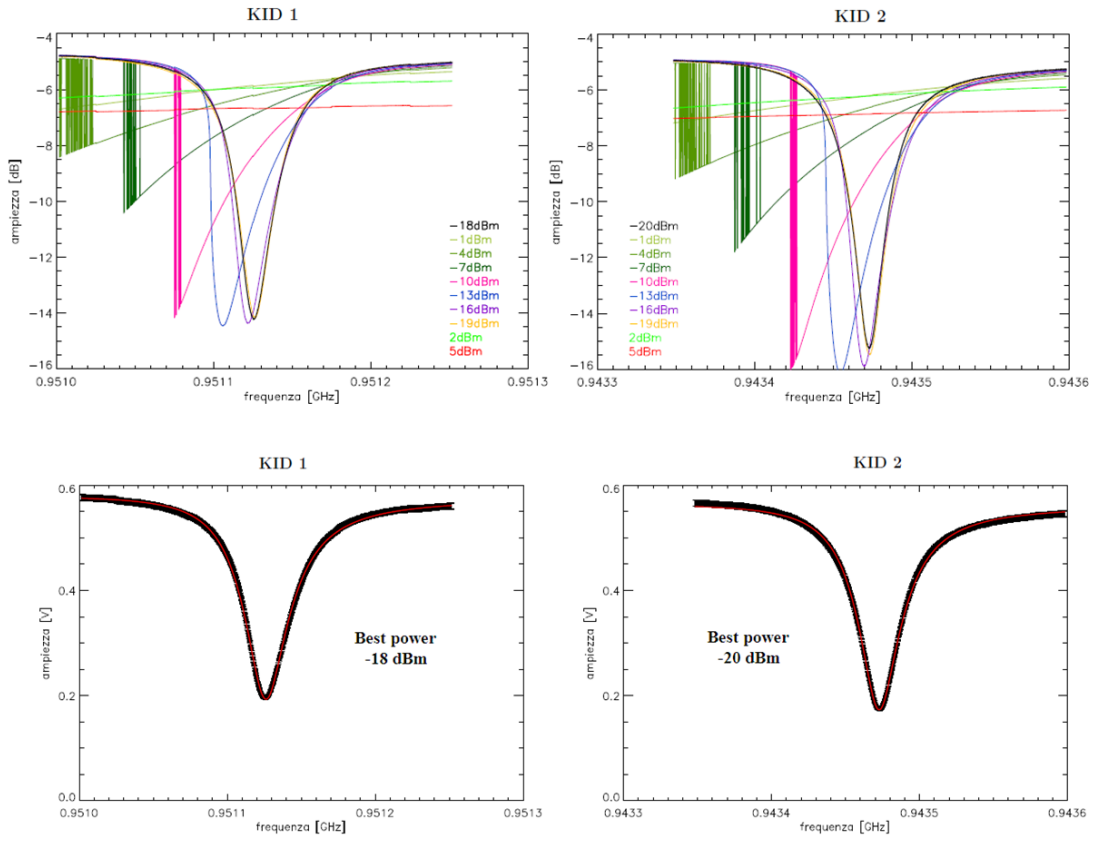

KID	$\nu_0 \pm \sigma_{\nu_0}$ [GHz]	$Q_i \pm \sigma_{Q_i}$	$Q_e \pm \sigma_{Q_e}$	$L \pm \sigma_L$	$c \pm \sigma_c$
1	$0.95112594 \pm 0.00000002$	$(5.9882 \pm 0.0151) \times 10^4$	$(3.0188 \pm 0.0054) \times 10^4$	$(6.6911 \pm 0.0906) \times 10^{-2}$	$(5.7715 \pm 0.0022) \times 10^{-1}$
2	$0.94347257 \pm 0.00000002$	$(6.6657 \pm 0.0165) \times 10^4$	$(2.9634 \pm 0.0048) \times 10^4$	$(5.2047 \pm 0.0899) \times 10^{-2}$	$(5.6266 \pm 0.0021) \times 10^{-1}$

Figure 5.17: *(Top) Power sweep performed with the VNA on the two resonances of the IFN3 chip; (middle) the two resonances fitted for best power value, and (bottom) the corresponding fitted resonance parameters.*

where ΔP, ΔS and ΔN are the differences in incoming power, observed signal and square root of the noise power spectrum, respectively. The signal and noise are experimentally measured (fig. 5.20). The noise spectra of the signals with different background illumination conditions are shown in fig. 5.19. The difference in incoming power can be calculated using

$$\Delta P = A\Omega \int_{\Delta\nu} \left[BB\left(300K\right) - BB\left(77K\right)\right] t_{300}\left(\nu\right) t_{240}\left(\nu\right) t_{150}\left(\nu\right) T_{lens1} T_{lens2} T_{window} d\nu \ ,$$

where

- t_{300} is the transmissivity of the LP filter at 300 GHz (previous par.);
- t_{240} is the transmissivity of the LP filter at 240 GHz (previous par.);

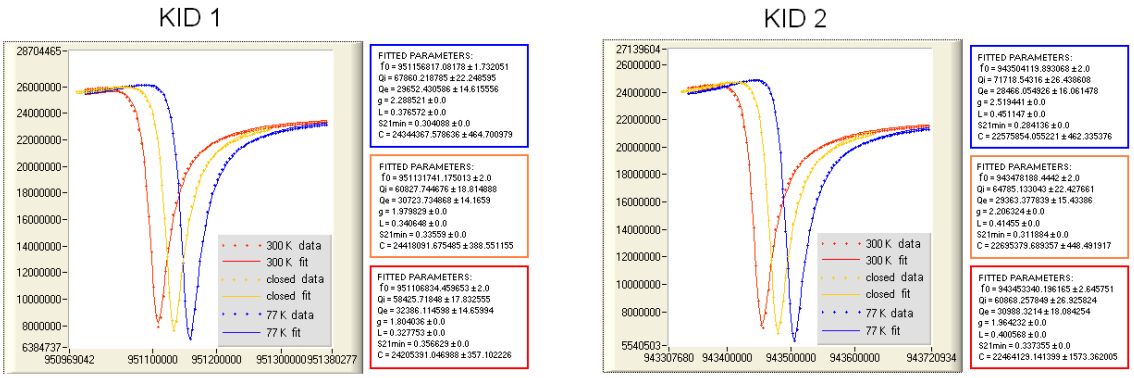

Figure 5.18: *Frequency sweeps of the IFN3 resonances with three different optical loads (BB at 300K, BB at 77K, cryostat with closed window).*

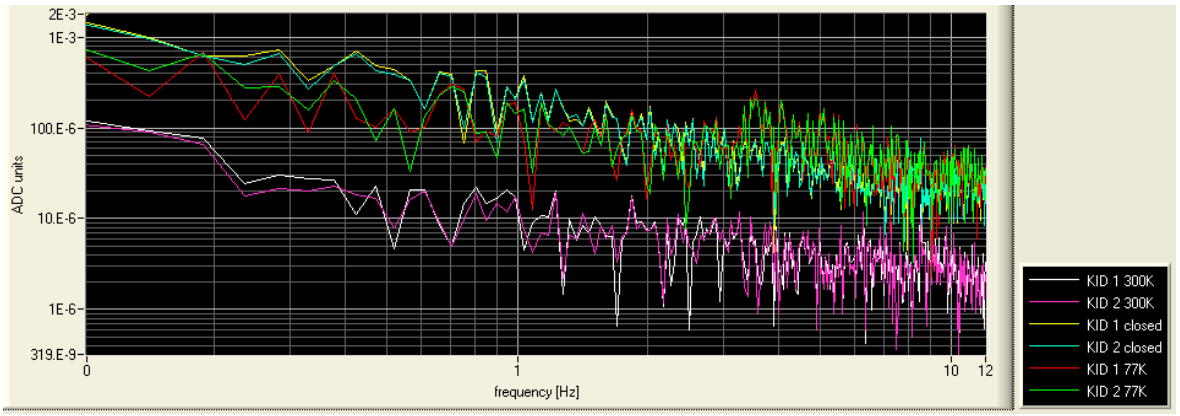

Figure 5.19: *Example of a measure of the noise power spectrum performed on the IFN3 chip, for the same three different optical loads of fig. 5.18.*

Measure	Amplitude		Phase	
	Kid 1	**Kid 2**	**Kid 1**	**Kid 2**
S (300 K)	4 356 964 DAQ	4 099 612 DAQ	2.72096 rad	3.47788 rad
S (77 K)	10 974 256 DAQ	11 592 063 DAQ	1.918444 rad	1.358617 rad
N (300 K)	20.0 DAQ/$\sqrt{\text{Hz}}$	20.0 DAQ/$\sqrt{\text{Hz}}$	2.0×10^{-5} rad /$\sqrt{\text{Hz}}$	2.0×10^{-5} rad /$\sqrt{\text{Hz}}$
N (77 K)	1.0×10^{3} DAQ/$\sqrt{\text{Hz}}$	1.0×10^{3} DAQ/$\sqrt{\text{Hz}}$	4.0×10^{-5} rad /$\sqrt{\text{Hz}}$	4.0×10^{-5} rad /$\sqrt{\text{Hz}}$
$\Delta S/\Delta N$	$6.752 \times 10^{3}\sqrt{\text{Hz}}$	$7.645 \times 10^{3}\sqrt{\text{Hz}}$	$4.013 \times 10^{4}\sqrt{\text{Hz}}$	$1.060 \times 10^{5}\sqrt{\text{Hz}}$

Figure 5.20: *Table of the measured signals and noise from the IFN3 chip. The measures have been performed either on the amplitude signal and on the phase signal calibrated with respect to the center of the resonance circle. The data highlight the higher responsivity of the latter.*

- t_{150} is the transmissivity of the BP filter centered at 150 GHz (previous par.);
- T_{lens1} is the transmissivity of the first lens at $40K$:

$$T_{lens1} = 1 - R \qquad \text{where} \qquad R = \left(\frac{n-1}{n+1}\right)^2$$

  and $n = 1.55$ is its refractive index;
- T_{lens2} is the transmissivity of the second lens at $200mK$ with refractive index $n = 1.56$;
- T_{window} is the transmissivity of the window at $300K$ with refractive index $n = 1.51$;
- $A\Omega$ is the system *throughput*:

$$A\Omega = \pi \left(\frac{d_k}{2}\right)^2 2\left\{1 - \cos\left[\arctan\left(\frac{d_L}{2d}\right)\right]\right\} ,$$

  where $d_L = 17.6mm$ its the illuminated diameter of the lens $200mK$, $d_k = 3mm$ its the lateral dimension of the KID, and $d = 8.8mm$ is the distance of the detector from the lens at 200mK.

The resulting difference of incoming power is

$$\Delta P = 7.93 \cdot 10^{-11} W$$

so that the final Noise Equivalent Power are $NEP_{KID1} \approx 2 \cdot 10^{-15} W/\sqrt{Hz}$ and $NEP_{KID2} \approx 7.5 \cdot 10^{-16} W/\sqrt{Hz}$ (fig. 5.21). We can also calculate the Noise Equivalent Temperature (NET), defined as the minimum variation of the BB temperature that can be detected over the detector noise in a 1Hz bandwidth

$$NET = NEP \frac{\Delta T}{\Delta P} \frac{e^x - 1}{x e^x} \tag{5.3}$$

with $x \equiv \frac{h\nu_c}{k_B \Delta T}$, and ν_c the band central frequency. The corresponding NET values are $NET_{KID1} \approx 5.5 \cdot 10^{-2} K/\sqrt{Hz}$ and $NET_{KID2} \approx 2 \cdot 10^{-3} K/\sqrt{Hz}$.

Measure	Amplitude		Phase	
	Kid 1	**Kid 2**	**Kid 1**	**Kid 2**
NEP $\left[\mathrm{W}/\sqrt{\mathrm{Hz}}\right]$	1.174×10^{-14}	1.037×10^{-14}	1.976×10^{-15}	7.482×10^{-16}
NET $\left[\mathrm{K}/\sqrt{\mathrm{Hz}}\right]$	3.251×10^{-2}	2.872×10^{-2}	5.471×10^{-3}	2.072×10^{-3}

Figure 5.21: *Noise Equivalent Power (NEP) and Noise Equivalent Temperature (NET) calculations.*

5.5 Conclusions and future perspectives

The AstroKID experience has been a very positive test bench. The preliminary 'dark' measurements of the quality factors for arrays fabricated on silicon substrates with different resistivities allowed us to validate the manufacturing process and the material quality of a new supplier company, the IFN in Rome. Successively, the will to extend the measurements to optical radiation has encouraged us to conceive and design an almost fully refurbishment of the existent dilution cryostat in our G31 laboratories in Rome. Although many aspect of the experimental setup can be surely improved, the dedicated laboratory setup that we have built up has demonstrated the capability of detectors calibration and to perform optical measurements. In this sense, the optical upgrade of the cryostat has been a decisive effort. Thank to this first design, we have gained an essential experimental tool in order to assess the optical capability of our KID arrays. The optical and mechanical refurbishment of the inner components of the cryostat has marginally perturbed the dilution process, slightly spoiling the refrigerator performances. The analysis on the thermal load has shown that this degradation must be attributed to several non-definitive mechanical and optical elements. We save the possibility to enhance the cryogenic performances improving or substituting these items in the next future:

- better thermal contact between the sample holder and the 100mK stage;
- introduction of a second thermal shader operating at 50K, whose use was strictly recommended by the supplying company;
- reduction of the thickness of the fiberglass tubes or substitution with a lower thermal conductivity material. In alternative, an intermediate thermal link on the $400mK$ stage should reduce sensibly the thermal load on the 100mK.

The main goal of demonstrating the capability to perform routine characterization and calibration procedure of KID arrays has been successfully achieved. The *NIXA* readout electronics and the *sNelloX* acquisition software, previously developed in Grenoble for initially different purposes, have worked praiseworthily proving their reliability and versatility. The first example is provided by the measurement of the energy gap of a 40nm aluminum detectors. The measured gap value is $\Delta = 198.5\mu eV$, with the corresponding cut-off frequency on the incoming radiation detected at $\nu_{gap} \approx 96GHz$. The second important result is the multiplexed measurement of the optical NEP of the IFN2 two-pixels array. The acquisition software procedure of detector calibration has enabled a more reliable estimation of its value, that amounts to $\sim 2 \cdot 10^{-15} W/\sqrt{Hz}$ and $\sim 7.5 \cdot 10^{-16} W/\sqrt{Hz}$. It is worth to stress that the experimental setup that we used has to be consider only a demonstrator version. As shown in this chapter, the current test bench has wide possibilities of improvement, so that

the NEP estimation must therefore be taken as an upper limit. Although very preliminary, the start-up operations of the AstroKID project led to a full functionally KID readout multiplexed instrument. The steps of the following phase will be focused on the improvement of the cryogenics and optic performances of the system, refining the cryostat design and the KID array geometry.

Part III

High-energy interactions in Kinetic Inductance Detectors arrays

Kinetic Inductance Detectors are suitable for many different applications. As illustrated in chapter 4, arrays of KIDs have demonstrated state-of-the-art performance in ground-based mm-wave instruments. The understanding of the physics of KIDs and the implementation of appropriate readout techniques have reached maturity, opening the path to the investigation of new possible applications. The most natural prosecution in millimeter astronomy is the extension of the KID technology to satellite-borne telescopes, requiring high-sensitivity thousand-pixels cameras for the post-Planck Cosmology experiments. Among the most challenging issues is the minimization of the observational time losses due to the high rate of cosmic ray impacts. Besides this, over the last five years the scientific community has spent some efforts in order to extend KID use to the next generation rare-event searches in Particle Physics, such as the direct detection of Dark Matter or neutrinoless double-beta decay. In this case, the scientific challenge is to provide an high-energy resolution tool such as to enable efficient background rejection. Although these two experimental applications are dedicated to very different fields of research, they share the same interest for the study of the high-energy interactions in KID arrays.

The main challenge in the detection of high-energy particles in a KID is related to the intrinsic difficulty of obtaining their direct absorption in a metal film few tens of nanometers thick. In order to get reasonable absorption coefficients, the thickness of the superconductor should be enhanced at least to some microns, killing the responsivity of the detectors (par. 2.6.3). A different approach consists in using the substrate as an absorber. An incoming particle hitting the detector array can releases energy into the substrate through ionization. The detectors can sense this energy through the so-called *phonon-mediated detection* (fig. 5.22). In the currently accepted theory of phonon generation, particle interactions create high-frequency optical phonons which rapidly ($< 1ps$) decay to acoustic phonons of order of the Debye frequency, $\sim 13.4THz$ in Silicon. Then, they branch into lower-energy phonons by anharmonic decay. After the phonons have propagated $\sim 1mm$ (in Si), the energy spectrum is roughly Gaussian and centered at $\sim 1.2THz$ ($\sim 58K$). We refer to them as *athermal phonons*, as their spectrum differs from that expected for Si at sub-Kelvin temperatures (*thermal phonons*). In a high-purity semiconductor at these temperatures, mean free path (m.f.p.) for the athermal phonons depends on their energy, the ones that has down-converted to lower frequencies having a long m.f.p. due to the absence of scattering with thermal phonons. In particular, if an athermal phonon has a m.f.p. large enough to propagate across the crystal with few or no additional scatterings, it is termed *ballistic* [118]. The rest of athermal phonons have a diffusive behavior, since they undergo many scatterings with each others: we call them *hot phonons*.

The athermal energy transport in silicon wafer is thus mediated by hot and ballistic phonons. Despite the largest part of the energy being stored in the hot diffusive component, this can propagate only over few mm. On the contrary, the ballistic phonons can easily prop-

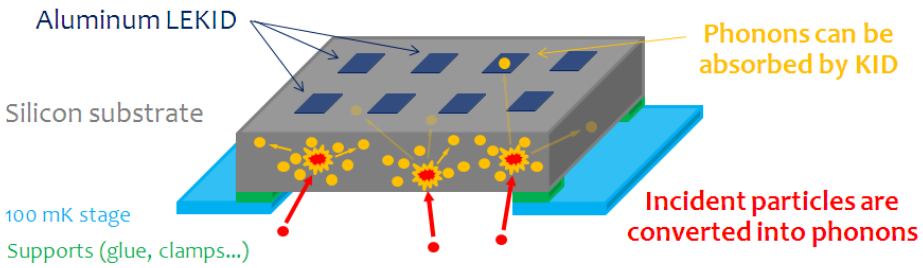

Figure 5.22: *Schematic representation of the phonon-mediated detection mechanism.*

agate far from the original particle interaction point, as they only undergo residual scattering with impurities of the substrate and its interfaces. If a phonon encounters an interface with another material, such as the Aluminum of a KID, there is a given probability that it is transmitted into this layer. Through this mechanism, a phonon with energy exceeding the gap can break Cooper Pairs and produce a detectable signal.

The efficiency of the phonon-mediated particle detection process (*pair breaking efficiency*, η_{pb}) is limited for several reasons: 1) not all the energy of the incident particle is converted into phonons; 2) only a fraction of the total phonon energy can propagate far from the impact point; 3) the conversion of this energy into quasi-particles will occur with a given efficiency; 4) not all the phonons can be sensed, but only the fraction with an energy exceeding the gap of the superconductor. All these factors can play in our favor in order to minimize the effect of the strong high-energy particles background in space environments. At the same time and despite these limitations with respect to bolometers in order to perform high precision calorimetric measurements, it has been shown that sub-keV resolution can be achieved using this same approach [45]. Finally, phonon-mediated KID could be used to resolve the position of the particle impact [46] and to study the energy propagation inside the substrate [48]. In the following we present our laboratory measurements deploying the phonon-mediated detection techniques devoted to the study of high-energy interactions in KID arrays.

Chapter 6

Cosmic Rays effect on KID arrays: the SPACEKIDS project

The SPACEKIDS project is driven by an European collaboration involving Cardiff, SRON, Delft, Grenoble and Madrid. Its purpose is to develop and demonstrate the capabilities and the suitability of Kinetic Inductance Detectors for use in future space missions at far infrared to millimeter wavelengths. Reaching photon noise limited performance at the lowest background loading powers, typical in space environments, requires significant development of detectors and materials. SPACEKIDS address the areas of KID development which are crucial for adapting this technology for use in space-based instruments:

1. Electromagnetic design of KID arrays to increase the multiplexing ratio and uniformity of responsivity.

2. Optimization of KID performance in the presence of cosmic ray flux representative of a space environment.

3. Optimization of KID sensitivity and optical coupling for different levels of optical loading and wavelength coverage.

4. Demonstration of wide band FPGA based digital electronics coupled to large format KID arrays.

The next two chapters concern mainly the work carried out for the objective 2.

One of the most challenging problems for space-borne experiments is that the detectors are exposed to an intense flux of high energy particles, referred to as Cosmic Rays (CR) [119]. As demonstrated by the Planck satellite [120], the impacts of CR on the detectors are a key problem for space based missions. The glitches caused by CR hits can mask the real data and lead to the loss of an important fraction of the observing time. Even worse, small amplitude glitches could remain hidden in the noise introducing an additional non-gaussian component.

In order to recover a clean time trace, the identification and characterization of the CR signals is mandatory for the deglitching process.

Before proposing a new technology such as KID for a satellite-borne applications, the problem of the CR hitting detectors during in-flight operation has to be studied in detail. Our understanding of KIDs susceptibility to CR in our arrays is relatively mature. The following three chapters describe the current knowledge we have gained of such high-energy interactions in the substrate supporting the resonators array. We have set up a dedicated test-bench, including the NIXA high-speed multiplexable electronics and the fully-automated acquisition software entirely developed by our collaboration and described in chapter 3. We present here several tests carried out with KID exposed to secondary CR and radioactive sources. We also report the results obtained adopting different solutions in terms of substrate materials and array geometries.

6.1 The Cosmic Rays issue

Any instrument working outside the Earth's atmosphere is constantly exposed to an intense flux of primary CR. These high-energy particles are produced by the Sun and by other galactic sources. CR are composed primarily by protons ($\sim 90\%$), with an important contribution of helium nuclei ($\sim 10\%$), and a few heavier nuclei ($\sim 1\%$) and electrons ($< 1\%$). The CR spectrum is peaked around $\sim 200MeV$ and decays with a power law at higher energies [121]. Considering this rapid decay, the bulk of the CR flux is composed by lower energy particles. The actual intensity of this flux, and the consequent rate of hits on the instrument, is modulated by the solar activity. The particles having sufficient energy to penetrate the satellite shields can reach the detectors and give an unwanted signal.

Charged hadrons like cosmic rays interact with matter essentially through ionization. Being much more massive than electrons, CR lose only a fraction of their energy in collisions with the atomic electrons and are only slightly deflected by them. Consequently, these heavy particles travel following nearly straight lines through matter. Because of the small, gradual amount of energy transferred from the impinging ion to the absorber material, the particle passage may be treated as a continuous slowing down process. The energy deposited is given by the Bethe-Bloch formula

$$-\frac{dE}{dx} = \frac{4\pi}{m_e c^2}\frac{nz^2}{\beta^2}\left(\frac{e^2}{4\pi\epsilon_0}\right)^2\left[ln\left(\frac{2m_e c^2\beta^2}{I(1-\beta^2)}\right)-\beta^2\right] \tag{6.1}$$

where n is the electron number density of the target material, I is its mean excitation potential, and z and βc are the charge and the speed of the particle. Considering that the most of CR have $200MeV$ or lower energies, this corresponds roughly to a deposited energy of 0.5 keV

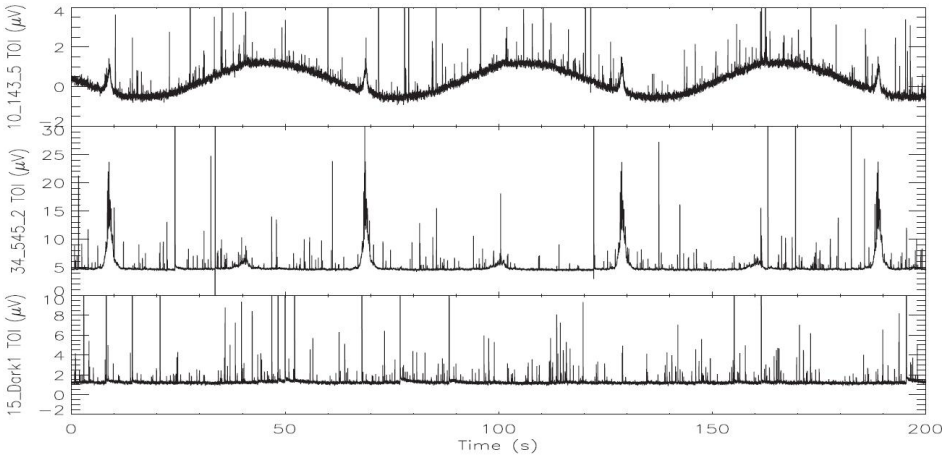

Figure 6.1: *Example of Planck time traces. Raw TOIs (Time-Ordered Informations) for three bolometers, 143GHz (top), 545GHz (middle), and a Dark1 bolometer (bottom) over three rotations of the spacecraft (at 1rpm). The typical maximum amplitude of a spike is between 100 and 500 μV depending on the bolometer. The typical rate is one event per second per detector.*

per μm traversed for a silicon target.

The energy released by a CR hit is followed by a lapse of time during which the detector is 'blind' to the incoming scientific signal. The length of this effective dead-time depends on the intrinsic time constant of the sensor, which in turn depends on the physical processes that convert the deposited energy into a measurable physical quantity.

6.2 Bolometer response to Cosmic Rays

Bolometers are thermal detectors; the optical power is first converted into thermal phonons and then transduced by a suitable thermistor into a measurable electrical signal. As far as the interactions with CR are concerned, this has two main consequences: 1) all the energy released by the CR can be sensed, and 2), bolometers exhibit relatively slow time constants. This response time is primarily determined by the thermalization of the energy released by the incident radiation, which essentially depends on the thermal contact between the thermistor and the temperature bath. In order to match high sensitivity requirements for space born missions, this contact has to be very weak, resulting in slow response times. These span from tens of milliseconds to several seconds depending on the type of interaction, on the hit point and on the propagation mechanism of the deposited energy to the thermistor.

The Cosmic Rays impacts have been one of the main problems during the reduction of the data taken by the Planck satellite mission [120]. The total amount of data lost due to CR impacts calculated by the Planck collaboration varies between 8% and 20%, larger

than what was expected (fig. 6.1). Due to the instrument shielding, only protons with energy exceeding $\sim 40MeV$ are able to reach the focal plane and induce a signal in the detectors. Considering the CR spectrum [121], this cut-off energy would translate in a rate of about $5events/min/mm^2$, modulated by the solar activity. Planck detectors were spider-web bolometers, in which the sensitive element, an NTD (Neutron Transmutation Doped) thermistor, had a small surface area ($0.03mm^2$ for normal incidence). Assuming that only the impacts on the thermistor itself or on the spider-web structure (around $0.1mm^2$) are able to cause a glitch in the data, this means that the expected event rate on Planck's detectors was roughly $0.5events/min$.

The rate actually observed in flight was 100 times higher, of the order of $1Hz$ [122]. This excess of glitches can be accounted for if also the CR interacting with the silicon die holding the spiderweb are sensed. In fact, each CR hit creates a cascade of high-energy phonons; a part of them, the ballistic phonons, can propagate rapidly ($\sim mm/\mu s$) and over large distances in the substrate, being reflected at each interface. Ballistic phonons then decay within hundreds of microseconds into thermal ones. Several laboratory and accelerator experiments following the Planck launch confirmed this [123], demonstrating that ballistic phonons can transfer part of the energy released by a CR hitting the silicon die through the spider-web absorber and into the NTD thermometer. Here the energy can be thermalized and induce a signal. The spider-web structure is therefore not enough insulating to suppress the unwanted signals coming from the silicon die. This means that, when estimating the CR events rate, also the surface of the silicon side-structure must be taken into account, explaining the increased observed rate. In Planck, the silicon die has an area between 0.4 and $0.8cm^2$, depending on the working frequency. If, as it has been suggested, every cosmic particle hitting the die is seen by the thermistor (through ballistic phonons mediation), from the total rate of glitches observed in Planck ($\sim 1Hz$) we could estimate the integrated rate of CR per unit surface of $1event/s/5 \cdot 10 - 5m2 = 2 \cdot 10^4 events/s/m^2$. This will be an important figure representative also for future space mission placed at Lagrangian point L2.

6.3 Estimating Cosmic Ray effect on KID

The operating principle of Kinetic Inductance Detectors is completely different compared to bolometers. The KID are pair-breaking detectors, sensitive to variations of the Cooper pair density in a superconductor. A signal can be induced into the detector only by particles able to release an energy higher than the binding energy of each Cooper pair, $2\Delta_0 \approx 3.5k_BT_c$ (eq. A.7). This makes the KID insensitive to phonons of energy below $2\Delta_0$. Only high energy phonons can cause a signal, and as soon as these decay to energy levels below the gap, they become, at the first order, invisible to the KID. For hot phonons the energy down-conversion occurs over very fast time scales, and they can only cover short distances before becoming

undetectable. On the other hand, ballistic phonons can propagate over long distances before losing their energy through scatterings with the die edges or with the impurities present in the substrate lattice [46]. This can lead to a glitch even in detectors far from the impact point. The energy down-conversion of the phonons depends on the geometry and on the properties of the substrate. Since the decay of the hot phonons below the gap is very fast, the phonon lifetime that we observe experimentally is essentially due to the ballistic ones. This is described by the time scale τ_{ph}, typically of the order of hundreds of microseconds for crystalline silicon [45]. The time evolution of a CR event in a KID is also determined by the quasi-particle recombination time, or quasi-particle lifetime τ_{qp}, described in paragraph 2.1.4. The time constants governing the KID behavior can be experimentally measured, although discriminating between the effect of quasi-particles and phonons lifetimes is not straightforward [74]. It has been shown that for very low-temperature aluminum KID fabricated on silicon substrate, the dominant time constant is of the order of fractions of millisecond [45], much faster than in the case of bolometers. This means that in general for the same CR event rate, less data are lost when using KID. For a preliminary estimate, we can compare the typical expected performance of a KID array with respect to a single Planck bolometer. The surface area of a typical NIKA-like array of LEKID ($\sim 100 \div 200$ pixels) operating at millimeter wavelength [89] [40] is roughly $13cm^2 = 1.3 \cdot 10^{-3}m^2$. The total rate of particles hitting the array should be, in the case of KID, of the order of 20 times higher than a single Planck pixel, i.e. $20events/s$. Assuming KID with a time constant of 0.1 ms, this translates in a data loss analogue to that of a single Planck pixel, i.e. about 15%.

6.4 The experimental setup

We have developed a dedicated test-bench to validate the technologies currently in use and the different solutions that can be adopted to mitigate the effect of CR impacts. In the following we will give a brief description of the main components of our experimental setup.

6.4.1 Cryostat

The cryostat, named *Sionludi*, is a two-stage cooler system with a base temperature of $\sim 100mK$. Liquid helium is used to reach 4K, while the sub-Kelvin cooler stage is provided by a $^3He/^4He$ dilution refrigerator. The radiation shields at the various temperatures are equipped with optical windows in order to be able to perform measurements under varying optical loads. The cryostat has two independent RF channels, each one equipped with a cold low-noise amplifier optimized for the working frequencies of our detectors. See figure 6.2(a).

(a) (b)

Figure 6.2: *(a) An image of the* Sionludi *dilution cryostat inner part. Each plate is cooled down to temperature decreasing upwards, reaching the base temperature at the top. Two arrays are mounted and ready to be tested. (b) A photo of the full test-bench including the cryostat with the liquid ^4He tank and the electronics rack. From the top, the warm amplifier (WA), the voltage generator for the Low Noise Amplifier (SiGe CITLF4 Cryogenic LNA) mounted in the cryostat, the Local Oscillator (LO), the FPGA electronics, the vacuum pumps and the data acquisition PC.*

6.4.2 Fast readout electronics

The readout is based on the NIXA high-speed electronics developed within our collaboration (3.3-3.3.2). Briefly, the board can excite and readout up to 12 tones simultaneously over a 100 MHz bandwidth; a custom internal threshold can be set for each tone and the data sampling rate can be varied from 500ksps up to 2Msps. Fig. 6.2(b) shows a photo of the electronics rack in our experimental setup.

The acquisition data process typically follows these steps (par. 3.4.1 for more details):

- Make a frequency sweep to localize the resonances and calibrate the relation between frequency and phase of the excitation tone;
- Place the tone on each resonance;
- Fix a specific threshold for each tone;
- Acquire the data.

When energy is absorbed in the detector the resonance will shift to lower frequencies. Since the tones are placed on the resonance, a positive spike in the transmitted amplitude (S_{21}) will be observed. If the spike exceeds the fixed threshold, the FPGA considers it as an 'event',

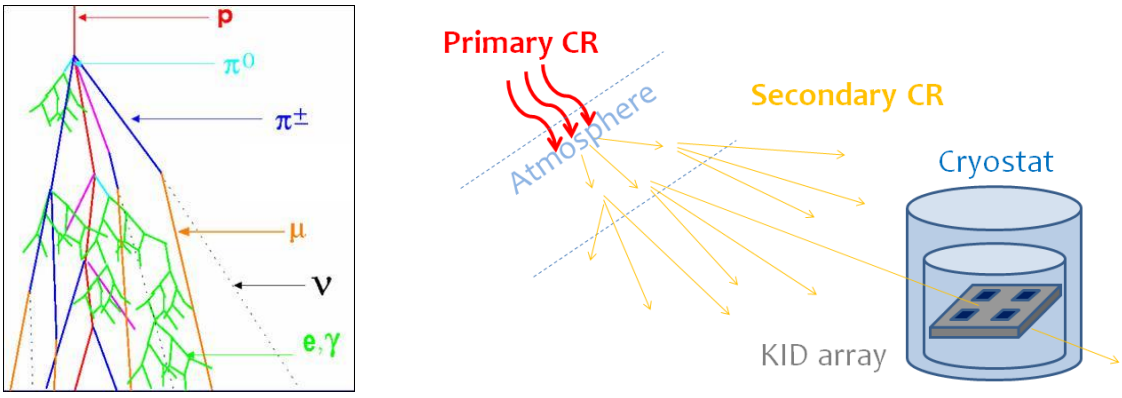

(a) (b)

Figure 6.3: *(a) A simple scheme of high energy particle showers produced by cosmic rays interaction in the atmosphere. A proton (red) collides with a molecule in the atmosphere and produces neutral (cyan) and charged (blu) pions. They can decay in positron-electron pairs and X-rays (green), with a relevant component of muons (orange) and neutrinos (dashed black) that can reach the ground. (b) Schematic representation of the experimental setup using atmospheric muons.*

records the data for a fixed amount of time and transmits them over an ethernet connection to the acquisition PC. Each time that at least one of the tones exhibits an event, the data are acquired simultaneously for all the tones. This allows us to check for coincidences among different pixels. Furthermore, it prevents us from missing the events in pixel far from the impact point. These exhibit a smaller signal and thus a lower SNR.

6.4.3 Lumped Element KID

All our detectors are designed and fabricated at the Institut Néel and were conceived primarly for millimeter astronomy purposes. Building on the NIKA experience, they are based on Lumped Element KID with an Hilbert geometry (par. 4.2.2). They are fabricated out of a single, thin (e.g. $15 \div 18nm$) aluminum film.

6.4.4 Secondary Cosmic Rays

Secondary Cosmic Rays are by-products of interactions of primary CR in the atmosphere. When CR enter the Earth's atmosphere, they strike atom's nuclei, mainly oxygen and nitrogen. The interaction produces a cascade of lighter energetic particles, commonly referred to as *secondary Cosmic Rays*. Typical particles produced in such collisions are neutrinos and charged mesons such as positive or negative pions and kaons [124]. Some of the latter subsequently decay into *muons*, a negatively charged particle with a tenth of the mass of proton. Although being unstable (lifetime $\sim 2.2\mu s$), energetic muons can cover distances of

kilometers before decaying. Thanks to the relativistic time dilatation, the most energetic ones ($> 2GeV$) can reach the sea-level with enough residual energy to penetrate for some distance into the ground. These muons ionize the traversed matter following eq. 6.1 and thus releasing $\sim 0.5keV/\mu m$ of traversed Silicon. As a consequence, these interactions can be used to mimic the primary CR interactions in space. The rate of secondary CR at sea-level, being issued of multi-GeV primaries, is $\sim 200events/s/m^2$ [125], about a factor 100 lower compared to the rate measured at L2 by Planck, $2 \cdot 10^4 events/s/m^2$ (par. 6.2).

In the following we present the preliminary measurements performed using secondary CR interacting with NIKA-like arrays. The results gave us useful indications for the prosecution of the work.

6.5 Secondary CR on NIKA-like arrays

Our main goal is to determine the effect of a CR on nearby and far away pixels on the same array. The first preliminary data have been taken on an array used for the NIKA experiment. In figure 6.4(a) we show a table with its main characteristics. This approach is not ideal under many aspects, especially because it is impossible to readout at a fast rate all the pixels of the array. Nevertheless, we decided to perform these measurements in order to get indications about the strategy to follow in the next set of experiments, better suited for the high-energy interaction study. As already said, our electronics can readout at high sampling rates (up to 2MHz) a maximum of 12 pixels, over a the total bandwidth of about $100MHz$. We thus selected 8 KID on the array, whose positions were determined thanks to previous optical characterization of the array in the NIKA cryostat [89] [91]. The pixel is shown in figure 6.4(b). If all CR events hitting the array are detected, we have a sensitive area of $36 \times 36mm^2$. Thus we expect a CR rate of $\sim 0.25events/s$.

We observed 921 events over 64 minutes integration time, at a base temperature of $\sim 100mK$. The average measured CR rate was of about $14events/min = 0.23events/s$, corresponding to roughly $180events/s/m^2$, in good agreement with the expected rate at sea level. This confirm that we are sensitive to the whole surface array.

An example of the observed temporal trace for a single event as observed by all the KID is shown in fig. 6.5(a). It is evident that pairs of nearby pixels tend to respond similarly. As a consequence, each CR gives in general the largest peak amplitudes in the two KID closer to the interaction. This explains the large majority of observed events having S/N ratios between 0 and 15 (fig. 6.5(d)), that correspond to the pulses observed by the far pixels. Notice that for high signals the detectors can saturate; the transmitted amplitude ranges from his minimum (on resonance) to his maximum (off resonance) values, so that the maximum observable signal is comparable to the width of the resonances. This fact limits therefore the dynamic of the detectors.

Array	NIKA 8f2
Size of array	36x36mm²
# of pixels	132
Geometry	Hilbert LEKID
Resonating frequencies	1.3-1.8 GHz
Pixels pitch	2.3mm
Material	Al 20nm PTA
Substrate	Si HR 300um

(a)

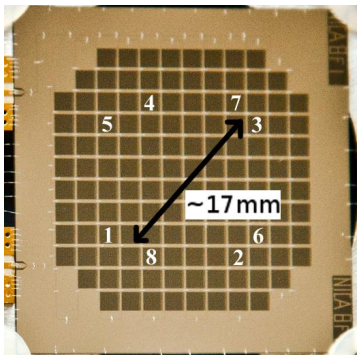

(b)

Figure 6.4: *(a) A table of the proprieties of the NIKA-like array we used for preliminary measurements; (b) a photograph of the same array, with the chosen 8 pixels highlighted.*

Plotting together all the events observed by a single pixel, we observe that different CR events can give very different pulse shapes (fig. 6.5(e)). This results from the sensitive area interacting with the phonons in the substrate, that depends on the impact angle of the CR. Choosing a sub-sample of events having similar amplitudes (high S/N but well below saturation), the traces look more similar. The fitted decay time constants on this sub-sample ranges from 150 to 700μs (fig. 6.5(f)).

Almost 50% of the observed events were seen by the totality of the selected pixels (see fig. 6.5(b)) at a level above 5σ. Fig. 6.5(c) shows the noise power spectra of the selected pixels. The KID number 7 and 8 (and to a smaller extent KID number 3 and 6), are roughly a factor of $2 \div 3$ more noisy than the others. This could prevent the detection in these KID, reducing the number of coincidences which thus might be even higher than observed. In any case, each Cosmic Ray event clearly affects a large portion of the array. The signal is detected even in pixels that are more than $\sim 15mm$ away from the impact point.

These indications confirms that further investigations are needed before adopting KID technology for space based missions.

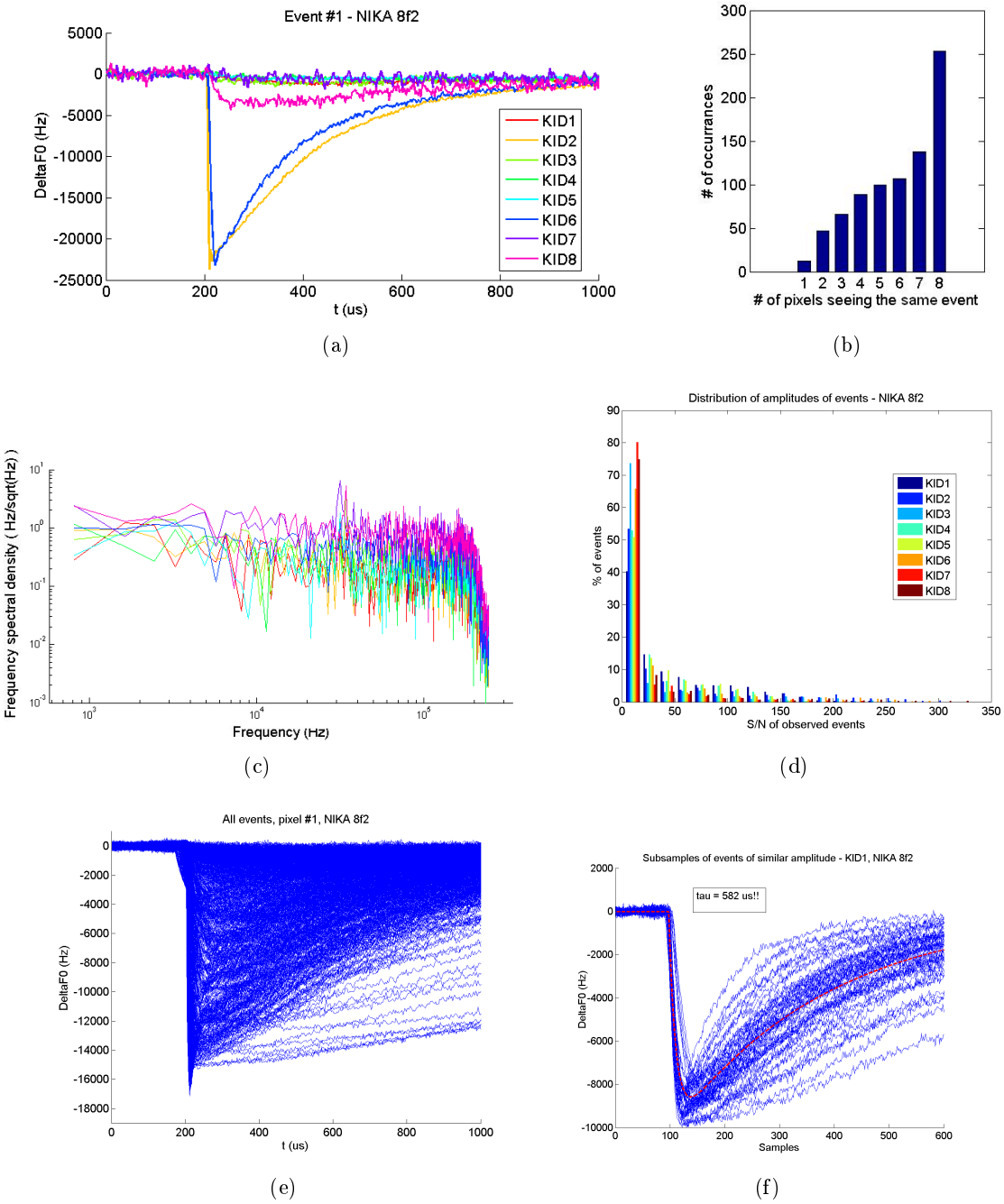

Figure 6.5: *(a) Sample time traces showing the same event seen by different KID. Pairs of nearby pixels respond in a similar way; for example KID 2 and 6 are clearly closer to the impact point of the CR. (b), Histogram of the observed coincidences. (c) Noise power spectra for all the pixels. (d) Histogram of the observed signal to noise ratios. Here the signal is represented by the peak amplitude of the sample trace. The higher noise of the KID number 3, 6, 7, and 8 reflects in a different signal to noise distribution. (e) All time traces for the KID number 1. (f) A sub-sample of event with measured peak amplitude between* $8kHz$ *and* $10kHz$*. The mean event calculated on this sub-sample is plotted in red, and exhibit a decay time constant of* $\sim 600\mu s$*.*

Chapter 7

Energy propagation in different substrates

We have started investigating the suitability of KID arrays as detectors for space based missions. Our study is devoted in particular for assessing the effect of the CR hits and to limit their impact on the final data. As shown in the previous chapter, we have realized that using the current KID array architecture could be tricky for satellite-borne missions. Few-hundred pixels arrays, like the NIKA ones, show that the effect of CR hits is sensed even in the furthest pixels. Besides affecting a large part of the array, the spikes induced by CR events decay with relatively slow time constants of the order of $500\mu s$.

This chapter is dedicated to a deeper study of the energy propagation in the substrate. We have tested in particular the use of lower resistivity substrates, the fabrication of KID on membranes, and the addition of a multilayered structure between the detectors and the substrate. We have then concentrated our efforts on arrays fabricated on full wafers made of high resistivity silicon ($> 1kOhm \cdot cm$). Thank to the use of radioactive high energy sources and the design of a dedicated KID array, we performed a more quantitative analysis on the phonon propagation, in particular investigating the effect of adding metallization layers over the substrate.

7.1 Dedicated detector arrays

For these purposes, a dedicated mask has been designed. In the following we will always refer to this mask with the acronym *SPK* (from SPaceKids). In order to provide spacing in frequency domain matching the limits imposed by our fast electronics, on each array there is a smaller number of pixels with respect to a typical array designed for astronomical applications. On the other hand, to still be able to sample the whole focal plane area, the pixels are sparsely scattered across the array. The arrays on the mask are of the same size of the NIKA-like chips,

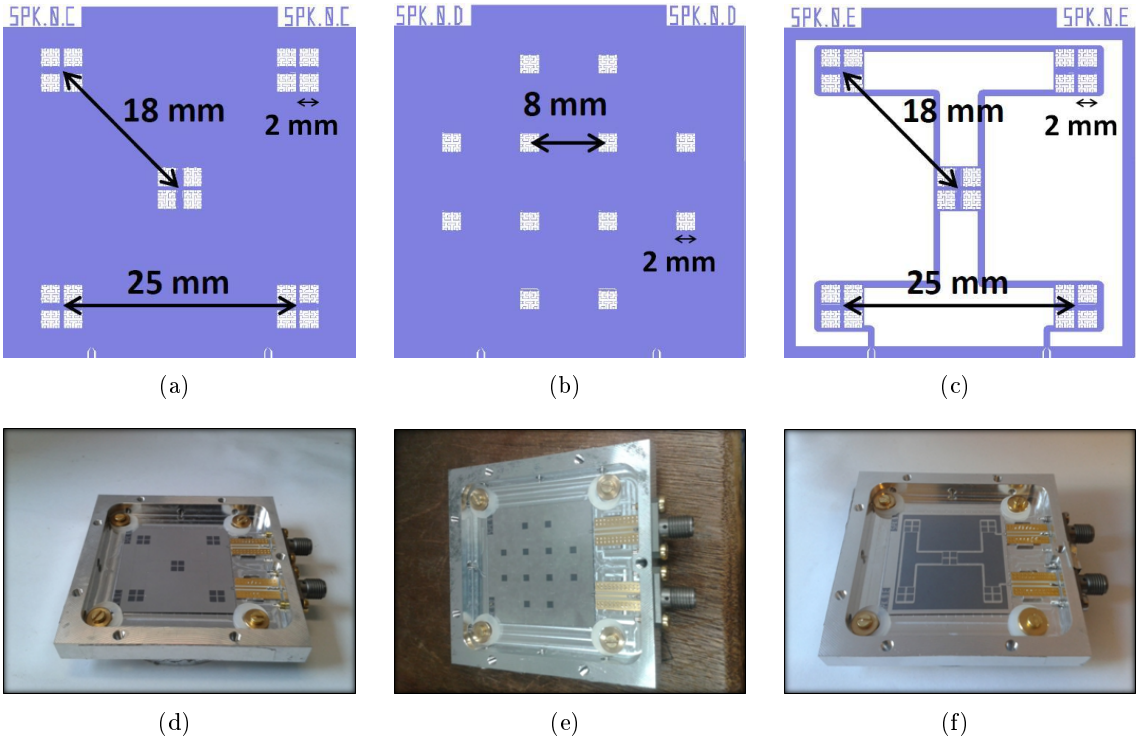

(a) (b) (c)

(d) (e) (f)

Figure 7.1: *The dedicated SPK mask. Blue is the Aluminum metallization. Hilbert LEKID pixels appears as white squares on the arrays. Starting from the left, the Island geometry array SPK-C with ground plane (a,d), the Distributed array SPK-D with ground plane (b,e), and the Island array SPK-E without ground plane (c,f). Aggiungi dimensione del pixel circa 2mm.*

$36 \times 36mm^2$, so as to share the same holders and being mechanically compatible. In order to study the energy propagation as a function of the distance from the point of impact, two main geometries have been conceived (see fig. 7.1):

- **Islands**: 5 well-spaced groups (that we call 'islands') of 4 very close pixels. This allows us to monitor the effect of the events on pixels that are very near to each other. At the same time this design allows to estimate the phonon velocity by measuring signal delays between different islands. This geometry has been designed either with a solid ground plane filling the surface of the array (SPK-C) or with the ground plane between pixels removed (SPK-E).

- **Distributed**: 12 pixels evenly spaced. This geometry is useful to sample an high number of distances from the impact point. The main goal is to fit a law for the energy decay as a function of distance. We call this array SPK-D;

This mask has been also replicated using different substrates to test their impact on the phonons propagation. In particular, we have performed measurements on substrates with

different resistivity to study how they affect the down-conversion of high energy phonons. We have also tested a multilayer coating to create a high thermal resistance, which could prevent these phonons from getting into the superconducting film (par. 7.3).

7.2 KID on thin membranes

The first solution that could be adopted to reduce the impact of CR on detectors in space is fabricating pixels on a thin membrane. This could help in two ways: 1) if a CR hits the membrane, a smaller fraction of its energy will be deposited. The signal is in fact directly proportional to the thickness of the traversed material; 2) the thin membrane could prevent a part of the ballistic phonons from entering it and thus limit their propagation. Item 2 is however unlikely considering the results found by Planck and described in 6.2.

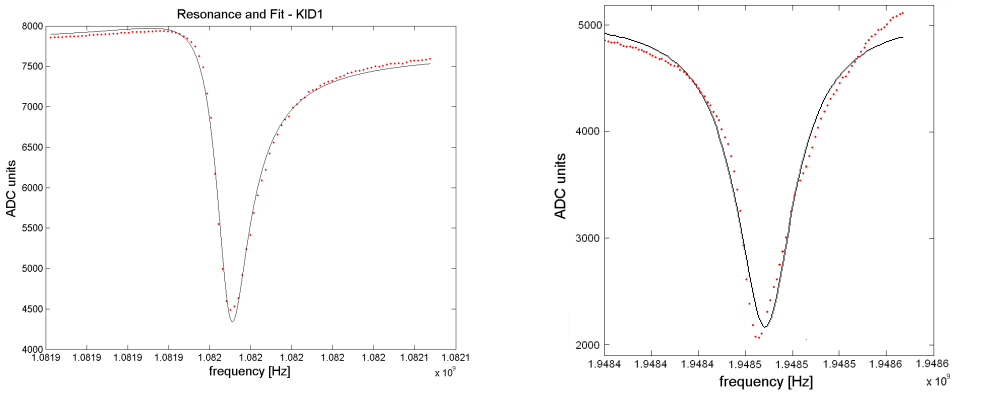

KID #	f_0 [Hz]	err f_0 [Hz]	Q_i	err Q_i	Q_e	err Q_e	Q_{tot}	err Q_tot	P	err P
full substrate	1081970047.01	114.8088	8.5618e+04	1.6183e+03	1.1737e+05	3.0662e+03	4.9505e+04	1.5962e+03	0.2057	0.0044
membrane	1948474073.13	786.8100	8.3144e+04	6.7263e+03	6.1436e+04	6.2899e+03	3.5330e+04	4.6096e+03	-0.0067	0.0003

Figure 7.2: *Resonances data (red point) and fit (black line) for KID on full substrate (left) and on membrane (right). The fitted parameters are summarized in the bottom table.*

Our data actually confirm this (fig. 7.3). The test was carried out using two pixels made on the same chip and with the same geometry. One of them lies on a full Si substrate, covered by a $2\mu m$ low-stress SiN layer. Under the second one the Si had been etched away to leave the SiN membrane suspended (see fig. 7.3(a)-7.3(b)). Fig. 7.2 shows the characterization of the two resonances.

About 100 secondary CR events were acquired at a temperature of $100mK$, with single pixel readout. The pulse shapes on the 2 pixels seem to be different (see fig. 7.3(e)). In particular, the decay time constant seems to be faster for the pixels on membrane. This is a very preliminary result, and more data should be taken to confirm this effect.

The observed rate is roughly $0.1event/min$ for both pixels, corresponding to around $4events/s/m^2$. The low rate compared to the previous test, is related to the presence of

	PIXEL 1 'full substrate'	PIXEL 2 'membrane'
Size of pixel	2x2 mm^2	2x2 mm^2
Geometry	Classical LEKID	Classical LEKID
Resonating frequencies	1.075 GHz	1.950 GHz
Material	Al 20nm PTA	Al 20nm PTA
Substrate	Si_3N_4 2um + Si HR 300um	Si_3N_4 2um

(a)

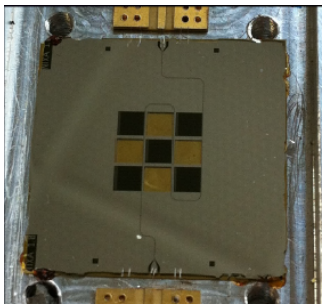

(b)

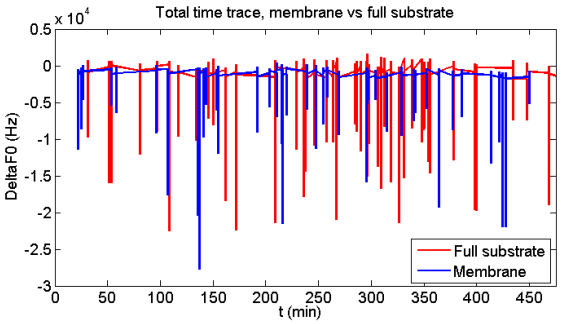

(c)

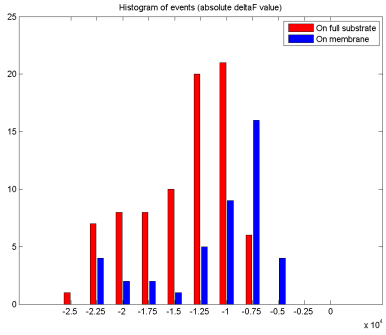

(d)

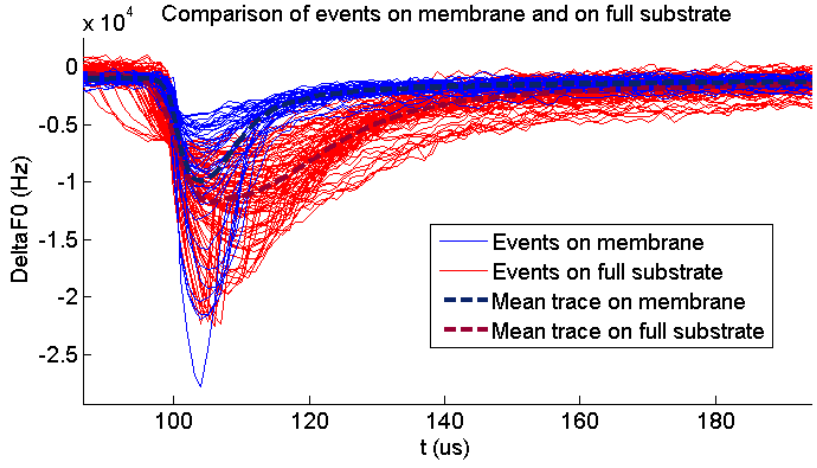

(e)

Figure 7.3: *(a) A table resuming the proprieties of the two pixels; (b) a photograph of a similar array with KID either on membrane and on full substrate; (c) the total time trace over a* ~ 480 *minutes acquisition; (d) histograms of the phase signals from the two pixels; (e) comparison between pulses acquired by the two KID.*

the SiN layer. This made the data noisier and forced us to set a considerably higher threshold. As a consequence, only large events could be observed. Furthermore, triggering on a single pixel reduces the sensitive area. Most of the events are concentrated at high S/N (fig. 7.3(d)). The fact that very few events are below S/N = 30 might be hint that effectively a too high value of threshold was chosen, contributing again to reduce the overall rate.

The most important conclusion is that basically no difference is observed in terms of rate between the two pixels (see fig. 7.3(c)). This implies that the presence of a thin membrane does not prevent the phonons from propagating from the substrate into it. This can be expected if, as we suppose, high energy phonons mediate the interaction with the CR. The athermal phonons produced are expected to have frequencies of around $1.2THz$ [118], corresponding to wavelengths of few nanometers. They can thus propagate freely in a membrane $2\mu m$ thick. The conclusion of this experiment is that pixels on a membrane of few microns exhibit the same CR event rate compared to those on full substrate. Thus, this is not a viable solution. Moreover, adding amorphous dielectrics beneath the superconducting film resulted in an excess noise that is not acceptable for high sensitivity applications.

7.3 Use of multilayer below the detectors

Another conceivable option is adding beneath the superconducting film a multilayered structure composed of very thin (few nm) layers of different dielectric materials. Each interface represents an impedance mismatch for the propagating phonons, giving a certain probability of reflecting them backwards into the substrate. It is basically similar to adding a series of Kapitza resistances. The multilayer should therefore block the high energy phonons with wavelengths of a few nm.

The first tests have been conducted with a multilayer made out of TiO_2 and Al_2O_3. 50 layers, each 4 nm thick, were deposited for a total thickness of 200 nm (see fig. 7.5(a)). These materials led to very strong dielectric losses, probably as a consequence of their strongly disordered structure, and made the detectors impossible to readout (no resonances were found).

A new test has then been made, in which the multilayer was obtained alternating PECVD (Plasma Enhanced Chemical Vapour Deposition) depositions of silicon and germanium. These materials have in principle better electromagnetic properties and should ensure lower losses. This was indeed the case, but the detectors shown nonetheless very low internal quality factors ($\sim 2 \cdot 10^4$) compared to detectors directly deposited on a HR silicon substrate (7.4). Moreover, the level of noise measured was still much higher than usual (fig. 7.5(c)). High losses and noise are in this case most probably due to TLS systems in the multilayer.

Despite non-optimal conditions we manage to detect Cosmic Ray hits. Only nearby pixels see the coincidences (fig. 7.5(b)), but once again this might be simply due to the higher noise with respect to HR-Si (see next paragraph). When observed with the SEM (Scanning Electron

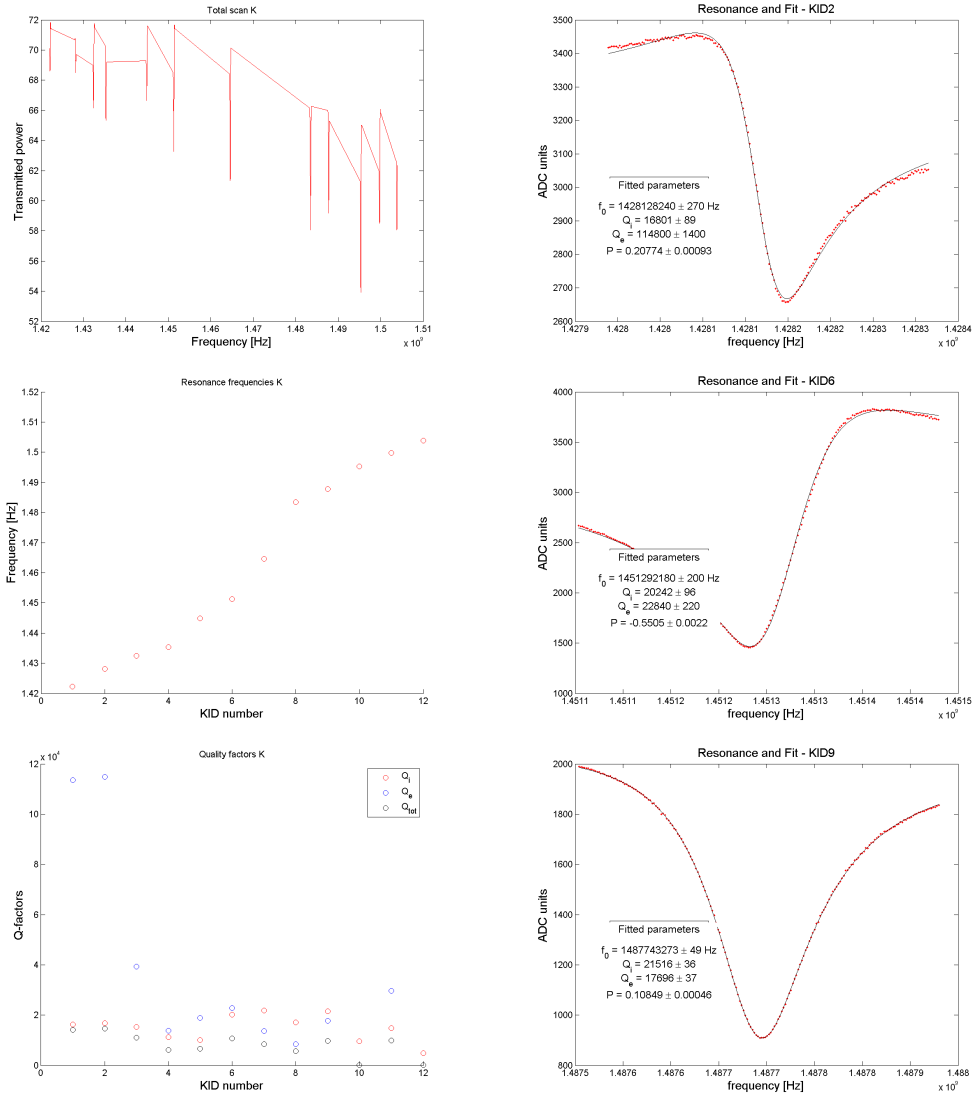

KID #	f_0 [Hz]	err f_0 [Hz]	Q_i	err Q_i	Q_e	err Q_e	Q_{tot}	err Q_tot	P	err P
1	1422142809.70	1.1316e+03	1.6434e+04	333.2101	1.1207e+05	8.2237e+03	1.4332e+04	1.0910e+03	-0.3218	1.0213e-03
2	1428128239.74	266.6615	1.6801e+04	89.2155	1.1481e+05	1.4446e+03	1.4656e+04	200.1631	0.2077	9.2721e-04
3	1432421101.40	76.2136	1.5284e+04	19.8351	3.9387e+04	142.5850	1.1011e+04	42.3454	-0.4796	5.3787e-04
4	1435279944.07	144.1712	1.1216e+04	31.3684	1.3809e+04	50.8087	6.1891e+03	28.6042	0.1398	8.6911e-04
5	1444922967.76	290.6980	1.0109e+04	36.2770	1.8921e+04	142.5209	6.5887e+03	54.9733	-0.3103	0.0014
6	1451292181.35	195.4346	2.0242e+04	96.2743	2.2836e+04	218.0327	1.0731e+04	114.4591	-0.5505	0.0022
7	1464564699.04	82.0177	2.1792e+04	57.6179	1.3705e+04	49.8955	8.4136e+03	37.8569	-0.2693	8.8298e-04
8	1483473362.43	134.3525	1.7025e+04	69.3318	8.4496e+03	42.8740	5.6470e+03	36.7402	-0.0156	0.0013
9	1487743273.46	49.1742	2.1516e+04	36.2654	1.7696e+04	37.3096	9.7101e+03	26.2099	0.1085	4.6471e-04
10	1495278950.73	6.1057e+03	9.5276e+03	719.3733	116.6119	5.4781e+06	115.2019	5.4119e+06	-4.9537	2.4948e+05
11	1499764687.99	137.8941	1.4855e+04	32.2933	2.9705e+04	209.0809	9.9029e+03	72.9506	-0.6523	0.0012
12	1503813988.40	7.2829e+03	4.9008e+03	470.5191	5.9032	1.6165e+05	5.8961	1.6145e+05	-0.2367	7.2479e+03

Figure 7.4: *Fitted parameters and calibration for KID fabricated on Si/Ge multilayer substrate (SPK-C geometry). On the left column,* sNelloX *scan of the resonances (top), their frequency spacing (middle), and the fitted quality factors (bottom). On the right column, the resonance data (red points) and fit (black line) for three KID. The KID parameters are summirized in the bottom table, together with their errors.*

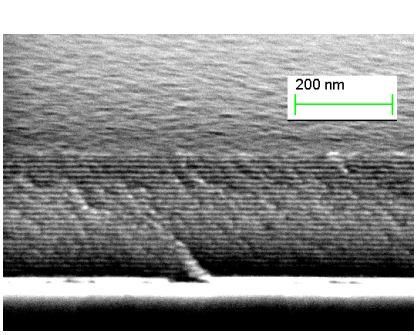

(a)

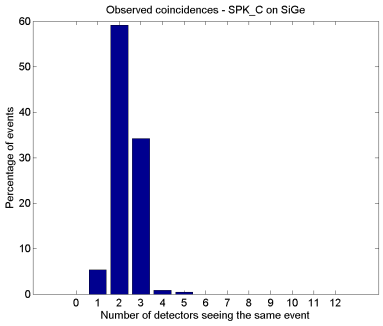

(b)

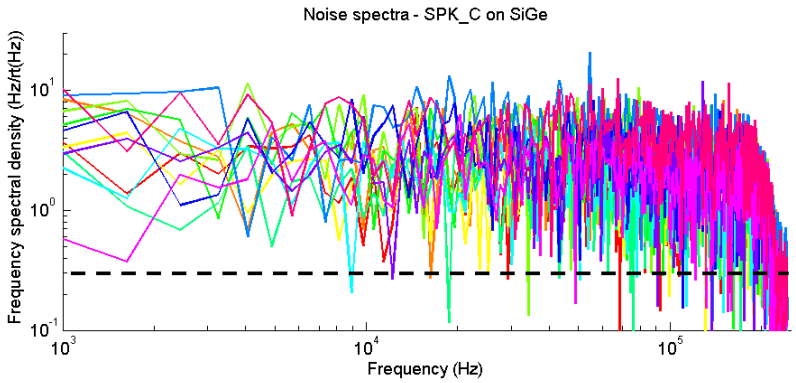

(c)

Figure 7.5: *(a) A SEM image of the Al_2O_3/TiO_2 multilayer. (b) CR coincidences observed on SiGe multilayer array. (c) Noise spectra of KID on SiGe multilayer. The measures show a noise considerably higher compared to HR-Si substrate (dashed line).*

Microscopy), the Si/Ge multilayer turns out to have a very uneven surface. This is likely due to the germanium that tends to grow forming pyramidal shapes. The irregularities on the surface might affect the performances of the detectors significantly. A possible improvement would be alternating silicon with silicon germanium, which does not show the same pyramidal structures. The Si/SiGe multilayer might therefore have noise performances in line with the standard technology, that is KID deposited on the bare substrate.

7.4 Comparison between substrate with different resistivities

A substrate with lower resistivity has a higher number of impurities in the lattice, which could act as scattering centers for ballistic phonons and enhance their thermalization. If the phonons down-conversion process governs the time evolution of the pulses, this solution should in principle make them shorter. Furthermore, impurities might decrease the distance over which the ballistic phonons can propagate, reducing the fraction of the array affected by

each impact.

First of all, we have characterized the resonances for the two arrays. The lower purity of the LR silicon affect the internal quality factors Q_i of the resonances, reducing the expected responsivity with respect to that of KID fabricated on the HR substrate (fig. 7.6). We have then observed the effect of secondary CR events using 'SPK-E' array and reading out two pixels per 'island', for a total number of 10 pixels. On a silicon substrate of low-resistivity

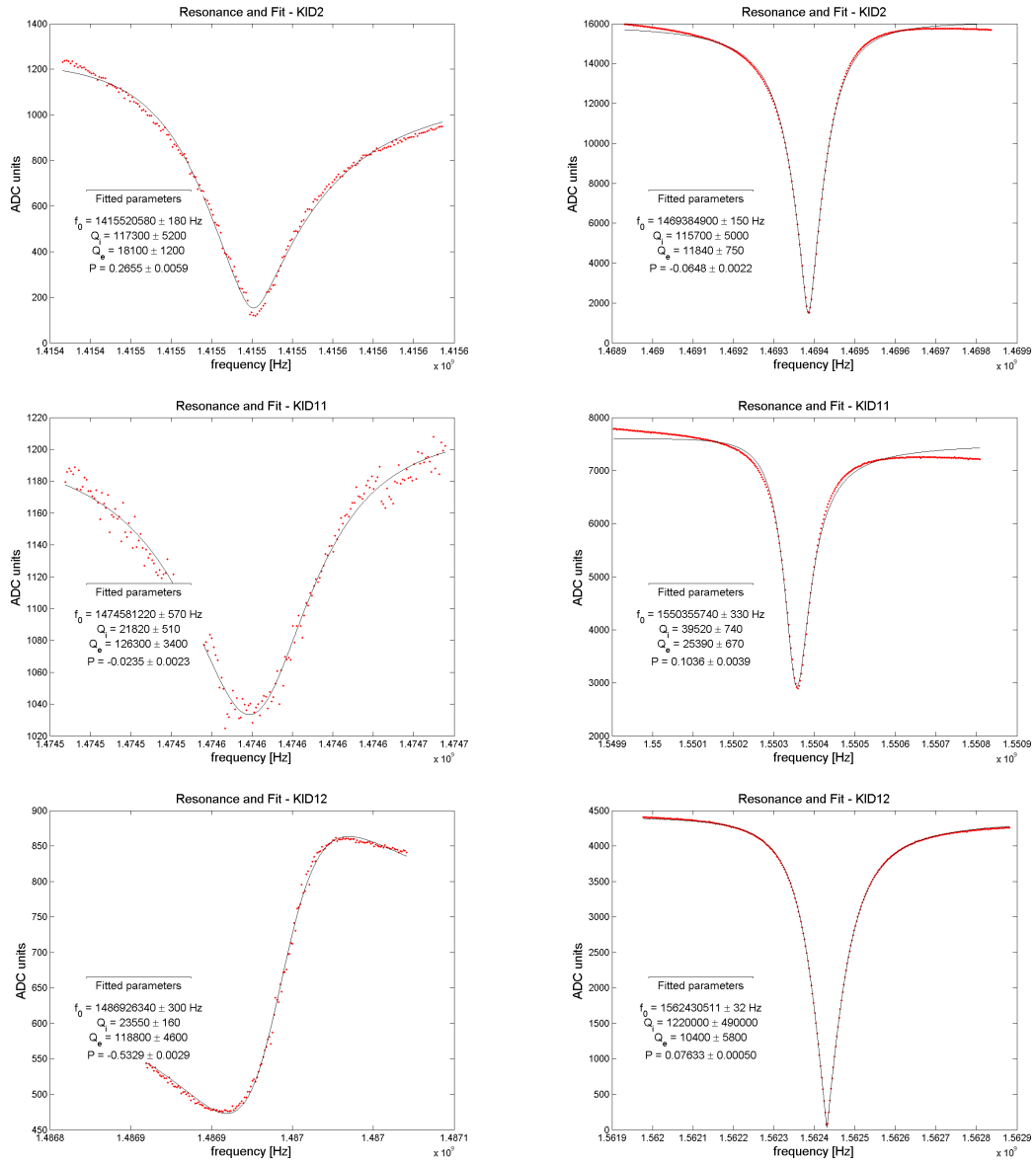

Figure 7.6: *Comparison between KID resonances with the same design (SPK-E array), but fabricated on LR* ($0.5 \div 1\Omega \cdot cm$, *left column) and HR* ($> 1k\Omega \cdot cm$, *right column) silicon substrate. The latter show higher internal quality factors.*

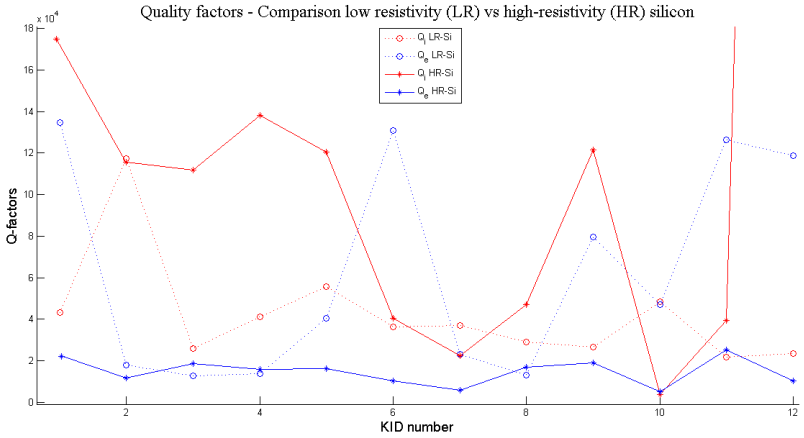

Figure 7.7: *Comparison between SPK-E arrays fabricated on LR* ($0.5 \div 1\Omega \cdot cm$) *and HR* ($> 1k\Omega \cdot cm$) *silicon substrate. The higher purity of the HR silicon means lower losses through the substrate, that in turn results in higher values of the fitted internal quality factors* Q_i *with respect to their counterpart on LR silicon. The* Q_i *of the KID number 12 exceeds* 10^5 *in the HR case. The fitted coupling quality factors* Q_e *are similar for both the arrays.*

(LR, $0.5 \div 1\Omega \cdot cm$), we could see that the number of coincidences was typically only 1 or 2 for each event (left histogram in fig. 7.8(a)). This result implies that we were able to see the same event in general only for nearby pixels and not on different islands. Yet, the noise on this array was again much higher than in the case of the high resistivity (HR, $> 1k\Omega \cdot cm$) ones (see fig. 7.8(b)). The fact that no coincidences were observed between islands might be simply due to the fact that the glitches were hidden in the noise. This would add a non-gaussian component to the noise itself, an effect that must be definitely avoided. Showing a noise ~ 10 times higher than in HR-Si, the low-resistivity substrate is not a viable solution.

7.5 Measurements with secondary CR on HR-Si substrate

To summarize the results obtained so far:

1. The thin membrane does not inhibit the higher energy phonons propagation, leaving the CR rate unchanged with respect to the full substrate;

2. The amorphous multilayer beneath the resonators film strongly increases the noise;

3. The 'dirty' substrate solutions did not give conclusive results due to higher noise.

The observed change in the shape of the events on membrane and the multilayer solution with lower noise levels would certainly deserve further studies, but these will not be subject of this thesis work. For the following measures, we have focused our effort in studying the high-energy interactions in KID array fabricated on High Resistivity Silicon (HR-Si) substrates.

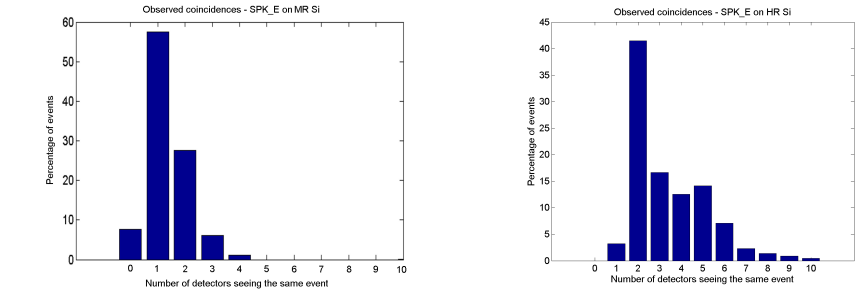

(a)

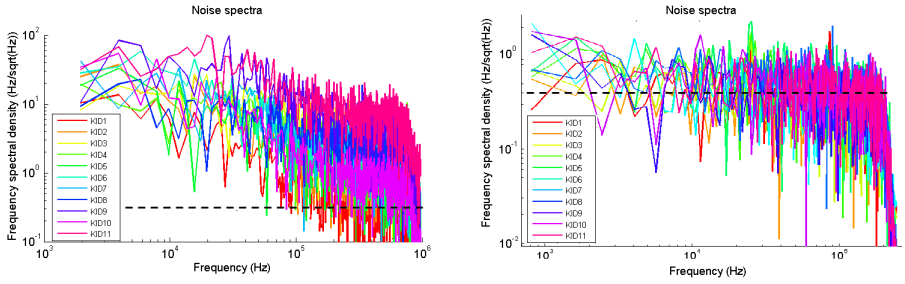

(b)

Figure 7.8: *(a) A comparison of the coincidences observed on the SPK-E array using a low resistivity (LR) substrate* ($0.5 \div 1\Omega \cdot cm$, *left) and a high resistivity (HR) one* ($> 1k\Omega \cdot cm$, *right). The number of readout pixels is 10. (b) The noise spectra of the signal observed on the SPK-E array fabricated on LR-Si or HR-Si. The spectra were measured for 11 KID, 10 of which were used also to plot the coincidences histograms. The spectrum of the lower resistivity substrate shows a noise level roughly 10 times higher and a clear 1/f contribution, explaining the lower number of coincidences.*

From what we observed in fact, this solution is the only viable choice able to ensure high internal quality factors and low noise. These are essential requirements in order to perform a systematic study of the phonon-mediated detection mechanisms. We first present our measurements using secondary CR following the scheme in fig. 6.3(b). As already said, (par. 6.1), our substrates have a thickness of 350 μm, which leads to an average deposited energy of the order of $200keV$ for normal incidence.

7.5.1 The effect of the ground plane metallization

We studied the effect of secondary CR on the SPK arrays presenting 'island' of detectors, with (SPK-E) and without the ground plane (SPK-C array). The characterization of these two arrays will be presented in the next chapter. From the total time trace of the array (fig. 7.9(a), left plot), we estimate a rate of about 18 events/min (corresponding to roughly $200events/s/m^2$ as expected). This is roughly the same value we obtained with the NIKA-

like array (see par. 6.5) and is again in good agreement with literature. A histogram of the number of pixel detecting the same event is shown in fig. 7.8(a). It can be seen that more than 50% of the events are sensed by 3 or more pixels. Since we were reading out the signal from 2 pixels per island, this means that most impacts are observed by at least 2 islands. The minimum separation between islands is of about 18 mm (see fig. 7.1(f)), which means that these CR events can be detected even in the furthest pixels.

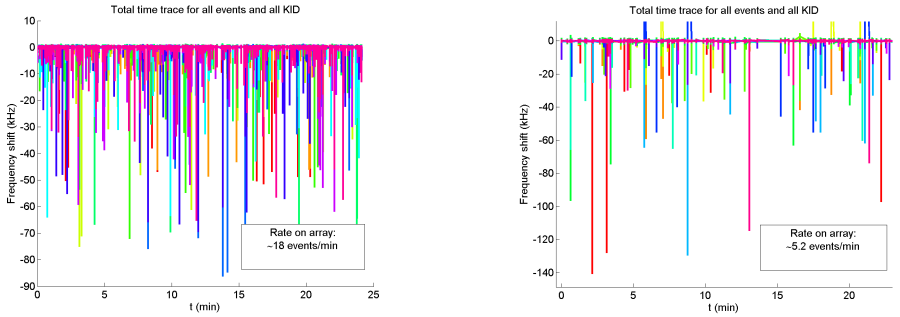

(a)

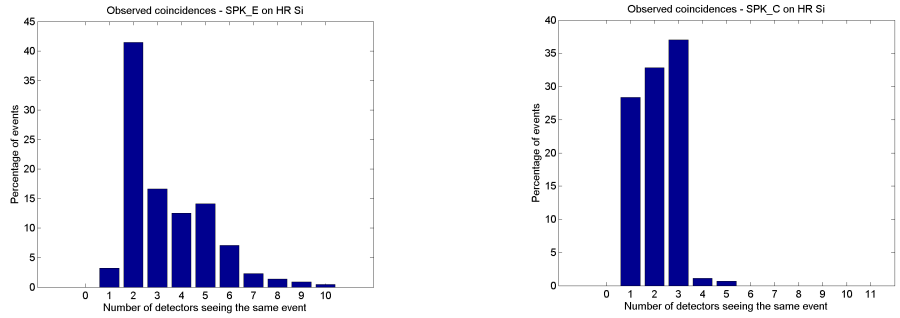

(b)

Figure 7.9: *(a) The total time trace of the acquisition of secondary CR events for the pixel on the SPK island geometry. The event rate observed is significantly different between the array without ground plane (SPK-E, on the left) and with ground plane (SPK-C, on the right). (b) A comparison of the coincidences observed on SPK-E array without ground plane (on the left) and SPK-C array with ground plane (on the right). 2 KID for each island were fed for SPK-E array, while there were between 1 and 3 pixels fed per island for the SPK-C array.*

One further conceivable option in order to reduce the portion of the array affected by CR events consists in increasing the fraction of the metallized surface. This surface can absorb part of the phonons through the pair-breaking mechanism (part III introduction), and enhance their energy down conversion. Therefore, we repeated the measurements on an SPK-C array from the same wafer. SPK-C has the same geometry of SPK-E, but with the ground plane filling the whole array surface between the pixels. During the acquisition, 1 to 3 excitation tones were active for each island. The histogram in fig. 7.9(b) shows that in this case we are

able to see the same event only on pixels belonging to the same island. This demonstrates that the ground plane effectively helps reducing the energy sensed by the detectors, most likely adding an additional channel for the phonons thermalization. This is further confirmed by the total time trace in the right plot of fig. 7.9(a), which shows a decrease of about a factor 3.5 in the rate of observed events with respect to SPK-E. The effective area sensitive to secondary CR impacts is thus reduced by the same amount. A back-of-the-envelope calculation allows us to estimate that we can detect only particles hitting the array less than 5 mm away from the center of an island. Although not yet conclusive, these results encourage us to further investigate the solution of adding metal layers when possible.

Chapter 8

Effect of a metal layer on phonon propagation

As demonstrated in section 7.5.1, the introduction of a metal layer on the substrate surface strongly affects the energy propagation. In fact, the in case of a bare substrate, the ballistic phonons have a high probability of being reflected at the interface. This process being elastic, the phonons don't lose their energy. Each ballistic phonon can undergo many specular reflections before being scattered by an impurity in the substrate or diffuse on its surface. On the other hand, if a metal layer is present on the surface, there is a large chance that the phonon will be absorbed in it. In particular, if the metal is a superconductor, the energy released by the phonon can break a Cooper Pair and create quasi-particles. Such quasi-particles can thermalize their energy within the superconductor, and release it back into the substrate in the form of lower-energy phonons, with energies near or below the gap. In the following we will refer to them as to *warm phonons*, since they have an equivalent temperature still higher than the thermal distribution at $100mK$, but much lower than the population of *hot phonons* produced near the interaction (see introduction part III). Although they are likely less affected by the metallization layers that can be added on the wafer, their diffusive motion implies that their effect is expected to be local. If this is the case, therefore the diffusive phonons, although more difficult to suppress, would have only a minor impact on a large array, affecting only the small fraction of the detectors that are very close to the impact point.

The extra metal layer would therefore introduce a mechanism to assist the energy down-conversion of the ballistic phonons, suppressing their effect over large distances. In the following, we refer to this mechanism as *pair-breaking losses*.

In the following we present the results obtained comparing the same geometries for different metal layers. Using the SPK mask (par. 7.1), we first compared the results on island geometries with bare or full Aluminum ground plane (SPK-E and SPK-C, respectively). Then, we studied the effect of adding a thin Titanium layer on the back side of the distributed geometry

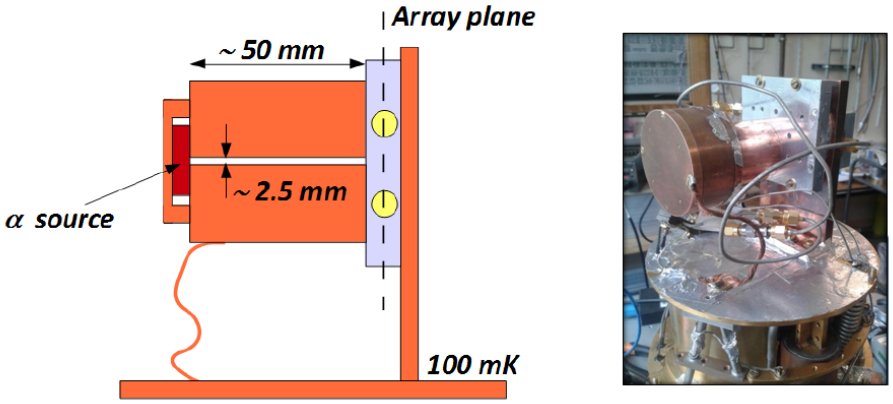

Figure 8.1: *(a) A schematic of the collimator used to define the area of impact of the α particles. (b) A photograph of the $\sim 100mK$ stage of the cryostat prepared with the collimator mounted on one of the SPK arrays.*

(SPK-D).

8.1 High energy sources

In order to reproduce the physical interaction induced by primary CR, a possible option is the use of secondary CR. As previously commented, these are essentially muons, which are produced by impacts of primary CR in the Earth's atmosphere. Losing $\sim 0.5keV/\mu m$, each muon deposits roughly 200 keV in our substrates (see par. 7.5), exactly like primary CR. They penetrate the whole thickness of the Silicon substrate, ionizing a large number of low energy electrons whose energy then translates into phonons. The atmospheric muons rate at sea-level is calculated around $200events/s/m^2$, corresponding to roughly $0.25events/s$ on a NIKA-like and SPK arrays ($36 \times 36mm^2$).

The expected rate of secondary CR on SPK arrays is relatively low, and, more important, the different position of the interactions (*impact points*) makes the shape of the pulses very variable. These constraints prevent us to make more quantitative and systematic considerations about the propagation of the phonons in the substrate. To avoid these limitations, we used a set of radioactive sources with a narrow collimator. This approach sensibly improved the statistics of our experiment to $\sim 1event/s$, and especially allows us to know the approximate impact point.

In order to simulate the interactions induced by CR, ^{241}Am and ^{244}Cm sources were chosen, emitting alpha particles of 5.4 MeV and 5.9 MeV respectively. Unlike CR, $\sim 6Mev$ α particles are completely stopped over a distance of the order of a few μm inside a silicon substrates [126] [127]. This means that all their energy is released into the substrate very

close to the impact point. Furthermore, since our radioactive sources emit α of about 6 MeV, this increments the energy deposited in the substrate by a factor of ~ 30 with respect to CR hits. It becomes therefore possible to detect a signal even in the furthest pixels, which in turns results in a better sampling of the function describing the phonons energy propagation. The α sources were mounted in front of the array, using a copper collimator with a length of about 5cm and an aperture diameter of 2.5mm (see fig. 8.1). As said before, this solution also constraints the impact area making it possible to determine with a good approximation the distances between the impact point and the detectors. Relying on the high hit rate and deposited energy, and on the known position of the impacts, we aim to perform a qualitative analysis of the propagation of the energy in the substrate.

We have available also a ^{109}Cd X-ray source, producing photons with an energy of $E_X = 20,1keV$. The X photons have a given probability to be absorbed by an atom of the substrate through the photoelectric effect. The atom thus ejects an inner shell electron with kinetic energy $E_{kin} = E_X - E_{shell}$, which is usually sufficient to produce a cascade of secondary photoelectrons (for example, $E_{shell} \sim 1.5keV$ for ^{109}Cd, so that $E_{kin} \approx E_X$). The probability of the primary X photon to be absorbed in the substrate lowers with its energy. It is expressed by the *penetration depth*, that is defined as the depth over which the initial flux of X-rays has been reduced by a factor e^{-1} due to photoelectric absorption in a given material. The penetration depth for $\sim 20keV$ X rays in silicon is $\sim mm$ [128]. Since we uses silicon substrate $350\mu m$ thick, the photons emitted by ^{109}Cd will be absorbed uniformly over its depth.

8.2 Time traces analysis pipeline

The analysis pipeline on the set of data consists of the following steps:

1. fit of the resonance parameters and calibration of the signal from each KID following the scheme described in par. 3.4.1. The calibrated phase is fitted to an arctangent;
2. removal of unwanted events (cosmic rays, doubles due to pile-up, ecc.);
3. calculation of the total time trace and total rate;
4. definition of the detection threshold, usually at 5σ;
5. calculation of the number of *coincidences* (number of pixels seeing the same event);
6. calculation of the *average pulse* (mean of the time traces of all the observed pulses) of for each KID;
7. calculation of the peak amplitude by fitting the time trace (single events and average pulse) for each KID, using the sum of different exponential terms;

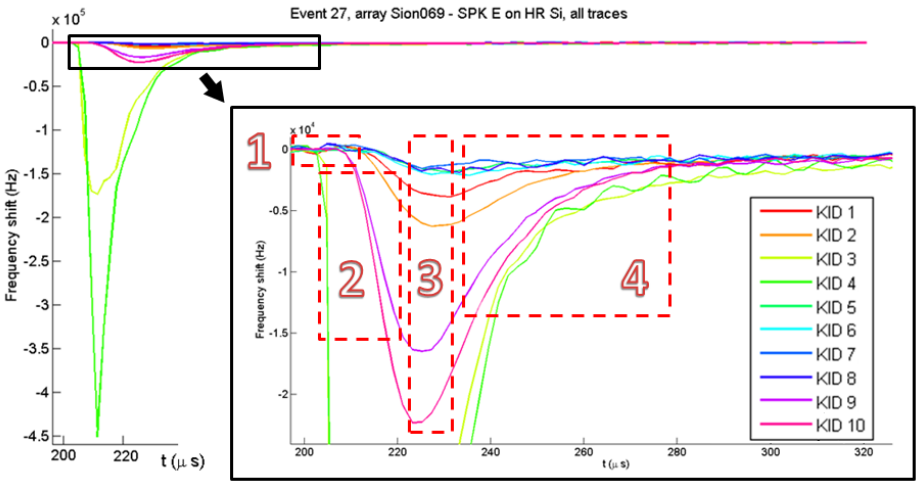

Figure 8.2: *An example of time traces on different KID induced by an alpha particle hit on the SPK-E array. The signals are plotted in unit of frequency shift, so that the effect is a negative glitch. In the bottom-right corner zoom four different zone are evidenced, each one corresponding to a particular feature of the time traces: delays (1); rise time (2); peak signal (3); decay time (4).*

8. split of the time trace in two parts: *'rise'*, from the beginning until 90% of the peak amplitude; *'fall'*, from 90% of the peak amplitude to the end of the time trace;

9. calculation of the rise (τ_{rise}) and fall time constants (τ_1, τ_2, ...) by fitting the 'rise' and the 'fall' parts of the pulse, respectively using a sigmoid ($\propto (1+e^{(-t/\tau_r)})^{-1}$) and a decay exponential function;

10. calculation of the impact point on the array from a 3-dimensional fit of the peak amplitudes and xy positions of the KID (single events and average pulse);

11. calculation of distances between impact point and detectors. The position of each KID on the array is assumed to be the geometric center of the Hilbert pattern of the inductor.

An example of a pulse as measured by different pixels on the same array, is shown in figure 8.2. We can identify in the time traces four main areas, each one evidencing a characteristic of the signal that varies in function of the distance between the detector and the impact point:

1. **Delays**: the signal starts to rise at a certain time t_{in}. Measuring the delays between different pixels we can calculate the phonon speed into the substrate;

2. **Rise times**: the slope of the rise decreases moving away from the impact point. This characteristic rise time t_{rise} describes the arrival of the all the available phonon energy

in the KID position, starting from when the signal begins to rise until it reaches its peak;

3. **Peak signals**: the amplitude of the peak is proportional to the energy deposited inside the detector. By fitting this trend it is possible to describe the damping of the energy in different kinds of substrate;

4. **Decay times**: the signal decays with one or more time constants, from which it is possible to calculate the lifetime of the quasi-particles and of the different phonons populations.

Unless otherwise specified, each set of analyzed data contains 1000 alpha events acquired at 1MHz sampling rate. This rate provides a good compromise between good sampling of the time trace and high signal to noise ratio.

8.3 Measurements of quasi-particle lifetimes

Without recurring to the radioactive sources, it is possible to measure the quasi-particles recombination time, τ_{qp} , just by taking noise data [129]. Following eq. 2.101, the spectral power density induced by generation-recombination noise shows a Lorentzian spectrum

$$S \propto (1 + (2\pi f \tau_{qp})^2)^{-1} \tag{8.1}$$

By measuring the fluctuations of the resonator signal both at the resonant frequency (*total noise*) and off-resonance (*system noise*), it is possible to extract the power spectral density corrected for system noise (*resonator noise*). This noise spectrum will thus depends only on the quasi-particles GR noise and can be fitted using eq. 8.1.

The τ_{qp} evaluated with this approach is actually an upper limit with respect to the τ_{qp} observed during a pulse. In fact, when the extra energy due to the particle impact is absorbed in the resonator, it will break additional Cooper Pairs, increasing the quasi-particles density and thus decreasing the lifetime. The data have been taken using the SPK-D array (KID 8), but the value found can be considered valid for all the arrays, since they are made out of the same film and measured in the same dark environment. In the noise spectra it is evident the cut-off around 10kHz. A Lorentzian fit allows us to estimate a cutoff time of $\sim 10\mu s$ (fig. 8.3(a)). The resonator ring-down time of KID 8 is $\tau \sim 5\mu s$, so the slower time constant given by the fit must be identified with that of the quasi-particles lifetime, so $\tau_{qp} = 9.8 \pm 0.1\mu s$ at the base temperature ($106mK$), in agreement with the literature [45]. Moreover, the same measurements allowed to calculate a lower value at $T = 175mK$ (fig. 8.3(b)), corresponding to $\tau_{qp} = 8.1 \pm 0.1\mu s$. This is what we expected from eq. 2.18, confirming that the origin of this cut-off is effectively the quasi-particles lifetime. As we will see in the following paragraphs,

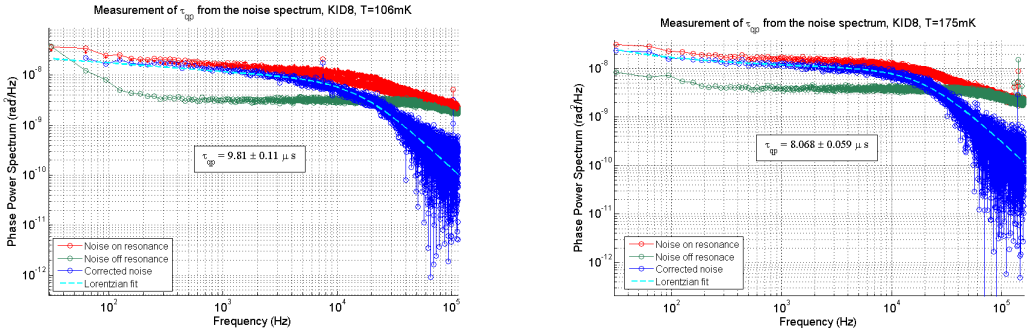

(a) (b)

Figure 8.3: *Noise measurements for the determination of the quasi-particles recombination time for the SPK-D array at 106 mK (a) and 175 mK (b). The total noise power spectrum (red) is given by the contributions of the system noise (green) and the resonator noise (blu). The latter shows a clear cut-off which is fitted by a Lorentzian spectrum,* $S \propto (1+(2\pi f \tau_{qp})^2)^{-1}$*, with a measured characteristic time of* $\tau_{qp} = (9.8 \pm 0.1)\mu s$ *and* $\tau_{qp} = (8.1 \pm 0.1)\mu s$ *at 106mK and 175mK, respectively. The power spectra have been evaluated using the calibrated phase of the KID8 signal. The system noise measurement has been performed 500kHz off-resonance.*

the pulses we observe are in general longer than that. Their time evolution is therefore governed by phenomena related to the creation, transport and downconversion of energetic phonons in the substrate, rather than by the effect of the quasi-particles recombining in the superconductor.

8.4 Effect of the Aluminum ground plane on 'island' geometries

8.4.1 Setup and preliminary considerations

The experiments were performed using the ^{241}Am source on the SPK-E and SPK-C arrays (see fig. 8.6). The only difference in these two arrays is given by the fraction of surface covered by Aluminum, which is much larger in the case of the SPK-C geometry. The collimator was placed in front of one of the corner islands, in order to maximize the distance between the hit point and the furthest island, which corresponds to about 36 mm. Ten resonators were read out in both configurations (fig. 8.4-8.5), two for each island when possible (fig. 8.9(a) and 8.9(c)).

The total event rate was similar for the two arrays, corresponding to about 150 events/min. The statistics for the SPK-E array is relatively poor, since we have acquired a total of roughly 100 valid α events. In fact, as it is evident from the histogram in fig. 8.6, there are two clearly distinct families of events. The dominant one contributes for around 80% of the total glitches. These events induce a signal only in pair of pixels belonging to the target island. Whereas, the α particle impacts are in general energetic enough to produce a detectable signal in all

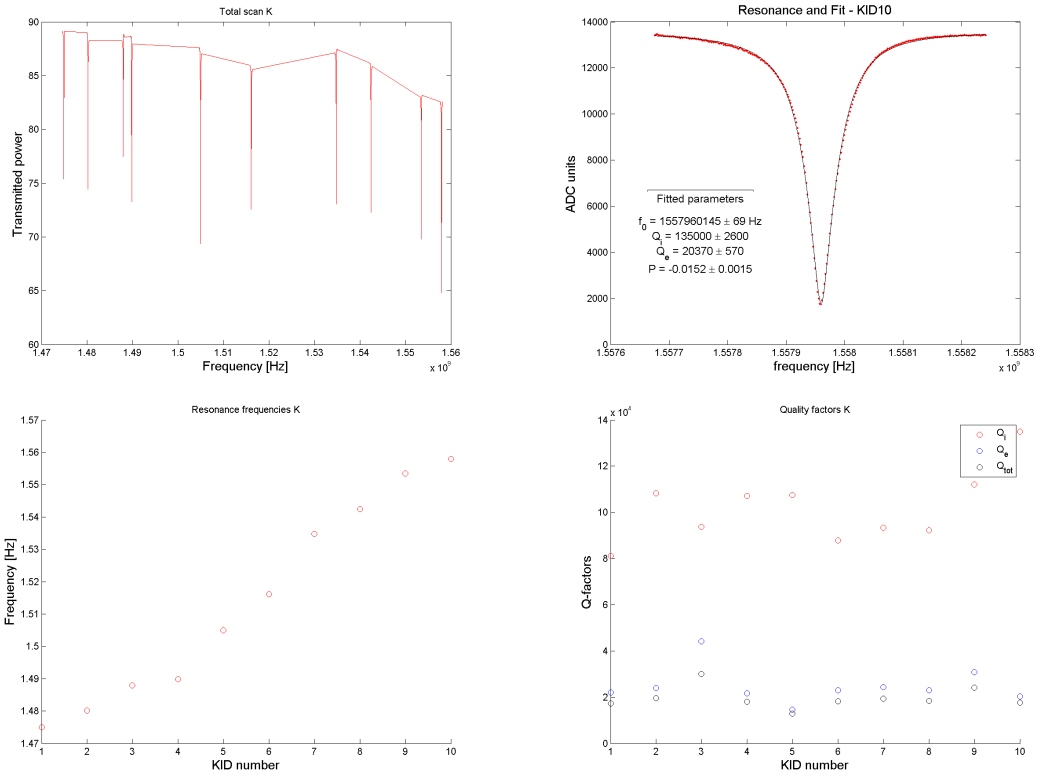

KID #	f_0 [Hz]	err f_0 [Hz]	Q_i	err Q_i	Q_e	err Q_e	Q_{tot}	err Q_tot	P	err P
1	1474909699.25	126.1579	8.1145e+04	1.5040e+03	2.1992e+04	591.5688	1.7303e+04	565.2230	-0.0284	0.0025
2	1480184477.29	125.7000	1.0829e+05	2.8366e+03	2.3860e+04	924.4963	1.9552e+04	914.4587	0.2799	0.0030
3	1487966383.95	130.8841	9.3748e+04	1.7964e+03	4.4061e+04	1.2344e+03	2.9974e+04	1.0174e+03	-0.2208	0.0036
4	1489832516.88	81.6113	1.0719e+05	1.8422e+03	2.1661e+04	549.5614	1.8020e+04	552.1997	0.2716	0.0019
5	1504946860.61	73.5336	1.0742e+05	1.8929e+03	1.4606e+04	375.4834	1.2858e+04	400.7394	0.1561	0.0013
6	1516092438.38	107.0647	8.7746e+04	1.4591e+03	2.2994e+04	559.8304	1.8220e+04	537.1827	0.1805	0.0022
7	1534795864.65	71.9212	9.3429e+04	1.1024e+03	2.4284e+04	419.0316	1.9274e+04	402.9131	-0.1536	0.0016
8	1542439492.00	50.7508	9.2247e+04	764.2243	2.3004e+04	278.0233	1.8412e+04	269.7921	0.1119	0.0011
9	1553484460.62	86.5135	1.1206e+05	1.8565e+03	3.0807e+04	744.4306	2.4164e+04	707.9633	-0.0238	0.0022
10	1557960145.00	68.6205	1.3502e+05	2.6046e+03	2.0374e+04	574.0626	1.7702e+04	604.4972	-0.0152	0.0015

Figure 8.4: *Fitted parameters and calibration for the KID of the SPK-E array fabricated on HR-Si: (top left) a sNelloX scan of the resonances; (top right) example of one resonance data (red points) and fit (black line); (middle left) resonance frequencies distribution; (middle right) internal, external and total quality factors obtained by the fit; (bottom) a table of the fitted parameters and errors for all the active resonances.*

the pixels, which means that their energy is detectable at least at a distance of 36mm, for both arrays. The events that gives the majority of the pulses observed in the SPK-E array therefore have a much lower energy compared to the alpha particles. Such events are probably produced by secondary X rays generated by the α particles interacting with the copper in the collimator. This family of events is neglected in our analysis, and this is the reason for the relatively poor statistics in the SPK-E data. During the cooldown dedicated to the SPK-C array, we acquire a part of the data setting a higher threshold to trigger the acquisition of a trace, in order to avoid this lower energy events population.

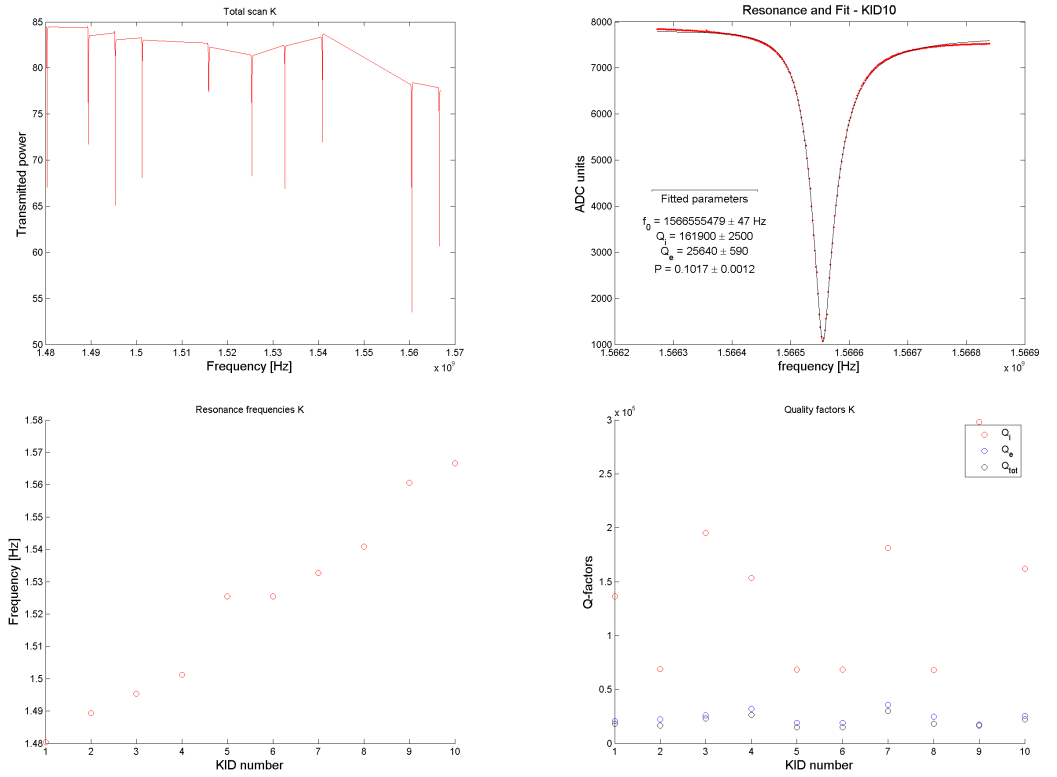

KID #	f_0 [Hz]	err f_0 [Hz]	Q_i	err Q_i	Q_e	err Q_e	Q_{tot}	err Q_tot	P	err P
1	1480318188.50	42.5143	1.3618e+05	1.7205e+03	2.0810e+04	384.3570	1.8051e+04	403.9510	0.0345	9.8743e-04
2	1489391931.11	67.3252	6.8812e+04	539.3888	2.2087e+04	256.1694	1.6720e+04	234.0602	0.3064	0.0013
3	1495304851.14	41.1745	1.9515e+05	3.6783e+03	2.5975e+04	721.8408	2.2924e+04	769.7543	0.3515	0.0012
4	1501229908.77	32.9926	1.5346e+05	1.5004e+03	3.1916e+04	458.5384	2.6421e+04	459.1492	0.1167	0.0010
5	1515871494.89	45.3651	1.6526e+04	18.8491	1.9786e+04	28.0732	9.0048e+03	16.3928	0.0954	2.7450e-04
6	1525368269.39	44.9970	6.8272e+04	365.2782	1.8915e+04	146.1117	1.4812e+04	139.1774	0.0527	7.5962e-04
7	1532620104.02	39.4661	1.8134e+05	2.4933e+03	3.5911e+04	725.0136	2.9975e+04	732.1829	0.0281	0.0013
8	1540879457.41	37.3903	6.8082e+04	277.0387	2.4805e+04	145.9139	1.8181e+04	130.0432	-0.1525	6.9346e-04
9	1560540188.00	28.2765	2.9831e+05	7.8376e+03	1.7399e+04	660.4020	1.6440e+04	758.9142	-0.0899	6.5179e-04
10	1566555478.85	47.2177	1.6191e+05	2.5235e+03	2.5635e+04	585.4779	2.2131e+04	611.9257	0.1017	0.0012

Figure 8.5: *Fitted parameters and calibration for the KID of the SPK-C array fabricated on HR-Si.*

The two histograms in fig. 8.6 are both related to acquisitions taken with a low threshold, in order to observe also the less energetic events. By comparing them, we can observe a slight diminution of coincidences on the array with the ground plane. X-events are seen almost always by both the KID of the target island in the SPK-E array, while almost one third of them are seen only by KID number 7 in the SPK-C. A similar behavior is observed for the α hits, which are detected by all the pixels of the SPK-E, and often by only 8 or 9 KID of the SPK-C. This is due to the fact that the pulse amplitudes in the furthest pixels of the second array often fall within their noise. This is a further evidence of the fact that the signal undergoes a stronger damping in the array with the additional metallization provided by the ground plane.

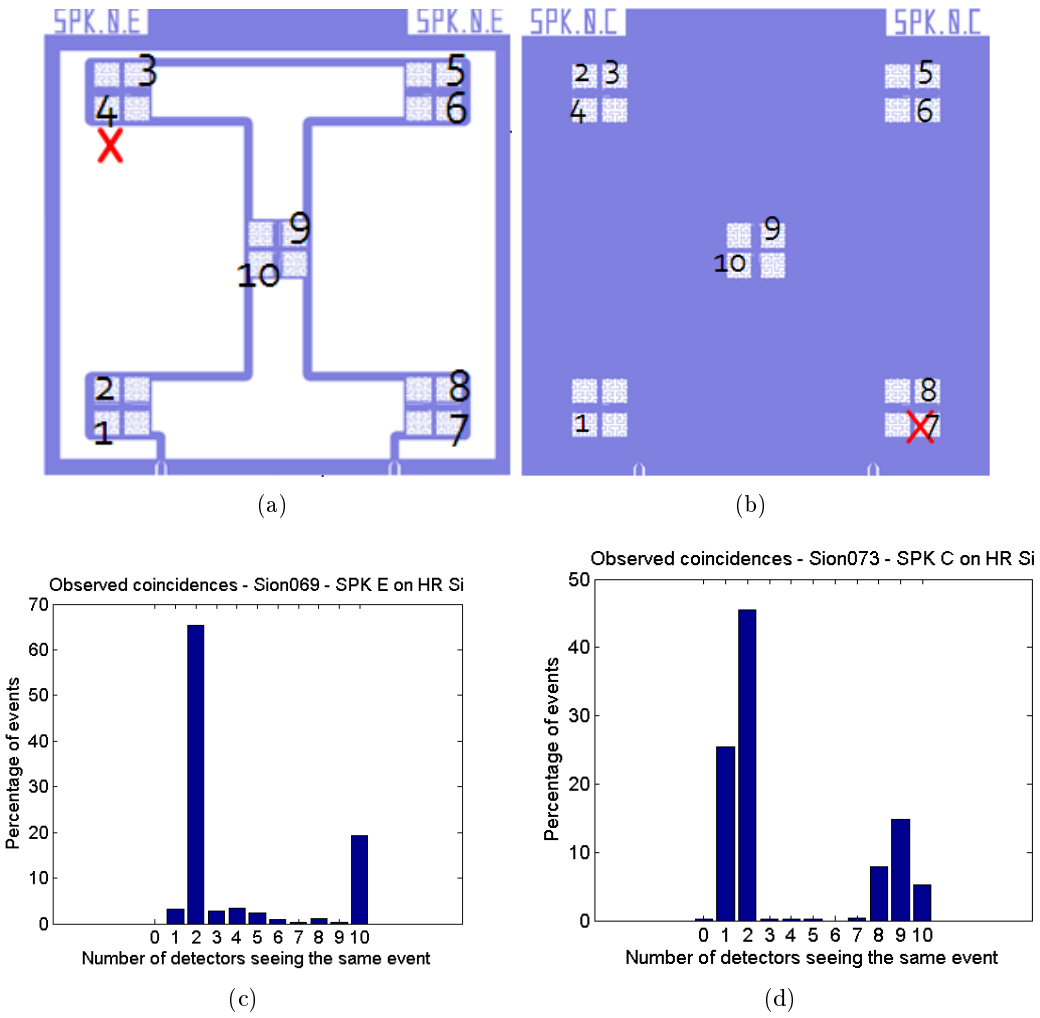

Figure 8.6: *Setup and observed coincidences for the SPK arrays, without ground plane (SPK-E) and with ground plane (SPK-C) exposed to a* ^{241}Am α *source. The figures (a) and (b) show the position of the active KID. Two KID per island were fed for the SPK-E array, while this was not possible for all the islands in SPK-C case. The* α *impact areas are indicated by a red cross. The figures (c) (d) show the histograms of the coincidences observed on the SPK-C and on the SPK-E using a low threshold value. The most common events cause a detectable glitch (at a 5 sigma level) in only two pixels at a time and are due to secondary X-rays. The 1-coincidence bar in the SPK-C histogram corresponds to event seen only by KID number 7. The presence of the ground-plane prevents lower energy events detection in KID number 8* $\sim$ *30% of the times. The detection of the secondary X-ray population has been almost completely avoided during the subsequent SPK-C acquisition by setting a higher trigger. Two pixels of the SPK-C array showed a high noise level, which accounts for the fact that often the glitch on their time traces is actually below 5-*σ *and is considered as not having been detected.*

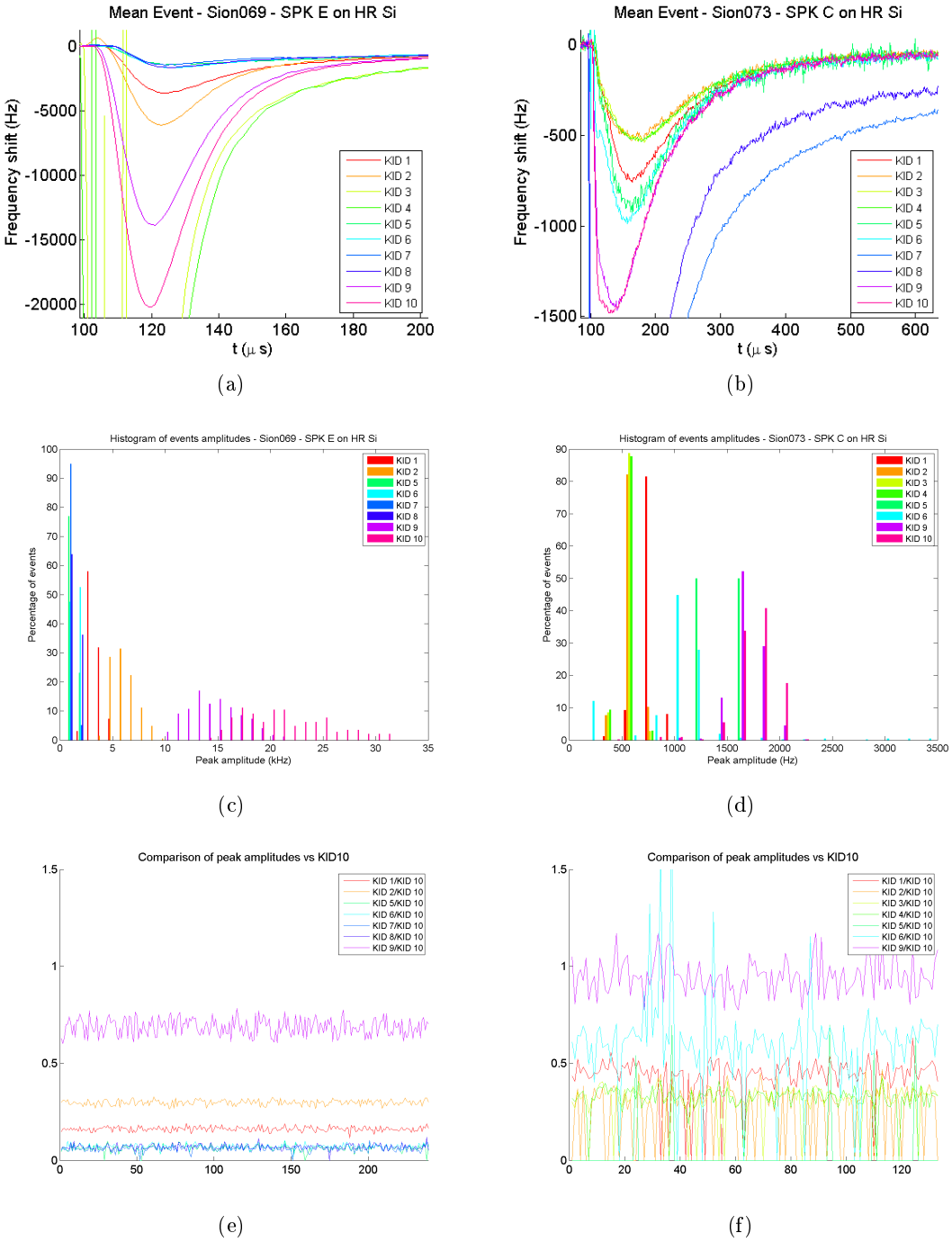

Figure 8.7: *(a) (b) The average pulse for all KID. The peak amplitudes are* ~ 1 *order of magnitude bigger in SPK-E, and depend in both array on the distance form the average impact point. The average pulse highlight the presence of different families of detectors, each one corresponding to a different island. The signals are plotted in unit of frequency shift, so that the effect is a negative glitch. (c) (d) histograms of peak amplitudes, families. In the bottom figures, the signals normalized to 10th KID in function of the event number for the array without ground plane (e) and with it (f). KID referred to target island are not considered because of their saturated signals.*

8.4.2 Peak amplitudes

The average pulses for all the KID on the two arrays are presented in fig. 8.7(a) and 8.7(b) and the relative spectra of the peak amplitudes are shown in fig. 8.7(c) and 8.7(d). Both these results highlight how KID are grouped in families belonging to the different islands. Pixels of the same island show similar delays in the arrival time of the signal, but also similar rise and fall slopes and comparable peak amplitudes. Neglecting in this analysis the pulses observed on the target KID, highly saturated, the peak amplitudes are clearly correlated with the distance from the hit area. The plot of the signals measured by different KID normalized to KID 10 is shown in fig. 8.7(e) for the SPK-E array. The measured ratios of peak amplitudes for this array are constant throughout the experiment, which demonstrates that they depend only on the distance from the impact point. On the other hand, the presence of the ground plane makes this kind of measure harder for the SPK-C array (fig. 8.7(f)).

The mean value of the peak amplitude is calculated from a gaussian fit of the spectra of the signals in each KID (see for example figs. 8.8(a) and 8.8(b)). The comparison between the two arrays is difficult for two reasons: 1) the positions of the pixels that we readout are not exactly the same with respect to the impact point; 2) the additional metal layer is made of the same material (Al) as our resonators. The pair-breaking mechanism therein helps in downconverting the energy of the substrate phonons down to values near the aluminum gap. Therefore, it is still possible for the pixels to detect phonons that have already undergone an absorption/re-emission process in the aluminum of the ground-plane.

Even considering this, our data do show a strong effect given by the increased fraction of metallized surface. For pixels at comparable distances from the impact point on the two arrays, the amplitude of the glitch is smaller in the sample with the full ground-plane, by a factor which depends on on the distance. Neglecting the saturated the detectors, we observe a reduction of the peak amplitude by a factor ~ 10 for the KID in the central island, and only ~ 2 for the farthest pixels (fig. 8.7(a)–8.7(d)). In order to perform a quantitative comparison of the phonon energy attenuation with and without ground plane, we need to give an estimation of the KID distances from the impact point.

8.4.3 Determination of the impact point position

We have calculated the impact point position of each pulse $(X_{impact,j}, Y_{impact,j})$ by fitting a power law on the peak amplitude data. In particular, the estimation was performed using a 3-dimensional fit of the data vectors $(x_i, y_i, A_{i,j})$, where x_i and y_i are the Cartesian coordinates on the array corresponding to the center of the Hilbert inductor pattern of the $i-th$ KID, and $A_{i,j}$ is the peak amplitude of the j-th pulse in unit of calibrated frequency shift Δf, as measure by $i-th$ KID. The results of this analysis are shown in figs. 8.9. Although hitting the corner of the array does not help in fitting the position of the impact point, its estimation is

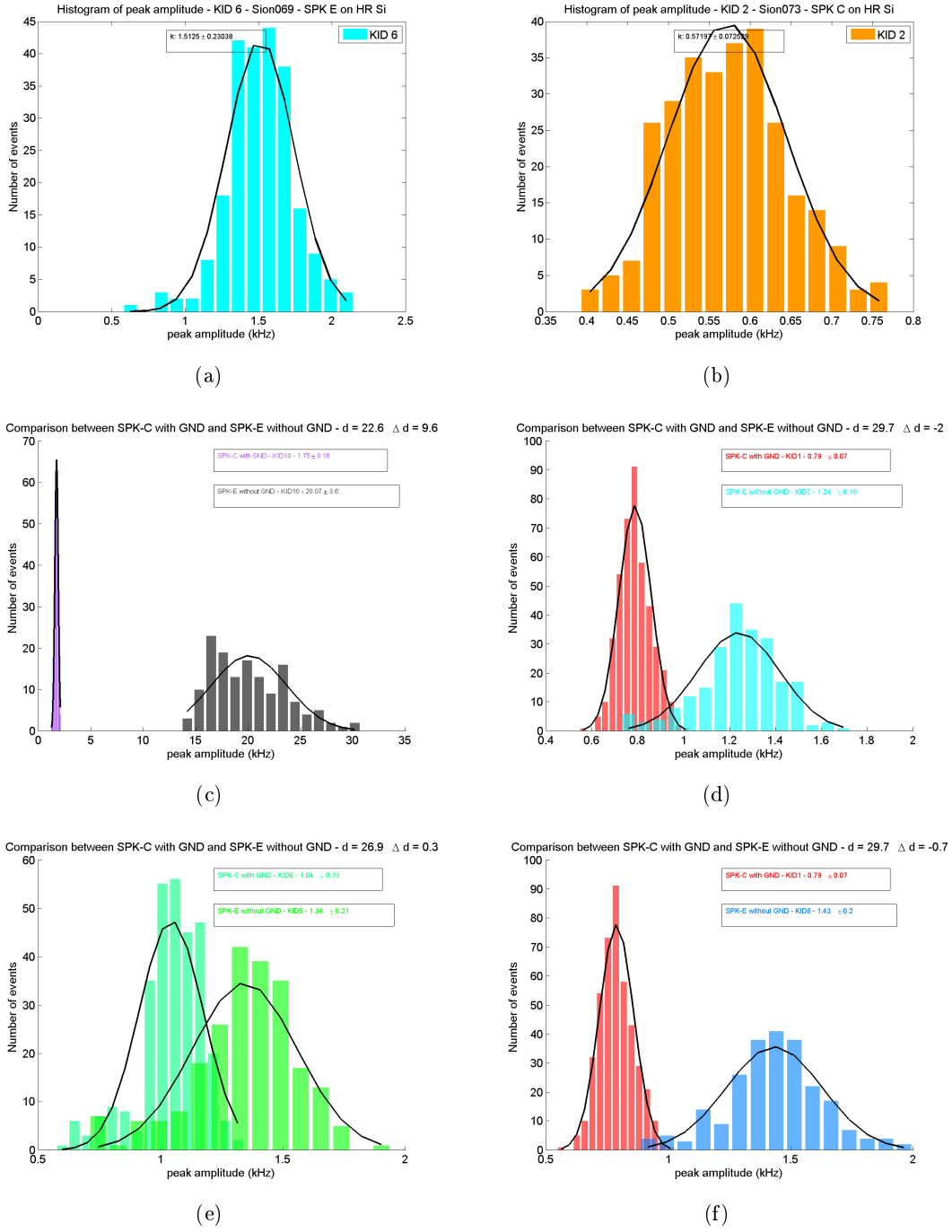

Figure 8.8: *(a),(b): example of spectra and gaussian fit of the signal in two KID. (c) Energy measured in the KID number 10 for both arrays; the signal in the GND plane array is attenuated by a factor* ~ 10*; the SPK-C pixel distance from the impact point is larger* ($\Delta d = 9.6mm$) *than in SPK-E one. (d–f) Energy measured in KID at similar distance from the impact point. For example: (d) the peak in the pixel on SPK-C array is attenuated by a factor* ~ 1.8*, despite the fact that the SPK-E pixel is more distant from the hit* ($\Delta d = -0.7mm$)

compatible with the alpha source position, which results are shown in figs. 8.9(b) and 8.9(d). We used the physical dimension of the array and of the collimator to discriminate good fits, and these limited values of the x and y coordinates are shown together with their fit in figs. 8.9(e)–8.9(h). An example of the fitted surface and the histogram of power exponent obtained by 3-dimensional fit are shown in figs. 8.9(i)–8.9(l) for both the arrays.

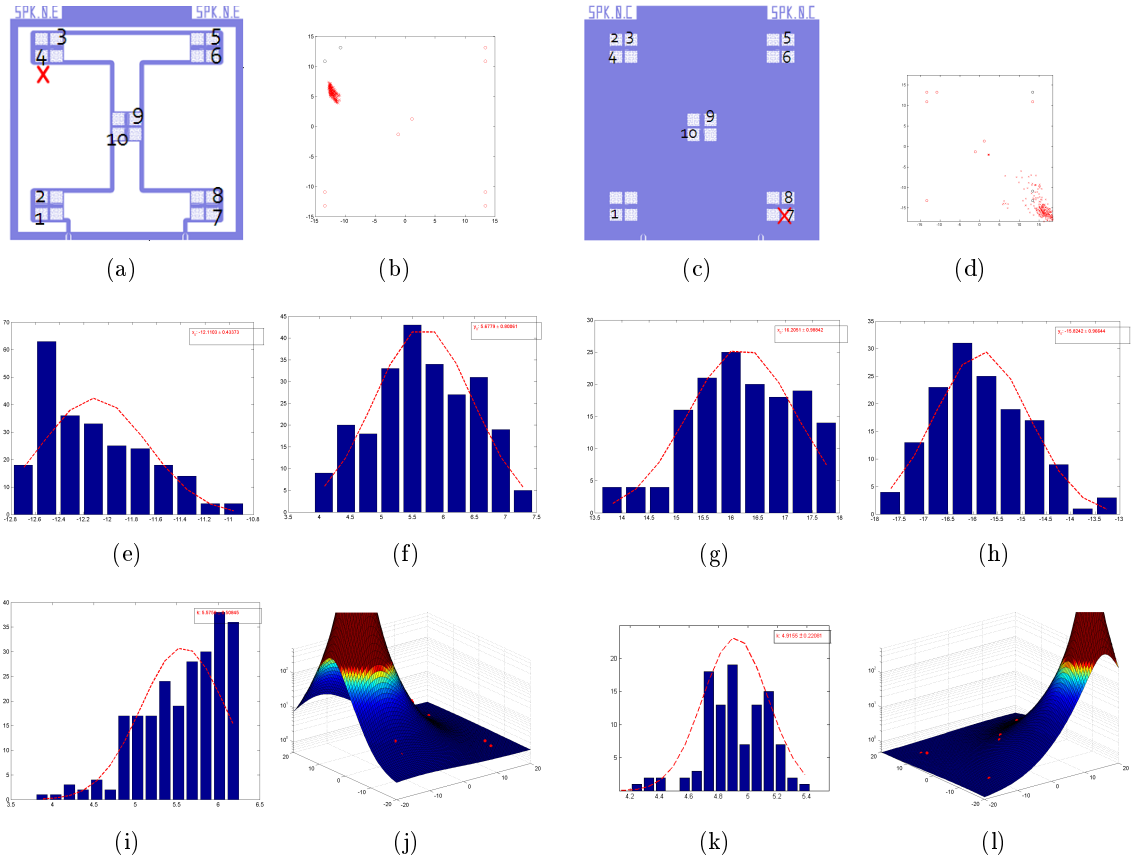

Figure 8.9: *Impact position analysis for the SPK-E (first and second columns) and SPK-C (third and fourth columns)arrays exposed to a* ^{241}*Am alpha source: (a, c) The array geometries with (b, d) the corresponding estimated impact point for each* α *event (red crosses); the circles represent the position of the KID used for the 3D fit (red) and of the rest of the active KID (black); histograms of the X (e, g) and Y (f, h) Cartesian coordinates of the estimated impact positions with the fitted gaussian (red dotted line); (i, k) histograms of the estimated exponents in the power lax used for the 3D fit; (j, l) examples of 3D fits of a singla* α *event.*

8.4.4 Comparing energy damping

Based on the estimation of the mean hit point, we can now compare spectra of KID at similar distances from the impact point for the two arrays. These do not in general correspond to

pixels of the same 'island' on the two arrays, as the collimator was differently positioned during the two experiments. For example, the distances of the KID 10 from the impact point were $d = 22.6mm$ and $d = 32.2mm$ in the experiments respectively mounting the SPK-C and SPK-E array (fig. 8.8(c)). Despite that, it is possible to search for KID at similar distances from the impact point. Some of these 'comparable' pixels from different arrays are shown in fig. 8.8(f). It is evident that the measured peak amplitudes of SPK-C are attenuated by a factor $\sim 1.5 \div 2$ with respect to those of SPK-E. This confirms that the added aluminum metallization of the ground plane dampens the energy propagation inside the substrate. The amount of data collected are not sufficient to provide a reliable estimation of this damping as a function of distance, principally because of the low number of sampled distances and the poor accuracy in the determination of the impact point.

8.4.5 Delays and phonon velocity

The propagation velocity can be measured from the signal delays. A preliminary estimation on the average pulse gives a delay of roughly $5\mu s$ between the pixel closest to the impact point (KID 3) and the KID 10. Considering the position of these pixels and the estimated mean position of the impact, we calculate a phonon propagation velocity of the order of $2mm/\mu s$, in good agreement with the values reported in literature for silicon [46]. A better determination of the phonon velocity could be achieved by using both the peak amplitudes and the measured delays to find the impact position. This could improve the accuracy of the velocity estimation and allow the use of these detectors for phonon-imaging application. This study is however beyond the scope of this thesis.

8.4.6 Fall time constants

The average time traces were calculated for all non-saturated KID and an exponential fit was applied. The preliminary analysis shows that an exponential with a single time constant is not sufficient to correctly describe the time evolution of the signal (fig. 8.10). At least a second exponential time constant is needed in order to provide a satisfying description of the energy damping as a function of time. Moreover, the introduction of a third, longer time constant further enhances the quality of the fit. Yet, the electronics during these acquisitions could handle time traces up to $2ms$ only. Since the data hint a third time constant longer than this, we decided to modify our firmware to be able to make longer measurements, as those described in par. 8.7.

Considering these limitations, for the following of the analysis in this section, we neglect this very slow time constant and we restrict the fit only to the 'fall' time trace. The average pulses observed on our detectors are presented in fig. 8.11. Their shape is not the same for all the pixels, depending clearly on distance from impact point. Without ground plane, the

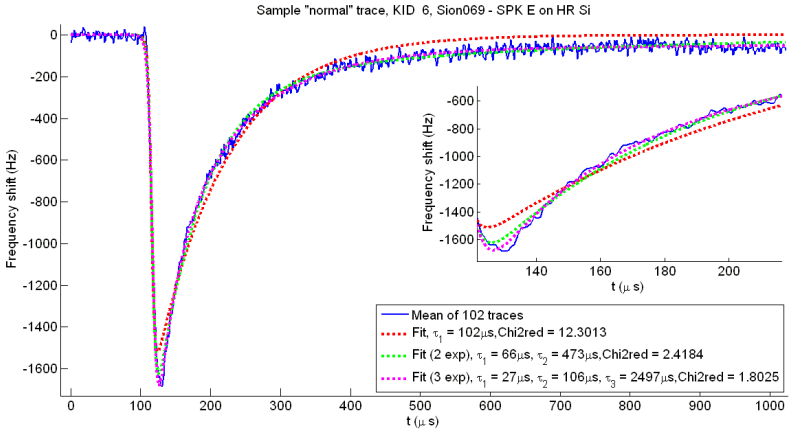

Figure 8.10: *An example of the time trace of one of the KID of the SPK-E array exposed to the alpha source. The blue line represents the mean of 102 traces induced in the KID number 6 by α particles. The exponential fits with one (red), two (green) or three (violet) time constants are plotted by the dotted lines, each one accompanied by the value of the reduced Chi-square. The variances were calculated over the pre-samples (almost 100 points).*

nearest KID show a strong peak with a rapid decay (few tens of μs), followed by a much slower tail (around 100 μs). The farthest pixels on the other hand show basically only this second exponential decay.

This can be explained if we assume that the ballistic phonons have a relatively short lifetime. After they are generated close to the particle interaction, ballistic energy is down-converted through anelastic scattering with impurities of the substrate or on the surface of the wafer. As a consequence, the pixels closer to the impact point are more likely hit by ballistic phonons that did not undergo any scattering. Then, once ballistic phonons have been down-converted to warm phonons, KID detect the relaxation of this lower-energy component to below the superconducting gap, which happens on longer time scales. In this picture, the farther pixels are only mildly affected by ballistic phonons, as only a small fraction of such phonons would be able to reach them before undergoing boundary or impurity scattering. On the other hand, they would still be able to sense the family of warm phonons generated by the downconversion of the original ballistic shower.

If this is the correct picture, than the different attenuation factor for near and far pixels can be easily explained. A strong enhancement in ballistic to warm down-conversion can be achieved through pair-breaking losses in additional metal layers. In this case, even the nearer pixels would have only a minor ballistic contribution, while most of the observed signal would be due to a cloud of warm phonons relaxing inside the substrate to energies below the aluminum gap.

In conclusion, the aluminum ground plane helps in reducing the energy detected by pixels

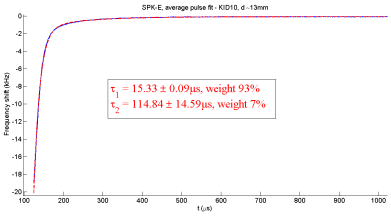

(a)

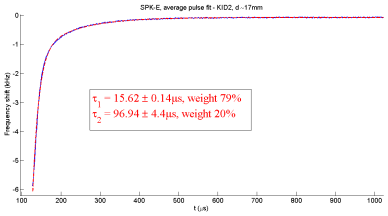

(b)

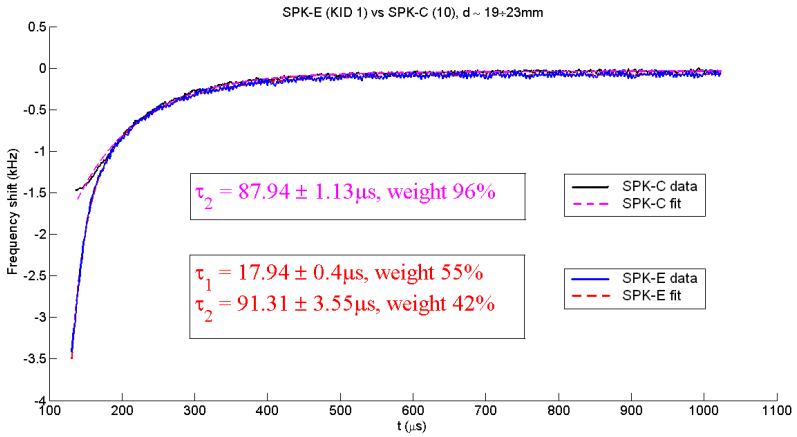

(c)

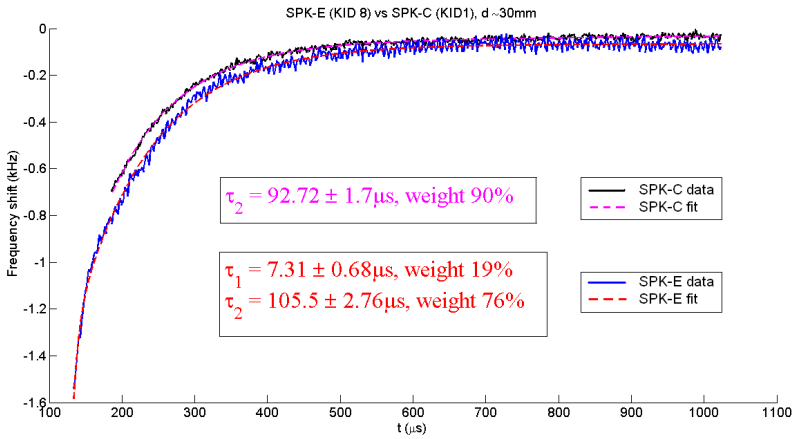

(d)

Figure 8.11: *Analysis of the time decay constants of the 'fall' part of the average pulse calculated for the SPK-E and SPK-C experiments. (a), (b) The average pulse (blu) with the corresponding fit (red) for KID close to the impact point on the SPK-E array. (c) Comparison between decay times on both the arrays for pixels near to the impact point. In the case without ground-plane, a fast component τ_1 related to the shower of ballistic phonons is evident and dominant with respect to the slower (τ_2) end of the pulse. Adding the ground-plane allows the ballistic phonons to switch rapidly to a lower energy levels. (d) The same comparison for pixels far from the impact point: in the case without ground-plane, there is a hint of a fast component τ_1. Its value is likely determined by the combined effect of the lifetime of ballistic phonon and that of quasi-particles. This fast component has a smaller amplitude compared to that relative to the warm phonons, which has a longer time constant (τ_2). In the case with ground-plane, the effect of the ballistic phonons can be neglected.*

at comparable distances. This additional metal layer reduces the array sensitivity to α hits by a factor ~ 2 on the farthest pixels. Presumably, the choice of the same superconductor material for the KID and metallization accounts for its limited effectiveness. In fact, ballistic phonons absorbed in the ground-plane are later re-emitted in the substrate with still enough energy to break Cooper Pairs in the detectors. This interpretation needs to be confirmed by investigating the effect of a superconducting metallization with a T_c well below that of aluminum.

8.5 The effect of an additional Ti layer on 'distributed geometry'

The critical temperature of Titanium is around 400mK, well below that of Aluminum. Therefore, adding a layer of such material could have a much stronger effect than what we obtained using the Aluminum ground-plane. In fact, each phonon absorbed in Ti will create quasiparticles that will rapidly scatter to energy levels just above its gap. As a consequence, the vast majority of the phonons re-emitted in the substrate are in this case expected at energy levels below the superconducting gap of Aluminum. To check the correctness of this prediction, we took two set of measurements on the same array, an SPK-D with uniformly distributed pixels and a full aluminum ground-plane on the front side. Between the two cool-downs, a layer of Titanium has been added on the backside of the wafer. In this case, since the array was exactly the same for the two runs, we could excite the same detectors in both configurations. This allows us to make more accurate comparison between the two data sets.

8.5.1 Correlation between signals from different KID

We placed the α source roughly between pixels 8 and 9. After the adding of the Ti layer, the KID number 10 was missing, so that eleven resonators were calibrated and read out (fig. 8.13-8.14). We then analyzed data signals coming from different KID, comparing the peak amplitudes for pixels lying on different areas with respect to the impact position. Referring to the inset images in figs. 8.15(a)–8.15(c), we will say that KID like 4 and 12 lie on the 'same side', while KID like 4 and 5 lie on 'opposite sides' with respect to the particle interaction, whose position is marked by a red cross. This analysis show a clear correlation of the signals coming from pixels lying on the same side of the impact point, and an anti-correlation for pixels lying on opposite sides. The linear and hyperbolic trends respectively correspond to the relationships $E_i/E_j \sim constant$ (correlated pixels) and $E_iE_j \sim constant$ (anti-correlated pixels), where E_i and E_j are the energies detected by the i-th and j-th KID. Referring to the x-y Cartesian axes drawn in inset figures, the variation of the y (x) coordinate of the hit position results in the linear (hyperbolic) trend, while the uncertainty on the x (y) coordinate

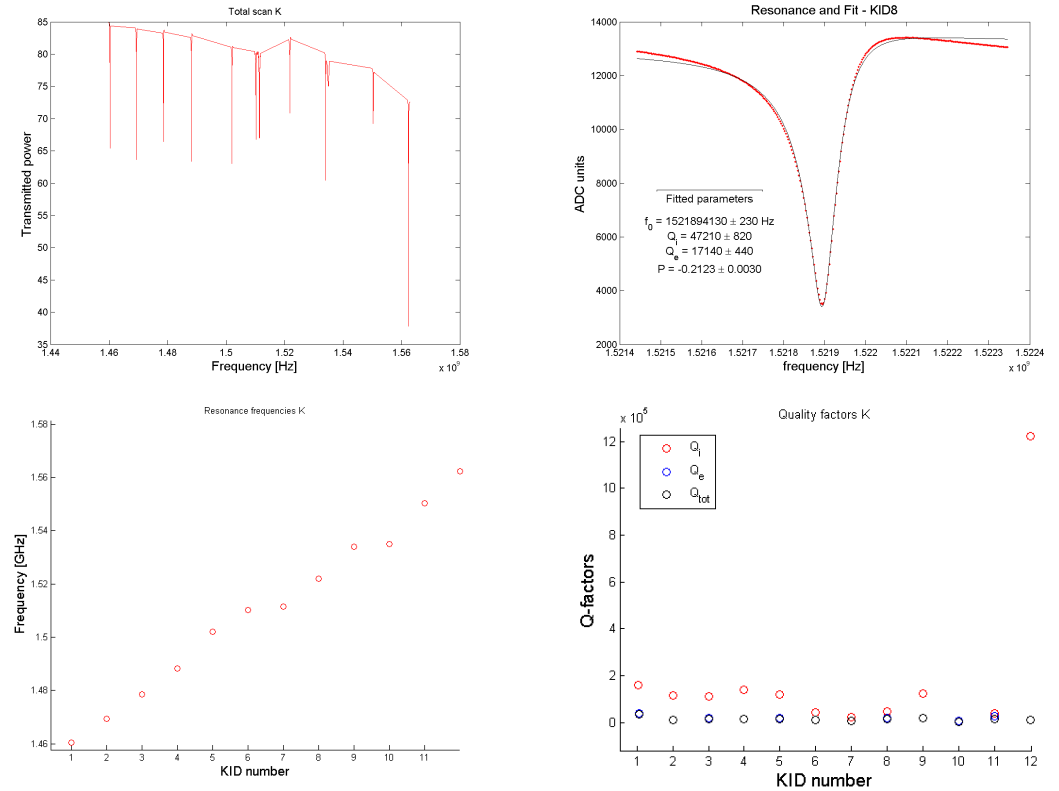

KID #	f_0 [Hz]	err f_0 [Hz]	Q_i	err Q_i	Q_e	err Q_e	Q_{tot}	err Q_tot	P	err P
1	1460321733.28	111.0225	1.7513e+05	5.0507e+03	2.1049e+04	885.7960	1.8791e+04	767.36	0.1479	0.0029
2	1469384900.23	145.4855	1.1566e+05	5.0255e+03	1.1838e+04	749.2881	1.0739e+04	818.60	-0.0648	0.0022
3	1478660971.97	134.7791	1.1179e+05	3.6124e+03	1.8657e+04	890.0600	1.5989e+04	922.55	-0.2666	0.0027
4	1488211628.83	146.1983	1.3807e+05	6.8753e+03	1.5998e+04	1.1683e+03	1.4337e+04	1.26e+03	-0.2739	0.0028
5	1502058122.86	187.1076	1.2036e+05	6.1401e+03	1.6290e+04	1.2178e+03	1.4348e+04	1.29e+03	-0.1431	0.0034
6	1510269194.91	296.5624	4.0528e+04	871.3286	1.0516e+04	326.5996	8.3493e+03	315.14	-0.0852	0.0030
7	1511423220.39	243.9887	2.2674e+04	225.0567	5.9276e+03	82.4004	4.6991e+03	80.19	-0.0018	0.0016
8	1521894134.60	228.3291	4.7205e+04	820.9601	1.7138e+04	435.2856	1.2573e+04	388.69	-0.2123	0.0030
9	1534075032.69	530.4970	1.2167e+05	1.6620e+04	1.9217e+04	3.8744e+03	1.6596e+04	4.04e+03	0.2811	0.0107
10	1535016078.56	179.1829	3.9646e+03	5.4310	5.0606e+03	9.2783	2.2230e+03	5.08	-0.0515	4.0334e-04
11	1550355744.39	329.9730	3.9519e+04	742.9823	2.5390e+04	669.6525	1.5458e+04	503.39	0.1036	0.0039
12	1562430510.86	32.3182	1.2246e+06	4.8645e+05	1.0355e+04	5.8409e+03	1.0268e+04	7.13e+03	0.0763	4.9690e-04

Figure 8.12: *Fitted parameters and calibration for the KID of the SPK-D array fabricated on HR-Si.*

of the impact point leads to the dispersion around this trend. This effect is highlighted by fig. 8.15(c), where we plot energy peak of KID4 vs KID5, as a function of the energy peak registered in KID 8. The higher its energy, the higher the ratio between the energies detected in KID 4 and KID 5, i.e. the higher the slope of the linear trend.

All these considerations are good indications that the energy damping dependency on d has a power law nature. In fact, if we denote with d_i and d_j the distances from the impact point of KID i-th and j-th respectively, then $d_i + d_j \sim c$ for opposite sides KID, while $d_i - d_j \sim 0$ for KID on same side. Then, the relationships $E_i/E_j \sim constant$ and $E_i E_j \sim constant$ follows directly assuming $E_i \propto E^{-d_i}$.

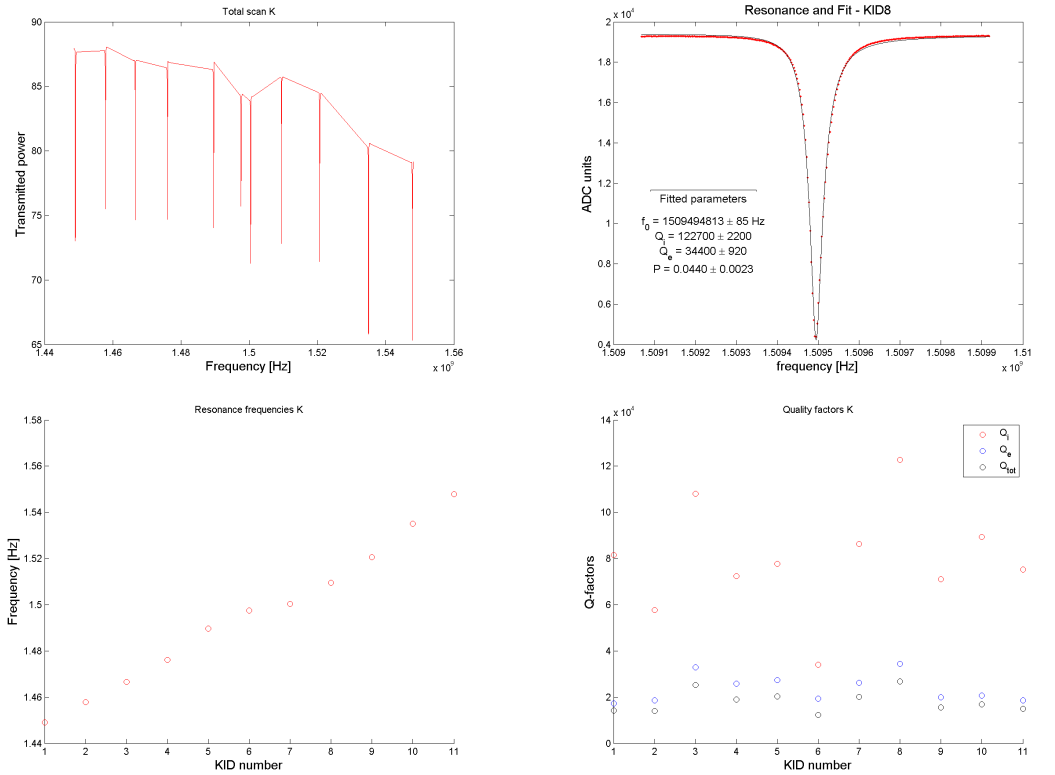

KID #	f_0 [Hz]	err f_0 [Hz]	Q_i	err Q_i	Q_e	err Q_e	Q_{tot}	err Q_tot	P	err P
1	1449022721.85	114.2714	8.1622e+04	1.5159e+03	1.7228e+04	470.6802	1.4225e+04	469.92	0.1826	0.0020
2	1457879041.34	94.0349	5.7614e+04	544.3501	1.8583e+04	254.9872	1.4051e+04	234.09	-0.0859	0.0014
3	1466580968.08	77.7257	1.0798e+05	1.5878e+03	3.2997e+04	710.7952	2.5274e+04	659.15	0.0449	0.0020
4	1476066186.78	70.7616	7.2460e+04	622.3744	2.5871e+04	326.8973	1.9064e+04	291.26	-0.2143	0.0014
5	1489610781.57	112.8824	7.7796e+04	1.1381e+03	2.7445e+04	592.0749	2.0288e+04	528.83	-0.2269	0.0023
6	1497596790.59	109.7025	3.4010e+04	194.5918	1.9402e+04	154.7271	1.2354e+04	121.26	0.0353	0.0012
7	1500445147.52	122.1061	8.6308e+04	1.5610e+03	2.6317e+04	695.9012	2.0167e+04	646.06	-0.0745	0.0025
8	1509494812.77	84.7400	1.2273e+05	2.2261e+03	3.4400e+04	915.8948	2.6869e+04	865.61	0.0440	0.0023
9	1520658862.48	69.7786	7.1053e+04	611.6003	1.9888e+04	249.8503	1.5539e+04	236.64	0.0779	0.0012
10	1534996101.91	61.9623	8.9341e+04	899.6499	2.0784e+04	307.0320	1.6862e+04	301.47	-0.1072	0.0012
11	1547832894.05	182.1709	7.5169e+04	1.8181e+03	1.8681e+04	661.2734	1.4963e+04	641.52	0.1101	0.0030

Figure 8.13: *Fitted parameters and calibration for the KID of the SPK-D array fabricated on HR-Si, with the additional backside titanium layer.*

8.5.2 Impact position

We can apply again the method used in par. 8.4.3 to calculate the distance d between the KID and the hit positions. The result of this analysis for the SPK-D array, before adding the Titanium layer, are shown in (fig. 8.16(b)–8.16(f)). This time the α hit the center of the array (fig. 8.16(a)), so we have KID positioned all around the particle interaction. This allows us to better triangulate the signals and results in a much more accurate estimation of the impact point (fig. 8.16(b)–8.16(c)), which in turn reflects in a more symmetric distribution of its estimated coordinates (fig. 8.16(e)–8.16(f)).

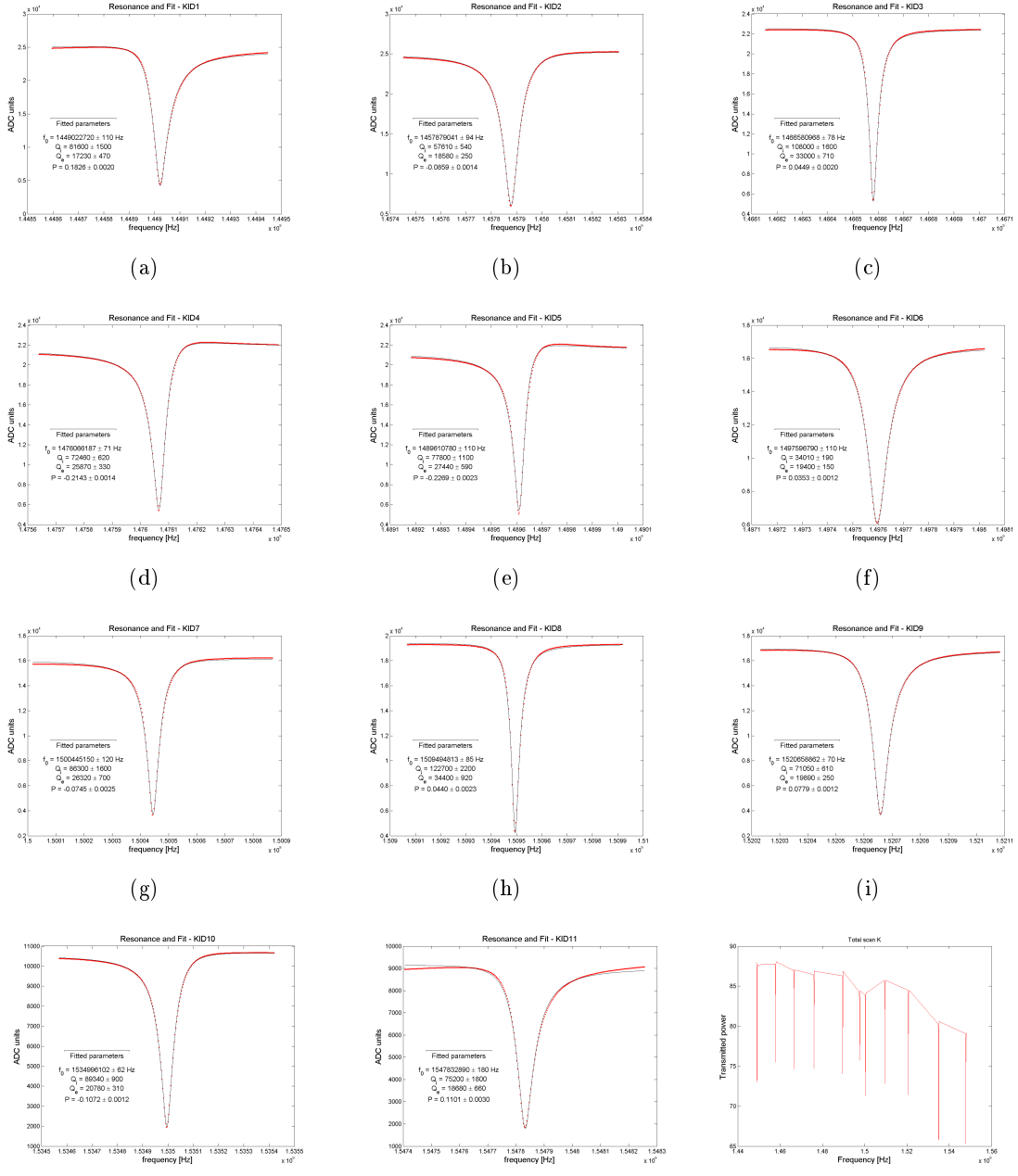

Figure 8.14: *All the active resonances (data and fits) of the SPK-D array fabricated on HR-Si, with the additional backside titanium layer.*

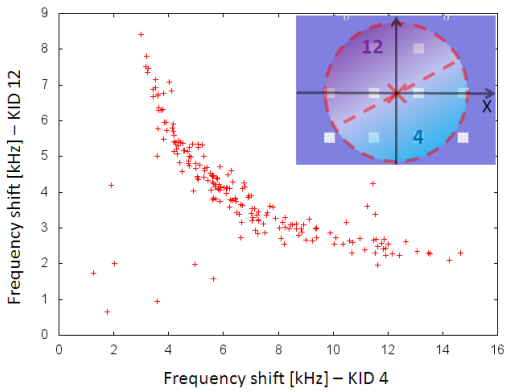

(a)

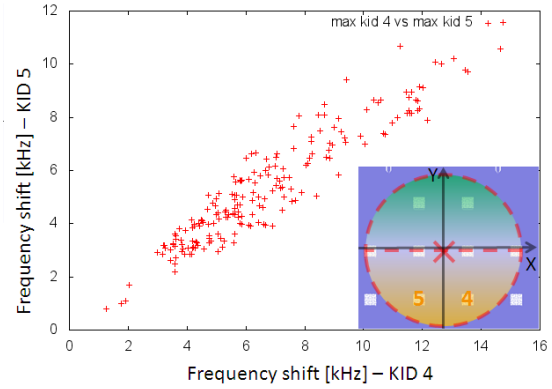

(b)

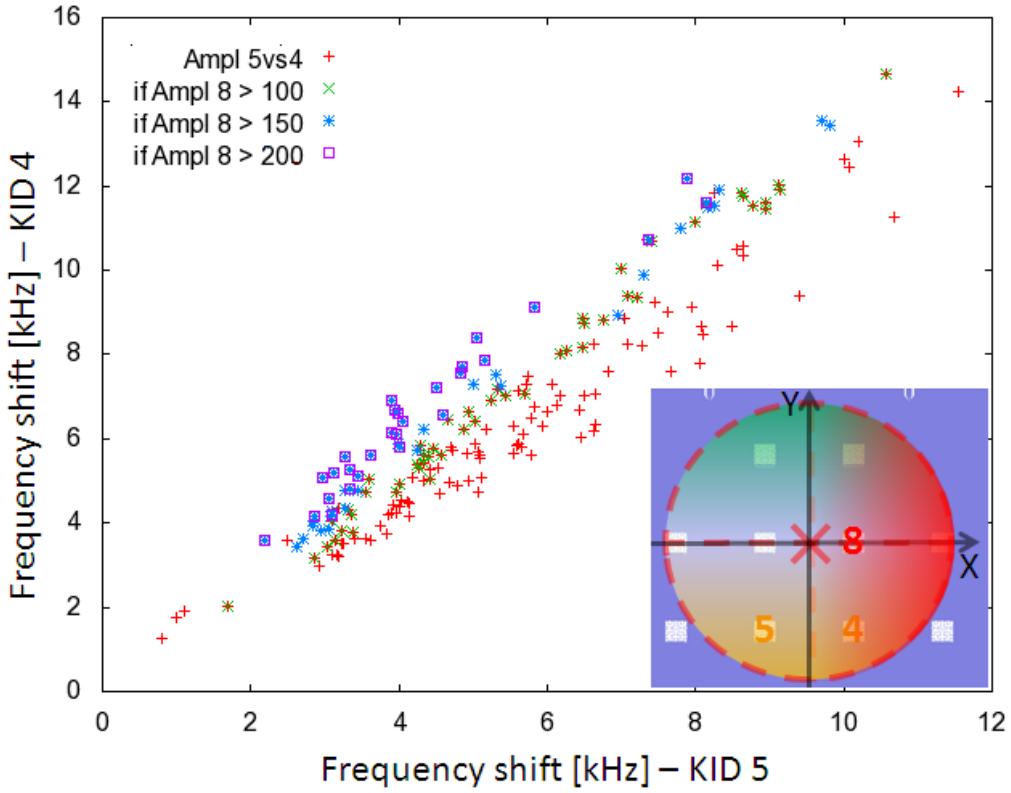

(c)

Figure 8.15: *(a) A plot of the calibrated peak amplitude for KID 12 versus KID 4, two pixels lying on opposite sides with respect to the hit point), and (b) for KID 5 versus KID 4, two pixels lying on the same side of the impact point. (c) The same plot (but inverting the axes), as a function of the energy peak registered in KID 8. KID 4 and 8 lie on the same side, so the higher the energy measured by KID 8, the higher that detected by KID 4. This translates in a larger ratio between the energies detected in KID 4 and KID 5, which in turn increases the slope of the linear trend.*

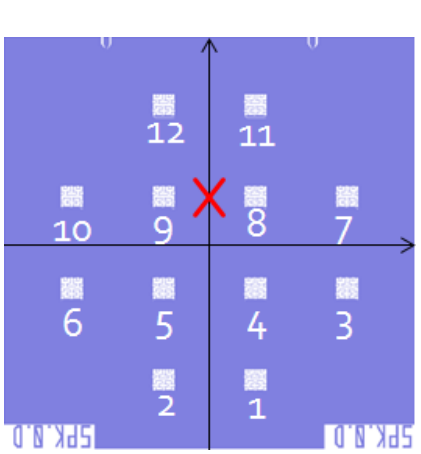

(a)

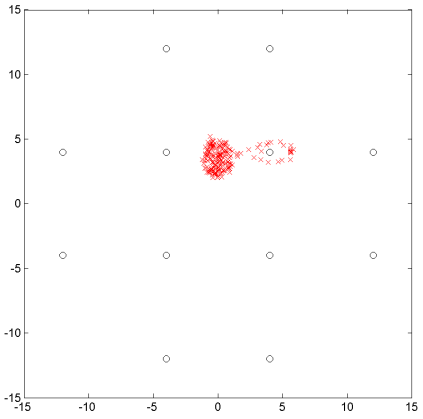

(b)

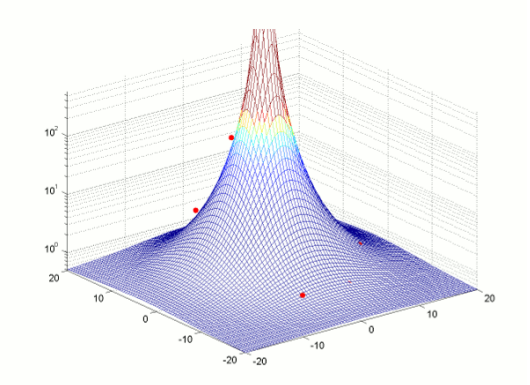

(c)

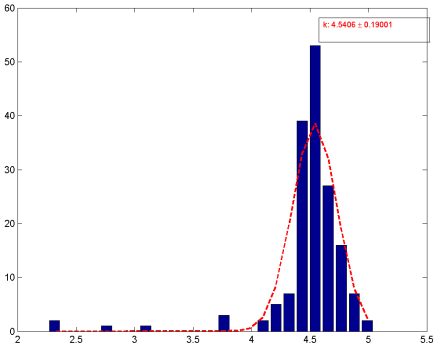

(d)

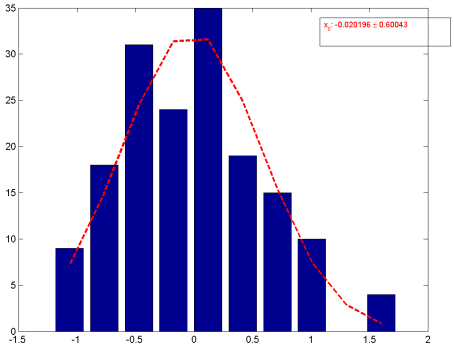

(e)

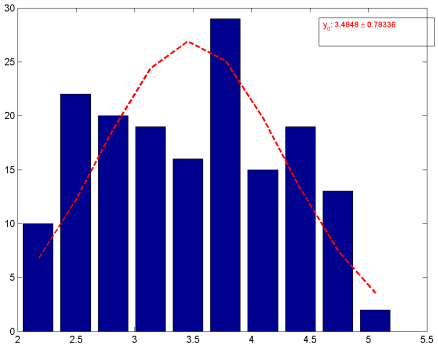

(f)

Figure 8.16: *Measurements performed on SPK-D array exposed to a ^{241}Cm source. In the first row: (a), the positioning of the detectors with respect to the collimator, highlighted by a red cross ; (c), an example of the 3-dimensional fit applied to one alpha particle hit and (b) the 2-dimensional projection of the fitted position of all the α hits. The position of the KID is given onto the x-y plane, and the peak amplitude of their signals in plotted onto the z axis by the red points. KID number 6, 7 and 10 showed low quality factors and were not used in the fit. Histograms of the fitted x (e) and y (f) position of the impact point, and the power law (d)*

8.5.3 Energy damping

Having determined the position of each impact, we can now study the amplitude of the peak as a function of the distance d from it. Our purpose is to compare the energy propagation inside the substrate with and without the Ti layer on face-back on the array. As it can be noticed by the histogram of the observed coincidences (fig. 8.17(a)), the situation changes radically adding the Titanium. Even the very energetic α particles ($\sim 5 \div 6 MeV$) produce a detectable signal only in the pixels nearer to the impact point (4, 5, 8 and 9) (fig. 8.17(b)). We stress again that such energy is about 30 times higher than the one we expect as a consequence of a CR impact in space. The Titanium layer is therefore, as expected, very effective in suppressing the phonon propagation inside the substrate, strongly dampening their energies to below the gap of the aluminum.

To better quantify this effect we can consider the average pulse observed by each pixel. Doing so, even in the furthest pixels we manage to see a very small pulse, corresponding to a frequency shift of only $\sim 100 Hz$. Comparing the average pulses in the two cases, we see that for almost all the pixels we observe a reduction in the peak amplitude by a factor ~ 10, the only exception being pixels 4 and 5, likely as a consequence of a slight offset in the positioning of the α source (fig. 8.18(a)). The fig. 8.17(c) shows the damping of the energy propagation in the substrate as function of the distance from the impact point. The power law fit gives powers of 4.42 ± 0.05 and 3.56 ± 0.37 respectively for the cases with and without Titanium. As expected, the Ti layer is much more effective than Al in attenuating the signal over the distance.

8.5.4 Decay times

We want now to quantify the effect on phonons relaxation times. We compare the average pulses for KID at comparable distances from the impact point, but on the array before and after adding the Ti layer. As previously commented, the KID on the array with Ti have a smaller peak amplitude (fig. 8.18(a)). There is however another significant effect: the SPK-D array with Ti shows a faster decay of the signal (fig. 8.18(b)) with respect to that of the array without Ti.

The pixel closer to the impact point (KID 4) show two decay time constants in both the cases. According to picture, the first is the mean-life of the ballistic phonons that hit the detectors directly, i.e. without undergoing any down-conversion process. The ballistic phonons are then down-converted through anelastic boundary and impurity scatterings. The pair-breaking mechanism in the additional superconducting layers (i.e. aluminum ground-plane, titanium film, ecc.) introduces an extra down-conversion channel in the system. The result is the conversion of the ballistic population in warm phonons. The second time constant represents the relaxation of this component to below the aluminum energy gap. The data

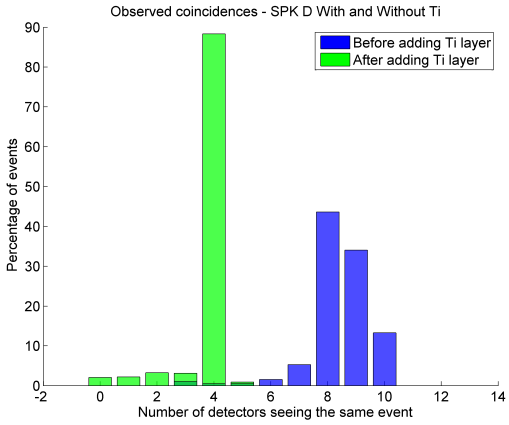

(a)

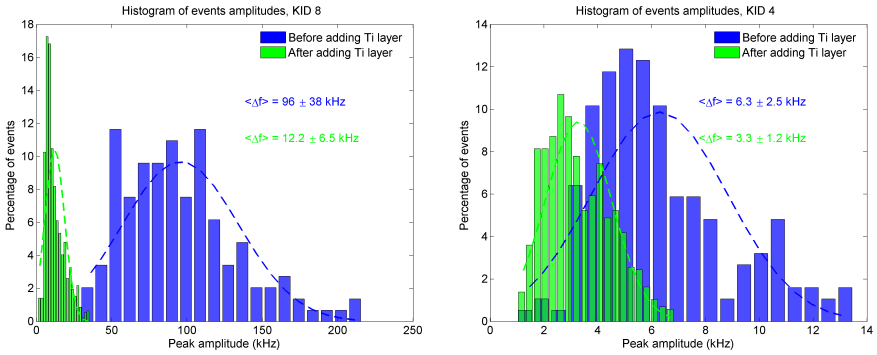

(b)

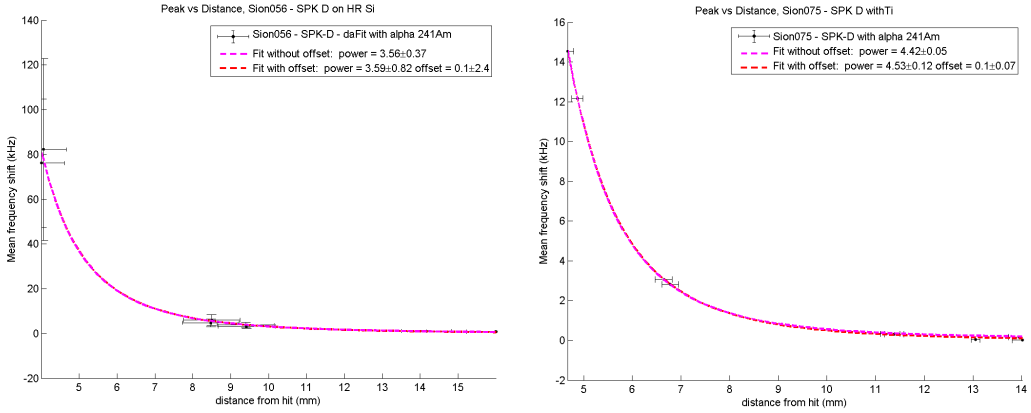

(c)

Figure 8.17: *(a) Histogram of the number of coincidences observed using an α source on the SPK-D array, before and after adding a Titanium layer. (b) Histogram of the peak amplitudes observed by two pixels lying near the impact point of the high energy particles. The small decrease in the amplitudes observed by pixel 4 and 5 is probably a consequence of the radioactive source being placed nearer to them during the second cooldown. (c) attenuation of the peak signal of the average pulse in function of the distance d from the mean position of the impact point $(\bar{x}, \bar{y})$. Before adding the Ti layer, $(\bar{x}, \bar{y})$ was estimated using the histograms 8.16(e) and 8.16(f); while after adding the Ti layer, we used the 3D-fit of the impact position of the average pulse.*

show that both these processes are sped up by the presence of the additional Ti layer (fig. 8.18(b), left).

Its effect is even more evident in the farthest pixels (fig. 8.18(b), right). Without the Ti, the time evolution of the pulse is dominated by the down-conversion of warm phonons below the aluminum gap, over time scales of order of $100\mu s$. On the contrary, adding the Ti, the signal shows only a very small pulse, with a rapid decay over time. This is to ascribe to the fraction of the ballistic phonons directly reaching the detectors. Being very tiny ($\sim 100Hz$), this component is likely hidden in the farthest KID when there is no Ti layer (KID 1).

To conclude, the Ti layer is not only able to speed up the ballistic to warm phonons transition, but also the thermalization of the latter component to below the Al gap. This is due to the high efficiency of the pair-breaking losses inside the titanium. With a $T_c \sim 400mK$, most of the warm phonons that the Ti re-emits are unable to break pairs in the Al. The tail corresponding to their relaxation is thus not observed in the furthest pixels.The small pulses that they show are likely due to the (very tiny) fraction of ballistic phonons that manages to reach them directly without interacting with the metal layers. Their time evolution is in fact accordingly very fast, around $10\mu s$, in good agreement with what was observed during the measurements on the SPK-E.

8.6 Comparing rise times

Using the mean time traces, we have fitted the rise times of the signals for the four arrays we have tested with α particles:

1. **SPK-E**: 'island' geometry without ground plane, hits in the corner;
2. **SPK-C**: 'island' geometry with Aluminum ground plane, hits in the corner;
3. **SPK-D**: 'distributed' geometry with Aluminum ground plane, hits in the center;
4. **SPK-D + Ti**: 'distributed' geometry with Aluminum ground plane and additional backside Titanium layer, hits in the center.

The calculated time constants are plotted in fig. 8.19 as a function of the distance d from the α interaction point. The results clearly show some trends. Without ground plane, the rise-time does not change with d. Adding the Aluminum ground plane, the furthest pixels need more time to reach their peak energy. This can be interpreted as follows. As already said, a part of the phonons that are propagating in the substrate are transmitted to the ground plane. Here they undergo down-conversion through a quasi-particles generation/recombination mechanism (that we named pair-breaking losses). Besides reducing the phonons energy to just above the Aluminum gap, this process also delays the restitution of this energy to the substrate. The

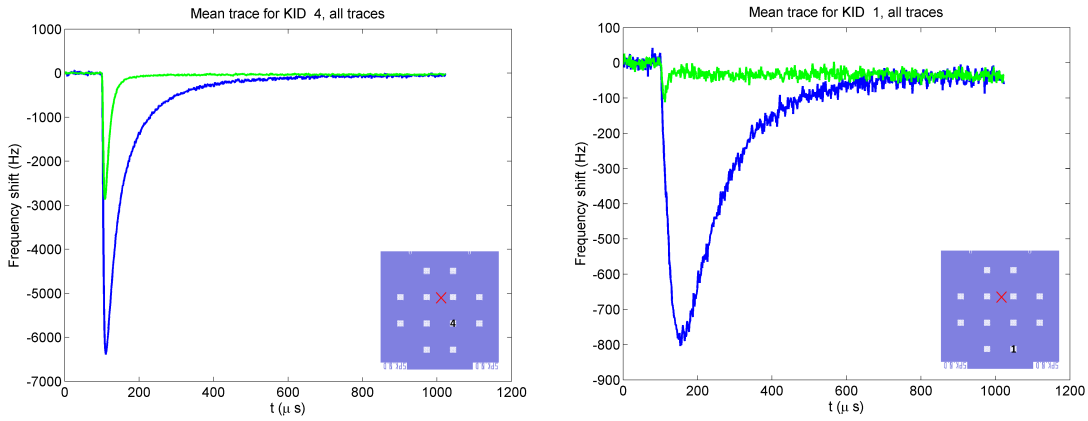

(a)

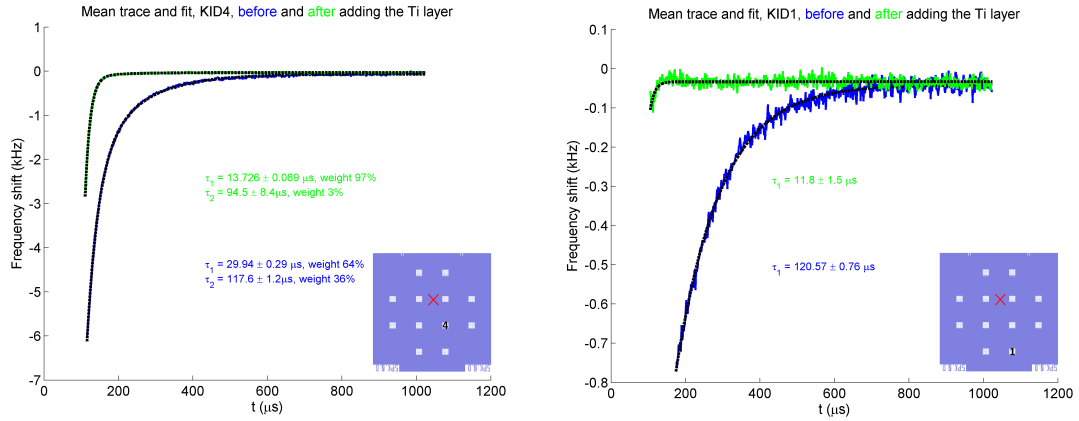

(b)

Figure 8.18: *An example of the signals observed before (blu) and after (green) adding the Titanium layer on faceback of the SPK-D array.(a) The average pulse of a pixel far from the impact point (on the left) and near to it (right). (b) An example of the fitted decay time on the 'fall' average pulses.*

larger the distance between the particle interaction and the detector, the larger the metallized surface interposed between them. This means that there is a larger retard in the recollection of the delayed energy, and the rise time of the detectors increases accordingly with the distance.

The data hint that introducing an additional Titanium layer restores a flat trend with distance. As already commented, its critical temperature (ans so its gap energy) are almost 3 times lower than that of Aluminum. This means that now the phonon energy is returned to the substrate well below the Aluminum gap, making it undetectable by KID. The signal is therefore induced only by the ballistic component that does not undergo down-conversion in

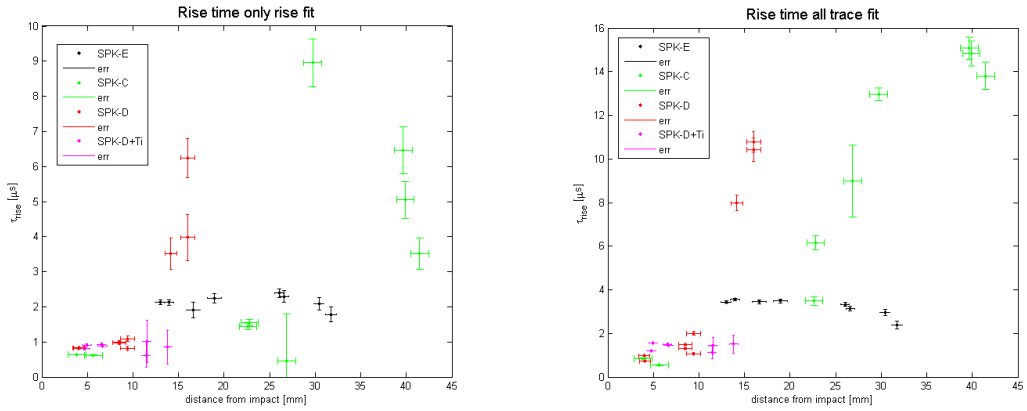

(a) (b)

Figure 8.19: *Rise times (τ_{rise}) plotted in function of the distance from α impact position for the four different arrays tested. τ_{rise} follows by fitting the data with a sigmoid function. The fitted values were calculated on the 'rise' time trace (a) (par. 8.2), or on the whole time trace (b). In the latter case, the sigmoid multiply all the fall contributions. This accounts for the fact that the signal start to decrease also during the rise.*

the metal layer, resulting in a rise of the signal independent by the impact position. Although this needs to be confirmed, this interpretation well explains our data and is in agreement with what we observed on the decay times.

8.7 Long decay time constant

We have analyzed the signals induced by $\sim 6MeV$ α particles in different arrays. The data always suggest the existence of a slower time constant (a few milliseconds). In order to confirm its effective presence, we need to perform acquisitions with longer time traces. As already said, the memory of our FPGA board was limited to the acquisition of a maximum of 1000 points over a fixed number of tones (12). This means a total time trace of about $2ms$ at the lowest sampling rate ($500Hz$), not sufficient to give a reliable estimation of this long time constant. We thus modified the FPGA firmware in order to deploy all the available memory for one single tone. In this case we cannot acquire more than a KID at a time, but we get temporal traces $32ms$ long. We repeated the last experiment (SPK-D array with Ti) with the modified electronics and we acquired 1000 α particle event on the KID 8 at a $500kHz$ sampling rate. We then calculated the average mean pulse and fitted its 'fall' part using the usual exponential function.

As can be notice from the fig. 8.20, the average pulse fit requires at least three time constants. The introduction of a fourth parameter doesn't enhance appreciably the quality of

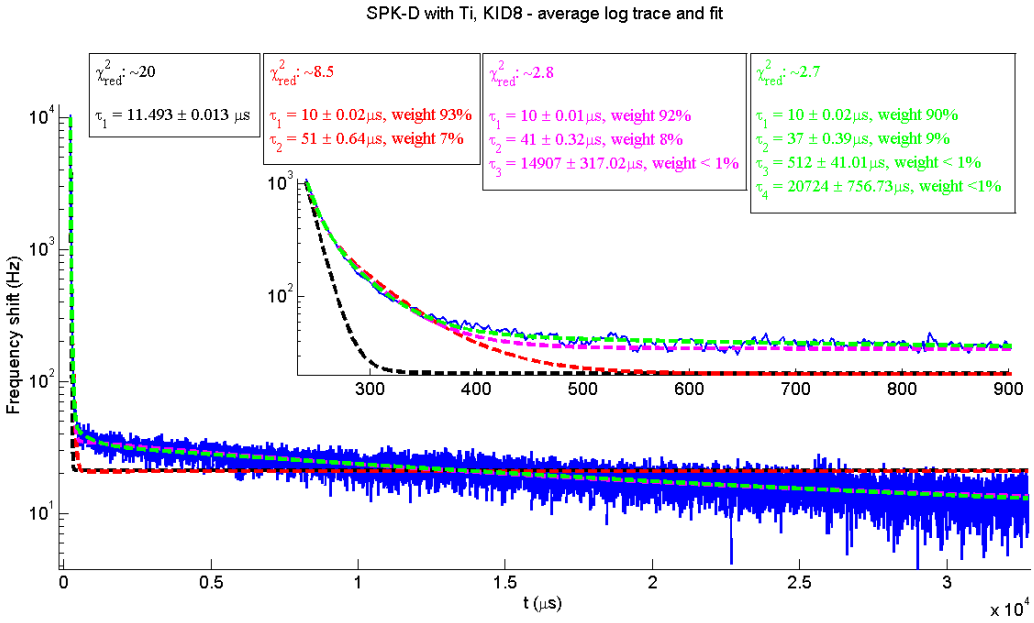

Figure 8.20: *Semi-logarithmic plot of the average pulse of long time traces ($\sim 32ms$) acquired on the SPK-D array with the Ti layer exposed to a ^{241}Am. The data (blue) are fitted using one (black), two (red), three (purple) or four (green) decay exponential time constants. The fitted values and values and errors are shown in the top inset squares, together with the corresponding reduced Chi-square value. The introduction of the fourth time constant does not enhance significantly the quality of the fit.*

the fit. In any case, we confirmed the existence of a third, much slower time constant, whose value is estimated around $15 \div 20ms$. The peak amplitude of this component is calculated to $\sim 40Hz$ (fig. 8.21). This is the same value that we found observing all other KID, and is in agreement with the signal offsets measured on all the other arrays $\sim 1ms$ after the trigger due to the α particle interaction. This non-zero signal might depend a tiny change in the temperature of the wafer. This is due to a third population of phonons, the *thermal phonons*, which accounts for the temperature of the substrate. If this is the correct explanation, we could calculate the expected signal induces in our detectors by an α particle releasing an energy of $\sim 6MeV$ in the silicon substrate. We refer to [130] and calculate a volumetric heat capacity of $71 \cdot 10^{-14} J/K/mm^3$ for silicon at $105mK$ (base T of this experiment). Our wafer has a volume of $(36 \times 36 \times 0.35)mm^3$, from which we calculate a heat capacity of $3.22 \cdot 10^{-10} J/K = 2.1GeV/K$. This means that an α particle with energy between $5.4 \div 5.9MeV$ completely absorbed in a our silicon substrate results in a increase of its temperature of $2.6 \div 2.8mK$. From the NIKA campaigns we measured a temperature sensitivity $\sim 15Hz/mK$ on the $2mm$ array, whose KID geometry was exactly the same our detectors (par. 4.4). Finally, the expected signal due to the heating of the substrate as a

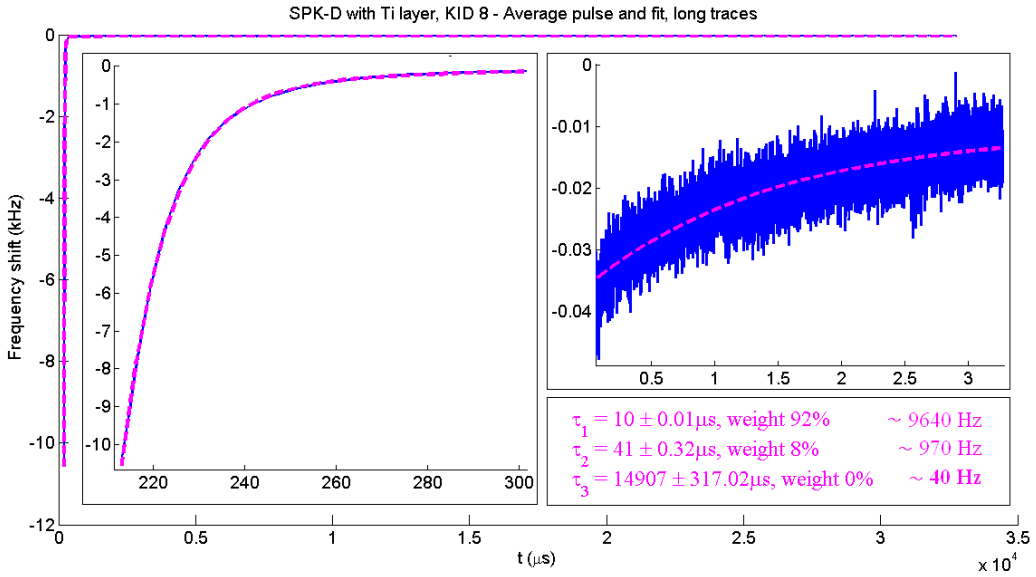

Figure 8.21: *The average pulse (blue) plotted with the three decay constants fit (purple). The inset zooms show the initial and final parts of the time trace. The fitted decay times and their errors are shown in the bottom right inset, with the relative weight and the absolute amplitude of each component. The fit estimates a* $\sim 40Hz$ *peak amplitude for the slowest component.*

consequence of a $5.4 \div 5.9 MeV$ *alpha* particle is $39 \div 42Hz$, in perfect agreement with our observations. The slowest time constant is therefore of thermal nature, and we thus call it *thermal decay time*. It represents the velocity in evacuating the excess of energy from the wafer to the sample holder, and leads to an estimation of the thermal conductance of $160 \div 220 \cdot 10^{-10} W/K$.

Having ~ 30 times less energy than an *alpha* particle, the expected thermal signal for a primary CR interaction in KID array is $1.4Hz$. This is a signal detectable by NIKA (4.4) and surely within the sensitivity required for future KID-based high-precision space mission. Therefore the thermal time constant, calculated in about $15ms$, must be reduced to sub-ms values. This can be achieved by optimizing the thermal link between the array and the sample-holder, which is currently realized by four, small clamps. Providing a better thermal contact with the bath at $\sim 100mK$ should thus not be a problem. This will improve the conductance and lead to considerably faster thermal decay times.

8.8 X-rays measurements

As a final measurement, we want to determine the Pair Breaking efficiency η_{pb} of our detectors (par. 2.6.4). In order to maximize the fraction of energy collected by the detectors, we used

the array without ground plane (SPK-E), exposed to the ^{109}Cd source producing photons of $20.1keV$. The collimator had an aperture of $\sim 8mm$, larger than that used for the α particles experiment. We mounted it in front of the central island.

We acquired 1000 pulses at the base temperature of $106mK$ and at a sampling rate of $\sim 1MHz$ for six KID, two of whom belonging to the target central island. We set the threshold at 7σ, where σ indicates the mean RMS of the signal calculated over the first 50 points of each time trace, before the peak. Coincidences have been observed only between the two pixels belonging to the target island. We observed an important noise on these two pixels, due to the crosstalk between the corresponding FPGA tones. This noise reduced the performances of the pixel with the highest energy pulses and completely prevented any analysis on the other one. We thus characterized only the first resonance, i.e. the KID likely closer to the impact point, performing the usual frequency shift - phase signal calibration (fig. 8.22(a)–8.22(c)). Figure 8.23 shows its average pulse plotted together with its temporal fit. We focus the attention on two results:

- there isn't any long time constant and the signal returns to values around zero within $\sim 1ms$. This is coherent with what we expect, since a released energy ~ 300 times lower than α particles produces an heating of the substrate of about $\sim 10\mu K$. This should result in a frequency shift signal well below $1Hz$, which we are not able to detect;

- the time constants can be compared to that obtained with the α particles experiment on the same array. In that case, we interpreted the fast component of the signal as the combined effect of the ballistic phonons and quasi-particles lifetimes. Considering the X-ray experiment and referring to the three-parameters fit, the fast component $\tau_1 = 8\mu s$ seems to reflect only the quasi-particle lifetime, and agrees with the values calculated for our film at the base temperature (par. 8.3). Then, $\tau_2 = 46\mu s$ likely represents the ballistic phonon component, consistent with the increased ballistic lifetime near to the impact point observed with the α (par. 8.4.6, fig.s 8.11(a)–8.11(d)). The last time constant, τ_3, could finally be ascribed to the warm phonon component. These hypotheses need to be confirmed with dedicated experiments.

In order to calibrate the frequency shift δf (fig. 8.24(c)) in term of a temperature variation δT, we measured the resonance at different temperature T (fig. 8.24(a)). We then use eq. A.10 to relate δT to the variation of the number of quasi-particles $\delta N_{qp} = \delta n_{qp}/V$ (fig. 8.24(b)), where V is the volume of the resonator calculated from the pixel dimensions. Considering that the total area sensitive to the phonons includes both the meander and the capacitor, we estimates an effective superconducting volume of $V = 17086\mu m \cdot 6\mu m \cdot 0.02\mu m = 2050\mu m^3$. Using the calculated value of the gap for a $20nm$ thick Al detectors $\Delta \approx \Delta_0 = 210\mu eV$ (par. 4.2.2) and assuming $N_0 = 1.73 \cdot 10^10 \mu m^{-3} eV^{-1}$ (eq. A.2) , we find the detected energy

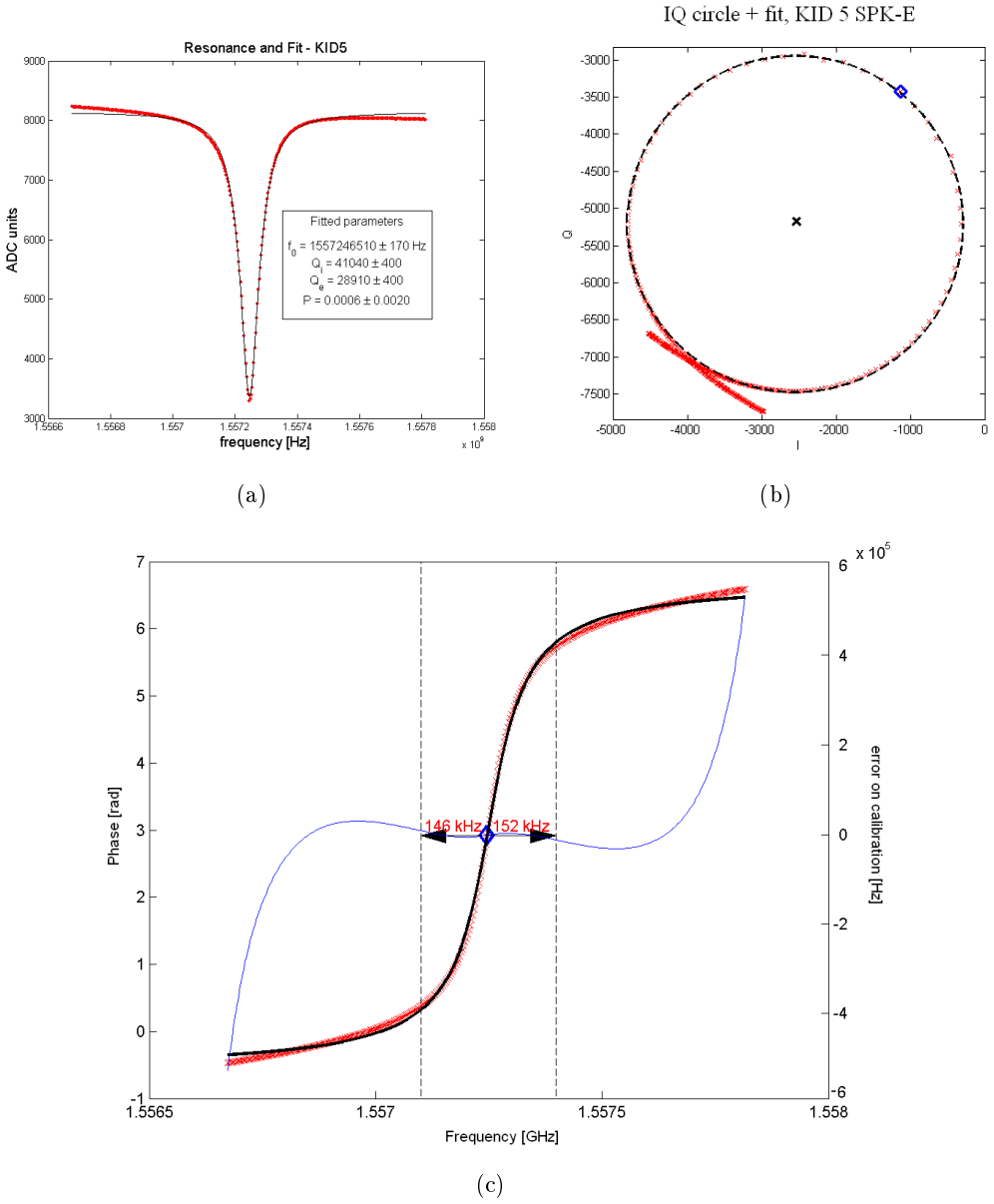

(a) (b)

(c)

Figure 8.22: *Characterization and calibration of the KID number 5 of the SPK-E array exposed to a* ^{109}Cm *X-ray source. The data are plotted by red points (or crosses), while the fit are represented the black lines (solid or dotted). (a) The resonance amplitude versus frequency plot, with the corresponding fitted parameters; (b) the IQ-circle in the complex plane, with its fitted center (black cross) and the selected working point (blue diamond); (c) calibration of the phase with respect to the center of the IQ-circle in unit of resonance frequency shift. The blue curve represents the error in the frequency calibration, considered valid within the range* $\pm 10kHz$ *(vertical dotted lines).*

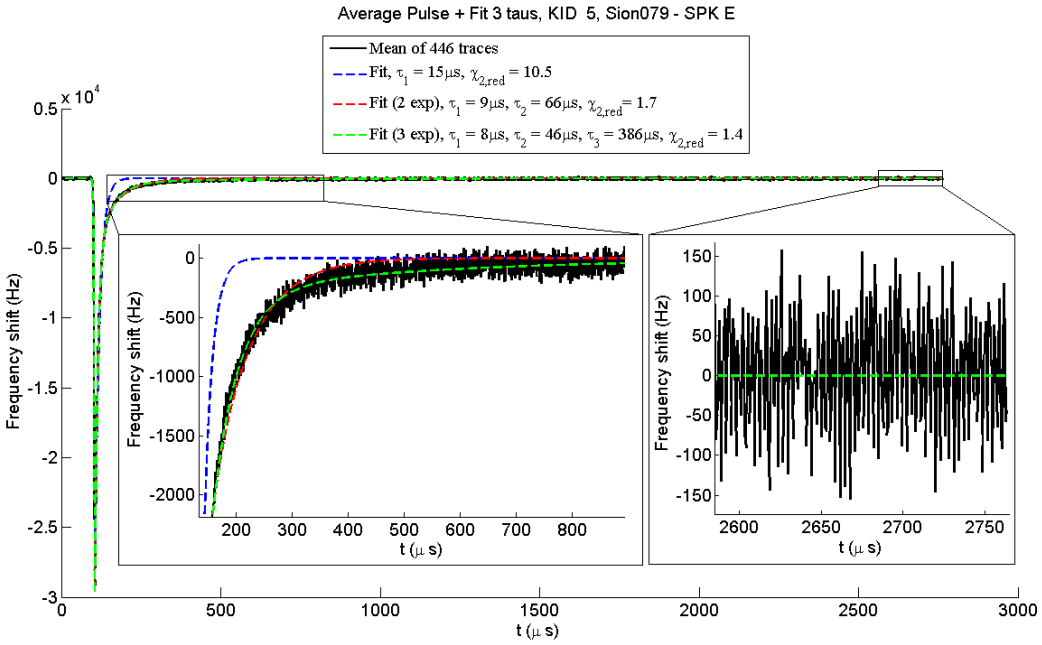

Figure 8.23: *The average pulse (black line) induced by the ^{109}Cm on the KID5 of the SPK-E array, with different exponential fits (dotted lines). The reduced Chi-square values show that three time constants are sufficient to fit the data. The left inset zooms the initial part of the pulse, while the right inset highlights the absence of signal in the final part of the temporal trace (after $\sim 2.6ms$).*

$E_{det} = \delta n_{qp}\Delta$ (fig. 8.24(d)) and the Pair Breaking efficiency as $\eta_{pb} = E_{det}/E_{in}$ (fig. 8.24(e)), with $E_{in} = 20.1keV$ in our case.

The measured efficiency is thus $\eta_{pb} \approx 1.9\%$, with maximum values not exceeding $\sim 5\%$. The minimum detectable signal for a 7σ threshold is roughly $190eV$, corresponding to a minimum detectable energy at 1σ level of $E_{RMS} \sim 27eV$. As previously explained, this relatively high value is caused by the the strong crosstalk between the pixels of the target island. This results in a very high noise observed in the KID, which has an RMS in unit of frequency shift of $\sigma = 817Hz$. In order to reduce this noise, the measurements have been repeated at the same sampling frequency turning off the less responsive KID, but unfortunately the acquisition was mistakenly aborted before reaching a statistics of 1000 events. Nevertheless, we can deploy these data calculating the ratio between the RMS in these two configuration. The RMS of the active KID was $\sigma = 431Hz$, 1.9 lower than before. This improves the minimum detectable signal by the same factor, so that $E_{RMS} \sim 14eV$. Further improvements should be easily obtained reducing the sampling rate and removing possible noise spectral lines at specific higher frequencies (see par. 9.5). Besides being partly affected by the same problematics, the current poor energy resolution of $\sim 380eV$ is principally due to a poor collimated beam.

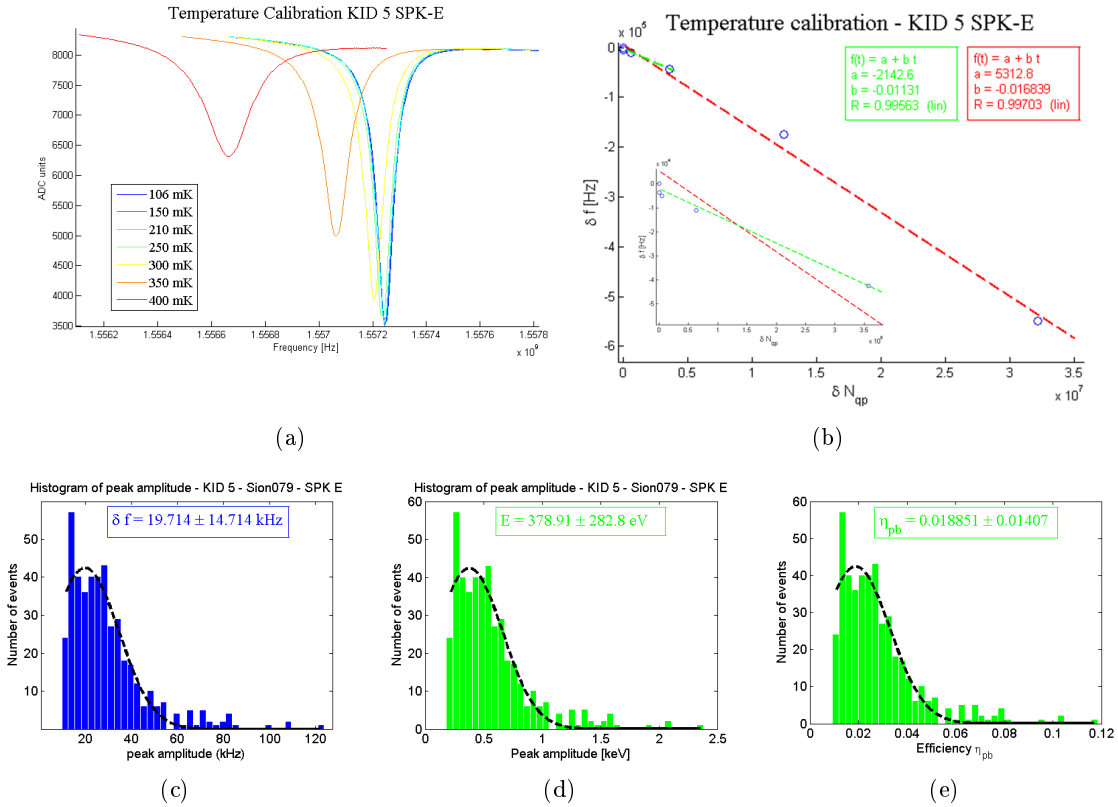

Figure 8.24: *The temperature calibration of the KID5 of the SPK-E array: (a) the shape of the resonance changing at different temperatures; (b) the shift in frequency calibrated with the calculated change in the quasi-particle number at a given temperature, by a linear fit using all (red) or only the first five temperature values (green); (c) histogram of the peak amplitude calibrated in units of frequency shifts δf and (d) absorbed energy E, with (e) the corresponding pair-breaking efficiency. A gaussian fit (black dotted curve) is applied to each histogram.*

The spatial distribution of the impact points over a large area widens the energy distribution in a single detector readout. A multi-channel readout will provide a decisive improvement of this value, strongly narrowing the spectrum calculated adding signals from different pixels.

8.9 Conclusions

One of the main advantages when using KID instead of bolometers is related to their typically faster time constants. Especially in space environments, where the detectors are continuously exposed to an intense flux of high energetic particle, the faster response of the detectors reduces the time losses allowing to save more observational time. For our detectors, we measured quasi-particle lifetimes of $\sim 10\mu s$ and phonon decay times in the range $\sim 30 \div 120\mu s$, in agreement with literature. The existence of a third, much slower time constant has been confirmed,

whose value was measured in $\tau_{slow} \sim 15ms$. Consideration on the thermal sensitivity of our detectors led us to conclude that this decay time has actually a thermal nature, with a calculated conductance of the order of $2 \cdot 10^{-8} W/K$. For comparison, a typical bolometer with a $1\mu m$ SiN membrane fabricated in our laboratories has measured thermal conductance of about $0.7nW/K$ at 300mK. At temperatures 3 times lower we can expect values of $10^{-10} W/K$, reasonable when compared to what we measure ($\sim$ 200 times higher). The optimization of the thermal contact between the array and the sample holder should improve this value, sensibly reducing the τ_{slow}. By taking the dominant time constant of the order of a few hundreds of microseconds and assuming a single CR to affect the whole substrate, a typical kilo-pixels array (NIKA-like) hosted on a single silicon die of $\sim 10cm^2$ would suffer a data loss comparable to that of one single Planck bolometer, e.g. within $\sim 15\%$.

We tested different solutions, such as membranes or multilayered structures to hinder the phonon propagation or low resistivity substrates to enhance their thermalization. For they time being though they did not prove effective, often as a consequence of the extra noise they induce. This increases of about 1 order of magnitude in low resistivity silicon ($0.5 \div 1 Ohm \cdot cm$) compared to the high resistivity one ($> 1kOhm \cdot cm$), convincing us in focusing on the latter solution.

The measurements performed with secondary CR on HR-Si indicated that additional metal layers represent a possible solution for confining the effect of higher energy phonons to shorter distances. In order to increase statistics, we used sources of α particles having energies 30 times higher ($\sim 6MeV$) than that of the typical CR. The tests carried out so far with α confirm that the use of metallization layer can play a crucial role in limiting the effect that CR impacts can have on the arrays and on the total data loss to be expected during a satellite mission. An Aluminium layer helps the ballistic to warm phonons downconvertion. On the other hand, it is not capable of lowering the energy of the phonons to below its energy gap, so that their thermalization does not become sensibly faster. For this reason we carried out tests using a superconductor with a lower energy gap such as Titanium. The improvement in this case is much more pronounced, as the Titanium layer shifts very rapidly almost all the phonons to energetic levels below the Aluminium gap. Both the peak amplitude of the observed glitches and their decay time constants decrease in this case. Although correctly quantifying this damping is still difficult in our experimental conditions, a preliminary analysis demonstrates that the presence of the Ti layer enhances the peak amplitude attenuation as function of the distance d from the impact point, increasing the fitted power law exponent from 3.6 to 4.4. On the other hand, we estimated ballistic phonon velocities of $\sim 2mm/\mu s$, in agreement with literature, and we demonstrated that their propagation inside the substrate is strongly suppressed over the distance d. Without Titanium layer, both ballistic ($\sim 30\mu s$) and warm ($\sim 120\mu s$) time constants are present, the former hidden by the latter in the furthest pixels. When adding Titanium, the warm component is completely washed out from the time

traces of furthest pixels, leaving only the ballistic component ($\sim 13\mu s$). This proves that a superconductor layer with T_c much lower than that of the KID definitively helps in down-converting ballistic phonons energies, killing the warm component for distances $> 15mm$.

Although Kinetic Inductance Detectors fabricated within the SPACEKID collaboration are not optimized for particle physics, they have shown good performances. Exposing the array with bare substrate (SPK-E) to a X-ray source, we measured a single pixel detection level of $E_{RMS} \sim 14eV$ at 1σ, with a sub-keV energy resolution ($\sim 380eV$). The relatively poor latter value should be easily improved using a narrower collimator and a multipixels readout.

8.10 Future prospects

More measurements will be carried out in the coming months to confirm these results and the consequent interpretation of the data presented in this chapter. On the other hand, a further suppression of CR glitches can be surely obtained by replacing a full substrate with slightly more complex structures:

- Creating a mosaic of smaller silicon dies: by replacing a single, large wafer with a series of smaller ones, interconnected to each other, it would be possible to lose, for each CR event, only the data of the sub-array where the impact has happened. This suppresses the loss of data by a factor proportional to the number of sub-arrays used and improves the overall observing efficiency.

- Etching of the substrate on bare areas: it is possible to etch the substrate on all areas where there is no metallization. The array would be then designed on a sort of thick grid. The resulting structure is still solid, and would lead to a smaller effective area exposed to the CR, thus decreasing the rate of events. The advantage of this solution is that it is not trying to mitigate the effect of an event after the impact, with the consequent risk of hiding its effect into the noise, but rather to completely suppress a part of the events, thus diminishing their rate.

- Implementation of phonon-blocking structures. If a structure as the grid described above is implemented, it is also possible to connect each detector to the main grid using thick silicon legs whose shape contains a high number of right angle turns. The ballistic phonons are reflected specularly at each interface, so the presence of such legs would imply that a large number of the phonons can be backscattered at each turn. Each detector might thus be isolated from the others and each event could affect only a small fraction of the array. Such an approach could mimic the effect of having a mosaic of silicon dies and has also the advantage of the reduced sensitive area. This solution must

be studied and confirmed by measurements to verify the effectiveness of the phonon-blocking structures and to eventually optimize the shape that they should have to work efficiently.

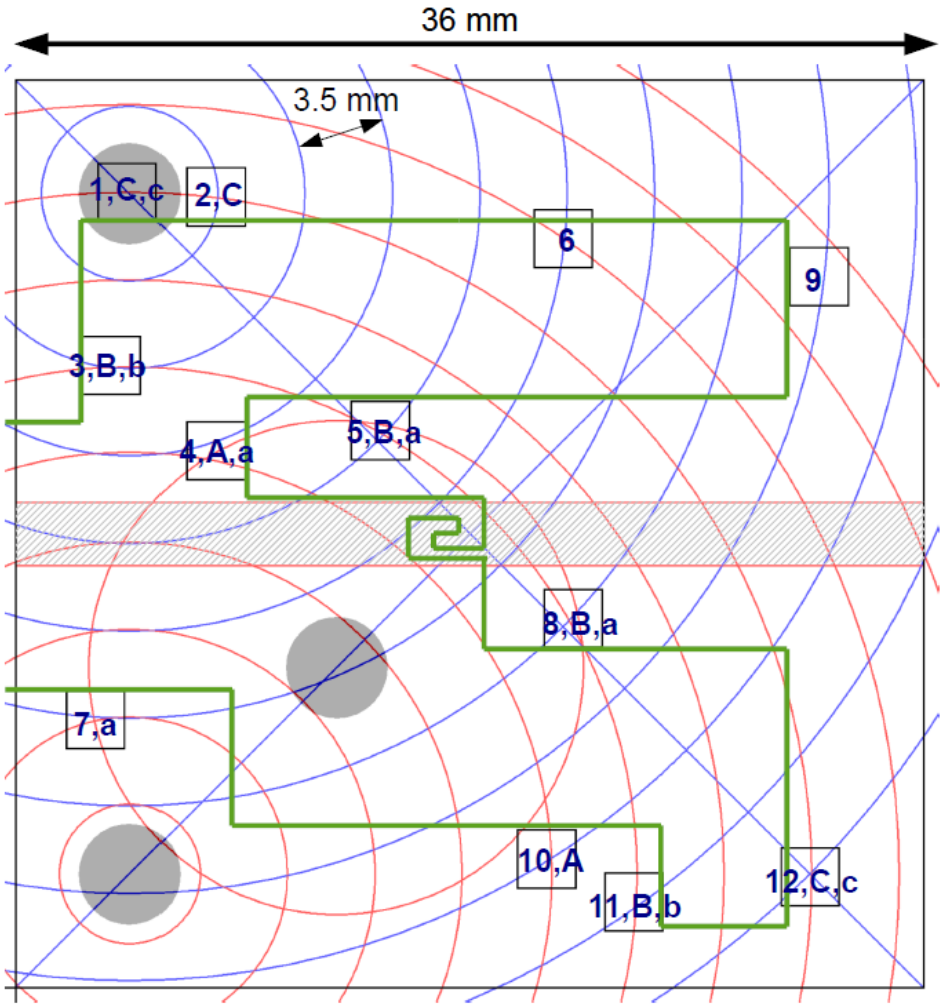

Figure 8.25: *Schematic representation of the pixels positions on the new SPK-2 arrays. The grey circles represent the different possible impact points. In green, a sketch of the approximate route of the feedline. The SPK-2 mask contains two copies of the same array, one with the ground-plane present on the whole surface of the frontside, the second with a bare silicon frontside and the ground-plane only around the central conductor of the feedline.*

We have designed a new mask - named SPK-2 - with this double purpose. The disposition of the pixels on the array is optimized to better investigate the phonon propagation in the substrate and the effect that the metallization layers have on it. Different tests can be carried out using the fabricated arrays by placing the radioactive source in front of the three available target points, marked as grey circles in the schematic image shown in figure 8.25.

- When shooting on the top, left spot, the pixels are distributed at regular distance intervals from the impact point. Measurements carried out with the source in this position will allow us to characterize the function relating the peak amplitude to the distance from the impact point much better than before. The number 1, 2, ..12 are assigned to the pixels from the nearest to the furthest from the hot spot.

- When shooting on the bottom, left spot, there are groups of two or more pixels at the same distance from the impact point (pixels indicated by the capital letters A, B, C). These will allow us to check that, as expected, pixels at an equal distance from the origin of the event lead to equal peak amplitudes. Furthermore, each group of pixels have at least one detector on each side of the greyed zone. This zone is intentionally left almost completely bare in order to be able, at a later stage, to etch the substrate and to split the array into two sub-arrays, held together by an appropriate phonon blocking structure. This solution could allow us to mimic the mosaic of sub-arrays approach described in the previous list, but still keeping the advantages of creating an array as one single component. Once the substrate is etched, we will be able to see if pixels equidistant from the hot spot but on the same or opposite 'sub-array' with respect to it effectively show a different behavior.

- If this is the case, it is then possible to shoot on the third, more central spot : again we have groups of equidistant pixels (small letters a,b,c), the nearest of them (a) being actually nearer to the spot than in the previous configuration. If some differences are seen, this last configuration can be used to better characterize the effect of the etching.

The effect of the superconducting layers can be further enhanced by forcing the phonons to interact more often with metallized surfaces. This can be achieved in many ways, for example by fabricating the arrays on a wafer whose backside has a 3D structures that cause the phonons to undergo multiple reflections, or by adding, as we said, phonon blocking structures (like spirals or zigzags) whose walls are also covered by a superconductor.

Chapter 9

Start-up operations of the CALDER experiment

The suppression of the radioactive background is crucial for several particle Physics experiments, especially for those operating underground. Examples are the two observatory facilities CUORE [53] and LUCIFER [59] at Laboratori Nazionali del Gran Sasso (LNGS) to search for neutrinoless double beta decay ($0\nu\beta\beta$), whose success depends on the capability to reject the background from alpha decays. LUCIFER uses scintillating bolometers as calorimeters, monitored by light detectors to tag the signal from betas and reject the background from alphas. CUORE uses bolometers without light read-out, therefore its sensitivity is limited by the background. It has been demonstrated that light detectors with a factor 5-10 better resolution with respect to present technologies could extend LUCIFER to detect also Dark Matter, as in the CRESST experiment [131], and would enable the background rejection in CUORE.

This is the framework within the CALDER collaboration was born [52], a new group of young particle physicists and astrophysicist from INFN (Istituto Nazionale di Fisica Nucleare), "Università degli Studi" of Genova and "Università Sapienza" of Rome that aims at the development of wide-area sensitive light detectors based on the Kinetic Inductance Detectors technology. The remarkable energy resolution and the possibility to read hundreds of channels with a single transmission line are at the base of the successful operation of KID in several low-temperature detectors sectors. Besides the NIKA success, the first successful phonon-mediated detection of cosmic and X-rays by SPACEKID project immediately shown the enormous possibilities for these devices to particle physics applications too (see chap. 6, 7 and 8). The CALDER collaboration has already taken this path, now porting this widely used technology to the field of particle physics, with the purpose of provides an alpha background rejection tool for CUORE.

CUORE [53] is an experiment that searches for neutrinoless double beta decay. It will

mount $\sim 1ton$ of TeO_2 bolometer operated at $\sim 10\,mK$. The technology of CUORE sets it in a very competitive position with the rest of the neutrinoless double beta decay experiments, except for the serious limiting background due to alpha's decays from the detector surface partly converting energy in the bolometers. Even if the bolometers used by the CUORE collaboration do not emit scintillation light at cryogenic temperatures, the detection of the tiny amount of Cherenkov light (100 eV) emitted (only) by electrons could allow to identify and reject alpha interactions, increasing the experiment sensitivity on the half-life of the neutrinoless double beta decay by a factor 6. In order to achieve this goal, ultra-sensitive light detectors not interfering with calorimetric energy measurements are needed [132]

Kinetic Inductance Detectors can provide such an independent discrimination tool and a way to overlack this problem. The CALDER collaboration has taken up this challenging bet and the great wealth of knowledge inherited by NIKA and SPACEKID are, today, benefiting the start-up of this activity. The CALDER collaboration is widely using the *NIXA* readout electronics and the *sNelloX* data acquisition software developed in Grenoble for KID multiplexed readout, resulting in the first detection of X-rays coming from a ^{55}Fe source ever taken in Rome laboratories.

9.1 A background discrimination tool for rare event search science

Bolometers are phonon detectors that work at cryogenic temperatures and feature an excellent energy resolution. They have demonstrated to be superior devices for the search of rare events, such as neutrinoless double beta decay ($0\nu\beta\beta$) and dark matter interactions. The $0\nu\beta\beta$ signal consists in a monochromatic peak produced by two electrons with a sum energy of about 3 MeV. This signal could be hidden by a continuous background produced by alpha particles emitted in natural radioactive decays occurring in the materials surrounding/constituting the bolometers. The dark matter signal is made of nuclear recoils that release in the bolometers an energy of few keV and can be hidden by beta and gamma interactions also originating from natural radioactivity. The reduction of this radioactive background has a fundamental importance for all experiments searching for rare events. For this reason it is a common practice to use only materials with low content of radioactive contamination, and to treat them chemically to further reduce the concentration of impurities. This passive form of background rejection is necessary, but not sufficient to guarantee the success of an experiment: active background rejection techniques, based on the capability of discriminating the nature of an interacting particle, must be used. in present experiments, bolometers rely on the readout of the thermal signal and they do not enable by themselves such a discrimination. For this reason many experiments use scintillating crystals as bolometers, and detect the light produced by interacting particles in coincidence with the thermal pulse. Alpha and beta particles of same

energy can be distinguished thanks to their different light yield, leading to a reduction of the background.

9.1.1 The CUORE experiment

CUORE is one of the most sensitive double beta decay experiments and will search for $0\nu\beta\beta$ of ^{130}Te. The detector will be an array of 988 $5 \times 5 \times 5 cm^3$ tellurium dioxide (TeO_2) crystals with a mass of 0.75 kg, kept at 10 mK by a dilution refrigerator. The TeO_2 crystals are operated as bolometers, using a neutron transmutation doped germanium (NTD-Ge) thermistor as thermal phonons sensor [133]. Tellurium dioxide has proven to be an excellent compound from the bolometric point of view but, since this material does not scintillate, it does not allow to discriminate the alpha background with the above described technique. It has been demonstrated recently that interacting particles can be identified in TeO_2 by detecting Cerenkov radiation. In the energy range of interest for double beta decay, indeed, Cerenkov light is emitted by beta particles and not by alpha particles [134]. By facing a light detector to a CUORE bolometer, it was found that beta particles with energies in the range of interest gave rise to a light signal with an average amplitude of 100 eV, while no light was detected in correspondence with alpha particles of same energy. This measurement demonstrated the feasibility of Cerenkov-based particle discrimination in TeO_2 bolometers, but also revealed that an event by event discrimination would be possible only by using a light detector with a noise lower than 10-20 eV RMS. In these conditions the signal amplitude would be as big as five times the detector noise, and it would be possible to completely reject the alpha background in CUORE, leading to an improvement on the double beta decay half-life sensitivity of the experiment from $1 \div 2 \times 10^{26}$ years to 6×10^{26} years at 68% confidence level (fig. 9.1(a)).

9.1.2 The LUCIFER experiment

LUCIFER is an R&D project investigating the possibility to make a double beta decay experiment based on zinc selenide (ZnSe) scintillating bolometers. These crystals have a light yield for beta particles of 7 keV per 1 MeV of released energy, while alpha particles of the same energy give rise to a light signal of about 21 keV (fig. 9.1(b)). This behavior is opposed to that of all other known scintillating crystals, where alpha particles emit less light than beta particles of the same energy. This anomaly could be of great interest for the detection of dark matter.

One would expected a WIMP dark matter to produce a signal in ZnSe bolometers nuclear recoils corresponding to energy releases in the range between 10 and 40 keV [135]. Assuming that nuclear recoils induced by WIMP would produce as much light as alpha particles, it is possible to estimate a minimum light signal of 210 eV and of 70 eV for nuclear recoils and beta/gamma interactions, respectively. It is clear that with a high-sensitivity light detector

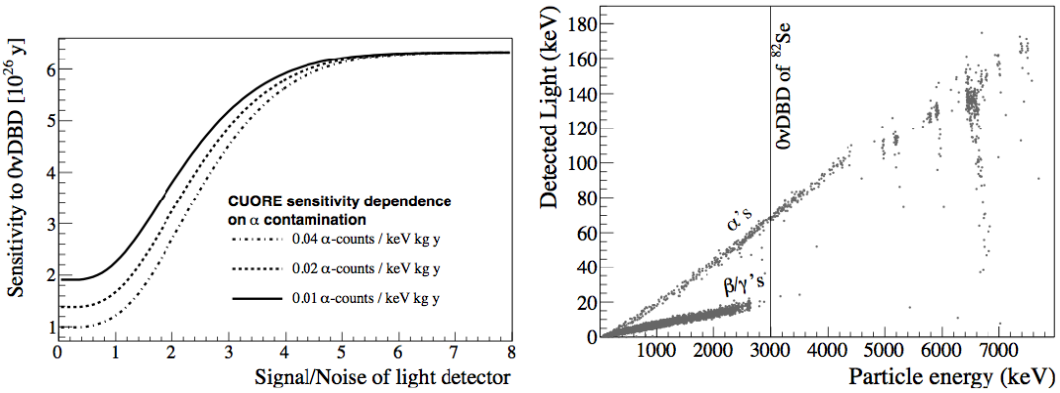

(a) (b)

Figure 9.1: *(a) CUORE sensitivity to $0\nu\beta\beta$ as function of the signal-to-noise ratio (SNR) of the light detectors. CUORE without light detectors corresponds to SNR=0. When SNR > 5 the alpha background is completely removed. (b) Scintillation light produced by a 480g ZnSe bolometer as function of the energy of interacting particles. Unlike in conventional scintillating crystals, alpha particles produce more light than beta ones. In spite of this anomaly, the identification capability of alpha background is excellent.*

LUCIFER would become a competitive experiment not only for double beta decay, but also for dark matter search.

9.1.3 Bolometers versus KID

Despite the main features of the light detectors will be the large size and high sensitivity, they will have to satisfy at the same time other constraints that make them usable in the above mentioned bolometric experiments. The detectors will have to work at temperatures of the order of 10 mK, they shall be built with low radioactivity materials, and their introduction shall guarantee a low impact on existing experiments.

Two main experimental tools are currently used as light detectors for the described purposes: 1) the neutron transmutation doped (NTD) thermistors, and 2) the transition edge sensors (TES). The NTD thermistors (1) are the sensors of the light detectors that are currently adopted in LUCIFER and that were used for the Cerenkov radiation measurements in TeO_2 crystals described above. Despite the many attempts, the maximum SNR they achieved is $101eV/72eV = 1.4$ [132], well below the value of 5 that would be needed to remove completely the alpha background in CUORE.

TES bolometers were developed for dark matter search experiments, mainly in the framework of the CRESST collaboration. Despite good energy threshold ($30 \div 80eV$), these light detectors suffered of relevant problems for what concerns reproducibility and reliability. Moreover they need to be cooled to the exact superconducting phase transition temperature, within

$\sim 1mK$. This range is too sharp for the purposes of CUORE, which working temperature will be adjusted between 8 and 20 mK at the time of data taking, to find the optimal working conditions of the bolometers. Finally, the readout technique implies the use of SQUIDs which need to be operated at cryogenic temperatures, further complicating the readout chain.

Because of these problems, the CALDER collaboration preferred to investigate the potential of a third solution, the Kinetic Inductance Detectors. As plenty seen in the previous chapters, the main features of these detectors reside in their excellent resolution, high reliability and in the possibility of reading hundreds of channels in parallel using a single pair of excitation/readout lines. This latter aspect is of fundamental importance for CUORE, because the use of KID-based light detectors would have a low impact in term of wire-count, only requiring minimal modifications to the cryostat. Furthermore, KID performances do not depend critically on the working temperature and the readout electronics can be entirely operated at room temperatures, with the exception of the low noise cryogenic amplifier. That represent two further advantages with respect to TES-based devices.

Despite their great development in the last decade, currently available KIDs have been developed for astrophysical applications and do not match all the specifications of a large-scale bolometric experiment. They have never been used at temperatures lower than $\sim 70mK$, they have dimensions of a few mm^2, and they have never been characterized from the radioactivity point of view.

9.2 Goals of the project

The goal of this research project is the study of high-sensitivity (baseline noise lower than 10-20 eV RMS), large area ($5 \times 5cm^2$) KID-based light detectors, in view of future applications in CUORE, LUCIFER and other bolometric experiments such as CRESST [131] and EURECA. In the first phase of the CALDER project, the main goal is to fabricate at least two light detector prototypes and to prove their performance and reproducibility in Rome laboratories. The strategy to develop the detectors will include design, simulations, calibrations and low temperature tests in dilution refrigerators.

Then, in a second phase of large scale production, the light detectors will be used in two bolometric measurements in the CUORE R&D cryostat at LNGS, interfaced firstly to the 988 TeO_2 CUORE bolometers and successively to the ZnSe LUCIFER bolometers. A few months of data acquisition will be sufficient to determine whether the discrimination power required for double beta decay and dark matter searches has been achieved. With such a test-bench, the CALDER team aims to create a new kind of light detector to be used in rare event search experiments. The scientific bet of the CALDER project is to provide a KID-based background discrimination tool performing much better than previous technologies. To obtain this, the final goals are:

- Implementation of two prototypes of light detector with the following requirements:

  1. Working temperature between 8 and 20 mK.
  2. Area of around $5 \times 5cm^2$.
  3. Noise RMS at the baseline below 10-20 eV RMS.
  4. Quantum efficiency greater than 50% for photons in the UV (Cerenkov in TeO_2) and visible (ZnSe scintillation) bands.
  5. Low radioactive contaminations of the materials.
  6. Rise time lower than 30 ms, the rise time of the heat signal in TeO_2 and $ZnSe$ bolometers.
  7. Low number of wires, to keep the thermal load below the cooling power of the CUORE cryostat.

  The KID feature low noise (point 3), high efficiency (point 4), fast response (point 6) and allow a high level of multiplexing (point 7). Nevertheless present sensors are operated at high temperatures (order of 100 mK, point 1), have small area of a few mm^2 (point 2), and their radioactive content has not yet been taken into account (point 5).

- Development of an electronics scalable to around 10^3 light detectors. As described in chap. 3, the KID electronics is normally digital and uses FPGA boards coupled to high-speed ADCs and DACs. The first system of CALDER electronics will be developed to readout the detector prototypes in Rome. Then the system will be expanded and to the 998 light detectors of CUORE. If the number of KID sensors on each detector will be of the order of 10, the total number of channels to be handled in parallel would be of the order of 10^4.

- Development of a data acquisition system integrated in the present CUORE and LUCIFER systems. After the testing phase with the electronics and the detectors installed in Rome, the system will be integrated in the CUORE and LUCIFER data acquisition.

The startup operations of the CALDER experiments concern the testing phase of these points, based in Rome laboratories.

During the process of porting the KID technology from astrophysics to our purposes, particular attention has to be paid to the pixel dimensioning, since KID electromagnetic features are intrinsically related to their size. The resonance frequency depends on the geometry of the device and decreases with its linear dimensions. It is important to have few GHz resonance frequencies because this value lies in the optimal range for both the low-noise cryogenic amplifiers and the electronics components used in the readout. For example, NIKA detectors have a size of some mm^2 and resonance frequency of $\sim 1.4 \div 1.9GHz$. The increase of the

KID size would lower the frequency below the readout chain optimal range, thus loosing the possibility to use already existing electronics components. Covering a $5 \times 5cm^2$ surface with present dimension devices would require thousands of pixels strongly weighting the multiplexing, and is thus a not viable solution. On the other hand, reducing the number of detectors means increase the pixel size, resulting in the aforementioned drawbacks. In this context the phonon-mediated detection enables an intermediate solution. As seen in previous chapters, phonons in the substrate can propagate along distances greater than a centimeter, so that a single KID sensor can be used to monitor areas much larger than its dimensions. In this scientific framework, the phonon-mediated represents a great advantage allowing to sample a large area with a few sensors. Deploying this technique, our goal is to developed detectors fabricated on a $5 \times 5cm^2$ substrate, sampled by no more than 10-20 KID.

Moreover, the choice of substrate and KID materials will be another a fundamental aspect. Wafer materials will be chosen in order to maximize the detector performances and at the same time to minimize the radioactive contaminants that could induce a background in CUORE and LUCIFER bolometers.

9.3 Experimental setup

The experimental setup consists in the NIXA electronic board connected to a dilution cryostat (fig. 9.2). The electronics setup is the same described in chap. 3: two DACs generates the in-phase (I) and quadrature-phase (Q) components of the signal, that are sent into the cryostat after have been mixed-up. Then the signal pass through the detector array, the cold and warm amplifiers and after the down-mixing it is sent to the ADC where it is properly demodulated and acquired.

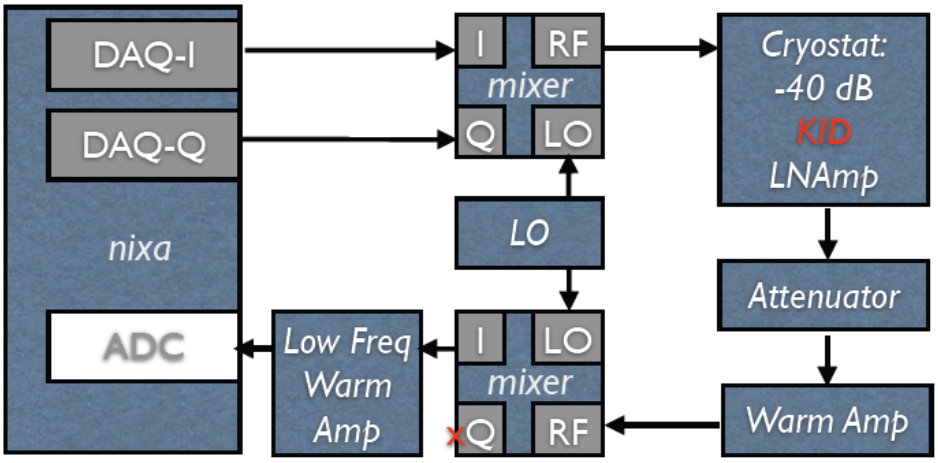

Figure 9.2: *The CALDER experimental setup.*

The dilution cryostat has a base temperature of about $\sim 50mK$. It is equipped with two niobium RF lines used to send and readout the feeding power to the KID array. Their thermalization is ensured by copper wires or copper 'blocks' at each thermal stage (4K stage, 1K-pot, 600 mK still, 50 mK mixing chamber). The output line is equipped with a low noise amplifier (CITLF4 Cryogenic SiGe), installed on the 4K plate by means of a copper element. An heater is installed on the still and it is used to start the dilution process. Thermometers to monitor the temperature of the different stages are mounted on the 4K plate, on the 1K-pot, on the still and on the mixing chamber.

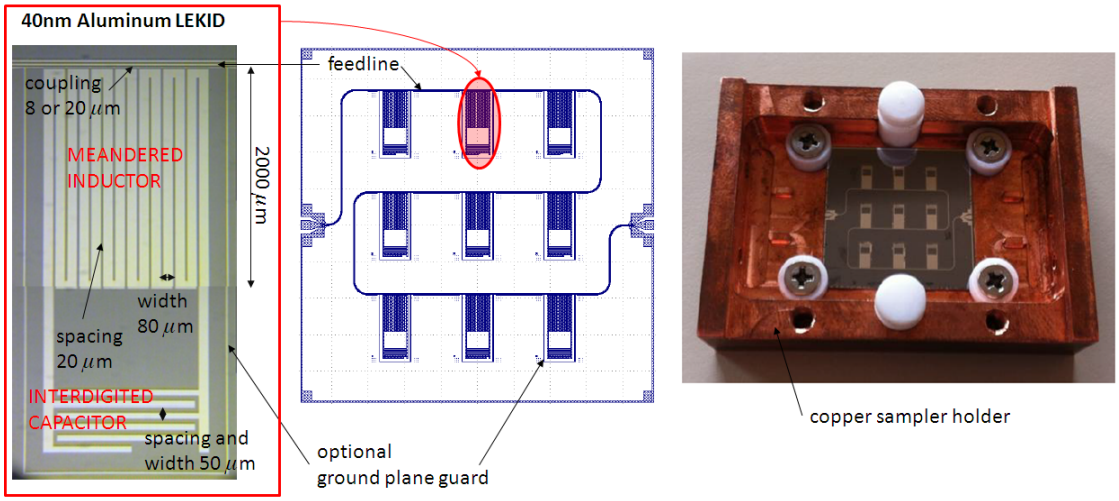

Figure 9.3: *(left) The pixel geometry as photographed with the Scanning Electron Microscope (SEM); (middel) the detector array design; (right) a photograph of the 'KID3' array mounted in its copper sample holder.*

The detectors arrays have been designed using *SONNET*. The first tested geometry consists in a 9-pixel array based on the LEKID architecture (fig. 9.3). It is made up by a large filling factor ($> 80\%$) meandered inductor, well separated from a classical interdigited capacitor. The LEKID are fabricated with a 40nm thick deposit of Aluminum. The planar size of each pixel is $\sim 6 \times 3mm^2$, larger compared to usual dimensions (see NIKA chap. 4, or ASTROKID chap. 5) in order to match the CALDER goals.

The arrays are fabricated on a $300\mu m$ thick Silicon substrate. All the manufacturing process of the CALDER arrays is managed by the IFN based in Rome, in parallel with the ASTROKID arrays fabrication (see par. 5.1.1). Each mask commissioned to the IFN actually contained arrays intended for both the projects. The same pixel geometry was replicated on two type of wafer, summarized here with their corresponding label:

1. *KID2* (fig. 9.4(a)): Doped non-intrinsic high-resistivity silicon (dopedHR-Si, $600 \div 1200\Omega \cdot cm$) wafer, oriented (111), dimension 2". The corresponding tested array from

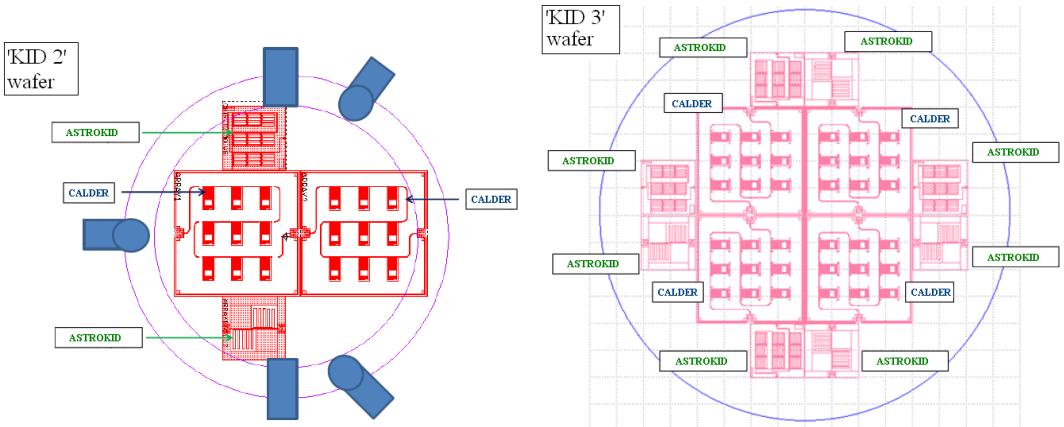

(a) (b)

Figure 9.4: *Design of the 'KID2' (left) and 'KID3' (right) masks. The detector arrays tested by us are two, one for array. In the text they have been referred to using the name of the corresponding entire mask.*

this wafer has nine 40nm thick pixels of evaporated Aluminum, with $20\mu m$ coupling to the feedline;

2. *KID3* (fig. 9.4(b)): Intrinsic high-resistivity silicon (HR-Si, $> 5000\Omega{\cdot}cm$), re-crystallized with floating zone method, [112]), oriented (100), dimension 3". The corresponding tested array from this wafer has nine 40nm thick pixels of evaporated Aluminum, with $8\mu m$ coupling to the feedline.

In the following, we will refer to the tested arrays with the label defined for the corresponding wafer on which they are fabricated.

In order to test the response to X-rays, we used a ^{55}Fe source, with an activity of $0.54Bq$. The final goal is to equip the cryostat with a fully controlled pulsed light source, as an optical fiber.

9.4 First results

We present here the first results obtained testing the arrays *KID2* and *KID3*. The test were performed in two successive runs, with the same experimental setup except for sample holder material, aluminum for *KID2* while copper for *KID3*. All the nine resonances where detected for both the array. A VNA scan of the *KID3* resonances is shown in fig. 9.5(a).

We then fitted the transmitted amplitude of the signal and compared the estimated quality factors for the two arrays. The external quality factor Q_e (fig. 9.6(a)) shows that the pixels are grouped three by three depending on the row they belong to in the geometric design (fig.

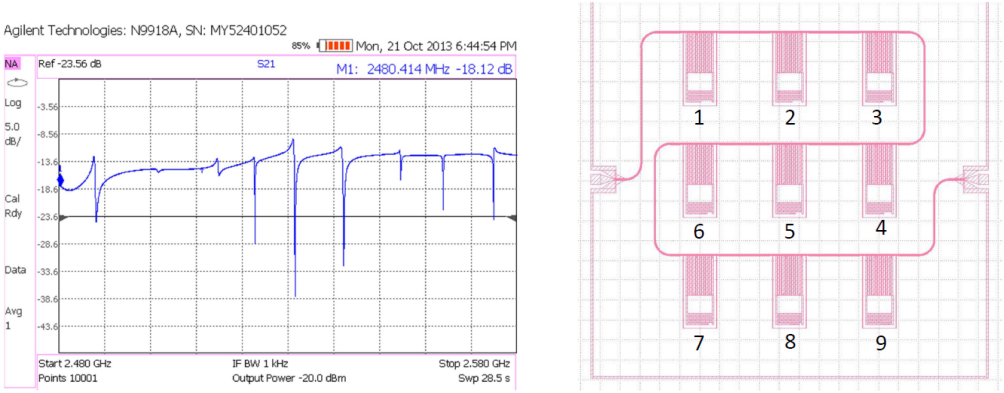

(a) (b)

Figure 9.5: *(a) A VNA scan of the 9 resonances of the 'KID3' array; (b) the 'KID3' array geometry with the chosen detector numbering.*

9.5(b)). This might depend on some electromagnetic crosstalk effects that need to be further investigated. The resonances of the first group (KID number 1, 2, 3) seems very deteriorated and their fitted parameters are not reliable. Comparing the other pixels, the more coupled 'KID3' array shows in general lower external quality factors than 'KID2'. Some differences between the two arrays arises also comparing the internal quality factors Q_i (fig. 9.6(b)). These differences depends on the different resistivities of the silicon substrate on the two wafers. Probably also the sample holder material changes the electromagnetic properties of the resonances, switching from a superconductor (aluminum) to a normal metal (copper). For completeness, a comparison with the ASTROKID resonance parameters in shown (fig. 9.6(c)). There is an evident different distribution of the resonances when plotting Q_i versus Q_e. Additional causes explaining the scattered Q_e values and the relatively low Q_i need to be further investigated.

The readout chain mainly consists in the *NIXA* electronics boards and the *sNelloX* acquisition and calibration software. The using of such widely tested and debugged tools have allowed to acquire the first light pulses in relatively short timeframe. Following the guidelines of the KID readout operations accrued in Grenoble, we readout the raw I and Q data and the calibrated amplitude and phase signals. The complete calibration procedure of the resonances is performed offline through a two-dimensional fit of the raw I-Q signals independently developed in Rome. Then the amplitude and phase signals are calibrated with respect to the center of the IQ circle using the usual procedure (fig. 9.7). Before to acquire data pulses we studied the RF chain noise as function of the number of feeding tones and their power (fig. 9.8). The phase signal increases with the feeding power because the IQ-circle radius increases, resulting in an higher corresponding SNR. However the output signals saturate (possibly the

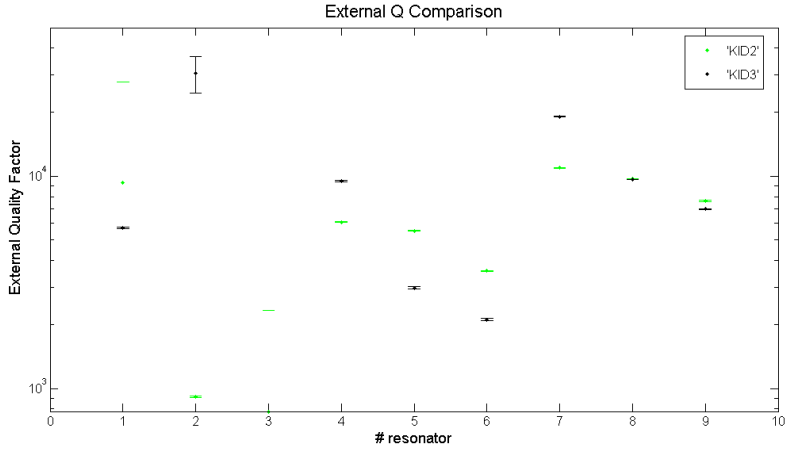

(a)

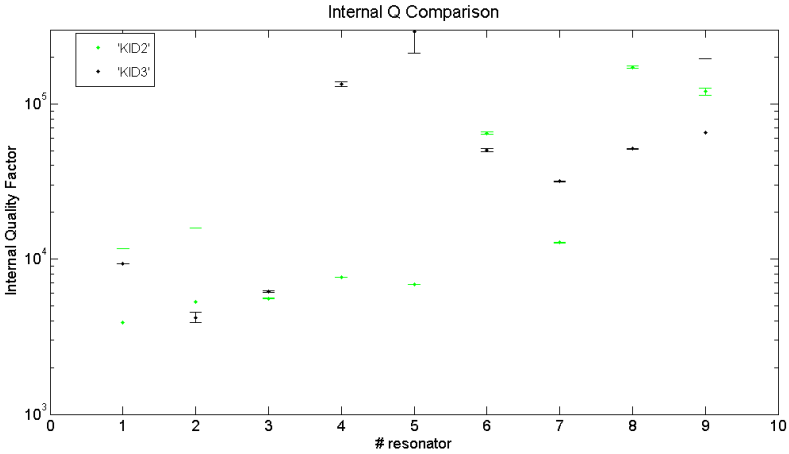

(b)

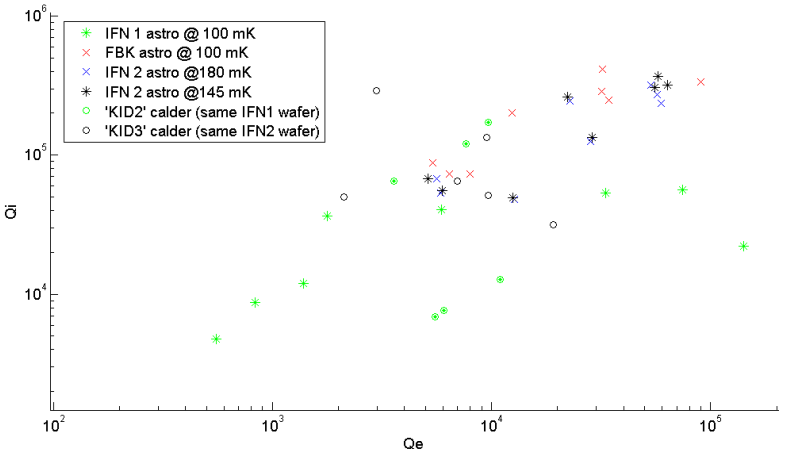

(c)

Figure 9.6: *(a) External quality factors Q_e and (b) internal quality factors Q_i calculated for the 'KID2' and the 'KID3' arrays; (c) comparison of the Q_i versus Q_e plot for the CALDER and ASTROKID arrays. The first three resonances of the CALDER chip were excluded.*

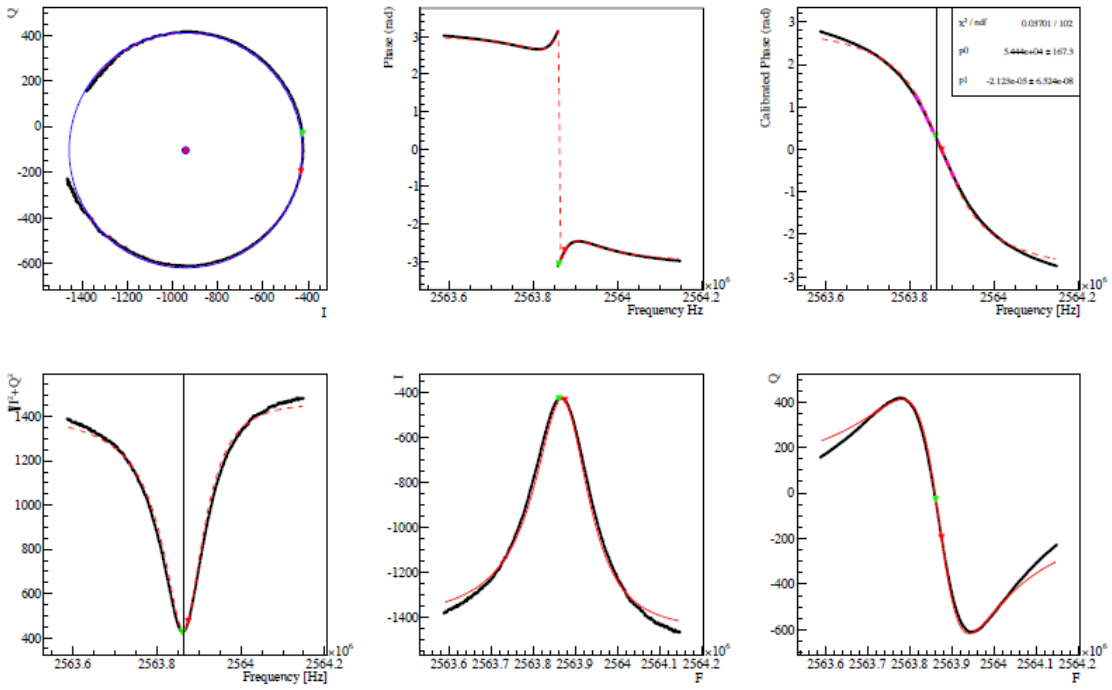

Figure 9.7: *Characterization and calibration of the CALDER detectors. First row: (left) the IQ resonance circle; (center) the not calibrated phase signal, i.e. with respect to the center of the IQ plane; (right) the calibrated phase signal, i.e. with respect to the center of the IQ resonance circle. Second row: (left) the amplitude signal with respect to the center of the IQ plane, i.e. non calibrated; (center) the I raw signal; (right) the Q raw signal. The fits are plotted in black, except for the IQ circle (blue). The working point is chose using the minimum of the A vs f plot (green point). An alternative calibration is possible using the point of maximum variation of the ϕ vs f (red point).*

IQ-mixers or the ADC) above a given value of the feeding power. The number of tones seems not to spoil the noise, except for the peak at high frequency. Therefore, we chose 7 tones configuration with the appropriate power, and set the sampling frequency to $1MHz$ to cutoff the high frequencies noise peaks. We then perform a ^{55}Fe pulses acquisition for 7 KID at once over 12 hours. The I and Q raw data are acquired, then the amplitude and phase signals are calculated following eq. B.1. Then the amplitude and phase signals are calibrated with respect to the IQ-circle center.

The data analysis were performed applying a one dimensional Optimum Linear Filter (OLF) technique. In X-ray signal processing, the OLF is a common known demodulation technique to maximize Signal-to-Noise Ratio (SNR) of a signal with a well known temporal template $S(t)$, in the presence of additive stochastic noise $N(t)$. This is equivalent to convolve the unknown signal $f(t) = a \cdot S(t) + N(t)$ with a conjugated time-reversed version of the template $S \cdot (\omega)$, which is given by the transfer function $H(\omega) = kS \cdot (\omega)/N(\omega)e^{j\omega t}$, where

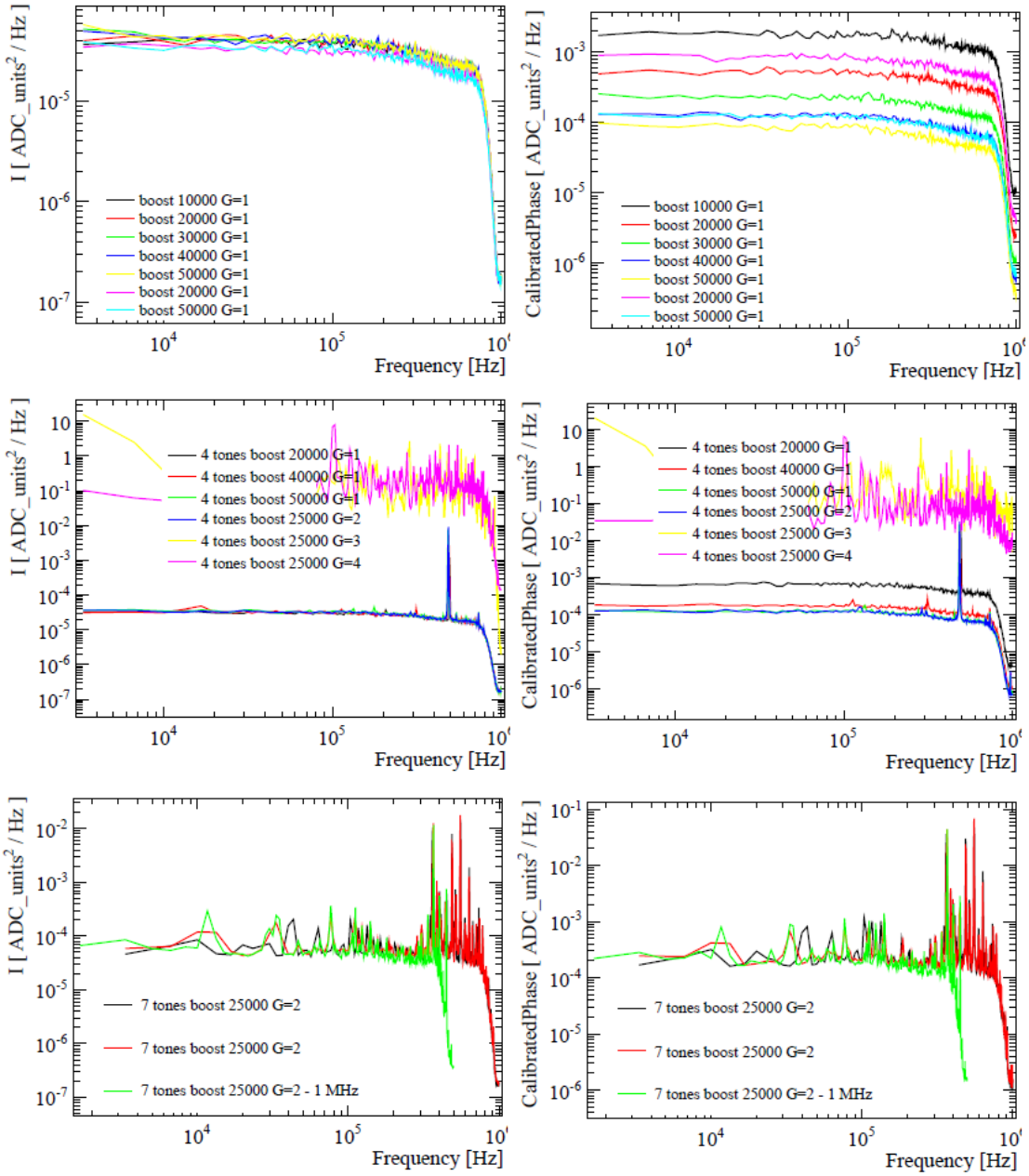

Figure 9.8: *The noise of the RF chain of the I raw data (first column) and the calibrated phase (second column), as function of the feeding power. This latter parameter is given by the product DAC boost × gain. The analysis has been performed for 1tone (first row), 4 tones (second row). For 7 tones (third row) we fixed the power boost and changed the sampling frequency. The noise reduces with the feeding power. Except for some peaks appearing at high frequencies, the noise does not increases with the number of tones as long as the signal are not saturated.*

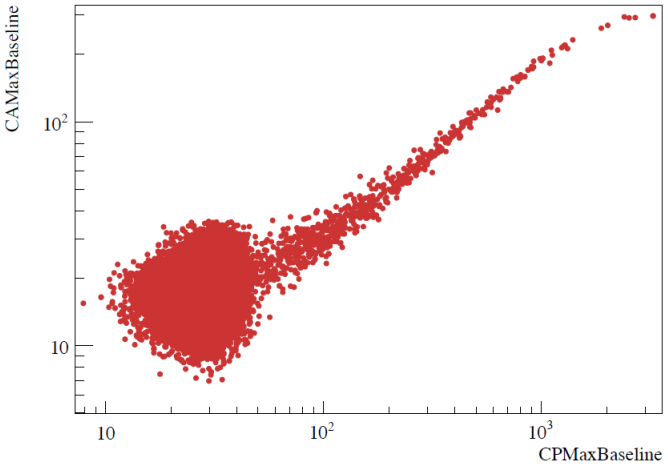

Figure 9.9: *Example of the peak signal of the calibrate amplitude (CA) versus the calibrated phase (CP) for the channel 7 before to have applied the OLF. The average pulse is calculated removing the low CA/CP 'blob' representing the noise events. From the plots it is evident that the amplitude signal saturates with respect to the phase one.*

$N(\omega)$ is the noise power spectrum of the stochastic component. Since we don't know the response of the detectors, the $S(t)$ function cannot be determined 'a priori'. In the hypothesis that the temporal template does not depend on the amplitude of the peak signal, the function $S(t)$ can be simply calculated by averaging many pulses after removing the noise events (fig. 9.9). The transfer function $H(t)$ is thus calculated for each detector and then applied to each pulse $f(t)$ to optimize the SNR (fig. 9.10).

As a very preliminary analysis, we extract the spectra of different KID and the total average signal (fig. 9.11). They have been calculated using the frequency calibration of the phase signal of 320 acquired pulses after the OLF filtering. At the current state, the KID prototypes we had developed are still not optimized for our scopes. Furthermore, an energy calibration is needed in order to reconstruct the energy spectrum of the radioactive source, so our results are not conclusive at the present state.

9.5 Present status and future prospects

We have successfully fabricated the first $40nm$ thick Aluminum KID array prototype with detectors over dimensioned with respect to usual format. This first design foreseeing a 'bold' meandered inductor with filling factor $\sim 80\%$ has shown all the expected nine resonances. At the current state however the KID prototypes we had developed are still not optimized for our scopes. Additional studies are however needed in order to explain the scattered Q_e values and the relatively low Q_i compared to the ASTROKID resonators, fabricated on the

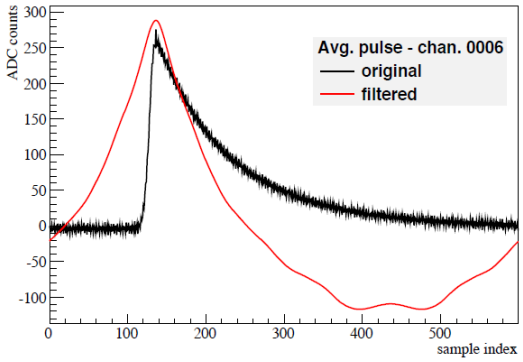

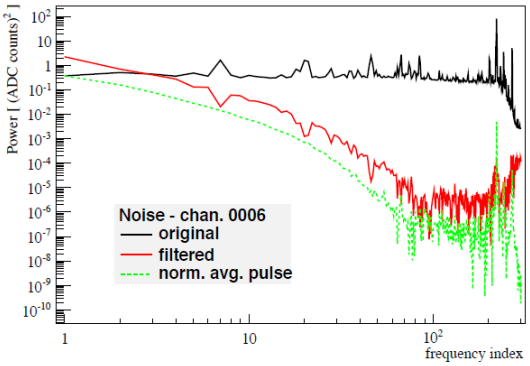

	Noise RMS in ADC counts (original → filtered)	
	Calibrated Phase	Calibrated Amplitude
Channel 1	17.8 → 1.5	26.2 → 2.6
Channel 2	8.4 → 1.7	8.8 → 1.8
Channel 3	5.6 → 0.9	10.0 → 1.9
Channel 4	6.2→ 1.1	7.9 → 1.8
Channel 5	11.3 → 2.2	8.1 → 2.7
Channel 6	14.6 → 2.0	7.3 → 1.2
Channel 7	15.8 → 1.4	9.5 → 0.9

Figure 9.10: *(left) The average pulse of the KID number 6 before (black) and after the OLF (red); (right) the noise power spectra of the KID number 6 before (black), and after the OLF filtering (red), also normalizing its value to the average pulse spectrum (green); (bottom) table of the noises of the calibrated amplitude and phase signals before and after applying the OLF, which clearly improves the RMS of a factor* ~ 10.

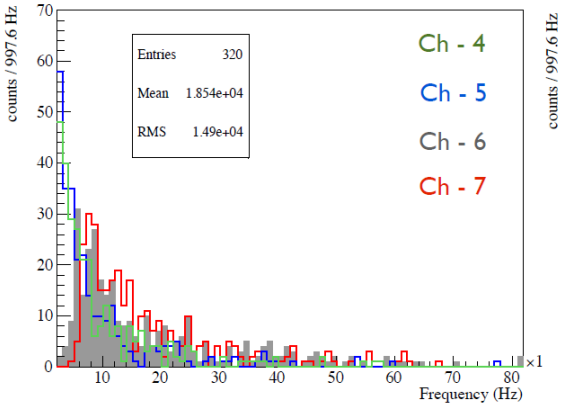

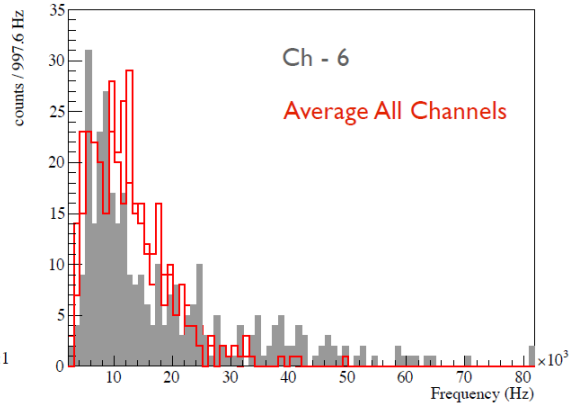

Figure 9.11: *On the left, the spectra of different KID (channels) of our array. On the right, the energy spectrum of the channel 6 compared to the average spectrum obtained from the sum of all the channels. All the phase signals are calibrated so that the spectra are expressed in units of frequency shift.*

same wafer. Some of the hypothesized explanations might be the different pixel geometry, the presence of the ground plane guard, some local differences in the quality of the aluminum film, the presence of the copper sample holder, differences in the array bonding, etc.

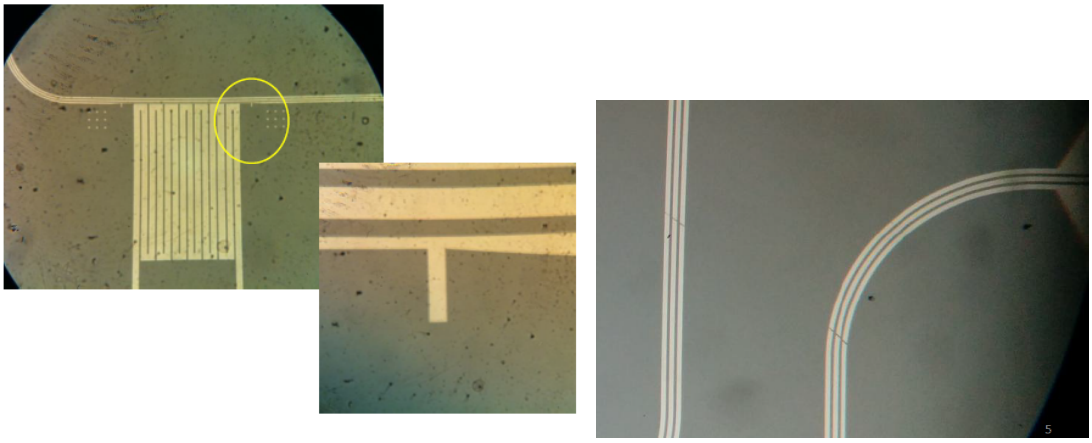

(a) (b)

Figure 9.12: *(a) A SEM image of the 'KID3' array after the ground plane guard removing; (b) particular of the feedline damaged by the process.*

The experimental setup and the readout chain have demonstrated to work properly. We have studied the response of the *NIXA* electronics as function of the number and power of the output tones. More studies to characterize the entire RF chain are currently ongoing. For the pulse acquisition during the first experiments, we have used the acquisition software *sNelloX* developed in Grenoble, improved and adapted for our purposes. A dedicated fully C++ based new software based on the *sNelloX* features and functionalities is currently under development. It has been tested during the last runs showing good performances and easy handling.

Several important improvements are currently under development:

1. removing of the ground plane guard from the 'KID3' array (fig. 9.12(a)). Unfortunately the process damaged the array, compromising the quality factors and so the detector responsivity. Despite this, the array was tested obtaining promising result (items 2. and 3.);

2. integration of an optical fiber down to the 50mK stage of the cryostat. The 'KID3' pixels have detected the first light pulsed with a LED (fig. 9.13(d)). The preliminary analysis estimated a nominal pulser energy of $\sim 100keV$ at room temperature. More studies are ongoing to better characterize its energy in order to use it as a reliable source calibrator;

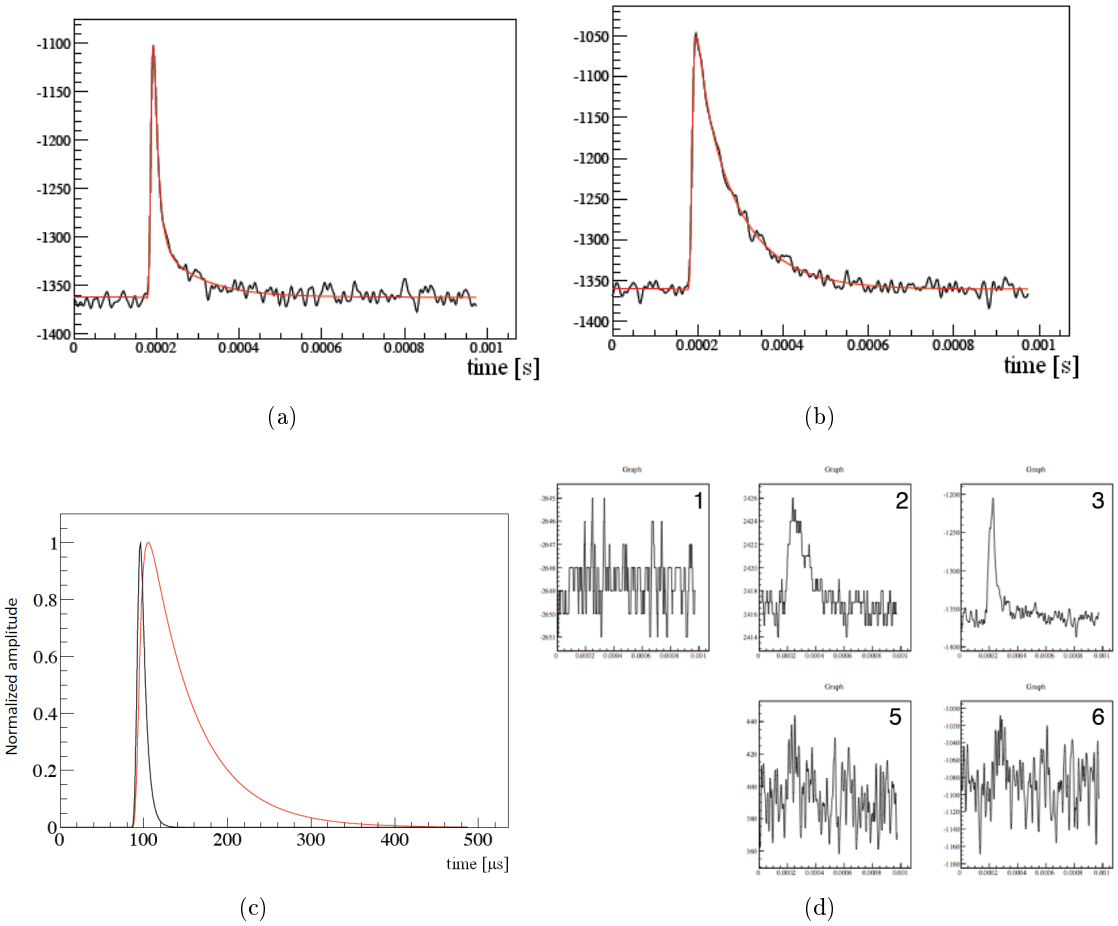

Figure 9.13: *Examples of a (a) fast and (b) slow pulses filtered with a low-pass Software FIR Filter at 60kHz, and fitted by an exponential decay law, with (c) the corresponding calculated signal templates; (d) first LED light detected by our KID.*

3. implementation of a more powerful analysis pipeline. We have studied secondary cosmic ray (CR) pulses on 'KID3' array. The data analysis showed a wide variation of the shape of the calibrated phase signal, depending on the impact point of the incoming particle. It is possible to calculate the signal template of a fast and a slow component fitting their temporal traces (fig. 9.13(c)). These components are likely due to the ballistic (fast signal) and warm (slow signal) phonons, with estimated lifetimes of $11\mu s$ and $112\mu s$ respectively. Each CR pulse is given by the sum of these two components, whose relative weight depend on the distance from the considered KID and the impact point. Event closer to a KID generates faster pulses with different shape, so that a better energy estimator is the integral of the calibrated phase signal rather than its peak amplitude. Using the integral of the pulse as estimator of the total energy, the detector versus

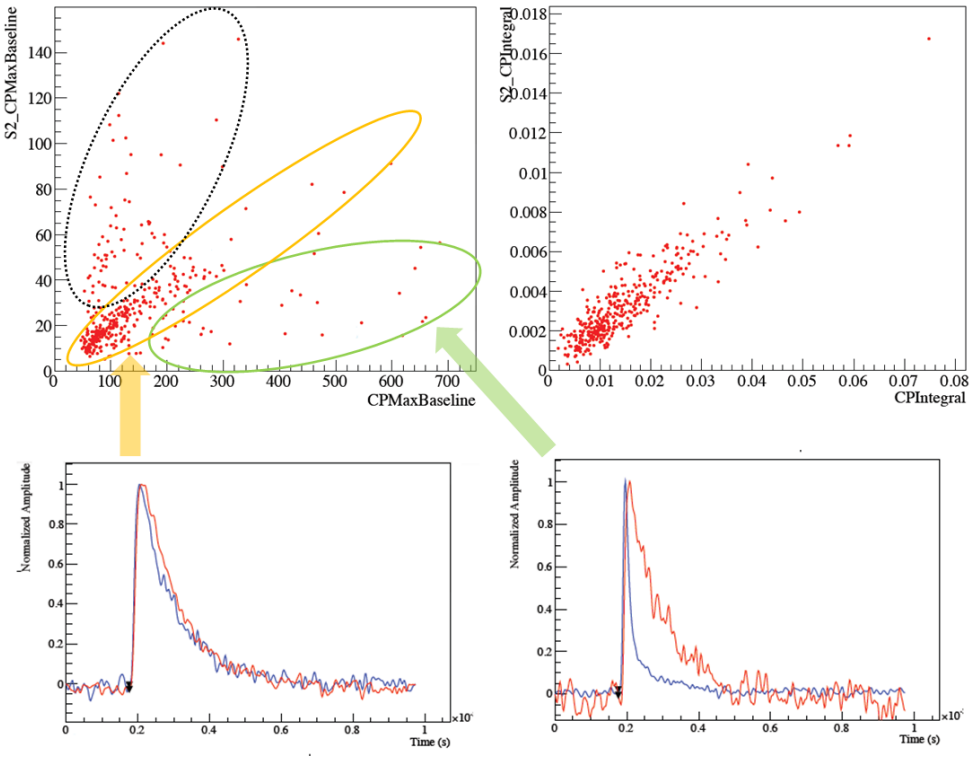

Figure 9.14: *The signals induced by CR interaction as measured by the KID number 2 versus KID number 6, in units of calibrated phase peak signal (top left). The plot shows three population of CR interactions, depending on the pulse shape in KID 2 (red) and KID 6 (blue): the central population (green) correspond to interaction far from both the KID (bottom left), while the lateral populations (orange and dotted black) refers to CR that have impacted near one of the two KID (bottom right). Using the integral of the calibrated phase signal as energy estimator linearizes the KID versus KID plot (top right)*

detector response is linearized (fig. 9.14) and can be used to inter-calibrate different pixels.

We then analyzed the signals coming from the LED pulser in order to use them as a raw energy calibration. The calibrated phase signals do not depends on the KID parameters, so we can sum the integrals coming from different channels, obtaining a total spectrum of the energy source for both LED and CR pulses (fig. 9.15(a)). Then using the $\sim 100keV$ nominal pulser energy, we calculated a CR energy of $(0.073/0.071) \cdot 100keV = 178keV$, compatible with CR releasing $140 \div 200keV$ into a $300\mu m$ thick silicon substrate, depending on the angle of impact ($90 \div 45$ deg). Using this calibration we therefore transformed the integral signals (fig. 9.15(b)) in energy spectra (fig. 9.15(c)) for all the KID. We finally used the templates of the two signal components calculated on the CR

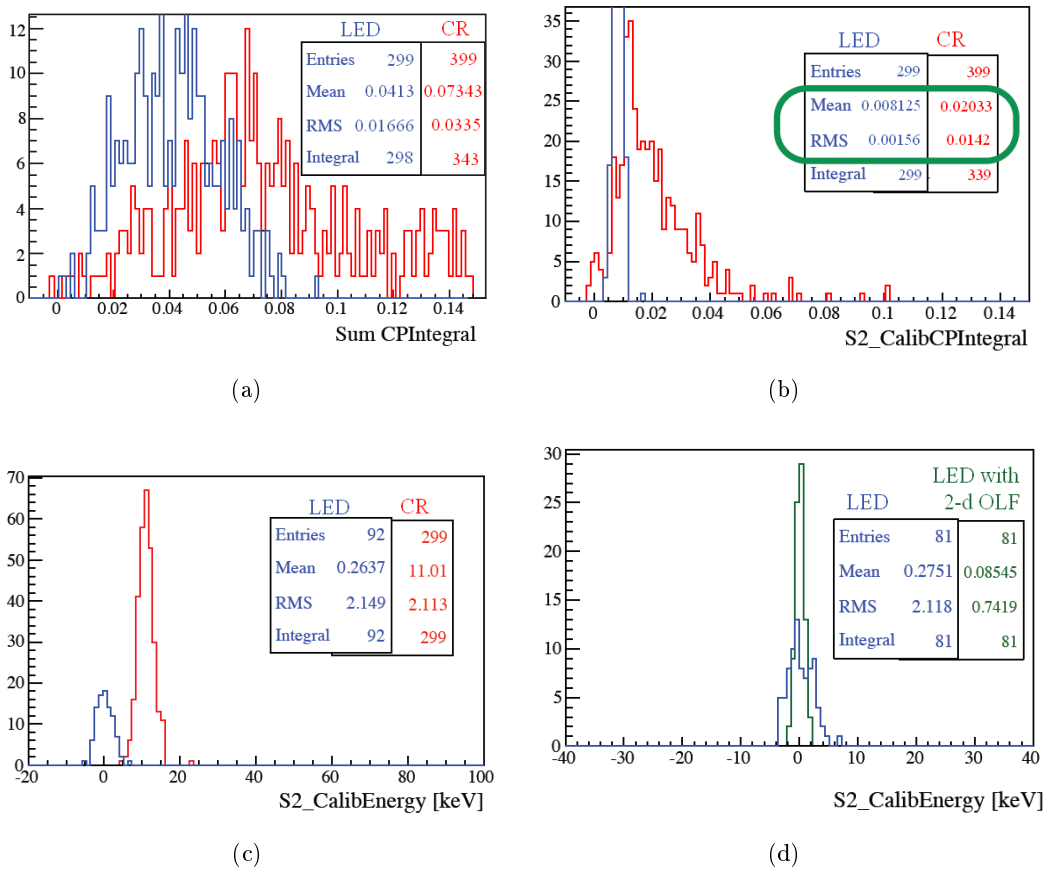

Figure 9.15: *Spectra of the signals for pulsed LED light and for secondary Cosmic Rays interactions (CR): (a) sum of the calibrated phase integral spectra of all the detectors; (b) calibrated phase integral spectrum and (c) energy spectrum for the KID number 2. (d) Energy spectrum of the KID number 2 before and after applying the two dimensional OLF, which improves the resolution of a factor* ~ 3.

pulses to apply a the two-dimensional OLF to the LED pulses.

At the current state, this analysis pipeline improves the energy resolution by a factor ~ 9, accounting for: 1) a factor 3 coming from the OLF (fig. 9.15(d)), and 2) another factor 3 due to the low-pass Software FIR Filter at 60kHz that has been applied on the temporal pulses (acquired at 500kHz) when calculating the templates of the signal factor. This total factor is consistent with that found using the one dimensional OLF analysis in the previous measurements (fig. 9.10).

4. a new mask with an easier geometry (labeled *KID4*) has been designed and fabricated (fig. 9.16(a)–9.16(c)). Each array of the mask provides four pixels with exactly the same geometry of the first generation KID, except of a different coupling to a straight feedline,

and the realization of PADs for ground bonding across the feedline. The resonance are expected to be separated of about $13MHz$, with quality factors of the order of $8 \cdot 10^4$. The new *KID4* mask has been recently tested in Rome laboratories;

5. the introduction of a second RF line in the cryostat has been planned before the end of the year. This improvement will allow to test two arrays at once, sensibly speeding up the array test phase.

The CALDER team is currently at work. The introduction of these improvements in the next experiments will provide more quantitative results in the forthcoming months.

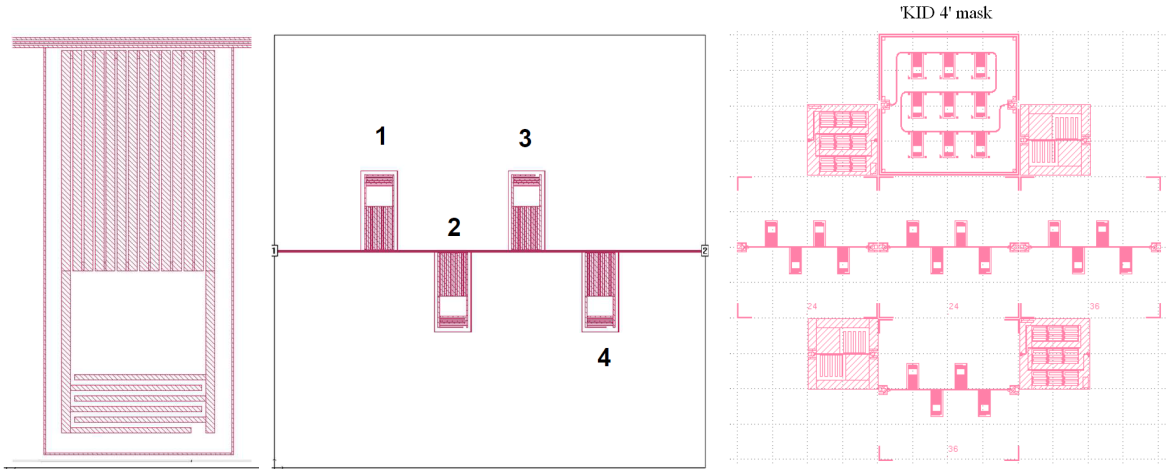

(a) (b) (c)

Figure 9.16: SONNET *screen-shot of the pixel (a) and of the array (b) geometries; (c) the design of the new 'KID4' mask.*

Conclusions

The Kinetic Inductance Detectors represent a valid and reliable technology, alternative to bolometers, for the development of light detectors. The most striking demonstration has been recently provided by the NIKA camera, equipped with 356 $18-20nm$ thick Al Lumped Element KID and installed at the focal plane of the IRAM 30-m telescope. With measured on-sky sensitivities of $40mJy/\sqrt{Hz}$ and $14mJy/\sqrt{Hz}$ in the $1.25mm$ and $2mm$ bands respectively, the *NIKA* instrument has reached performances comparable to current bolometric experiments operating at the same wavelengths. In terms of the optical NEP we estimate an average of $\sim 7 \cdot 10^{-17} W/\sqrt{Hz}$ for the 2mm band. This value is a reference in order to evaluate the optical performances of a KID-based camera for mm-astronomy. The first laboratory measurements of the *AstroKIDs* camera demonstrator showed an optical NEP of $\sim 7.5 \cdot 10^{-16} W/\sqrt{Hz}$ on the better pixel, one order of magnitude worse than the *NIKA* on-sky measurements.

One of the main advantages of KID with respect to bolometers is their high Frequency Domain Multiplexing factor. In order to take full advantage of this, we successfully developped a complete electronics system devoted to the multiplexed readout of KID arrays. Two main versions of the electronics have been adopted: 1) the *NIKEL electronics* for mm-astronomy applications, currently used by the NIKA (Granada, Spain) and NIKA-2 (Grenoble, France) instruments, and 2) the *NIXA high-speed electronics*, that can be operated both in a slow-mode devoted to mm-astronomy, and in a fast-mode, dedicated to particle physics applications. Concerning the item 2., we also implemented an intuitive client to operate the electronics, called *sNelloX*. This software allows us to fully command and control all the calibration and readout procedures for the KID arrays. The *NIXA* board equipped with the *sNelloX* software have proven their effectiveness and reliability, and currently provide the readout chain for the *AstroKIDs* (Rome, Italy), the *SPACEKIDS* (Grenoble, France) and *CALDER* (Rome and LNGS, Italy) experiments.

Another main advantage of the KID is linked to their time constants, which are typically much faster than those of bolometers. The measurements done with our detectors give quasi-particle lifetimes of $\sim 10\mu s$ and phonon decay times in the range $30 \div 120\mu s$, in agreement with literature. Although the existence of a slower ($\sim 15ms$) thermal time constant has been

confirmed, its value should be sensibly reduced optimizing the thermal contact between the array and the sample holder. If nonetheless the primary CR interactions will be expected to produce a detectable thermal signal, this can be easily fitted and removed from the data time trace. Then, assuming that the KID response is dominated by a time constant of the order of a tenth of millisecond, an array of few hundreds KID hosted on a single silicon die of $\sim 10cm^2$ would suffer a data loss within roughly 15%, comparable to that of one single Planck bolometer. It is worth to stress that we made the assumption that every Cosmic Ray hit produces a signal in the whole array, regardless of the point of impact.

Our measurements showed that however, over large distances, this is in general not the case. The KID array exposed to secondary CR on HR-Si indicates that additional metallization layers might provide a possible solution for confining the effect of higher energy phonons on shorter distances. Where present, the aluminum ground plane layer reduces sensibly the number of observed coincidences, showing that a CR hit only affects an area of roughly $1cm^2$ around the impact point. This correspond to 10 times less than the total surface of a typical focal plan hosting few hundreds KID. By using sources of α particles having energies $\sim 6MeV$ we confirmed that an additional metallization limits the propagation of the energy released inside the substrate. The use of superconductors such as the Titanium, with an energy gap ~ 3 times lower than that of Aluminum, sensibly enhances the thermalization of the ballistic phonon. Our results showed that a Ti layer added on the backside of the KID array efficiently downconverts the ballistic phonons to energies below the Al gap. As a consequence, even the effect of the α hits, which actually release in the substrate an energy 30 times higher than a typical CR, is killed over distances $\sim 15mm$. The use of additional metal layers can thus play a crucial role in the optimization of KID arrays for spatial environments and in reducing the total data loss to be expected during a satellite mission.

Besides showing excellent performances in millimeter Astronomy observations, KID arrays are remarkably versatile, as they have proved by adapting to several and very different fields of research. The Lumped Element Kinetic Inductance Detectors optimized during this thesis have shown phonon imaging and time-resolved particle detection capabilities. Although these detectors were not at all optimized for particle physics, they have demonstrated low noise performances ($E_{RMS} \sim 14eV$) with sub-keV energy resolutions ($< 400eV$). Furthermore, LEKID could be used as a background discrimination tool in rare event search physics. Deploying the high-speed multiplexed readout system implemented during this thesis, the CALDER collaboration has already undertaken this path. The preliminary CALDER results have shown that the realization of an ultra-sensitive tool for CUORE appears to be at hand, and this could also be spendable for other applications like WIMP search, subject to the successful development of light detectors with resolution of $10 \div 20eV$. This might be the key that opens large-scale bolometric experiments to dark matter search and could provide an essential tool for underground physics experiments.

Appendix A

Basics of BCS theory

A.1 Cooper pairs

The mechanism that describes the electron-electron interaction at low temperature was explained by the Bardeen-Cooper-Schrieffer microscopic theory of superconductivity (known as BCS theory) in 1957 [136]. In a superconductor, the electrons of equal and opposite spin and momenta are bound two-by-two in the so called *Cooper pairs*. The maximum distance over which the binding of the two electrons is effective is called the coherence length ξ_0 of a Cooper pair. This distance is metal dependent and from the BCS theory is given by

$$\xi_0 = \frac{0.18 v_F}{k_B T_c} \tag{A.1}$$

where v_F is the Fermi velocity. Two bound electrons act like a single particle of integer spin and then obey to Bose-Einstein statistic. Therefore it is not forbidden for several Cooper pairs to exist in the same quantum state. They condensate filling-up available states and this allow to accommodate all of them below the Fermi energy E_F. We can describe the density of electron states (paired and non paired) as [137] [138]

$$N(\epsilon) = \begin{cases} \frac{N_0 \epsilon}{\sqrt{\epsilon^2 - \Delta^2(T)}} & |\epsilon| \geq \Delta \\ 0 & |\epsilon| < \Delta \end{cases} \tag{A.2}$$

where N_0 is the normal single-spin density of electron states calculated at the Fermi energy for the metal, and $\epsilon \equiv E - E_F$, with E the energy of the electron. The equation A.2 points out that the whole range of energy $E_F - \Delta < E < E_F + \Delta$ is forbidden. The creation of Cooper pairs gives rise to an gap energy of size 2Δ, forcing the states in the gap zone into regions either side of $E_F \pm \Delta$. An enhanced density of states is formed leaving the total number of states constant, as shown in fig. A.1(a). In this sense 2Δ describes the gap energy between the last available state below E_F and the first available state above E_F at the temperature T. As Cooper pairs can exists only below the gap, 2Δ represents the energy necessary to break a Cooper pair into two quasi-particles. If only Cooper pairs were present, the value of the gap would be constant. This is actually the case at T= $0K$, where the gap reaches its maximum defined as $\Delta(T = 0) \equiv \Delta_0$. As the temperature increases from $0K$ towards T_c,

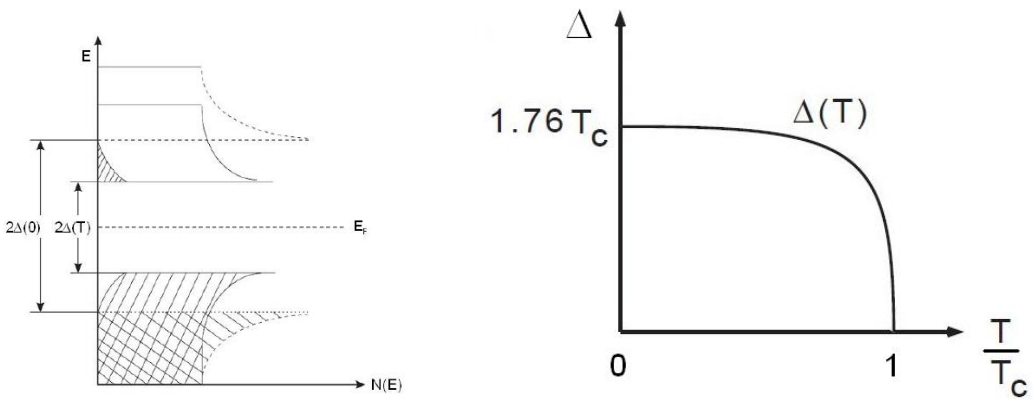

(a) (b)

Figure A.1: *(a) Density of state of Cooper pairs and quasi-particles depending on the temperature T. Non-zero temperatures reduce the density of available states below E_F and so the gap energy $\Delta(T)$. (b) Dependence of the energy gap Δ from the temperature.*

energy is furnished to the system through thermal agitation resulting Cooper pair breaking and quasi-particles creation. The existence of a quasi-particle without its partner with the same and opposite momentum, prevents the formation of a Cooper pair occupying that specific momentum state, that leads to a reduction of the number of available momentum states below E_F. In order to leave total number of states unchanged, the gap $\Delta(T)$ is reduced until it becomes zero at T_c. From this temperature onwards, no Cooper pairs can be formed. The dependence on the temperature of the density of states results in the temperature dependance of the gap energy, which can be described by [138]

$$\frac{1}{N_0 V} = \int_{-\hbar\omega_D}^{\hbar\omega_D} \frac{tanh\left(\frac{\sqrt{\epsilon^2+\Delta^2(T)}}{2k_B T}\right)}{2\sqrt{\epsilon^2+\Delta^2(T)}} d\epsilon \tag{A.3}$$

where k_B is the Boltzmann constant, ω_D is the Debye frequency of the superconductor and V is the potential of the electron-phonon interaction. $N_0 V$ represents therefore the total phonon interaction potential, a material dependent quantity.

It can be found by setting $\Delta(T) = 0$ at $T = T_c$

$$k_B T_c = 1.14\hbar\omega_D e^{-\frac{1}{N_0 V}} \tag{A.4}$$

Calculating eq. A.7 at $T = 0K$ gives $\Delta(T) = \Delta_0$ and all integrand weights *tanh* equals to 1, from which

$$\frac{1}{N_0 V} = \int_{\Delta_0}^{\hbar\omega_D} \frac{1}{\sqrt{\epsilon^2+\Delta_0^2}} d\epsilon \approx \ln\frac{2\omega_D}{\Delta_0} \Rightarrow \Delta_0 \approx 2\hbar\omega_D e^{-\frac{1}{N_0 V}} \tag{A.5}$$

and substituting A.4 in A.5 we finally obtain

$$\Delta_0 \approx 1.76 k_B T_c \tag{A.6}$$

The binding energy of a Cooper pair is thus

$$2\Delta_0 \approx 3.5 k_B T_c \tag{A.7}$$

In fig. A.1(b) is shown the dependance of Δ from the temperature.

A.2 Quasi-particles density

The density of states is symmetrical about E_F as pointed out in the plot A.1(a), with the states below E_F being referred to as quasi-holes. One can find the number of quasi-particle excitations by integrating under the curve $f(E)N(E)$ from $E_F + \Delta \rightarrow \infty$. This operation essentially counts the number of states available and multiplies this by the occupation probability, i.e. the Fermi-function $f(E)$. The number of quasi-particles created by external excitation is equal to twice the number of pairs broken. However the reduction in the gap energy produces quasi-holes. This now allows some of the electrons below $E_F - \Delta$ to change their momentum and hence take part in normal state conduction. The number of unpaired electrons which can take part to normal state conduction is therefore [139]

$$n_{qp}(T) = 4 \int_0^\infty f(\epsilon) N(\epsilon) d\epsilon \tag{A.8}$$

where the density of states is defined in eq. A.2 and the Fermi function is defined as

$$f(\epsilon) = \frac{1}{1 + e^{\frac{\epsilon}{k_B T}}} \tag{A.9}$$

The factor of 4 before the integral in eq. A.8 is due to the fact that each state can accommodate two electrons (spin up and spin down) and the density of states is for both quasi-holes and quasi-particles (i.e. the hole states allow electrons below $E_f - \Delta$ to contribute to conductivity). For $T \ll T_C$ eq. A.8 gets the simple expression [79] [138]

$$n_{qp} = 2N_0 \sqrt{2\pi k_B T \Delta_0} e^{-\frac{\Delta_0}{k_B T}} \tag{A.10}$$

A.3 Two fluids model

The phenomenological description of two different populations of charge carriers coexisting in a superconductor was developed by Gorter and Casimir in 1956 and is known as the *two fluids model of conductivity* [140] . According to the schematic representation in A.2, the two fluids model states that the current in a superconductor can flows in two different paths, one through the superconductive carriers (Cooper pairs of density n_s, leading to current density $J_s = \sigma_s E$), and the other through the thermally excited electrons (quasi-particles of density n_{qp}, leading to current density $J_{qp} = \sigma_{qp} E$). This effect can be expressed by calculating the

contributions of the two populations to the total conductivity

$$\sigma = \sigma_{qp} + \sigma_s \tag{A.11}$$

where σ_{qp} and σ_s are the conductivities respectively of the normal and superconducting electrons.

A.3.1 The Drude model

According to the Drude model for normal metals, the classical mechanics of motion of the conduction electrons under an applied electric field E results from their opposite motion of the scattering by the lattice ions and the acceleration by the electric field. This dynamics is described in this model by the equation of motion

$$m\frac{\delta v}{\delta t} = eE - \frac{mv}{\tau} \tag{A.12}$$

where m and e are respectively the mass and the charge of the electron, v the average velocity of the electrons and τ their relaxation time, i.e. the time an electron needs to bring its average velocity to zero when turning off the electrical field. The mean free path between two scattering is simply given by $l_{mfp} \equiv v_F/\tau$. Considering n_n as the number of normal electron per unit of volume, eq. A.12 can be written in terms of current density as $J_n = n_n ev$. Applying a constant electrical field, the average velocity v can be calculated by eq. A.12 at equilibrium ($\delta v/\delta t = 0$)

$$v = \frac{eE\tau}{m} \tag{A.13}$$

and this leads to the *Ohm's law* $J_0 = \sigma_0 E$, where $\sigma_0 = ne^2\tau/m$ is the residual conductivity, i.e. the normal conductivity just above the critical temperature T_c. It is a material dependent quantity which is linked to the residual resistivity of the material $\rho_0 \equiv \sigma_0^{-1}$. For typical aluminum $\sigma_0 \approx 10^8 \Omega^{-1} m^{-1}$, $n = 1.8 \cdot 10^{29}$ and so $\tau \approx 10^{-15} s$.

Now applying a sinusoidal electric field of the form $E = E_0 e^{j\omega t}$, the equation A.12 has the solution

$$J_n = \sigma_n E \tag{A.14}$$

with

$$\sigma_n = \frac{n_n e^2 \tau}{m(1+\omega^2\tau^2)} - j \cdot \frac{n_n e^2 \omega \tau}{m(1+\omega^2\tau^2)} \tag{A.15}$$

defined as the complex conductivity for a normal conductor. If $\tau\omega \ll 1$ we can neglect the imaginary term and write

$$\sigma_n \sim \frac{n_n e^2 \tau}{m(1+\omega^2\tau^2)} \tag{A.16}$$

Even at ac frequencies up to microwaves ($\leq 100GHz$) $\tau \ll 1/\omega$. There isn't enough time for the field to revert before charge carriers scatter and lose their energy. This means that in a conductor in his normal state, electrons do not store appreciable energy. The electromagnetic energy of the field is transformed into the kinetic energy of the normal electrons, and then dissipated throughout scattering by the crystal lattice ions, that results in heating the

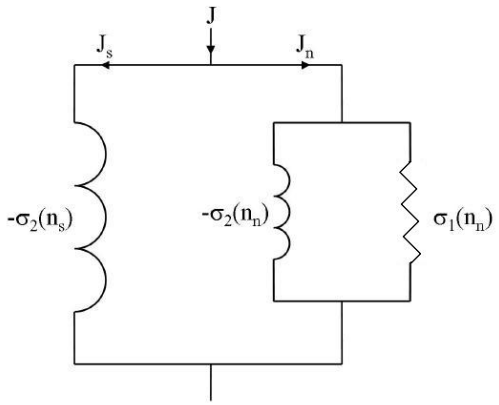

Figure A.2: *Equivalent circuit describing the two fluid model for the current in a superconductor. Accordingly to equations A.11 and A.20, $\sigma_1(n_n)$ represents the real part of the conductivity due to quasi-particles and $\sigma_2(n_n)$ the imaginary part. $\sigma_2(n_s)$ stands for the conductivity due to Cooper pairs and it is purely reactive.*

conductor (Joule effect).

A.3.2 The London model

The theory of superconductivity predicts a zero dc-resistance of the material below its critical temperature T_c. In that case we have no scattering effects and electrons can move freely in the crystal lattice. To apply the Drude model to the superconducting case, we have to modify eq. A.12 as in the London model [141]. The relaxation time τ has a finite value for normal conductors due to the interaction of electrons and the crystal lattice as described above. Without scattering with the lattice, we can assume that $\tau = \infty$. This simplifies the equation of motion to

$$m\frac{\delta v}{\delta t} = eE \tag{A.17}$$

If we write this equation in term of the superconducting current density $J_s = n_s e v$ we obtain the *first London equation* [142]

$$\frac{\delta J_s}{\delta t} = \frac{n_s e^2}{m} E \tag{A.18}$$

This equation describes the zero resistance effect and the resulting super-current. Applying an ac-electrical field analog to the normal conducting case leads to the conductivity

$$\sigma_s = -j \cdot \frac{n_s e^2}{\omega m} \tag{A.19}$$

which is purely reactive for superconductors.

A.3.3 Total complex conductivity

We can thus calculate the total conductivity as described in eq. A.11. The two contributions coming from Cooper pairs and quasi-particles are described respectively by eq.s A.19 and A.15, replacing in the latter $n \to qp$, i.e. assuming that all non-paired electrons behaves as normal conduction electrons. Definitively we have

$$\sigma = \sigma_{qp} + \sigma_s$$

with

$$\sigma_{qp} = \frac{n_{qp}e^2\tau}{m(1+\omega^2\tau^2)} - j \cdot \frac{n_{qp}e^2\omega\tau}{m(1+\omega^2\tau^2)} \qquad \sigma_s = -j \cdot \frac{n_s e^2}{\omega m}$$

We can also write the total conductivity as

$$\sigma = \sigma_1 - j \cdot \sigma_2 \tag{A.20}$$

where σ_1 expresses the pure resistive part of the conductivity which is responsible for the losses, while the phase displacement of the current depends only on the pure reactive term σ_2. According to the two fluid model, the real resistive part is only due to quasi-particles (see eq. A.15)

$$\sigma_1 = \frac{n_{qp}e^2\tau}{m(1+\omega^2\tau^2)} \tag{A.21}$$

while the imaginary reactive part arises from both quasi-particles and Cooper-pairs (see eq.s A.15, A.19),

$$\sigma_2 = \frac{n_{qp}e^2\omega\tau}{m(1+\omega^2\tau^2)} + \frac{n_s e^2}{\omega m} \tag{A.22}$$

For microwave signals ($\tau\omega \ll 1$) the reactive contribution of the quasi-particles can be neglected and the imaginary conductivity is purely superconductive

$$\sigma_2 \approx \sigma_s = \frac{n_s e^2}{\omega m} \tag{A.23}$$

A.4 Meissner effect and London depth

The generation of currents with no electrical resistance results in the complete expulsion of any external magnetic field from the bulk of the superconductor. This property, known as Meissner-effect [143], was first discovered by Meissner and Ochsenfeld in 1933 and was described two years later by the London brothers [142] with the *second London equation*

$$\nabla \times \vec{J}_s = \frac{\mu_0 n_s e^2}{m}\vec{H} \tag{A.24}$$

where μ_0 is the magnetic permeability of vacuum while H is the magnetic field strength. Though the surface currents are able to screen the bulk from the magnetic field, it is not completely canceled near the surface. Substituting the *Ampere Law's* ($\nabla \times \vec{H} = \vec{J}$) into the eq. A.24, it is found that an external magnetic fields into a superconductor is exponentially

suppressed with a typical attenuation length

$$\lambda_L = \sqrt{\frac{m}{\mu_0 n_s e^2}} \tag{A.25}$$

called the London penetration depth. For a magnetic field parallel to the surface of the superconductor, the London penetration depth λ_L describes the distance in the bulk from the edge of the superconductor, perpendicular to the surface, where the magnetic field is reduced by a factor of e.

A.5 Pippard non-locality and Mattis-Bardeen integrals

To understand correctly the capability of the superconductor to screen magnetic fields, one needs to compare λ_L with the coherence length ξ_0 defined in eq. A.1. In the case of large coherence length, comparable to the London penetration depth, the rapidly varying electrical field can not be considered constant over the length of ξ_0. In 1953 Pippard introduced a non-local treatment of superconductors [144] to describe metals with $\xi_0 \gg \lambda_L$, which are therefore called Pippard-superconductors. The non-locality of Pippards theory gives rise to an effective London penetration depth λ_{eff} , which can be significantly larger than $\lambda_L(T)$. It can be approximated with [137] [138]

$$\lambda_{eff} = 0.65(\lambda_L(T)^2 \xi_0)^{\frac{1}{3}} \tag{A.26}$$

The correct non-local treatment of BCS theory leads to integrals expressions of the real and imaginary part of the conductivity. According to the Mattis-Bardeen theory [145], these values are given respectively by

$$\frac{\sigma_1}{\sigma_n} = \frac{2}{\hbar\omega}\int_{\Delta}^{\infty} \frac{[f(\epsilon) - f(\epsilon - \hbar\omega)]\,(\epsilon^2 + \Delta^2 + \hbar\omega\epsilon)}{\sqrt{\epsilon^2 - \Delta^2}\sqrt{(\epsilon + \hbar\omega)^2 - \Delta^2}} d\epsilon + \frac{1}{\hbar\omega}\int_{\Delta - \hbar\omega}^{-\Delta} \frac{[1 - 2f(\epsilon - \hbar\omega)]\,(\epsilon^2 + \Delta^2 + \hbar\omega\epsilon)}{\sqrt{\epsilon^2 - \Delta^2}\sqrt{(\epsilon + \hbar\omega)^2 - \Delta^2}} d\epsilon \tag{A.27}$$

$$\frac{\sigma_2}{\sigma_n} = \frac{1}{\hbar\omega}\int_{\Delta - \hbar\omega, -\Delta}^{\Delta} \frac{[1 - 2f(\epsilon - \hbar\omega)](\epsilon^2 + \Delta^2 + \hbar\omega\epsilon)}{\sqrt{\Delta^2 - \epsilon^2}\sqrt{(\epsilon + \hbar\omega)^2 - \Delta^2}} d\epsilon \tag{A.28}$$

where the lower limits of the σ_2-integral have to be chosen for $\hbar\omega \ll \Delta$ and $\hbar\omega \gg \Delta$ respectively.

Appendix B

Calculating LEKID signal

B.1 Transmitted amplitude and phase

The transmission scattering parameter S_{21} is described by equation 2.82

$$S_{21} = S_{21,min}\frac{1 + j2Q_i x}{1 + jS_{21,min}2Q_i x}$$

To deal with real quantities, we can proceed with two different approaches. The first consists in measuring the phase and amplitude of the transmitted signal. The second option is to measure the real and imaginary components of the scattering parameter S_{21}, in phase ($I \equiv Re(S_{21})$) and in quadrature ($Q \equiv Im(S_{21})$) with respect to the signal incident on the resonator. The two solutions are linked by the equations

$$Amplitude = |S_{21}| = \sqrt{I^2 + Q^2} \qquad \text{and} \qquad Phase = arctan(\frac{Q}{I}) \tag{B.1}$$

In order to make the calculations easier to read, let us define in the following

$$s \equiv S_{21,min} \quad \text{and} \quad y \equiv 2Q_i x \quad \text{, with } x \equiv \frac{\Delta\omega}{\omega_0} \tag{B.2}$$

So we first need to rationalize the eq. 2.80

$$S_{21} = s\frac{1 + sy^2 + jy - jsy}{1 + (sy)^2} \tag{B.3}$$

then extract the real and imaginary parts

$$I \equiv Re(S_{21}) = s\frac{1 + sy^2}{1 + (sy)^2} \tag{B.4}$$

$$Q \equiv Im(S_{21}) = s\frac{y(1 - s)}{1 + (sy)^2} \tag{B.5}$$

and calculate the transmitted amplitude

$$|S_{21}| = \frac{s}{1+(sy)^2}\sqrt{[1+sy^2]^2+[y(1-s)]^2} = \frac{s}{1+(sy)^2}\sqrt{(1+y^2)(1+(sy)^2)} = s\sqrt{\frac{1+y^2}{1+(sy)^2}} \tag{B.6}$$

We can thus write the explicit expression for transmitted amplitude

$$|S_{21}| = S_{21,min}\sqrt{\frac{1+(2Q_ix)^2}{1+(S_{21,min}2Q_ix)^2}} \tag{B.7}$$

or for transmitted power

$$|S_{21}|^2 = S_{21,min}^2\frac{1+(2Q_ix)^2}{1+(S_{21,min}2Q_ix)^2} \tag{B.8}$$

The transmitted phase is simply

$$\phi = arctan\frac{2Q_ix(1-S_{21,min})}{1+S_{21,min}(2Q_ix)^2} \tag{B.9}$$

B.2 Effect of parasitic reactance on S_{21}

Suppose now to add a series reactance X_{par} into the feedline, in series with its proper impedance Z_0. Using eq. B.10 we get

$$S_{21} = \frac{2}{2+\frac{Z_{eff}+j2X}{Z_0}} \tag{B.10}$$

By performing the same calculation of paragraph B.1, we get the result

$$S_{21} = s\frac{1+jy}{1-syp+js(y+p)} \tag{B.11}$$

where we have adopted the usual notation (eq. B.2), further defining

$$p \equiv \frac{X_{par}}{Z_0} \tag{B.12}$$

Now on resonance (x=0) s is no more the minimum of the S_{21} function. Imposing $x = 0$ we can find the relation linking these two quantities

$$S_{21,min} = \frac{s}{\sqrt{1+(sp)^2}} \tag{B.13}$$

This means that for parasitic reactance on the feedline, the minimum of the function is not reached at the resonance frequency. With these definitions, we can thus calculate the transmitted amplitude

$$|S_{21}| = s\sqrt{\frac{1+y^2}{(1-syp)^2+[s(y+p)]^2}} \tag{B.14}$$

Finally we can razionalize and then extract the real and imaginary parts

$$I \equiv Re(S_{21}) = s\frac{1+sy^2}{(1-syp)^2+s^2(y+p)^2} \tag{B.15}$$

$$Q \equiv Im(S_{21}) = s\frac{y(1-s)-sp(1-y^2)}{(1-syp)^2+s^2(y+p)^2} \tag{B.16}$$

The transmitted phase is therefore given by

$$\phi = arctan\frac{y(1-s)-sp(1-y^2)}{1+sy^2} \tag{B.17}$$

In this thesis we use overcoupled LEKID resonators $g > 3 \rightarrow s < 0.25$, with internal quality factors of $\sim 5 \cdot 1O^5$ and external quality factors of $\sim 3 \cdot 10^4$. For resonance frequencies $\sim GHz$, this implies $y < 1$ at FWHM of the resonance, reaching maximum values of ~ 5 off resonance. For low value of parasitic reactance $X_{par} \ll Z_0 \rightarrow p \ll 1$, we can neglect the syp term in eq. B.14 and identify $s \sim S_{21,min}$ (eq. B.13). We can thus write the explicit approximated expression for the transmitted amplitude, power and phase of a LEKID with a parasitic reactance X_{par}

$$|S_{21}| \approx S_{21,min}\sqrt{\frac{1+(2Q_ix)^2}{1+(S_{21,min}(2Q_ix+X_{par}/Z_0))^2}} \tag{B.18}$$

$$|S_{21}|^2 \approx S_{21,min}^2\frac{1+(2Q_ix)^2}{1+(S_{21,min}(2Q_ix+X_{par}/Z_0))^2} \tag{B.19}$$

$$\phi \approx arctan\frac{2Q_ix(1-S_{21,min})-S_{21,min}X_{par}/Z_0(1-(2Q_ix)^2)}{1+S_{21,min}(2Q_ix)^2} \tag{B.20}$$

B.3 Effect of lossy dielectrics on Q_i

The circuit are always fabricated on a substrate. There are thus additional losses associated to the capacitance due to the fact that the varying field is not in vacuum. This terms is due to the conductivity of the capacitive section and it can be represented by a conductance G in parallel to the capacitor C. The calculation of this term can be performed using the loss model of a parallel plate capacitor with the dielectric loss tangent ($tan\delta_e = \frac{\epsilon''}{\epsilon'}$), defining a complex dielectric constant (permittivity) $\epsilon = \epsilon' - j\epsilon''$. The presence of complex permeability should be taken into account because add new dissipation channels to the system, with quality factors given by $Q = (tan\delta)^{-1}$. This changes the capacitor contribution to the total impedance of the circuit, that is now described by a term $Z_C = \frac{1}{j\omega\epsilon C} = \frac{1}{j\omega\epsilon' C(1-j\epsilon''/\epsilon')} \approx \frac{1}{\omega\epsilon' C}(-j + tan\delta_e)$. Furthermore, for an inter-digital capacitor designed for a LEKID, the field distribution is not entirely within the substrate (only half), hence, we need to replace δ_e with $\delta_{e,eff}$ to account for this. Identifying $\epsilon' C \rightarrow C$ we can write the impedance of RLC circuit modifying eq. 2.53 and

$$Z_{RLC} = R + j\omega L + \frac{1}{j\omega C} + \frac{1}{\omega C}tan\delta_{e,eff} \tag{B.21}$$

and the internal quality factor, adding to eq. 2.70 the contribute of the dielectric losses

$$Q_i = \frac{\omega_0 L}{R + \frac{tan\delta_{e,eff}}{\omega_0 C}} \tag{B.22}$$

Our typical Al LEKID show capacitance values of $C \sim 1pF$ and $tan\delta_{e,eff} \sim 10^4$ [76], which means for our detectors resonating at frequencies around $1 \div 2GHz$, $tan\delta_{e,eff}/(\omega_0 C) \sim 2 \cdot 10^{-4}$ with a residual resistance at $\sim 100mK$ calculated to $R \sim 10^{-6}\Omega/\square$. For a typical 2.3×2.3 mm^2 LEKID with a $4\mu m$ wide meander and a filling factor around 1%, this means $R \sim 5 \cdot 10^{-3}\Omega$. We can thus neglect the tangent loss term for our detectors.

List of Figures

Bibliography

[1] K.D. Irwin and W.R. Hilton, *Transition-Edge Sensors*, Top. Appl. Phys., vol. 99, pp. 63-149, 2005

[2] J.E. Ruhl, *The South Pole Telescope*, Proc. SPIE, vol. 5498, pp. 11-29, 2004

[3] D. Schwan et al., *APEX-SZ: The Atacama Pathfinder EXperiment Sunyaev-Zel'dovich Instrument*, The Messenger, vol. 147, pp. 7-12, 2012

[4] G. Siringo et al., *The large APEX bolometer camera LABOCA*, Astronomy and Astrophysics, vol. 497, pp. 945-962, 2009

[5] A.L. Woodcraft, *Scuba-2: a 10,000-pixel submillimeter camera for astronomy*, Joint 32nd International Conference on Infrared and Millimeter Waves and 15th International Conference on Terahertz Electronics, vols. 1 and 2, IEEE MTTS, 2007.

[6] The BICEP2 Collaboration, *BICEP2-II: Experiment and Three-year Data Set*, ApJ, vol. 792, p. 62, 2014

[7] P.K. Day et al., *A broadband superconducting detector suitable for use in large arrays*, Nature, 425, 817, 2003

[8] P. L. Richards, *Bolometers for infrared and millimeter waves*, J. Appl. Phys., vol. 76, p. 1, 1994

[9] V.V. Schmidt, *The Physics of Superconductors*, ed. A. U. P. Muller (Berlin, Heidelberg: Springer-Verlag), 1997

[10] S. Doyle, *Lumped Element Kinetic Inductance Detectors*, PhD thesis, Cardiff University, Cardiff, UK, 2008

[11] A.A. Penzias, R.W. Wilson, *A measurement of excess antenna temperature at 4080 Mc/s*, Astrophysical Journal, vol. 142, pp. 419-421, 1965

[12] P. de Bernardis et al., *A flat universe from high-resolution maps of the cosmic microwave background radiation*, Nature, vol. 404, pp. 955-959, 2000

[13] M.G. Hauser and E. Dwek, *The Cosmic Infrared Background Measurements and Implications*, Ann. Rev. Astron. Astrophys., vol. 39, pp. 249-307, 2001

[14] D. Ward-Thompson et al., *The James Clerk Maxwell Telescope Legacy Survey of Nearby Star-forming Regions in the Gould Belt*, The Publications of the Astronomical Society of the Pacific, Volume 119, Issue 858, pp. 855-870, 2007

[15] E. Kreysa et al., *Bolometer array development at the Max-Planck-Institut fuer Radioastronomie*, Proc. SPIE, Vol. 3357, pp. 319-325, 1998

[16] G.L. Pilbratt et al., *Herschel Space Observatory. An ESA facility for far-infrared and submillimetre astronomy*, Astronomy and Astrophysics, Volume 518, id.L1, 6 pp., 2010

[17] D. Arzoumanian; et al., *Characterizing interstellar filaments with Herschel in IC5146*, Astronomy and Astrophysics, vol. 529, L6, 2011

[18] D. Ward-Thompson et al. *First Observations of the Magnetic Field Geometry in Prestellar Cores*, Astrophysical Journal, vol. 537, L135, 2000.

[19] , J. Glenn et al., *Bolocam: A millimeter-wave bolometric camera*, Proc. SPIE, vol. 3357, p. 326, 1998

[20] W.S. Holland et al., *SCUBA: A common-user submillimetre camera operating on the James Clerk Maxwell Telescope*, Mon. Not. Roy. Astron. Soc., vol. 303, p. 659, 1999

[21] S. Lilly et al. *The Canada-United Kingdom Deep Submillimeter Survey. II. First Identifications, Redshifts, and Implications for Galaxy Evolution*, The Astrophysical Journal, vol. 518, p. 641, 1999

[22] Lagache et al., *Dusty Infrared Galaxies: Sources of the Cosmic Infrared Background*, Annual Review of Astronomy & Astrophysics, vol. 43, Issue 1, pp.727-768, 2005

[23] A.W. Blain et al., *Submillimeter galaxies*, Phys. Rept., vol. 369, pp. 111-176, 2002

[24] D.J.B. Smith et al., *Herschel-ATLAS: counterparts from the UV–NIR in the science demonstration phase catalogue*, Monthly Notices of the Royal Astronomical Society, Vol. 416, Issue 2, pp. 857-872, 2011

[25] C.L. Bennet et al. -year Wilkinson Microwave Anisotropy Probe (WMAP) Observations: Are There Cosmic Microwave Background Anomalies?. The Astrophysical Journal Supplement 192, id. 17, 2011.

[26] The Planck Collaboration, *Planck 2013 results. I. Overview of products and scientific results*, Astronomy & Astrophysics, Vol. 571, id. A1, pp. 48, 2014

[27] R. Williamson et al., *A Measurement of the Damping Tail of the Cosmic Microwave Background Power Spectrum with the South Pole Telescope*, Astrophysical Journal, vol. 743, p. 28, 2011

[28] J. Dunkley et al., *The Atacama Cosmology Telescope: Cosmological Parameters from the 2008 Power Spectrum*, The Astrophysical Journal, vol. 739, id. 52, 2011

[29] M. Birkinshaw, *The Sunyaev-Zel'dovich effect*, Physics Reports-Review Section of Physics Letters 310 (2-3), pp. 98-195, 1999

[30] The Planck Collaboration, *Planck Early Results: Statistical properties of extragalactic radio sources in the Planck Early Release Compact Source Catalogue*, Astronomy and Astrophysics, vol. 536, A13, 2011

[31] R. Williamson et al., *A Sunyaev-Zel'dovich-selected Sample of the Most Massive Galaxy Clusters in the 2500 deg3 South Pole Telescope Survey*, The Astrophysical Journal, vol. 738, id. 139, 2011

[32] T.A. Marriage et al., *The Atacama Cosmology Telescope: Sunyaev- Zel'dovich-Selected Galaxy Clusters at 148 GHz in the 2008 Survey*, The Astrophysical Journal, vol. 739, id. 52, 2011

[33] The BICEP2 Collaboration, *BICEP2-I: Detection of B-mode Polarization at Degree Angular Scales by BICEP2*, Phys. Rev. Lett. 112, 241101, 2014

[34] A. G. Polnarev, *Polarization and Anisotropy Induced in the Microwave Background by Cosmological Gravitational Waves* Soviet Astronomy, vol. 29, pp. 607-613, 1985

[35] D. Baumann et al., *Probing Inflation with CMB Polarization*, AIP Conf. Proc., 1141:10-120, 2009

[36] B. Reichborn-Kjennerud; et al., *EBEX: a balloon-borne CMB polarization experiment.* SPIE Proc., Vol. 7741, pp. 77411C, 2010

[37] M.D. Niemack; et al., *ACTPol: a polarization-sensitive receiver for the Atacama Cosmology Telescope*, Proc. SPIE, Vol. 7741, 77411S, 2010

[38] J.J. McMahon; et al., *SPTpol: an instrument for CMB polarization measurements with the South Pole Telescope*, Proc. SPIE, vol. 8452, 84520E, 2012

[39] The LSPE Collaboration, *The Large-Scale Polarization Explorer (LSPE)*, SPIE Proc., Vol. 8446, article id. 84467A, 2012

[40] A. Monfardini et al., *The Néel IRAM KID Arrays (NIKA)*, Journal of Low Temperature Physics, Volume 167, Issue 5-6, pp. 834-839, 2012

[41] A. Catalano et al. *Performance and calibration of the NIKA camera at the IRAM 30m telescope*, A&A 569, A9, 2014

[42] A. Monfardini, et al., *Latest NIKA results and the NIKA-2 project*, Journal of Low Temperature Physics, vol. 176, Issue 5-6, pp. 787-795, 2014

[43] S.R. Golwala et al., *Status of MUSIC, the MUltiwavelength Sub/millimeter Inductance Camera*, Proc. SPIE, vol. 8452, id. 845205, 2012

[44] D.C. Moore, *A Search for Low-Mass Dark Matter with the Cryogenic Dark Matter Search and the Development of Highly Multiplexed Phonon-Mediated Particle Detectors*, PhD thesis, California Institute of Technology, Pasadena, California, US, 2012

[45] D.C. Moore et al., *Position and energy-resolved particle detection using phonon-mediated microwave kinetic inductance detectors*, Appl. Phys. Lett. 100, 232601, 2012

[46] L.J. Swenson et al., *High-speed phonon imaging using frequency-multiplexed kinetic inductance detectors*, Appl. Phys. Lett., 96, 23, 2010

[47] A. Cruciani, *Conception and Development of Kinetic Inductance Detectors for millimeter astronomy and X-rays*, PhD thesis, UniversitÃ Sapienza, Roma, Italy

[48] A. D'Addabbo et al., *High-energy interactions in kinetic inductance detectors arrays*, SPIE Proc., vol. 9153, id. 91532Q, 2014

[49] M. Daal et al., *Kinetic Inductance Phonon Sensors for the Cryogenic Dark Matter Search Experiment*, Journal Of Low Temperature Physics, vol. 151, p. 544, 2008

[50] S. Golwala; et al. A WIMP Dark Matter Detector Using MKIDs. Journal Of Low Temperature Physics 151, 550, 2008

[51] M. Faverzani; et al. Development of Microresonator Detectors for Neutrino Physics in Milano. Journal of Low Temperature Physics, in press, 2011. 20, 101

[52] S. Di Domizio et al., *Cryogenic wide-area light detectors for neutrino and dark matter searches*, Proceedings of Low Temperature Detectors 15 (LTD−15), to be published on JLTP

[53] C. Arnaboldi et. al., *CUORE: A Cryogenic Underground Observatory for Rare Events*, Nucl. Instrum. Meth. A 518, 775, 2004

[54] S. Hannestad, *Cosmological neutrinos*, New J.Phys. 6, 108, 2003

[55] The IceCube Collaboration, *Measurement of Atmospheric Neutrino Oscillations with IceCube*, Phys. Rev. Lett., vol. 111, 081801, 2013

[56] C. Amsler et al., *Review of Particle Physics*, Phys. Lett. B 667, vol. 1, issue 1, pp. 1-7, 2008

[57] E. Ferri et al., *The MARE experiment: Microcalorimeter Array for a Rhenium Experiment*, Il Nuovo Cimento C 031, 489-495, 2008

[58] M. Faverzani et al., *Development of Microresonator Detectors for Neutrino Physics in Milano*, Journal of Low Temperature Physics, Volume 167, Issue 5-6, pp. 1041-1047, 2011

[59] F. Ferroni, *LUCIFER: A New Technique for Double Beta Decay*, Nuovo Cim. C033N5, 27-34., 2010

[60] C. Arnaboldi et al., *Results from a search for the* $0\nu\nu\beta$*-decay of* Te^{130}, Phys. Rev. C 78, 035502, 2008

[61] P. J. E. Peebles, *Principles of Physical Cosmology*, Princeton, NJ: Princeton University Press, 1993

[62] J. Lesgourgues et al., *Massive neutrinos and cosmology*, Physics Reports, Vol. 429, Issue 6, pp. 307-379, 2006

[63] M. W. Goodman and E. Witten, *Detectability of certain dark matter candidates*, Phys. Rev. D , vol. 31, pp. 3059-3063, 1985

[64] J. R. Primack, D. Seckel, and B. Sadoulet, *Detection of cosmic dark matter*, vol. 38, pp. 751-807, 1988

[65] G. Jungman, M. Kamionkowski, and K. Griest, *Supersymmetric dark matter*, Phys. Rep. , vol. 267, pp. 195-373, 1996

[66] Z. Ahmed et al., *Dark Matter Search Results from the CDMS II Experiment*, Science 327, p.1619, 2010

[67] V. Sanglard et al., *Final results of the EDELWEISS-I dark matter search with cryogenic heat-and-ionization Ge detectors*, Phys. Rev. D. 71, p. 12202., 2005

[68] H. Kraus et al., *EURECA: The European future of cryogenic dark matter searches*, Journal of Physics: Conference Series, Vol. 39, Issue 1, pp. 139-141, 2006

[69] J. Gao, *The Physics of Superconducting Microwave Resonators*, PhD thesis, California Institute of Technology, Pasadena, California, USA, 2008

[70] R. Pöpel., *Surface impedance and reflectivity of superconductors*, Journal of Applied Physics, 66(12):5950-5957, 1989

[71] C. J. Gorter and H. B. G. Casimir, *On superconductivity*, I. Physica, 1:306 320, 1934

[72] B. Geilikman and V. Kresin, *Kinetic and Nonsteady-state Effects in Superconductors*, John Wiley and Sons, 1974

[73] H. G. Leduc et al., *Titanium Nitride Films for Ultrasensitive Microresonator Detectors*, Applied Physics Letters, Volume 97, Issue 10, id. 102509, 2010

[74] S.B. Kaplan et al., *Quasiparticle and phonon lifetimes in superconductor*, Phys. Rev. B, vol 14, pp. 4854-4873, 1976

[75] R. Barends et al., *Quasiparticle relaxation in optically excited high-Q superconducting resonators*, Phys. Rev. Lett. 100, 257002, 2008

[76] M.J. Rösch, *Development of lumped element kinetic inductance detectors for mm-wave astronomy at the IRAM 30m telescope*, PhD thesis, Karlsruher Instituts für Technologie, Karlsruher, Germany, 2013

[77] A. Monfardini et al., *NIKA: A millimeter-wave kinetic inductance camera*, A&A, Vol. 521, id.A29, 2010

[78] M. Calvo, *Development of Kinetic Inductance Detectors for the study of the Cosmic Microwave Background Polarization*, PhD thesis, UniversitÃ Sapienza, Rome, Italy, 2008

[79] B. A. Mazin, *Microwave kinetic inductance detectors*, PhD thesis, California Institute of Technology, Pasadena, California, US, 2005.

[80] D. M. Pozar., *Microwave Engineering*, Wiley, 2005

[81] A. V. Sergeevl et al., *Ultrasensitive hot-electron kinetic-inductance detectors operating well below the superconducting transition*, Applied Physics letters, 80((5)):817-819, 2002

[82] P.J. de Visser et al., *Fluctuations in the electron system of a superconductor exposed to a photon flux*, Nature Communications, Volume 5, id. 3130, 2014

[83] R.W. Boyd, *Photon bunching and the photon-noise-limited performance of infrared detectors*, Infrared Physics, Volume 22, Issue 3, p. 157-162, 1982

[84] R. Barends et al., *Noise in NbTiN, Al, and Ta Superconducting Resonators on Silicon and Sapphire Substrates*, IEEE Transactions on Applied Superconductivity, vol. 19, issue 3, pp. 936-939, 2009

[85] J. Gao et al., *A semiempirical model for two-level system noise in superconducting microresonators*, Applied Physics Letters, vol. 92, Issue 21, id. 212504, 2008

[86] S. Kumar et al., *Temperature dependence of the frequency and noise of superconducting coplanar waveguide resonators*, Appl. Phys. Lett., vol. 92, Issue 12, id. 123503, 2008

[87] O. Noroozian, J. Gao, J. Zmuidzinas, H.G. Leduc, and B.A. Mazin. *Two-level system noise reduction for Microwave Kinetic Inductance Detectors*, AIP Conference Proceedings LTD13, 1185:148-152, 2009

[88] L.J. Swenson et al., *Operation of a titanium nitride superconducting microresonator detector in the nonlinear regime*, Journal of Applied Physics, Volume 113, Issue 10, pp. 104501-104501-9, 2013

[89] A. Monfardini et al., *A dual-band millimeter-wave kinetic inductance camera for the IRAM 30m telescope*, ApJ Supplment Series, Vol. 194, Num. 2, 24, 2011

[90] L. Swenson et al., *A fast, ultra-sensitive and scalable detection platform based on superconducting resonators for fundamental condensed-matter and astronomical measurements*, 13th international workshop on Low Temperature Detectors, AIP Conf. Proc. 1185, 84, 2009

[91] O. bourrion et al., *Electronics and data acquisition demonstrator for a kinetic inductance camera*, doi: 10.1088/1748-0221/6/06/P06012, JINST 6 P06012, 2011

[92] J. Volder, *The CORDIC trigonometric computing technique*, IRE Trans. Electron. Comput. 8, pp. 330-334, 1959

[93] O. Bourrion et al., *NIKEL: Electronics and data acquisition for kilopixels kinetic inductance camera*, doi: 10.1088/1748-0221/7/07/P07014, JINST 7 P07014, 2012

[94] O. Bourrion et al., *High speed readout electronics development for frequency-multiplexed kinetic inductance detector design optimization*, Proceedings of the TWEPP−13, doi: 10.1088/1748-0221/8/12/C12006, JINST 8 C12006, 2013

[95] M. Calvo et al., *Improved mm-wave photometry for kinetic inductance detectors*, Astronomy & Astrophysics, Volume 551, id.L12, 4 pp., 2013

[96] S. Doyle et al., *Lumped Element Kinetic Inductance Detectors*, Journal of Low Temperature Physics, Volume 151, Issue 1-2, pp. 530-536, 2008

[97] M. J. Griffin, J. J. Bock and W. K. Gear, *Relative performance of filled and feedhorn-coupled focal-plane architectures*, Applied Optics, vol. 41, iss. no. 31, pp. 6543-6554, 2002

[98] M. Carter, *The EMIR multi-band mm-wave receiver for the IRAM 30-m telescope*, Astronomy & Astrophysics, Volume 538, id.A89, 13 pp., 2012

[99] J.G. Staguhn, *Latest results from GISMO: A 2-Millimeter Bolometer Camera for the IRAM 30m Telescope*, EAS Publications Series, Volume 52, pp.267-271, 2011

[100] J.R. Pardo, M. Ridal,D. Murtagh, J. Cernicharo, *Microwave temperature and pressure measurements with the Odin satellite: I. Observational method*, Canadian Journal of Physics. Vol. 80, p.443, 2002

[101] T. Durand, *RÂ´ealisation d'un interfÂ´erometre de Martin-Puplett pour le dÂ´eveloppement d'une camÂ´era bolomÂ´etrique*, Université Joseph-Fourier, Grenoble, France, 2007

[102] R.H. Dicke et al., *Atmospheric Absorption Measurements with a Microwave Radiometer*, Physical Review, vol. 70, Issue 5-6, pp. 340-348, 1946

[103] Hily-Blant et al., *Velocity field and star formation in the Horsehead nebula*, Astronomy & Astrophysics, Volume 440, Issue 3, pp. 909-919, 2005

[104] E. Kreysa, *Submm/FIR bolometers*, Proceedings of an ESA Symposium on Photon Detectors for Space Instrumentation pp. 207-210, 1992

[105] R. Adam et al., *First observation of the thermal Sunyaev-Zel'dovich effect with KID*, A&A 569, A66, 2014

[106] S. Marnieros, *Couches Minces d'Isolant Anderson. Application à la Bolométrie à Très Basse Température*, PhD Thesis, Université de Paris-Sud, UFR Scientifique d'Orsay, France, 1998

[107] A. Bideaud et al., *Antenna-coupled arrays of NbSi micro-bolometers*, Experimental Astronomy, Volume 32, Issue 2, pp. 179-191, 2011

[108] 8. C. Nones et al., *High-impedance NbSi TES sensors for studying the cosmic microwave background radiation*, Astronomy & Astrophysics 548, A17, 2012

[109] M. Calvo et al., *Niobium Silicon alloys for Kinetic Inductance Detectors*, Proceedings of Low Temperature Detectors 15 (LTDâ15), JLTP Vol. 176, Issue 3-4, pp 518-523, 2013

[110] B. Sacèpè et al., *Disorder-Induced Inhomogeneities of the Superconducting State Close to the Superconductor-Insulator Transition*, Physical Review Letters, vol. 101, Issue 15, id. 157006, 2008

[111] O. Rigaut, *Nouveaux concepts pour les matrices de bolom'etres destinÂ´ees 'a lâexploration de lâUnivers dans le domaine millimÂ´etrique*, PhD thesis, UniversitÂ´e Paris Sud, Paris, France, 2014

[112] P.H. Keck, *Floating Zone Recrystallization of Silicon*, Review of Scientific Instruments, Vol. 25 , Issue 4 , pp. 331-334, 2009

[113] S. J. Melhuish et al., *A tiltable single-shot miniature dilution refrigerator for astrophysical applications*, Cryogenics, Volume 55, pp. 63-67, 2013

[114] A. Coppolecchia, *Cryogenic detectors for sub-millimeter and millimeter wave Astronomy*, PhD thesis, Universitá Sapienza, Rome, Italy, 2014

[115] L. Adam, *Recommended values for the thermal conductivity of aluminium of different purities in the cryogenic to room temperature range, and a comparison with copper*, Cryogenics, Volume 45, Issue 9, pp. 626â636, 2005

[116] M. Barucci et al., *Aluminum alloys for space applications: low temperature thermal conductivity of A6061-T6 and A1050*, Proceedings of the 8th Conference of Astroparticle, particle and space physics, detectors and medical physics applications, doi: 10.1142/9789812702708-0079, 2004

[117] M.C. Runyan and W.C. Jonesa, *Thermal Conductivity of Thermally-Isolating Polymeric and Composite Structural Support Materials Between 0.3 and 4 K*, Cryogenics, v. 48, iss. 9-10, p. 448-454, 2008

[118] A.T. Lee et al., *Measurements of the ballistic-phonon component resulting from nuclear and electron recoils in crystalline silicon*,Physical Review B, Volume 54, Issue 5, pp.3244-3256, 1996

[119] O. Adriani et al., *PAMELA Measurements of Cosmic-Ray Proton and Helium Spectra*, Science, 332, 69, 2011

[120] The Planck Collaboration, *Planck 2013 results. X. HFI energetic particle effects: characterization, removal, and simulation*, A&A, Astronomy Astrophysics, Volume 571, id.A10, 23 pp., 2014

[121] R.A. Mewaldt et al., *Record-setting Cosmic-ray Intensities in 2009 and 2010*, ApJ, 723, L1, 2010

[122] The Planck Core Team, *Planck early results. VI. The High Frequency Instrument data processing*, A&A, Volume 536, A6, 2011

[123] A. Catalano et al., *Impact of particles on the Planck HFI detectors: Ground-based measurements and physical interpretation*, A&A, accepted for publication, arXiv:1403.6592

[124] I. Morison, *Introduction to Astronomy and Cosmology*, John Wiley & Sons., p. 198. ISBN 978-0-470-03333-3, 2008

[125] Haino S. et al., *Measurement of primary and atmospheric cosmic-ray spectra with the Bess-TeV spectrometer*, Phys.Lett. B594, 35-46, 2004

[126] C.F. Williamson, J.P. Boujot and J. Picard, *Tables of Ranges and Stopping Power of Chemical Elements for Charged Particles of Energy 0.05 to 500 MeV*, Report CEA-R3042, Centre d'Etudes Nucleaires, Saclay, France, 1966

[127] S. Tavernier, *Experimental techniques in nuclear and particle physics*, Ed. Springer, 30, 2010

[128] *Modern Developments in X-Ray and Neutron Optics*, Erko, A., Idir, M., Krist, Th., Michette, A.G. (Eds.), 2008

[129] P.J. de Visser et al., *Number fluctuations of sparse quasiparticles in a superconductor*, Physical Review Letters, vol. 106, Issue 16, id. 167004, 2011

[130] T.O. Niinikoski et al., *Heat Capacity of a Silicon Calorimeter at Low Temperatures Measured by Alpha-Particles*, EPL (Europhysics Letters), Vol. 1, p.499, 1986

[131] CRESST Collaboration, *Results on low mass WIMPs using an upgraded CRESST-II detector*, The European Physical Journal C, Volume 74, Issue 12, Article 3184, 2014

[132] N. Casali et al., *TeO_2 bolometers with Cherenkov signal tagging: towards next-generation neutrinoless double beta decay experiments*, doi:10.1140/epjc/s10052-014-3225-4, Eur. Phys. J. C 75, 12, 2015

[133] K. M. Itoh, et al., *Neutron transmutation doping of isotopically engineered Ge*, Appl. Phys. Lett. 64, 2121, 1994

[134] T. Tabarelli de Fatis, *Cerenkov emission as a positive tag of double beta decays in bolometric experiments*, Eur. Phys. J. C 65, pp. 359-361, 2010

[135] J.W. Beeman et al., *Performances of a large mass ZnSe bolometer to search for rare events*, doi: 10.1088/1748-0221/8/05/P05021, JINST 8 P05021, 2013

[136] J. Bardeen et al., *Microscopic theory of superconductivity*, Phys. Rev. 106, 162, 1957.

[137] M. Tinkham, *Introduction to superconductivity*, 2nd edition, McGraw-Hill International Editions, Singapore, 1996

[138] T. Van Duzer and C. W. Turner, *Principles of Superconducting Devices and Circuits*, Edward Arnold, 1981

[139] G. Vardulakis, *Superconducting Kinetic Inductance Detectors, Theory, Simulations and Experiments*, PhD thesis, Cambridge University, Astrophysics Group - UK, 2007

[140] C. J. Gorter and H. B. G. Casimir, *The thermodynamics of the superconducting state*, Physic. Z., 15:539-542, 1956

[141] F. London and H. London, *The Electromagnetic Equations of the Superconductor*, Proceedings of the Royal Society Series, A(149):71-88, 1935

[142] F. London; et al., *The electromagnetic equations of the superconductor*, Proceedings of the Royal Society of London A 149, 71, 1935

[143] W. Meissner and R. Ochsenfeld, *Ein neuer Effekt bei Eintritt der Supraleitfähigkeit*, Naturwissenschaften, 21(44):787-788, 1933

[144] A. B. Pippard, *An experimental and theoretical study of the relation between magnetic field and current in a superconductor*, Proc. Roy. Soc., A216:547-568, 1953

[145] D. C. Mattis and J. Bardeen, *Theory of the anomalous skin effect in normal and superconducting metals*, Phys. Rev., vol. 111, pp. 412-417, 1958